biomimetics

MDPI

Perspective

Revealing the Wonder of Natural Photonics by Nonlinear Optics

Dimitrije Mara [1], Bojana Bokic [2], Thierry Verbiest [3], Sébastien R. Mouchet [4,5,*] and Branko Kolaric [2,6,*]

1 Institute of General and Physical Chemistry, Studentski trg 12/V, 11158 Belgrade, Serbia
2 Center for Photonics, Institute of Physics, University of Belgrade, Pregrevica 118, 11080 Belgrade, Serbia
3 Molecular Imaging and Photonics, Department of Chemistry, KU Leuven, Celestijnenlaan 200D, 3001 Heverlee, Belgium
4 Department of Physics and Astronomy, University of Exeter, Stocker Road, Exeter EX4 4QL, UK
5 Department of Physics & Namur Institute of Structured Matter (NISM), University of Namur, Rue de Bruxelles 61, 5000 Namur, Belgium
6 Micro- and Nanophotonic Materials Group, University of Mons, Place du Parc 20, 7000 Mons, Belgium
* Correspondence: sebastien.mouchet@unamur.be (S.R.M.); branko.kolaric@umons.ac.be (B.K.)

Abstract: Nano-optics explores linear and nonlinear phenomena at the nanoscale to advance fundamental knowledge about materials and their interaction with light in the classical and quantum domains in order to develop new photonics-based technologies. In this perspective article, we review recent progress regarding the application of nonlinear optical methods to reveal the links between photonic structures and functions of natural photonic geometries. Furthermore, nonlinear optics offers a way to unveil and exploit the complexity of the natural world for developing new materials and technologies for the generation, detection, manipulation, and storage of light at the nanoscale, as well as sensing, metrology, and communication.

Keywords: natural photonics; photonics; linear and nonlinearspectroscopy; fluorescence; fluorescence spectroscopy; two-photon fluorescence; second-harmonic generation; third-harmonic generation

check for updates

Citation: Mara, D.; Bokic, B.; Verbiest, T.; Mouchet, S.R.; Kolaric, B. Revealing the Wonder of Natural Photonics by Nonlinear Optics. *Biomimetics* **2022**, *7*, 153. https://doi.org/10.3390/biomimetics7040153

Academic Editors: Silvia Vignolini, Rox Middleton and Stanislav N. Gorb

Received: 28 July 2022
Accepted: 30 September 2022
Published: 5 October 2022

Publisher's Note: MDPI stays neutral with regard to jurisdictional claims in published maps and institutional affiliations.

Copyright: © 2022 by the authors. Licensee MDPI, Basel, Switzerland. This article is an open access article distributed under the terms and conditions of the Creative Commons Attribution (CC BY) license (https://creativecommons.org/licenses/by/4.0/).

1. Introduction

It has been known for a long time that colors in nature are not designed for beauty but are of the utmost importance for communication. Structural colors belong to a special class of colors that have no chemical origin, but they arise from the interaction of light with structures, such as periodically arranged materials [1,2]. Structural colors are ubiquitous colors among insects, fish, and birds. In addition, they are a main topic of research in fields such as biophotonics and biomimetics. In this perspective article, we demonstrate the interest and impact of nonlinear optical studies of photonic structures. We highlight the benefit of nonlinear optical techniques for revealing the details of structured matter at the nanoscale and its interaction with light. We also emphasize that the control of structural colors is essential for various applications in materials science. After introducing the readers to basic concepts of nonlinear optics and natural photonics, we present different cases of natural photonic structures (sometimes combined with artificial materials) investigated by nonlinear optical techniques.

2. Basics of Nonlinear Optics

Nonlinear optics is a part of optics that studies light propagation in nonlinear media. In such media, the polarization P has a nonlinear response to the electric field E. Such optical behavior usually occurs at a high intensity of light, such as the one generated by a laser.

In the linear regime, when an electromagnetic wave interacts with some materials, e.g., a medium containing electric charges, a dipolar type of interaction appears between the dipoles in the medium and the incident electromagnetic fields at a frequency ω [3]. This

interaction can be described by an induced polarization P_{ind} that is linear with the electric field E of the incident light and acts as the source of radiation:

$$P_{\text{ind}} = \chi^{(1)} E, \tag{1}$$

with $\chi^{(1)}$, the linear susceptibility that is related to the refractive index. The response can be modelled by a classical harmonic oscillator, yielding a linear complex refractive index of the medium that scales with ω [3].

However, in the case of high-intensity incident electromagnetic fields, such as laser light (Figure 1), the harmonic oscillator response is not sufficient anymore to describe the observed phenomena [4–7]. The oscillations become anharmonic, i.e., they do not respond linearly to the incident electromagnetic wave. In the nonlinear regime, the induced polarization P_{ind} is expanded in a Taylor series as a function of the total applied electric field. The induced polarization is then written as [7]:

$$P_{\text{ind}} = P^{(1)} + P^{(2)} + P^{(3)} + \cdots = \chi^{(1)} E + \chi^{(2)} EE + \chi^{(3)} EEE + \cdots \tag{2}$$

with $P^{(1)}$, the linear part of the induced polarization; $P^{(2)}$, the second-order nonlinear response; and $P^{(3)}$, the third order nonlinear response. $\chi^{(1)}$, $\chi^{(2)}$, and $\chi^{(3)}$ are the linear, the first nonlinear, and the second nonlinear susceptibilities, respectively. The latter two quantify the second-order and third-order nonlinear optical response. Since all susceptibilities are related to the refractive index, a nonlinear complex refractive index is obtained.

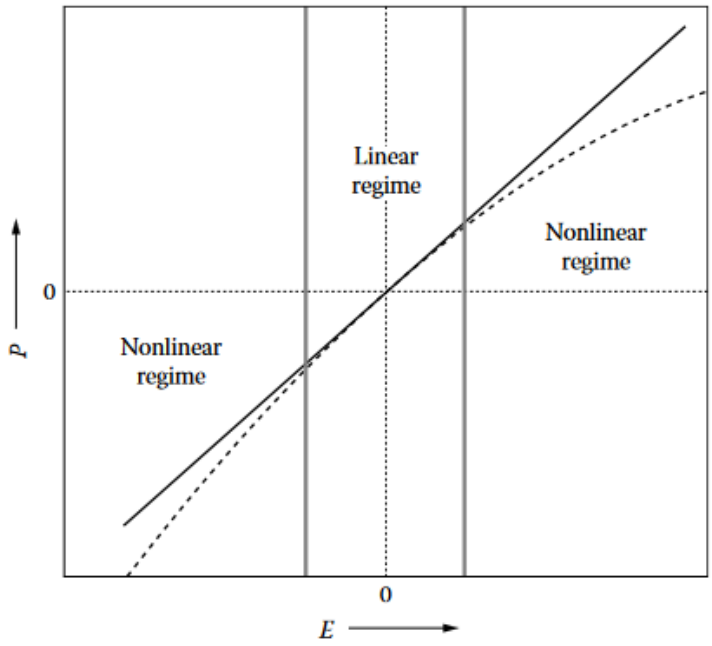


Figure 1. Depending on the intensity of the incident electric field (E), the electric polarization (P) will respond linearly or nonlinearly. As long as the intensity of the electric field is small, the electric polarization is linear to the electric field intensity. This case corresponds to the linear regime. When the intensity of the electric field is high, P is not proportional to E and the regime is nonlinear. Reproduced from Verbiest, T., Clays, K., and Rodriguez, V., 2009. Second-order Nonlinear Optical Characterization Techniques: An Introduction, with permission from Taylor and Francis Group, LLC, a division of Informa plc.

One of the advantages of nonlinear optical techniques is due to the nature of the nonlinear susceptibilities, which are tensors of third and fourth rank, respectively. Especially, second-order nonlinear optical effects, which are described by the third-rank tensor $\chi^{(2)}$, have extremely interesting symmetry properties. In general, $\chi^{(2)}$ is a third-rank tensor with 27 components, but the number of independent and nonvanishing components is

dependent on the symmetry of the medium. All of the components of $\chi^{(2)}$ will vanish in a medium with inversion symmetry. On the other hand, any surface where the symmetry is necessarily broken will typically yield four independent susceptibility components [7]. Since the nonlinear susceptibility directly determines the magnitude and phase of the nonlinear response, the measured response can serve as a means to evaluate the symmetry of the sample.

In addition to the optical properties of matter that can be probed by linear techniques, much more information is available by exploiting the interaction of matter with higher-intensity laser beams. Multiphoton (including two-photon) excitation fluorescence is certainly the most used nonlinear optical technique. In the case of two-photon excitation fluorescence (TPEF), high-intensity photons illuminate a sample [7]. Because of this high intensity, two photons simultaneously interact with the sample, following different selection rules from the photons in the linear light–matter interaction regime. Since two photons are absorbed initially and give rise to only one emitted photon, the resulting photon has a higher energy than each of the two absorbed photons. Multiphoton absorption and fluorescence originate from a third-order nonlinear optical response [7].

In second harmonic generation (SHG), the material also interacts with two photons [7]. Unlike two-photon excitation fluorescence, a third photon is instantaneously emitted (within ca 10^{-15} s) with exactly twice the energy (and, thus, half the wavelength) of the two initial photons. Since SHG is a second-order nonlinear optical process, selection rules that are different from TPEF apply: symmetry requirements such as non-centrosymmetric samples are essential to observe SHG [4–7]. Similarly, third harmonic generation (THG) corresponds to the instantaneous emission of a single photon following the interaction of three incident photons [7]. The generated photon has three times the energy and a third of the wavelength of the three initial photons.

There are multiple advantages to nonlinear techniques with respect to linear optical techniques [8,9]. An important feature is the increase in imaging depth, which can be attributed to multiple factors: first, there is a low probability of multiple photons interacting simultaneously, resulting in a minimal imaging volume at the femtoliter scale by reducing out-of-focus fluorescence. It is therefore possible to image accurately at different depths, similarly to confocal microscopes, and to create 3D reconstructions of the investigated material without the use of a pinhole. Due to the absence of a pinhole, more light can be collected and thus a clearer image can be formed. This also results in an increase in the practical resolution as the pinhole of confocal microscopes is often opened to increase the amount of incoming light to image fluorescing samples. This results in a lower resolution. Practically, the resolution of a multiphoton microscope was shown to approach 250 nm, which equals the best possible resolution of the confocal fluorescence microscopy. Another significant advantage of nonlinear optical techniques is the use of near-infrared excitation light with wavelengths corresponding to the transparency window of biological tissue. This leads to an increase in penetration depth, and it is therefore possible to image sensitive samples without damaging the structure or with minimal damage. Furthermore, most multi-photon microscopes use femtosecond-lasers as an excitation source, which further reduces the risk of photodamage. In addition, no sample preparation is necessary. This constitutes the main advantage over more complicated microscopy techniques such as scanning electron microscopy (SEM) or transmission electron microscopy (TEM) [10,11]. Finally, another interesting application of multiphoton microscopy is the imaging of the local polarization anisotropy via SHG, enabling the user to seperately determine the orientation and degree of organization of each non-centrosymmetric component within a sample.

3. Introduction to Natural Photonics

Colours in nature originate from chemical or physical properties of matter, light sources, or combinations of them [1,2]. Chemical colours are caused by pigments. These molecules selectively absorb incident light within a given wavelength band. Examples are eumelanins and pheomelanins, which give rise to brown/black and yellow/red human

skins, respectively [12,13]. Light that is not absorbed by pigments is scattered, giving rise to colours that an observer may perceive. Physical colours are due to interference between incident light and a physical structure. Hence, they are often called structural colours, as a synonym. Structures giving rise to such colours have geometrical dimensions at the micro- or nanoscale. They encompass optical thin films [14–17], diffraction gratings [18–20], Bragg mirrors [21–26], chirped multilayer reflectors [27,28], and photonic crystals [29–34], as well as quasi-ordered [35–40] and randomly disordered [41–44] photonic structures.

Natural photonics is the field of research that studies the interaction between light and such physical structures in nature. Natural structural colours occur in organisms ranging from mammals such as primates (including human blue eyes) and marsupials, fish, or birds such as hummingbirds and pigeons to insects such as butterflies and beetles (Figure 2) [1,2,45].

This section introduces key concepts and presents some selected case studies from natural photonics, in the linear regime.

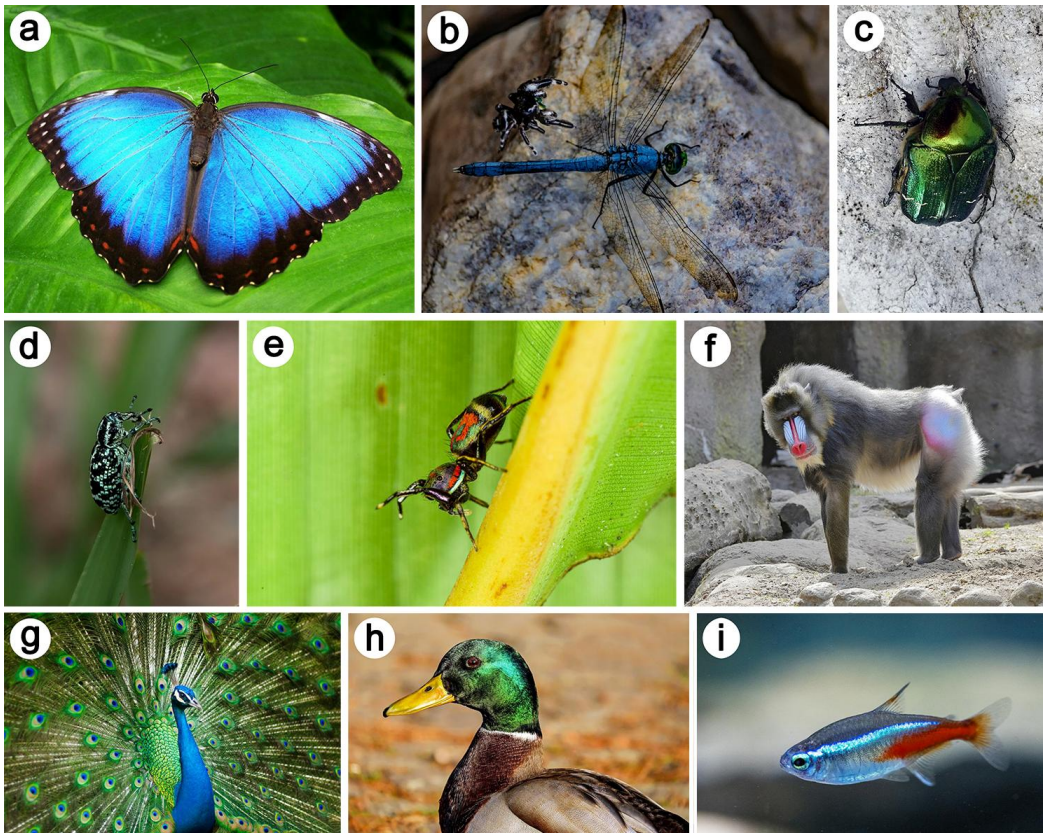


Figure 2. Many examples of structural colours are found in the integuments of natural organisms. They include the wings of the common morpho *Morpho peleides* (**a**), the body of some dragonfly species (**b**), the thorax and elytra of the green rose chafer *Cetonia aurata* (**c**), the body of the Botany Bay diamond weevil *Chrysolopus spectabilis* (**d**), the integuments of some jumping spider species (**e**), the skin of the mandrill *Mandrillus sphinx* (**f**), the feathers of the Indian peafowl *Pavo cristatus* (**g**), the head of the mallard *Anas platyrhynchos* (**h**), and the body of the neon tetra fish *Paracheirodon innesi* (**i**). Reproduced from from https://pixabay.com/ accessed on 27 July 2022.

One striking example is the case of the male beetle *Hoplia coerulea* (Figure 3). The blue-violet iridescent colour of its elytra and body observed in reflection with incident visible light arises from a photonic structure, namely, a porous periodic multilayer, within the round scales occurring on its body [46,47].

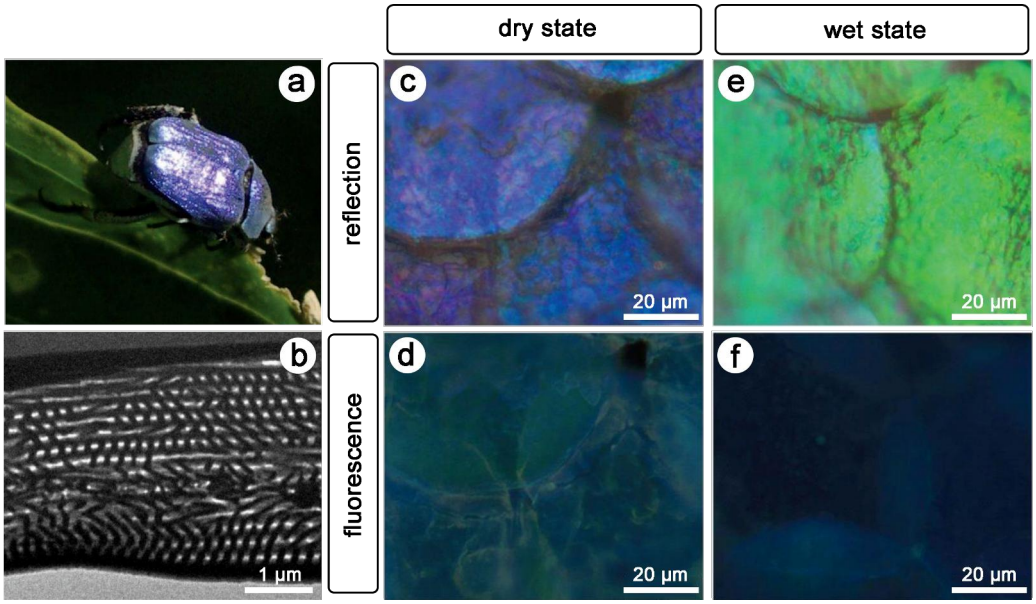


Figure 3. The blue-violet colour of the male beetle *Hoplia coerulea* (**a**) originates from a multilayer photonic structure. This porous periodic multilayer (**b**) occurs in the scales covering the elytra (**c**) and body of the insect. Upon UV light illumination, the scales display a turquoise colour through fluorescence (**d**). When in contact with water, the scales turn to green (**e**) and navy blue (**f**) under visible and UV lightillumination, respectively. Reproduced from Mouchet, S.R., Lobet, M., Kolaric, B., Kaczmarek, A.M., Van Deun, R., Vukusic, P., Deparis, O., and Van Hooijdonk, E., 2016. Controlled fluorescence in a beetle's photonic structure and its sensitivity to environmentally induced changes. Proc. R. Soc. B 283, 20162334, with permission from The Royal Society.

This multilayer is mainly composed of chitin, the building material of insects [1,2]. Upon contact with liquids and vapour, these scales change their colour to green [48–52]: the spectral reflectance peak red-shifts. This colour change arises from the penetration of some liquid into the pores of the scales, filling the pores and changing the refractive index.

Furthermore, one-photon excitation fluorescence (OPEF) emission was observed when the beetle was illuminated with UV light (Figure 3d) [53,54]. The colour of the scales covering the elytra and body of this insect is turquoise. This phenomenon arises in biological organisms, the integuments of which contain so-called fluorophores [55,56]. Examples include birds [44,57–59], insects [60–71], arachnids [72,73], mammals [74], amphibians [75,76], reptiles [77], marine animals [78,79], and plants [80,81] (Figure 2). These molecules emit longer-wavelength light (typically, visible photons) following the absorption of incident shorter-wavelength light (typically, UV, violet or blue photons).

Fluorescence emission results from transition between two real electron states with the same multiplicity of spin. The role, if any, of fluorescence (Figure 4) in visual communication is unclear [55,56]. Biopterin, the green fluorescent protein (GFP), papiliochrom II, psittacofulvin, and resilin are examples of fluorophores.

When light emission takes place in photonic structures, the structure may modify the directionality, the decay time, and the spectral intensity of the emitted light [82,83]. Light emission can be reduced or even inhibited if the emission wavelength is in the range of the photonic bandgap of the structure. The decay time of the excited is then increased and can, theoretically, be infinite. When such light emitted in a photonic structure originates from fluorescence, this phenomenon is often referred to as controlled fluorescence. The confinement of fluorophores in natural photonic structures was found in several species [84–88], including the male beetle *H. coerulea* [53,54]. Upon contact with water, the peak in the fluorescence emission spectrum from the scales of this beetle blue-shifts, giving rise to a navy blue colour (Figure 3d,f). Following the penetration of the porous structure by water, the local density of optical states (LDOS) is modified, leading to the observed colour change.

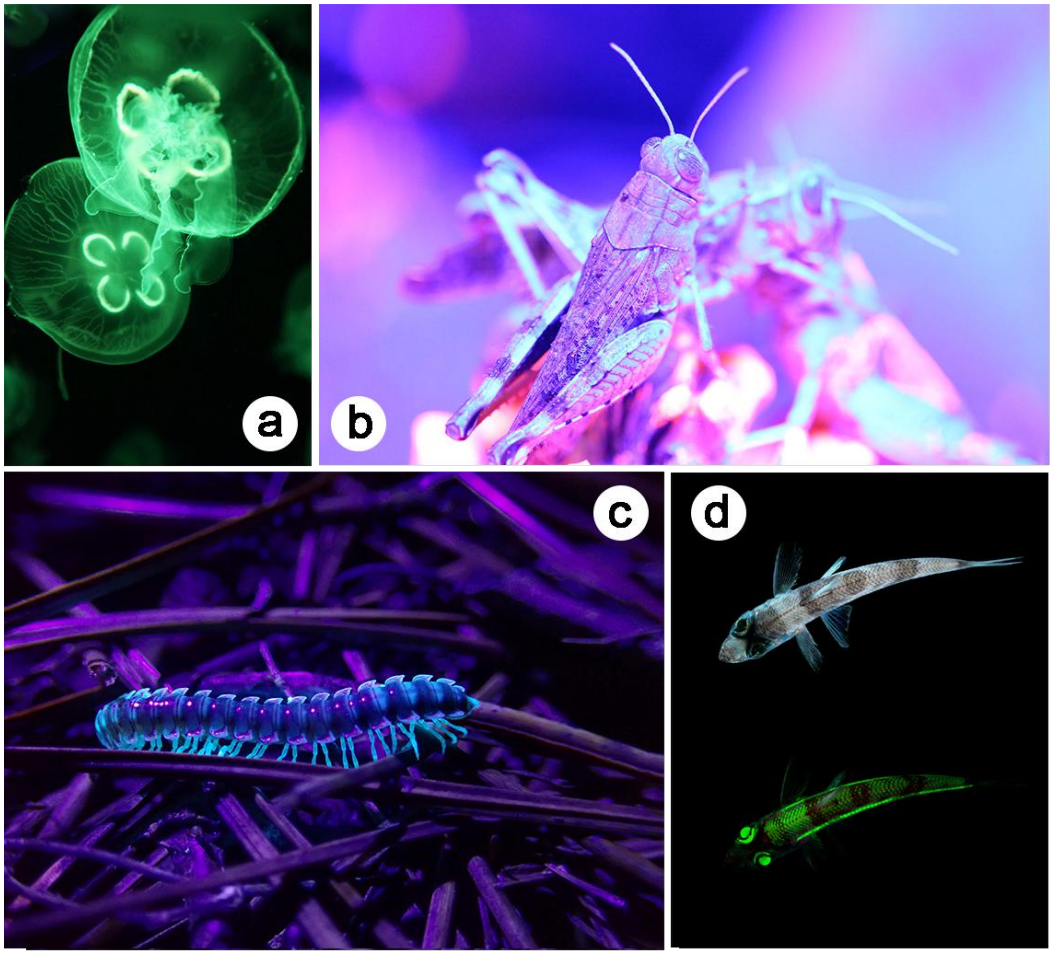


Figure 4. Fluorescence is ubiquitous in the integuments of natural organisms. The integuments of some jellyfish species (**a**), some grasshopper species (**b**), some millipede species (**c**), and some greeneye fish species (**d**) are known for their fluorescent properties. (**d**) Top (bottom): greeneye fish under visible (UV) light. Reproduced from from pixabay.com.

The interaction between fluorescent light and photonic structures was also highlighted in the scales covering the elytra of longhorn beetles *Celosterna pollinosa sulfurea* and *Phosphorus virescens* [68]. These scales exhibit yellow and turquoise colours under visible and UV incident light, respectively, with an underlying basal brown membrane (Figure 5a–d), akin to the beetles *Euchroea auripigmenta* and *Trictenotoma childreni* [69,70]. Through scatterograms and detailed series of simulations, it was demonstrated that the scales play the role of waveguides for light emitted by the embedded fluorophores (Figure 5e,f).

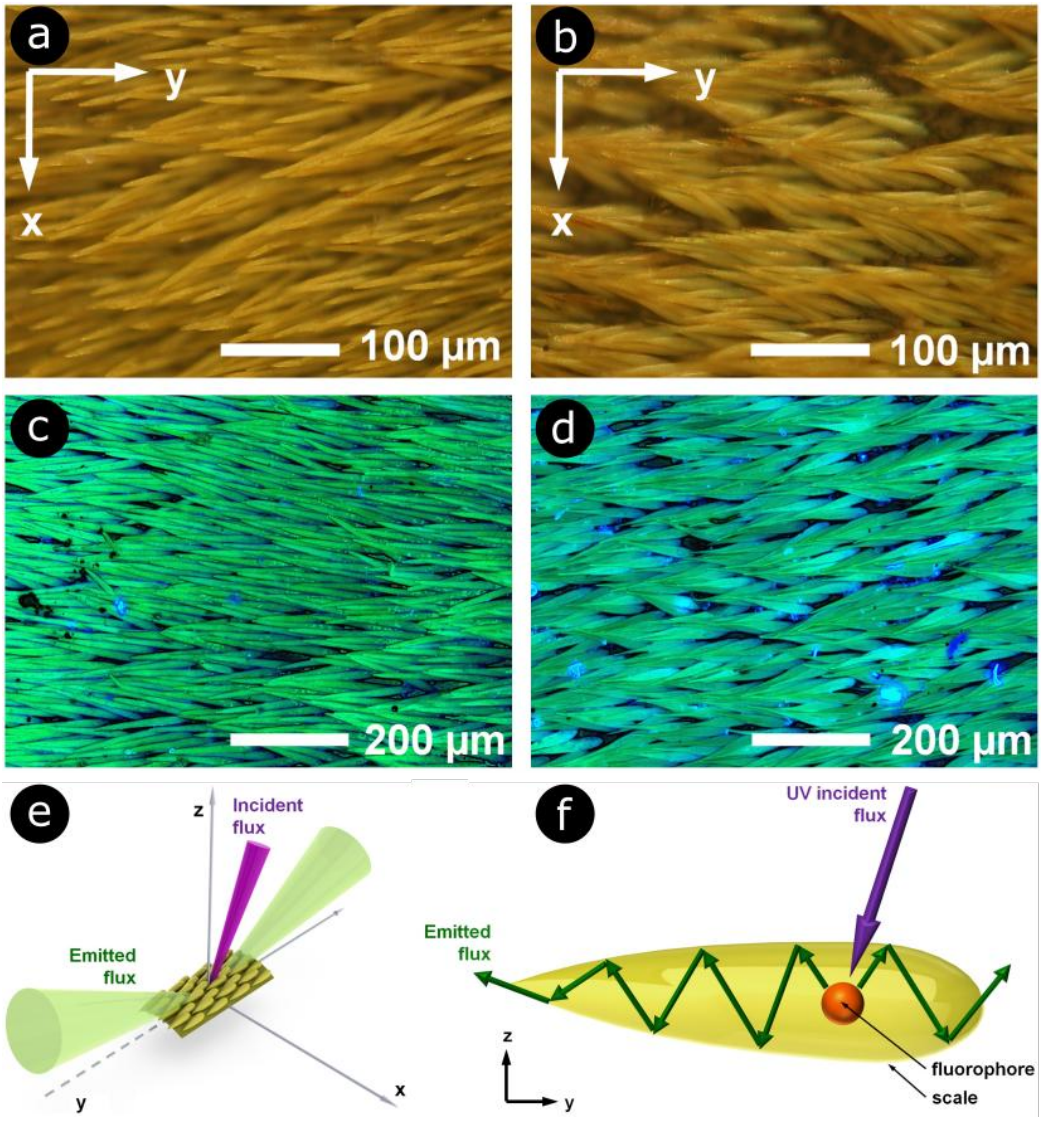


Figure 5. The elytra of longhorn beetles *Celosterna pollinosa sulfurea* and *Phosphorus virescens* are covered by elongated scales, in which fluorophores are embedded. These scales act as waveguides for the light emitted by the fluorophores. They display a yellow colour under visible light for *C. pollinosa sulfurea* (**a**) and *P. virescens* (**b**) (here, observation by optical microscopy). Under UV light, the observed colour is turquoise in both respective cases (**c**,**d**). Upon illumination with UV light (represented in magenta), embedded fluorophores mostly emitted within two emission cones (in green) (**e**) due to a waveguide effect taking place within the scales (**f**). Reproduced from Van Hooijdonk, E., Barthou, C., Vigneron, J.-P., and Berthier, S., 2013. Yellow structurally modified fluorescence in the longhorn beetles *Celosterna pollinosa sulfurea* and *Phosphorus virescens* (Cerambycidae). J. Lumin. 136, 313–321, with permission from Elsevier.

4. Nonlinear Optical Study of Natural Photonic Structures

Harnessing light–matter interaction in a nonlinear regime, researchers and engineers developed various tools for imaging and spectroscopy analyses of biological samples [8,62,89–105]. Nonlinear optical imaging and spectroscopy have proved to be versatile and efficient techniques in biomedical and biological research, with many benefits, including an increase in analytic depth and a reduction in photodamage, with respect to classical linear optical techniques [8]. In general, nonlinear optical studies led to a better understanding of the link between the optical response and geometries of natural photonic structures that are essential for potential applications of these structures in biomimetics and quantum technology [9].

For instance, the multi-excited states character of the fluorophores embedded in the integuments of *H. coerulea* were revealed by comparing OPEF spectra with TPEF measurements [106] (Figure 6a–d).

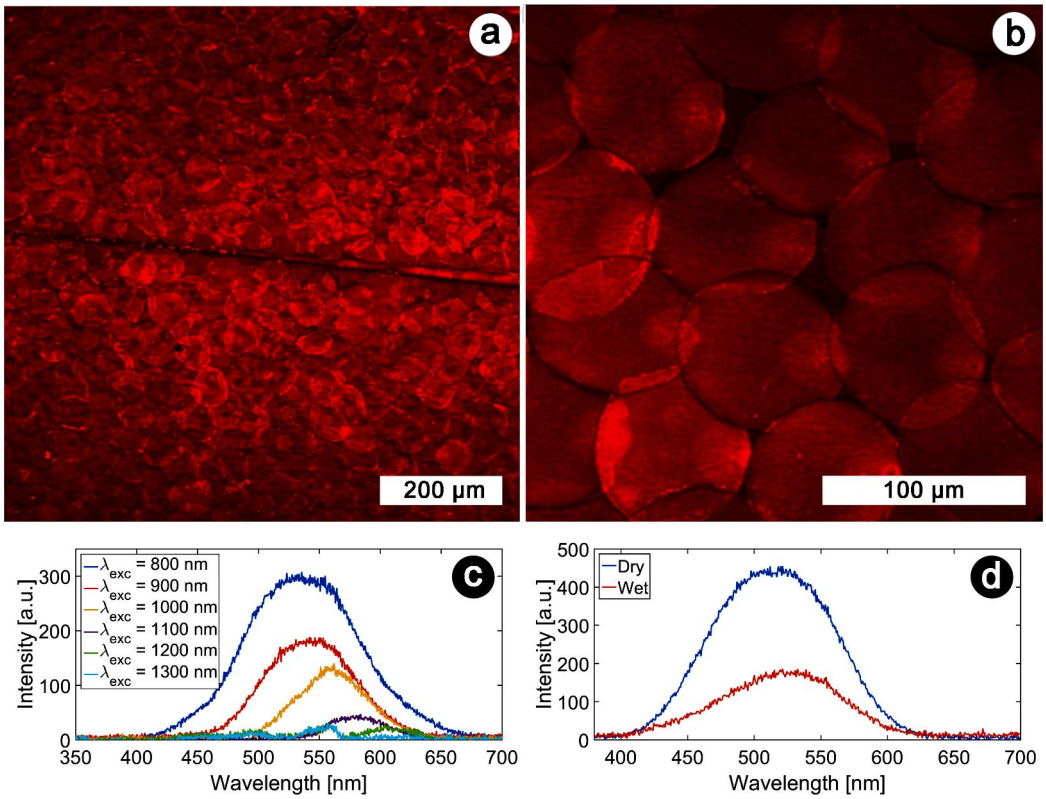


Figure 6. TPEF microscopy and spectroscopy of the scales covering *H. coerulea*'s elytra. An intense TPEF response was detected from the elytra of the male beetle *H. coerulea* with an excitation wavelength equal to 900 nm (**a**) and 800 nm (**b**). TPEF excitation spectra were measured with various excitation wavelengths (**c**). Upon contact with water (**d**), the emitted intensity decreases and the peak wavelength red-shifts slightly (the excitation wavelength equals 800 nm). Scale bars: (**a**) 200 µm and (**b**) 100 µm. Reproduced from Mouchet, S. R., Verstraete, C., Mara, D., Van Cleuvenbergen, S., Finlayson, E. D., Van Deun, R., Deparis, O., Verbiest, T., Maes, B., Vukusic, P., and Kolaric, B., 2019 Nonlinear optical spectroscopy and two-photon excited fluorescence spectroscopy reveal the excited states of fluorophores embedded in a beetle's elytra, Interface Focus 9(1), 20180052, with permission from The Royal Society.

This provided insight into the electron structure of the embedded fluorophores.

Furthermore, local-form anisotropy arising from local-direction-dependent subwavelength morphology was shown to influence both linear and nonlinear optical responses (in reflection and emission) thanks to THG spectroscopy [106]. The anisotropy is caused due to the subwavelength spacers located in the mixed air-chitin layers (Figure 3b). These spacers are locally parallel.

This finding highlighted the need to take a more accurate model into account for predicting some of the optical properties of the elytra of this beetle.

Similarly, the yellow and fluorescent elongated scales covering the elytra of the log-boring beetle *Trictenotoma childreni* were investigated by nonlinear optical methods, including OPEF, TPEF, and SHG microscopy and spectroscopy (Figure 7) [70]. These scales appear similar to the ones of the longhorn beetles *Celosterna pollinosa sulfurea* and *Phosphorus virescens* (Figure 5) [68]. They contain fluorophores that give rise to a yellow visual appearance upon UV illumination. These observations allowed one to highlight the non-centrosymmetric nature of the fluorophores embedded within these scales [70].

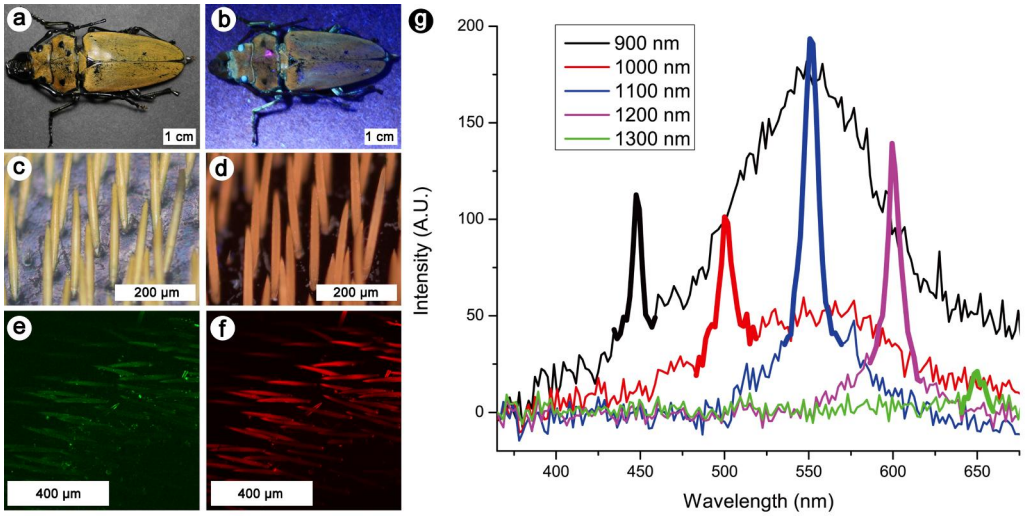


Figure 7. The yellow and fluorescent scales occurring on the elytra of the log-boring beetle *T. childreni* were investigated by nonlinear optical techniques, including OPEF, TPEF, and SHG microscopy and spectroscopy. The elytra exhibit a yellow colour under both incident visible white (**a**) and UV (**b**) light. This colour is due to the presence of elongated scales covering the elytra (**c**,**d**). Under visible (**c**) or UV light (**d**), they appear in shades of yellow. Upon excitation with a fundamental wavelength of 1000 nm, a SHG (**e**) and a TPEF (**f**) signal can be detected from the scales (here observed by microscopy in false colours). Multiphoton emission spectra of the log-boring beetle's scales measured with various excitation wavelengths (**g**) exhibit SHG peaks at half the excitation wavelengths (thick lines). TPEF peaks were observed around 550 nm at most excitation wavelengths. Reproduced from Mouchet, S. R., Verstraete, C., Kaczmarek, A. M., Mara, D., van Cleuvenbergen, S., Van Deun, R., Verbiest, T., Maes, B., Vukusic, P., and Kolaric, B., 2019, Unveiling the nonlinear optical response of *Trictenotoma childreni* longhorn beetle, J. Biophot. 12(9), 12:e201800470, with permission from John Wiley and Sons.

So far, various natural photonic structures from different insects, including butterflies and cicadas, have been investigated for sensing and materials-oriented applications. For example, corrugated natural photonic structures offer a unique possibility to develop new sensing platforms by combing corrugation at different scales, plasmonic properties, and surface-enhanced Raman spectroscopy (SERS) [107–111]. The work of Garrett and coworkers clearly shows the benefit of natural and bioinspired structuring, which can be used for different sensing applications (Figure 8) [108–110]. The development of such novel platforms relying on SERS will lead to the fast and accurate screening of chemical, biochemical, and pharmaceutical compounds, which is crucial for the growing fields of proteomics, genomics, molecular medicine, and biophysics, as well as for the development of assays for the detection of diseases [107,112].

The work of Stoddart and coworkers highlighted that practical applications of SERS for sensing depend on the development of manufacturing methods that will be used to mimic the complex morphology of insect integuments [107]. It pointed out the importance of biomimetics for the advancement of materials science [107]. In addition, it was shown that the enhancement of SERS also depends on the aspect ratio of metallic nanoparticles. The presence of different multiscale groove-like structures presented the possibility of developing smart surfaces for controlling optical response and wetting properties [113]. Structuring materials have a significant effect on the latter, as was demonstrated both theoretically and experimentally, specifically at different length scales [114–116].

Furthermore, the natural photonic structures occurring in the wings of the butterfly *Cymothoe sangaris* were used for tuning the upconversion luminescence of nanoparticles doped with lanthanide ($NaYF_4 : Yb^{3+}, Er^{3+}$) [117]. Upon illumination with a light at 980 nm, both red and green emission bands of $NaYF_4 : Yb^{3+}, Er^{3+}$ could be controlled, producing different luminescent colours Figure 9. Doping natural photonic structures with

materials including metals and oxides also presents the possibility of using these structures as templates to design nanocorrugated materials (with complex shapes and geometries) on demand for various material applications [118].

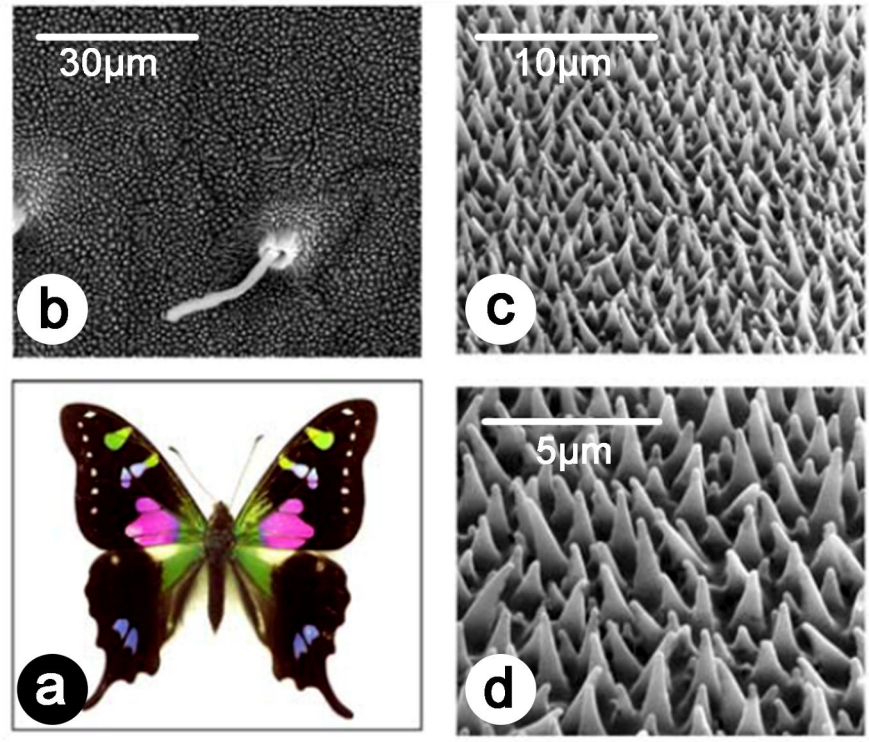


Figure 8. The structures occurring on the wings of the purple spotted swallowtail butterfly (*Graphium weiskei*) coated with a metal thin film were found to be an excellent substrate for SERS, in terms of biocompatibility and sensitivity [108–110]. *G. weiskei* (**a**) exhibit conical microstructures on its wings (**b**–**d**) as observed here by SEM. After coating by gold or silver, these structures can be used to detect protein binding from direct observation of the modifications in the SERS response. Reproduced from Garrett, N. L., Vukusic, P., Ogrin, F., Sirotkin, E., Winlove, C. P., and Moger, J., 2009, Spectroscopy on the wing: Naturally inspired SERS substrates for biochemical analysis, J. Biophot. 2(3), 157–166.

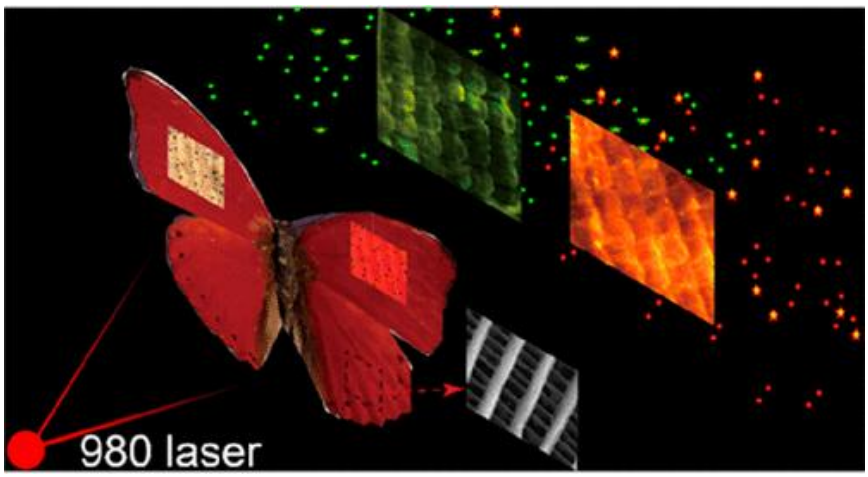


Figure 9. The upconversion luminescence of nanoparticles doped with lanthanide ($NaYF_4 : Yb^{3+}, Er^{3+}$) was controlled thanks to the natural photonic crystals occurring in the wings of the butterfly *Cymothoe sangaris*. With a 980 nm incident light, various luminescent colours were generated. Reproduced from Gao, T., Zhu, X., Wu, X. J., Zhang, B., and Liu, H. L., 2021, Selectively Manipulating Upconversion Emission Channels with Tunable Biological Photonic Crystals, J. Phys. Chem. C, 125(1), 732–739, with permission from ACS Publications.

5. Conclusions

In this perspective article, we presented theoretical key concepts of nonlinear optics and discussed the results of nonlinear optical studies in the field of natural photonics. Because nonlinear optical techniques are inherently sensitive to symmetry; the presence of interfaces; and chirality, they offer a more detailed insight into the molecular properties of biomaterials . This is crucial for applications in different areas of material science. Even though, at the moment, nonlinear optical investigations of natural photonics are still at their infant stage of development, the primary aim of this article is to draw the attention of the broad material, photonic, and biological scientific communities to the capability of nonlinear optics, which could be used to forge new horizons in physical, biological and material research.

Author Contributions: Conceptualization, B.K. and S.R.M.; writing—original draft: S.R.M. and B.K.; and writing—review & editing: all authors. All authors have read and agreed to the published version of the manuscript.

Funding: DM acknowledges KU Leuven Postdoctoral Mandate Internal Funds (PDM) for a Postdoctoral fellowship (PDM/20/092). BB and BK acknowledge financial support of the Ministry of Education, Science, and Technological Development of the Republic of Serbia (grant III 45016). BB, BK, and DM acknowledge the support of the Office of Naval Research Global through the Research Grant N62902-22-1-2024. SRM was supported by a BEWARE Fellowship (Convention n°2110034) of the Walloon Region (Marie Skłodowska-Curie Actions of the European Union #847587), as a Postdoctoral Researcher. TV acknowledges financial support from the Hercules Foundation. BK acknowledges support from the Belgian National Fund for Scientific Research (FRS-FNRS).

Conflicts of Interest: The authors declare no conflict of interest. The funders had no role in the design of the study; in the collection, analyses, or interpretation of data; in the writing of the manuscript; or in the decision to publish the results.

References

1. Kinoshita, S. *Structural Colors in the Realm of Nature*; World Scientific Publishing Co.: Singapore, 2008.
2. Mouchet, S.R.; Deparis, O. *Natural Photonics and Bioinspiration*; Artech House: Boston, MA, USA, 2021.
3. Hecht, E. *Optics*; Addison-Wesley Publishing Company: Reading, MA, USA, 2001.
4. Stratton, J. *Electromagnetic Theory*; McGraw-Hill: New York, NY, USA, 1941.
5. Böttcher, C. *Theory of Electric Polarization*, 2nd ed.; Elsevier: Amsterdam, The Netherlands, 1973.
6. Zernike, F.; Midwinter, J. *Applied Nonlinear Optics*; Wiley: New York, NY, USA, 1973.
7. Verbiest, T.; Clays, K.; Rodriguez, V. *Second-Order Nonlinear Optical Characterization Techniques: An Introduction*; CRC Press Taylor & Francis Group: Boca Raton, FL, USA, 2009.
8. Zipfel, W.R.; Williams, R.M.; Webb, W.W. Nonlinear magic: Multiphoton microscopy in the biosciences. *Nat. Biotechnol.* **2003**, *21*, 1369. [CrossRef] [PubMed]
9. Verstraete, C.; Mouchet, S.R.; Verbiest, T.; Kolaric, B. Linear and nonlinear optical effects in biophotonic structures using classical and nonclassical light. *J. Biophotonics* **2019**, *12*, e201800262. [CrossRef]
10. Pathan, A.; Bond, J.; Gaskin, R. Sample preparation for scanning electron microscopy of plant surfaces—Horses for courses. *Micron* **2008**, *39*, 1049–1061. [CrossRef] [PubMed]
11. Ayache, J.; Beaunier, L.; Boumendil, J.; Ehret, G.; Laub, D. *Sample Preparation Handbook for Transmission Electron Microscopy*; Springer: New York, NY, USA, 2010.
12. Slominski, A.; Tobin, D.J.; Shibahara, S.; Wortsman, J. Melanin Pigmentation in Mammalian Skin and Its Hormonal Regulation. *Physiol. Rev.* **2004**, *84*, 1155–1228. [CrossRef]
13. Ito, S.; Wakamatsu, K. Diversity of human hair pigmentation as studied by chemical analysis of eumelanin and pheomelanin. *J. Eur. Acad. Dermatol. Venereol.* **2011**, *25*, 1369–1380. [CrossRef] [PubMed]
14. Stavenga, D.G.; Giraldo, M.A.; Leertouwer, H.L. Butterfly wing colors: Glass scales of Graphium sarpedon cause polarized iridescence and enhance blue/green pigment coloration of the wing membrane. *J. Exp. Biol.* **2010**, *213*, 1731–1739. [CrossRef]
15. Stavenga, D.G.; Matsushita, A.; Arikawa, K.; Leertouwer, H.L.; Wilts, B.D. Glass scales on the wing of the swordtail butterfly Graphium sarpedon act as thin film polarizing reflectors. *J. Exp. Biol.* **2012**, *215*, 657–662. [CrossRef]
16. Stavenga, D. Thin film and multilayer optics cause structural colors of many insects and birds. *Mater. Today Proc.* **2014**, *1S*, 109–121. [CrossRef]
17. Siddique, R.; Vignolini, S.; Bartels, C.; Wacker, I.; Hölscher, H. Colour formation on the wings of the butterfly *Hypolimnas Salmacis* Scale Stacking. *Sci. Rep.* **2016**, *6*, 36204. [CrossRef]

18. Vukusic, P.; Sambles, J.R.; Lawrence, C.R.; Wootton, R.J. Limited-view iridescence in the butterfly *Ancyluris Meliboeus*. *Proc. R. Soc. Lond. Ser. B Biol. Sci.* **2002**, *269*, 7–14. [CrossRef]
19. Vukusic, P.; Kelly, R.; Hooper, I. A biological sub-micron thickness optical broadband reflector characterized using both light and microwaves. *J. R. Soc. Interface* **2009**, *6*, S193–S201. [CrossRef] [PubMed]
20. Vigneron, J.P.; Simonis, P.; Aiello, A.; Bay, A.; Windsor, D.M.; Colomer, J.F.; Rassart, M. Reverse color sequence in the diffraction of white light by the wing of the male butterfly *Pierella Luna* (Nymphalidae: Satyrinae). *Phys. Rev. E* **2010**, *82*, 021903. [CrossRef] [PubMed]
21. Biró, L.P.; Bálint, Z.; Kertész, K.; Vértesy, Z.; Márk, G.I.; Horváth, Z.E.; Balázs, J.; Méhn, D.; Kiricsi, I.; Lousse, V.; et al. Role of photonic-crystal-type structures in the thermal regulation of a Lycaenid butterfly sister species pair. *Phys. Rev. E* **2003**, *67*, 021907. [CrossRef] [PubMed]
22. Yoshioka, S.; Kinoshita, S. Single-scale spectroscopy of structurally colored butterflies: measurements of quantified reflectance and transmittance. *J. Opt. Soc. Am. A* **2006**, *23*, 134–141. [CrossRef] [PubMed]
23. Noyes, J.A.; Vukusic, P.; Hooper, I.R. Experimental method for reliably establishing the refractive index of buprestid beetle exocuticle. *Opt. Express* **2007**, *15*, 4351–4358. [CrossRef] [PubMed]
24. Kertész, K.; Molnár, G.; Vértesy, Z.; Koós, A.; Horváth, Z.; Márk, G.; Tapasztó, L.; Bálint, Z.; Tamáska, I.; Deparis, O.; et al. Photonic band gap materials in butterfly scales: A possible source of "blueprints". E-MRS 2007 Spring Conference Symposium A: Sub-wavelength photonics throughout the spectrum: Materials and Techniques. *Mater. Sci. Eng. B* **2008**, *149*, 259–265. [CrossRef]
25. Wilts, B.D.; Leertouwer, H.L.; Stavenga, D.G. Imaging scatterometry and microspectrophotometry of lycaenid butterfly wing scales with perforated multilayers. *J. R. Soc. Interface* **2009**, *6*, S185–S192. [CrossRef] [PubMed]
26. Stavenga, D.G.; Wilts, B.D.; Leertouwer, H.L.; Hariyama, T. Polarized iridescence of the multilayered elytra of the Japanese jewel beetle, *Chrysochroa Fulgidissima*. *Philos. Trans. R. Soc. B Biol. Sci.* **2011**, *366*, 709–723. [CrossRef]
27. Vigneron, J.P.; Pasteels, J.M.; Windsor, D.M.; Vértesy, Z.; Rassart, M.; Seldrum, T.; Dumont, J.; Deparis, O.; Lousse, V.; Biró, L.P.; et al. Switchable reflector in the Panamanian tortoise beetle *Charidotella Egregia* (Chrysomelidae: Cassidinae). *Phys. Rev. E* **2007**, *76*, 031907. [CrossRef]
28. Pasteels, J.M.; Deparis, O.; Mouchet, S.R.; Windsor, D.M.; Billen, J. Structural and physical evidence for an endocuticular gold reflector in the tortoise beetle, *Charidotella Ambita*. *Arthropod Struct. Dev.* **2016**, *45*, 509–518. [CrossRef]
29. Kertész, K.; Bálint, Z.; Vértesy, Z.; Márk, G.I.; Lousse, V.; Vigneron, J.P.; Rassart, M.; Biró, L.P. Gleaming and dull surface textures from photonic-crystal-type nanostructures in the butterfly Cyanophrys remus. *Phys. Rev. E* **2006**, *74*, 021922. [CrossRef] [PubMed]
30. Michielsen, K.; Stavenga, D. Gyroid cuticular structures in butterfly wing scales: Biological photonic crystals. *J. R. Soc. Interface* **2008**, *5*, 85–94. [CrossRef] [PubMed]
31. Saranathan, V.; Osuji, C.O.; Mochrie, S.G.J.; Noh, H.; Narayanan, S.; Sandy, A.; Dufresne, E.R.; Prum, R.O. Structure, function, and self-assembly of single network gyroid ($I4_132$) Photonic Cryst. Butterfly Wing Scales. *Proc. Natl. Acad. Sci. USA* **2010**, *107*, 11676–11681. [CrossRef] [PubMed]
32. Pouya, C.; Vukusic, P. Electromagnetic characterization of millimetre-scale replicas of the gyroid photonic crystal found in the butterfly *Parides Sesostris*. *Interface Focus* **2012**, *2*, 645–650. [CrossRef]
33. Mouchet, S.R.; Vigneron, J.P.; Colomer, J.F.; Vandenbem, C.; Deparis, O. Additive photonic colors in the Brazilian diamond weevil: *Entimus imperialis*. *Proc. SPIE* **2012**, *8480*, 848003. [CrossRef]
34. Mouchet, S.; Colomer, J.F.; Vandenbem, C.; Deparis, O.; Vigneron, J.P. Method for modeling additive color effect in photonic polycrystals with form anisotropic elements: The case of *Entimus Imp. Weevil. Opt. Express* **2013**, *21*, 13228–13240. [CrossRef]
35. Prum, R.O.; Torres, R.H.; Williamson, S.W.; Dyck, J. Coherent light scattering by blue feather barbs. *Nature* **1998**, *396*, 28–29. [CrossRef]
36. Prum, R.O.; Torres, R.H. A Fourier Tool for the Analysis of Coherent Light Scattering by Bio-Optical Nanostructures1. *Integr. Comp. Biol.* **2003**, *43*, 591–602. [CrossRef]
37. Prum, R.O.; Torres, R. Structural colouration of avian skin: Convergent evolution of coherently scattering dermal collagen arrays. *J. Exp. Biol.* **2003**, *206*, 2409–2429. [CrossRef]
38. Prum, R.O.; Torres, R.H. Structural colouration of mammalian skin: Convergent evolution of coherently scattering dermal collagen arrays. *J. Exp. Biol.* **2004**, *207*, 2157–2172. [CrossRef]
39. Henze, M.J.; Lind, O.; Wilts, B.D.; Kelber, A. Pterin-pigmented nanospheres create the colours of the polymorphic damselfly *Ischnura Elegans*. *J. R. Soc. Interface* **2019**, *16*, 20180785. [CrossRef] [PubMed]
40. Mouchet, S.R.; Luke, S.; McDonald, L.T.; Vukusic, P. Optical costs and benefits of disorder in biological photonic crystals. *Faraday Discuss.* **2020**, *223*, 9–48. [CrossRef] [PubMed]
41. Morehouse, N.I.; Vukusic, P.; Rutowski, R. Pterin pigment granules are responsible for both broadband light scattering and wavelength selective absorption in the wing scales of pierid butterflies. *Proc. R. Soc. B Biol. Sci.* **2007**, *274*, 359–366. [CrossRef] [PubMed]
42. Stavenga, D.G.; Stowe, S.; Siebke, K.; Zeil, J.; Arikawa, K. Butterfly wing colours: Scale beads make white pierid wings brighter. *Proc. R. Soc. Lond. Ser. B Biol. Sci.* **2004**, *271*, 1577–1584. [CrossRef] [PubMed]
43. Stavenga, D.G.; Giraldo, M.A.; Hoenders, B.J. Reflectance and transmittance of light scattering scales stacked on the wings of pierid butterflies. *Opt. Express* **2006**, *14*, 4880–4890. [CrossRef]

44. Ladouce, M.; Barakat, T.; Su, B.L.; Deparis, O.; Mouchet, S.R. Scattering of ultraviolet light by avian eggshells. *Faraday Discuss.* **2020**, *223*, 63–80. [CrossRef]
45. Mouchet, S.R.; Vukusic, P. Structural Colours in Lepidopteran Scales. *Adv. Insect Physiol.* **2018**, *54*, 1–53. [CrossRef]
46. Vigneron, J.P.; Colomer, J.F.m.; Vigneron, N.; Lousse, V. Natural layer-by-layer photonic structure in the squamae of *Hoplia Coerulea* (Coleoptera). *Phys. Rev. E* **2005**, *72*, 061904. [CrossRef]
47. Mouchet, S.; Lobet, M.; Kolaric, B.; Kaczmarek, A.; Van Deun, R.; Vukusic, P.; Deparis, O.; Van Hooijdonk, E. Photonic scales of *Hoplia Coerulea* Beetle: Any Colour You Like. *Mater. Today Proc.* **2017**, *4*, 4979–4986. [CrossRef]
48. Rassart, M.; Simonis, P.; Bay, A.; Deparis, O.; Vigneron, J.P. Scale coloration change following water absorption in the beetle *Hoplia Coerulea* (Coleoptera). *Phys. Rev. E* **2009**, *80*, 031910. [CrossRef]
49. Mouchet, S.R.; Su, B.L.; Tabarrant, T.; Lucas, S.; Deparis, O. *Hoplia Coerulea*, A Porous Nat. Photonic Struct. Template Opt. Vap. Sensor. *Proc. SPIE* **2014**, *9127*. [CrossRef]
50. Mouchet, S.R.; Tabarrant, T.; Lucas, S.; Su, B.L.; Vukusic, P.; Deparis, O. Vapor sensing with a natural photonic cell. *Opt. Express* **2016**, *24*, 12267–12280. [CrossRef] [PubMed]
51. Mouchet, S.; Van Hooijdonk, E.; Welch, V.; Louette, P.; Colomer, J.F.; Su, B.L.; Deparis, O. Liquid-induced colour change in a beetle: The concept of a photonic cell. *Sci. Rep.* **2016**, *6*, 19322. [CrossRef] [PubMed]
52. Mouchet, S.; Van Hooijdonk, E.; Welch, V.; Louette, P.; Tabarrant, T.; Vukusic, P.; Lucas, S.; Colomer, J.F.; Su, B.L.; Deparis, O. Assessment of environmental spectral ellipsometry for characterising fluid-induced colour changes in natural photonic structures. *Mater. Today Proc.* **2017**, *4*, 4987–4997. [CrossRef]
53. Van Hooijdonk, E.; Berthier, S.; Vigneron, J.P. Bio-inspired approach of the fluorescence emission properties in the scarabaeid beetle *Hoplia Coerulea* (Coleoptera): Model. Transf.-Matrix Opt. Simulations. *J. Appl. Phys.* **2012**, *112*, 114702. [CrossRef]
54. Mouchet, S.R.; Lobet, M.; Kolaric, B.; Kaczmarek, A.M.; Van Deun, R.; Vukusic, P.; Deparis, O.; Van Hooijdonk, E. Controlled fluorescence in a beetle's photonic structure and its sensitivity to environmentally induced changes. *Proc. R. Soc. Lond. B Biol. Sci.* **2016**, *283*. [CrossRef]
55. Lagorio, M.G.; Cordon, G.B.; Iriel, A. Reviewing the relevance of fluorescence in biological systems. *Photochem. Photobiol. Sci.* **2015**, *14*, 1538–1559. [CrossRef]
56. Marshall, J.; Johnsen, S. Fluorescence as a means of colour signal enhancement. *Philos. Trans. R. Soc. Lond. B Biol. Sci.* **2017**, *372*. [CrossRef]
57. Arnold, K.E.; Owens, I.P.F.; Marshall, N.J. Fluorescent Signaling in Parrots. *Science* **2002**, *295*, 92. [CrossRef]
58. McGraw, K.J.; Toomey, M.B.; Nolan, P.M.; Morehouse, N.I.; Massaro, M.; Jouventin, P. A description of unique fluorescent yellow pigments in penguin feathers. *Pigment Cell Res.* **2007**, *20*, 301–304. [CrossRef]
59. Ladouce, M.; Barakat, T.; Su, B.L.; Deparis, O.; Mouchet, S.R. UV scattering by pores in avian eggshells. *Proc. SPIE* **2020**, *11481*, 101–109. [CrossRef]
60. Cockayne, E.I. The Distribution of Fluorescent Pigments in Lepidoptera. *Trans. R. Entomol. Soc. Lond.* **1924**, *72*, 1–19. [CrossRef]
61. Vukusic, P.; Hooper, I. Directionally Controlled Fluorescence Emission in Butterflies. *Science* **2005**, *310*, 1151. [CrossRef] [PubMed]
62. Israelowitz, M.; Rizvi, S.H.; von Schroeder, H.P. Fluorescence of the "fire-chaser" beetle *Melanophila Acuminata*. *J. Lumin.* **2007**, *126*, 149–154. [CrossRef]
63. Trzeciak, T.M.; Wilts, B.D.; Stavenga, D.G.; Vukusic, P. Variable multilayer reflection together with long-pass filtering pigment determines the wing coloration of papilionid butterflies of the *Nireus* Group. *Opt. Express* **2012**, *20*, 8877–8890. [CrossRef]
64. Hooijdonk, E.V.; Vandenbem, C.; Berthier, S.; Vigneron, J.P. Bi-functional photonic structure in the *Papilio Nireus* (Papilionidae): Model. Scatt.-Matrix Opt. Simulations. *Opt. Express* **2012**, *20*, 22001–22011. [CrossRef]
65. Van Hooijdonk, E.; Berthier, S.; Vigneron, J.P. Contribution of both the upperside and the underside of the wing on the iridescence in the male butterfly *Troïdes Magellanus* (Papilionidae). *J. Appl. Phys.* **2012**, *112*, 074702. [CrossRef]
66. Welch, V.L.; Van Hooijdonk, E.; Intrater, N.; Vigneron, J.P. Fluorescence in insects. *Proc. SPIE* **2012**, *8480*, 848004. [CrossRef]
67. Wilts, B.D.; Trzeciak, T.M.; Vukusic, P.; Stavenga, D.G. Papiliochrome II pigment reduces the angle dependency of structural wing colouration in *Nireus* Group Papilionids. *J. Exp. Biol.* **2012**, *215*, 796–805. [CrossRef]
68. Van Hooijdonk, E.; Barthou, C.; Vigneron, J.P.; Berthier, S. Yellow structurally modified fluorescence in the longhorn beetles Celosterna pollinosa sulfurea and Phosphorus virescens (Cerambycidae). *J. Lumin.* **2013**, *136*, 313–321. [CrossRef]
69. Mouchet, S.R.; Kaczmarek, A.M.; Mara, D.; Deun, R.V.; Vukusic, P. Colour and fluorescence emission of *Euchroea Auripigmenta* Beetle. *Proc. SPIE* **2019**, *10965*, 72–82. [CrossRef]
70. Mouchet, S.R.; Verstraete, C.; Kaczmarek, A.M.; Mara, D.; van Cleuvenbergen, S.; Van Deun, R.; Verbiest, T.; Maes, B.; Vukusic, P.; Kolaric, B. Unveiling the nonlinear optical response of *Trictenotoma Child. Longhorn Beetle. J. Biophotonics* **2019**, *12*, e201800470. [CrossRef] [PubMed]
71. Mouchet, S.R.; Verstraete, C.; Bokic, B.; Mara, D.; Dellieu, L.; Orr, A.G.; Deparis, O.; Deun, R.V.; Verbiest, T.; Vukusic, P.; et al. Naturally occurring fluorescence in transparent insect wings. *arXiv* **2021**, arXiv:2110.06086.
72. Lawrence, R.F. Fluorescence in Arthropoda. *J. Entomol. Soc. S. Afr.* **1954**, *17*, 167–170.
73. Pavan, M.; Vachon, M. Sur l'existence d'une substance fluorescente dans les téguments des Scorpions (Arachnides). *Comptes Rendus L'Académie Sci.* **1954**, *239*, 1700–1702.
74. Tani, K.; Watari, F.; Uo, M.; Morita, M. Fluorescent Properties of Porcelain-Restored Teeth and Their Discrimination. *Mater. Trans.* **2004**, *45*, 1010–1014. [CrossRef]

75. Taboada, C.; Brunetti, A.E.; Pedron, F.N.; Carnevale Neto, F.; Estrin, D.A.; Bari, S.E.; Chemes, L.B.; Peporine Lopes, N.; Lagorio, M.G.; Faivovich, J. Naturally occurring fluorescence in frogs. *Proc. Natl. Acad. Sci. USA* **2017**, *114*, 3672–3677. [CrossRef]
76. Deschepper, P.; Jonckheere, B.; Matthys, J. A Light in the Dark: The Discovery of Another Fluorescent Frog in the Costa Rican Rainforests. *Wilderness Environ. Med.* **2018**, *29*, 421–422. [CrossRef]
77. Mohd Top, M.; Puan, C.L.; Chuang, M.F.; Othman, S.N.; Borzée, A. First record of ultraviolet fluorescence in the Bent-toed Gecko *Cyrtodactylus Quadrivirgatus* Taylor, 1962 (Gekkonidae: Sauria). *Herpetol. Notes* **2020**, *13*, 211–212.
78. Gruber, D.F.; Gaffney, J.P.; Mehr, S.; DeSalle, R.; Sparks, J.S.; Platisa, J.; Pieribone, V.A. Adaptive Evolution of Eel Fluorescent Proteins from Fatty Acid Binding Proteins Produces Bright Fluorescence in the Marine Environment. *PLoS ONE* **2015**, *10*, e0140972. [CrossRef]
79. Gruber, D.F.; Loew, E.R.; Deheyn, D.D.; Akkaynak, D.; Gaffney, J.P.; Smith, W.L.; Davis, M.P.; Stern, J.H.; Pieribone, V.A.; Sparks, J.S. Biofluorescence in Catsharks (Scyliorhinidae): Fundamental Description and Relevance for Elasmobranch Visual Ecology. *Sci. Rep.* **2016**, *6*, 24751. [CrossRef] [PubMed]
80. Iriel, A.; Lagorio, M.G. Is the flower fluorescence relevant in biocommunication? *Naturwissenschaften* **2010**, *97*, 915–924. [CrossRef] [PubMed]
81. Iriel, A.; Lagorio, M.G. Implications of reflectance and fluorescence of *Rhododendr. Indicum* Flowers Biosignaling. *Photochem. Photobiol. Sci.* **2010**, *9*, 342–348. [CrossRef] [PubMed]
82. Purcell, E.M. Spontaneous emission probabilities at radio frequencies. *Phys. Rev.* **1946**, *69*, 681.
83. Yablonovitch, E. Inhibited Spontaneous Emission in Solid-State Physics and Electronics. *Phys. Rev. Lett.* **1987**, *58*, 2059–2062. [CrossRef]
84. Kumazawa, K.; Tanaka, S.; Negita, K.; Tabata, H. Fluorescence from Wing of *Morpho Sulkowskyi* Butterfly. *Jpn. J. Appl. Phys.* **1994**, *33*, 2119–2122. [CrossRef]
85. Lawrence, C.R.; Vukusic, P.; Sambles, J.R. Grazing-incidence iridescence from a butterfly wing. *Appl. Opt.* **2002**, *41*, 437–441. [CrossRef]
86. Vigneron, J.P.; Kertész, K.; Vértesy, Z.; Rassart, M.; Lousse, V.; Bálint, Z.; Biró, L.P. Correlated diffraction and fluorescence in the backscattering iridescence of the male butterfly *Troides Magellanus* (Papilionidae). *Phys. Rev. E* **2008**, *78*, 021903. [CrossRef]
87. Van Hooijdonk, E.; Barthou, C.; Vigneron, J.P.; Berthier, S. Detailed experimental analysis of the structural fluorescence in the butterfly *Morpho Sulkowskyi* (Nymphalidae). *J. Nanophotonics* **2011**, *5*, 053525. [CrossRef]
88. Hooijdonk, E.V.; Barthou, C.; Vigneron, J.P.; Berthier, S. Angular dependence of structural fluorescent emission from the scales of the male butterfly *Troïdes Magellanus* (Papilionidae). *J. Opt. Soc. Am. B* **2012**, *29*, 1104–1111. [CrossRef]
89. Verbiest, T.; Kauranen, M.; Persoons, A.; Ikonen, M.; Kurkela, J.; Lemmetyinen, H. Nonlinear Optical Activity and Biomolecular Chirality. *J. Am. Chem. Soc.* **1994**, *116*, 9203–9205. [CrossRef]
90. Campagnola, P.J.; Millard, A.C.; Terasaki, M.; Hoppe, P.E.; Malone, C.J.; Mohler, W.A. Three-dimensional high-resolution second-harmonic generation imaging of endogenous structural proteins in biological tissues. *Biophys. J.* **2002**, *82*, 493–508. [CrossRef]
91. Friedl, P.; Wolf, K.; Harms, G.; Andrian, U.H. Biological Second and Third Harmonic Generation Microscopy. *Curr. Protoc. Cell Biol.* **2007**, *34*, 4.15.1–4.15.21. [CrossRef] [PubMed]
92. Ries, R.S.; Choi, H.; Blunck, R.; Bezanilla, F.; Heath, J.R. Black Lipid Membranes: Visualizing the Structure, Dynamics, and Substrate Dependence of Membranes. *J. Phys. Chem. B* **2004**, *108*, 16040–16049. [CrossRef]
93. Brown, D.J.; Morishige, N.; Neekhra, A.; Minckler, D.S.; Jester, J.V. Application of second harmonic imaging microscopy to assess structural changes in optic nerve head structure ex vivo. *J. Biomed. Opt.* **2007**, *12*, 5. [CrossRef]
94. Lis, D.; Guthmuller, J.; Champagne, B.; Humbert, C.; Busson, B.; Tadjeddine, A.; Peremans, A.; Cecchet, F. Selective detection of the antigenic polar heads of model lipid membranes supported on metals from their vibrational nonlinear optical response. *Chem. Phys. Lett.* **2010**, *489*, 12–15. [CrossRef]
95. Nguyen, T.T.; Conboy, J.C. High-Throughput Screening of Drug-Lipid Membrane Interactions via Counter-Propagating Second Harmonic Generation Imaging. *Anal. Chem.* **2011**, *83*, 5979–5988. [CrossRef]
96. Theer, P.; Denk, W.; Sheves, M.; Lewis, A.; Detwiler, P.B. Second-Harmonic Generation Imaging of Membrane Potential with Retinal Analogues. *Biophys. J.* **2011**, *100*, 232–242. [CrossRef]
97. Chen, X.; Nadiarynkh, O.; Plotnikov, S.; Campagnola, P.J. Second harmonic generation microscopy for quantitative analysis of collagen fibrillar structure. *Nat. Protoc.* **2012**, *7*, 654. [CrossRef]
98. Akerboom, J.; Carreras Calderón, N.; Tian, L.; Wabnig, S.; Prigge, M.; Tolö, J.; Gordus, A.; Orger, M.B.; Severi, K.E.; Macklin, J.J.; et al. Genetically encoded calcium indicators for multi-color neural activity imaging and combination with optogenetics. *Front. Mol. Neurosci.* **2013**, *6*, 2. [CrossRef]
99. Rabasović, M.D.; Pantelić, D.V.; Jelenković, B.M.; Ćurčić, S.B.; Rabasović, M.S.; Vrbica, M.D.; Lazović, V.M.; Ćurčić, B.P.; Krmpot, A.J. Nonlinear microscopy of chitin and chitinous structures: A case study of two cave-dwelling insects. *J. Biomed. Opt.* **2015**, *20*, 016010. [CrossRef] [PubMed]
100. Chen, Y.C.; Lee, S.Y.; Wu, Y.; Brink, K.; Shieh, D.B.; Huang, T.D.; Reisz, R.R.; Sun, C.K. Third-harmonic generation microscopy reveals dental anatomy in ancient fossils. *Opt. Lett.* **2015**, *40*, 1354–1357. [CrossRef]
101. Lis, D.; Cecchet, F. Unique Vibrational Features as a Direct Probe of Specific Antigen–Antibody Recognition at the Surface of a Solid-Supported Hybrid Lipid Bilayer. *ChemPhysChem* **2016**, *17*, 2645–2649. [CrossRef] [PubMed]

102. Rowlands, C.J.; Park, D.; Bruns, O.T.; Piatkevich, K.D.; Fukumura, D.; Jain, R.K.; Bawendi, M.G.; Boyden, E.S.; So, P.T. Wide-field three-photon excitation in biological samples. *Light Sci. Appl.* **2017**, *6*, e16255. [CrossRef] [PubMed]
103. Reynaud, C.; Thoury, M.; Dazzi, A.; Latour, G.; Scheel, M.; Li, J.; Thomas, A.; Moulhérat, C.; Didier, A.; Bertrand, L. In-place molecular preservation of cellulose in5,000-year-old archaeological textiles. *Proc. Natl. Acad. Sci. USA* **2020**, *117*, 19670–19676. [CrossRef]
104. Raoux, C.; Schmeltz, M.; Bied, M.; Alnawaiseh, M.; Hansen, U.; Latour, G.; Schanne-Klein, M.C. Quantitative structural imaging of keratoconic corneas using polarization-resolved SHG microscopy. *Biomed. Opt. Express* **2021**, *12*, 4163–4178. [CrossRef]
105. Schmeltz, M.; Robinet, L.; Heu-Thao, S.; Sintès, J.M.; Teulon, C.; Ducourthial, G.; Mahou, P.; Schanne-Klein, M.C.; Latour, G. Noninvasive quantitative assessment of collagen degradation in parchments by polarization-resolved SHG microscopy. *Sci. Adv.* **2021**, *7*, eabg1090. [CrossRef]
106. Mouchet, S.R.; Verstraete, C.; Mara, D.; Cleuvenbergen, S.V.; Finlayson, E.D.; Deun, R.V.; Deparis, O.; Verbiest, T.; Maes, B.; Vukusic, P.; et al. Nonlinear optical spectroscopy and two-photon excited fluorescence spectroscopy reveal the excited states of fluorophores embedded in a beetle's elytra. *Interface Focus* **2019**, *9*, 20180052. [CrossRef]
107. Stoddart, P.R.; Cadusch, P.J.; Boyce, T.M.; Erasmus, R.M.; Comins, J.D. Optical properties of chitin: Surface-enhanced Raman scattering substrates based on antireflection structures on cicada wings. *Nanotechnology* **2006**, *17*, 680. [CrossRef]
108. Garrett, N.L.; Vukusic, P.; Ogrin, F.; Sirotkin, E.; Winlove, C.P.; Moger, J. Spectroscopy on the wing: Naturally inspired SERS substrates for biochemical analysis. *J. Biophotonics* **2009**, *2*, 157–166. [CrossRef]
109. Garrett, N.L. *Naturally Inspired SERS Substrates: Datasheet from · Volume: "Raman Spectroscopy for Nanomaterials Characterization"*; SpringerMaterials: Cham, Switzerland, 2012. [CrossRef]
110. Garrett, N.L.; Sekine, R.; Dixon, M.W.A.; Tilley, L.; Bambery, K.R.; Wood, B.R. Bio-sensing with butterfly wings: Naturally occurring nano-structures for SERS-based malaria parasite detection. *Phys. Chem. Chem. Phys.* **2015**, *17*, 21164–21168. [CrossRef] [PubMed]
111. Palmer, L.D.; Brooks, J.L.; Frontiera, R.R. Probing the coupling of butterfly wing photonic crystals to plasmon resonances with surface-enhanced Raman spectroscopy. *J. Mater. Chem. C* **2019**, *7*, 13887–13895. [CrossRef]
112. Langer, J.; Jimenez de Aberasturi, D.; Aizpurua, J.; Alvarez-Puebla, R.A.; Auguié, B.; Baumberg, J.J.; Bazan, G.C.; Bell, S.E.; Boisen, A.; Brolo, A.G.; et al. Present and Future of Surface-Enhanced Raman Scattering. *ACS Nano* **2020**, *14*, 28–117. [CrossRef] [PubMed]
113. Zhang, G.; Zhang, J.; Xie, G.; Liu, Z.; Shao, H. Cicada Wings: A Stamp from Nature for Nanoimprint Lithography. *Small* **2006**, *2*, 1440–1443. [CrossRef]
114. Dellieu, L.; Sarrazin, M.; Simonis, P.; Deparis, O.; Vigneron, J.P. A two-in-one superhydrophobic and anti-reflective nanodevice in the grey cicada *Cicada Orni* (Hemiptera). *J. Appl. Phys.* **2014**, *116*, 024701. [CrossRef]
115. Deparis, O.; Mouchet, S.R.; Dellieu, L.; Colomer, J.F.; Sarrazin, M. Nanostructured Surfaces: Bioinspiration for Transparency, Coloration and Wettability. *Mater. Today Proc.* **2014**, *1S*, 122–129. [CrossRef]
116. Kovačević, A.; Petrović, S.; Mimidis, A.; Stratakis, E.; Pantelić, D.; Kolaric, B. Molding Wetting by Laser-Induced Nanostructures. *Appl. Sci.* **2020**, *10*, 6008. [CrossRef]
117. Gao, T.; Zhu, X.; Wu, X.J.; Zhang, B.; Liu, H.L. Selectively Manipulating Upconversion Emission Channels with Tunable Biological Photonic Crystals. *J. Phys. Chem. C* **2021**, *125*, 732–739. [CrossRef]
118. Zhang, D. *Morphology Genetic Materials Templated from Nature Species*; Springer: Berlin/Heidelberg, Germany, 2012.

applied sciences

MDPI

Article

Fluorimetry in the Strong-Coupling Regime: From a Fundamental Perspective to Engineering New Tools for Tracing and Marking Materials and Objects

Mohamed Hatifi [1,2,*], Dimitrije Mara [3], Bojana Bokic [4], Rik Van Deun [5], Brian Stout [1], Emmanuel Lassalle [1,6], Branko Kolaric [4,7] and Thomas Durt [1]

1 Aix Marseille Univ, CNRS, Centrale Marseille, Institut Fresnel, UMR 7249, 13013 Marseille, France
2 Quantum Dynamics Unit, Okinawa Institute of Science and Technology Graduate University, Onna, Okinawa 904-0495, Japan
3 Institute of General and Physical Chemistry, Studentski trg 12/V, 11158 Belgrade, Serbia
4 Center for Photonics, Institute of Physics, University of Belgrade, Pregrevica 118, 11080 Belgrade, Serbia
5 L^3—Luminescent Lanthanide Lab, Department of Chemistry, Ghent University, Krijgslaan 281-S3, 9000 Ghent, Belgium
6 Institute of Materials Research and Engineering, A*STAR (Agency for Science, Technology and Research), Singapore 138634, Singapore
7 Micro- and Nanophotonic Materials Group, University of Mons, Place du Parc 20, 7000 Mons, Belgium
* Correspondence: hatifi.mohamed@gmail.com

Abstract: Under exceptional circumstances, light and molecules bond together, creating new hybrid light–matter states with far-reaching consequences for these strongly coupled entities. The present article describes the quantum-mechanical foundation of strong-coupling and experimental evidence for molding the radiation properties of nanoprobes by strong-coupling. When applied to tracing and marking, the new fluorometry technique proposed here, which harnesses strong-coupling, has a triple advantage compared to its classical counterparts such as DNA tracing. It is fast, and its signal-to-noise ratio can be improved by spectral filtering; moreover, it reveals a specific quantum signature of the strong-coupling, which is extremely difficult to reproduce classically, thereby opening the door to new anti-counterfeiting strategies.

Keywords: strong-coupling; light-matter interaction; steady-state and time-resolved fluorescence spectroscopy; metallic cavities

check for updates

Citation: Hatifi, M.; Mara, D.; Bokic, B.; Van Deun, R.; Stout, B.; Lassalle, E.; Kolaric, B.; Durt, T. Fluorimetry in the Strong-Coupling Regime: From a Fundamental Perspective to Engineering New Tools for Tracing and Marking Materials and Objects. *Appl. Sci.* **2022**, *12*, 9238. https://doi.org/10.3390/app12189238

Academic Editors: Principia Dardano and Maria Antonietta Ferrara

Received: 23 July 2022
Accepted: 4 September 2022
Published: 15 September 2022

Publisher's Note: MDPI stays neutral with regard to jurisdictional claims in published maps and institutional affiliations.

Copyright: © 2022 by the authors. Licensee MDPI, Basel, Switzerland. This article is an open access article distributed under the terms and conditions of the Creative Commons Attribution (CC BY) license (https://creativecommons.org/licenses/by/4.0/).

1. Introduction

Fluorophores possess numerous biomedical applications where they are used as tracers and markers. For instance, they can be linked to DNA branes in devices aimed at detecting the presence of viruses in blood samples. Lab-on-a-chip applications of such techniques present promising applications [1], especially in the times of pandemic, where it offers possibilities for the fast detection of viruses in airports or other public places. They could also be used as markers for authenticating the origin of certain manufactured products and avoiding copies and counterfeits as we propose here. The most significant advantages of fluorimetry are its extremely fast response time, the sensitivity of the excited states to the local environment, and the possibility of incorporating fluorophore in a chip/device and simultaneously measuring many samples for a short time [2].

This article proposes a new fluorescence technique that exploits the strong light–matter interaction of an embedded nanoprobe within a plasmonic cavity. The signature of strong light–matter interactions between nanoprobes and cavity modes is typically detected through changes in the excitation spectrum (electronic or vibrational) of the coupled system [3–8].

When strong-coupling occurs, the isolated excited emitter is no longer an eigenstate of the system but corresponds to a superposition of the higher and lower polaritons, which evolve at different frequencies, leading to coherent oscillations of the excitation between the emitter and the cavity mode. On account of these vacuum Rabi oscillations, the emitter cycles through absorption and emission instead of exhibiting the more familiar exponential decay process. Amplification of the signal in a resonant cavity therefore plays an essential role and is accompanied by a specific quantum effect (frequency shift). It presents significant advantages regarding tracing and marking applications:

- Frequency shifts make it possible to improve the signal-to-noise ratio;
- Frequency splitting constitutes a signature of strong-coupling which is difficult to counterfeit.

The paper is structured as follows. In Section 2, we outline the basic principles of our proposal, aimed at applying the properties of strongly coupled emitters for authentication and tracing. In Section 3, we summarize the theory of strong-coupling, and we explain the transition from the weak to the strong-coupling regimes in terms of Poincaré recurrences. In Section 4, we describe our experimental set-up. In Section 5, we discuss its specific advantages regarding tracing and marking. The Supplementary Material contains details concerning the implementation of our experimental set-up and a theoretical derivation of the spectrum of emission of the cavity in the strong-coupling regime.

2. Concept of "Quantum Filigran" Based on Strong-Coupling

2.1. Physically Unclonable Functions

A physically unclonable function (PUF) is a physical structure that is widely used as a unique identifier for various objects. PUFs depend on the uniqueness of their physical microstructure [9]. Generally, PUF microstructures depend on random physical factors introduced during manufacturing to create a unique response, or on biologically induced randomness (cellular noise) during the morphogenesis of natural photonic structures [9,10]. These factors are unpredictable and uncontrollable, which makes it virtually impossible to duplicate or clone the structure. However, the dependence of PUF on modern colloidal or biological self-assembly processes makes this approach, in many cases, complicated and limited. In this article, we offer an entirely different approach that can be used for authentication and marking based on quantum filigran where uniqueness is achieved by controlling the light–matter interaction in the strong-coupling regime. The advantage of the present method, besides its uniqueness, is that it also offers a fast and unique read-out that could be exploited for different sensing and marking applications at large scale. The first example of quantum PUF can be traced back to Wiesner quantum money protocol [11] which is based on the quantum no cloning theorem. Here, we propose a semi-classical protocol in which quantized light–matter interaction plays a prominent role, the "quantum filigran".

2.2. Quantum Filigran

The principle of the filigran used for authenticating banknotes is common knowledge. In summary, when we submit the banknote to a specific optical excitation (illumination at normal incidence), a specific response is induced at the level of the filigran (the image of the filigran becomes visible if we observe it in transparency along the axis joining it to the source). It is not easy to counterfeit such filigrans, which differ from usual 2D images by the fact that they are not visible under grazing illumination. Ultimately, it is this specific response of the filigran that explains why it is a useful tool for authentication. Our goal, roughly expressed, is to conceive quantum filigrans based on the specific optical response of well-chosen fluorophores, in the quantum strong-coupling regime. The scheme of principle of our idea is depicted in Figure 1: a solution containing fluorophores is placed inside a tunable Fabry–Pérot cavity; a fluorophore is resonantly excited by a laser source and absorbs a photon at a wavelength of 440 nm. A part of the energy is lost in

an initial non-radiative process, followed by a radiative quantum jump at wavelengths of 530 ± 25 nm.

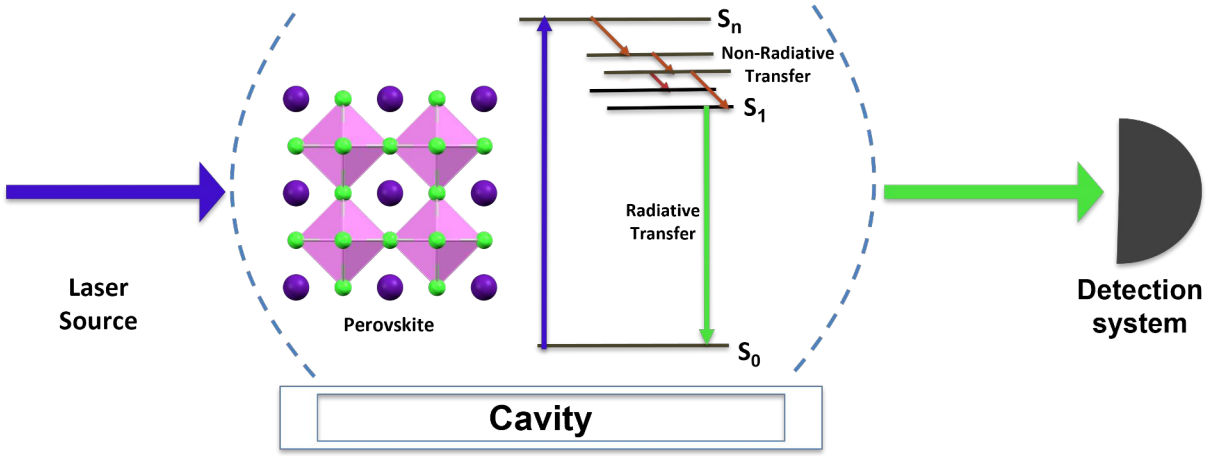


Figure 1. Scheme of *Quantum Filigran* experiment. The blue arrow represents the light emitted by the laser, resonant with the peak of absorption of the fluorophore (440 nm). The green arrow represents the emitted photon. Note that in the strong coupling regime, photons are emitted at two possible wavelengths (530 ± 25 nm), a manifestation of frequency splitting.

This frequency splitting is the signature of quantum strong coupling which is ensured by placing the fluorophore in a cavity resonant at 530 nm (for more details, see Section 4). The single photons emitted one at a time by the fluorophores are filtered in frequency around one of the two emission peaks and collected in a typical fluorescence device consisting of a single photon detector coupled to an acquisition table. The statistical distribution of the arrival times of the photons emitted by the fluorophore is well-approximated by a double exponential distribution. As a last resort, this distribution is, as explained in Section 4), the signature of the presence, at the level of the fluorophore, of two competing non-radiative processes, a short one and a long one. This specific response of the fluorophore (single photon emission, plus frequency splitting and frequency shift, plus specific temporal statistics) is extremely difficult to clone by classical methods; it will play the role of a quantum filigran in our proposal.

3. Fluorophore Coupled to a Resonant Cavity in the Strong-Coupling Regime

3.1. Strong-Coupling with a Perfect Lossless Cavity

Strong-coupling naturally appears if we consider a two-level system (atom, fluorophore) resonantly coupled to an ideal, lossless and isolated, cavity mode. The Hamiltonian describing such a system is well-known. It is the so-called Jaynes–Cumming (J–C) Hamiltonian. It is obtained after performing various approximations (such as dipolar coupling and rotating wave approximation). In an empty cavity, for an atom dipole moment $\mathbf{d} = d\vec{u}_d$ and a perfect polarization and position matching with the mode, the dipolar interaction is equal to the product $-dE_0$ between the dipole moment and the effective cavity electric field (in the absence of photon). The electric field of the empty cavity is $E_0 = \sqrt{\hbar\omega_c/(2\epsilon_0 V_c)}$, where V_c is the cavity volume and ω_c is the cavity mode frequency. The coupling strength is characterized by $g = dE_0/\hbar = \Omega_0/2$.

$$\hbar g = d\sqrt{\frac{\hbar\omega_c}{2\epsilon_0 V_c}} \tag{1}$$

The J–C Hamiltonian [12] then reads

$$\hat{H}_{\mathrm{JC}} = \hbar\omega_0\hat{\sigma}^\dagger\hat{\sigma} + \hbar\omega_c\hat{a}^\dagger\hat{a} + \hbar g\left(\hat{\sigma}\hat{a}^\dagger + \hat{\sigma}^\dagger\hat{a}\right) \tag{2}$$

The parameters of this Hamiltonian are the atomic transition frequency ω_0, the cavity mode frequency ω_c, and the coupling constant g. When a single dipole (atom/fluorophore) is considered, the state of the system is

$$|\psi(t)\rangle = \alpha(t)|e, 0_c\rangle + \beta(t)|g, 1_c\rangle \tag{3}$$

where the state $|e, 0_c\rangle$ stands for dipole in the excited state and no photon in the cavity and $|g, 1_c\rangle$ stands for dipole in the ground state and one photon in the cavity. The J–C Hamiltonian then reduces to a 2×2 matrix

$$\hat{H}_{\text{J-C}} = \hbar \begin{bmatrix} \omega_0 & g \\ g & \omega_c \end{bmatrix} \tag{4}$$

It is worth noting that $\hat{H}_{\text{JC}}$ is Hermitian. In what follows, we shall consider a nearly resonant cavity ($\omega_c \approx \omega_0$ so that the detuning $\delta = \omega_c - \omega_0$ is small).

The new eigenenergies of the coupled system are [13]

$$E_{\pm} = \hbar\omega_c \pm \frac{1}{2}\hbar\sqrt{\delta^2 + \Omega_0^2} \tag{5}$$

where we defined the so-called vacuum Rabi frequency:

$$\Omega_0 \equiv \sqrt{4g^2} \tag{6}$$

At resonance ($\delta = 0$), the energy difference between the two modes is minimal and equal to $\hbar\Omega_0$. The energy eigenstates are given by

$$\begin{aligned} |+\rangle &= \sin\theta\, |e, 0_c\rangle + \cos\theta\, |g, 1_c\rangle \\ |-\rangle &= \cos\theta\, |e, 0_c\rangle - \sin\theta\, |g, 1_c\rangle \end{aligned} \tag{7}$$

The parameter θ defines the entanglement strength [3] between the dipole and the cavity mode ($\tan 2\theta = \Omega_0/\delta$). At resonance, entanglement is maximal ($\theta = \pi/4$) and the dressed states have matter and field components of equal weight. The separation between two distinct matter–radiation subsystems is then impossible. Far from resonance ($\theta \approx 0$ and $\theta \approx \pi/2$), these states exhibit dominant matter or electromagnetic components. These polaritonic states inherit dispersion relations from their electromagnetic component. Let us note that the pair of eigenenergies $E_{\pm}$ and eigenstates $|\pm\rangle$ are only the lowest of an infinite ladder of pairs. Similar pairs exist for the quantum superposition of states $|n_c, e\rangle$ and $|n_c + 1, g\rangle$ involving the presence of n_c or $n_c + 1$ photons in the cavity, respectively. Their energy gap at resonance is given by $\hbar\Omega_0\sqrt{n_c + 1}$.

In practice, perfectly lossless cavities do not exist and the criterium to enter the strong-coupling regime is that the Rabi frequency Ω_0 must be significantly larger than the widths γ_c and γ related to the cavity mode and matter excitation lifetimes, respectively. In other words, coupling must dominate over dissipative processes. This condition is required to preserve quantum coherence, as the Rabi frequency describes the rate of coherent energy conversions between matter and the radiation field in the dressed states. In general, to increase the coupling g, one needs to select quantum emitters with a strong transition dipole and to confine the electromagnetic field in a small volume. To decrease γ_c, high-finesse cavities are required. The team of S. Haroche (Nobel prize 2012), which is at the same time a pioneering and a leading team in the domain of strong coupling, developed high-finesse superconducting cavities cooled down to a few millikelvins, and reached huge values for the coupling factors g by using, as two-level systems, Rydberg atoms resonant with the cavity [14]. In our approach, it is rather the Purcell effect [15] that plays a prior role in increasing the value of g. This explains why we realize strong coupling even at room temperatures, as explained in Section 4.

3.2. Strong-Coupling with a Lossy Cavity

In order to phenomenologically describe losses [16] let us now consider the pure state (3) dynamics described by a *non-Hermitian* "effective" Hamiltonian $\hat{H} = \hat{H}_{\text{J-C}} + \hat{H}_{\text{loss}}$ where $\hat{H}_{\text{loss}}$ is introduced phenomenologically and, in the basis $\{|e, 0_c\rangle, |g, 1_c\rangle\}$, reads:

$$\hat{H}_{\text{loss}} = \hbar \begin{bmatrix} 0 & 0 \\ 0 & -\mathrm{i}\frac{\gamma_c}{2} \end{bmatrix} \tag{8}$$

where the parameter γ_c is called the cavity decay rate.

The coefficients $\alpha(t)$ and $\beta(t)$ are obtained by solving the Schrödinger equation with the non-Hermitian Hamiltonian $\hat{H} = \hat{H}_{\text{J-C}} + \hat{H}_{\text{loss}}$:

$$\mathrm{i}\hbar \frac{\partial}{\partial t} \begin{bmatrix} \alpha(t) \\ \beta(t) \end{bmatrix} = \hbar \begin{bmatrix} \omega_0 & g \\ g & \omega_c - \mathrm{i}\frac{\gamma_c}{2} \end{bmatrix} \begin{bmatrix} \alpha(t) \\ \beta(t) \end{bmatrix} \tag{9}$$

In order to solve the dynamics of such a system, let us diagonalize the above matrix. Upon diagonalization, one finds the following eigenvalues:

$$\omega_{\pm} = \frac{\omega_0 + \omega_c}{2} - \mathrm{i}\frac{\gamma_c}{4} \pm \frac{\Omega}{2} \tag{10}$$

where we defined the quantity:

$$\Omega \equiv \sqrt{4g^2 + \left(\delta + \mathrm{i}\frac{\gamma_c}{2}\right)^2} \tag{11}$$

(where $\delta \equiv \omega_0 - \omega_c$ represents the detuning). We are first of all interested in the probability of finding the atom in the excited state, the *survival probability* defined as $P_{\text{surv}}(t) \equiv |\alpha(t)|^2$, so we want to find the expression of $\alpha(t)$. Its general expression reads:

$$\alpha(t) = A_+ \mathrm{e}^{-\mathrm{i}\omega_+ t} + A_- \mathrm{e}^{-\mathrm{i}\omega_- t} \tag{12}$$

where the constants A_+ and A_- are determined by the initial conditions $\alpha(0) = 1$ and $\dot{\alpha}(0) = -\mathrm{i}\omega_0$ (coming from the fact that $\beta(0) = 0$ in Equation (9)):

$$A_{\pm} = \frac{1}{2} \pm \frac{\delta + \mathrm{i}\gamma_c/2}{2\Omega} \tag{13}$$

It is worth noting that for one excitation (photon), the phenomenological approach is equivalent to a rigorous dissipative approach using a master equation (see, e.g., Ref. [17] Chapter 6, especially Section 6.2, entitled "Spontaneous emission: From irreversible decay to Rabi oscillations").

3.3. Weak and Strong-Coupling Regime in the Resonant Case $\omega_0 = \omega_c$

In the *resonant case*, $\omega_0 = \omega_c$, the eigen-frequencies in Equation (10) become:

$$\omega_{\pm} = \omega_c - \mathrm{i}\frac{\gamma_c}{4} \pm \frac{\Omega}{2} \tag{14}$$

where Ω now reads:

$$\Omega = \sqrt{4g^2 - \left(\frac{\gamma_c}{2}\right)^2} \tag{15}$$

One can clearly see that two different regimes in the time-domain are possible depending on the values of g and γ_c:

(i) For a small coupling constant, $g < \frac{1}{4}\gamma_c$, Ω becomes purely imaginary, and the eigen-frequencies $\omega_\pm$ (Equation (14)) are now complex, leading to a monotonic decay of the amplitude $\alpha(t)$ in time (Equation (12)), known as the **weak-coupling regime.**

(ii) For a large coupling constant, $g > \frac{1}{4}\gamma_c$, Ω is real, and the eigen-frequencies $\omega_\pm$ (Equation (14)) show a different real part, leading to *oscillations* of the amplitude $\alpha(t)$ in the time-domain, known as the **strong-coupling regime**.

The general solution will not be considered in detail here but we shall focus on the (very) strong-coupling regime, i.e., when $g \gg \gamma_c$. A very good approximation of the solution may be derived in this case by means of power series expansion:

$$\Omega \simeq 2g - \frac{\gamma_c^2}{16g} \tag{16}$$

$$\omega_\pm \simeq -\mathrm{i}\frac{\gamma_c}{4} \pm g \tag{17}$$

$$\begin{aligned} A_\pm &\simeq \frac{1}{2} \pm \mathrm{i}\frac{\gamma_c}{8g}\left(1 + \frac{\gamma_c^2}{32g^2}\right) \\ &\simeq \frac{1}{2} \end{aligned} \tag{18}$$

Then, $\alpha(t)$ becomes

$$\alpha(t) \simeq \mathrm{e}^{-\frac{\gamma_c}{2}\frac{t}{2}}\cos(gt) \tag{19}$$

which gives a survival probability $P_{\mathrm{surv}}(t) = |\alpha(t)|^2$

$$\boxed{P_{\mathrm{surv}}(t) = \mathrm{e}^{-\frac{\gamma_c}{2}t}\cos^2(gt) = \frac{1}{2}\mathrm{e}^{-\frac{\gamma_c}{2}t}[1 + \cos(2gt)]} \tag{20}$$

One can see in this equation that $P_{\mathrm{surv}}(t) = |\alpha(t)|^2$ oscillates at the frequency $\Omega = 2g$. These oscillations, also called "vacuum Rabi oscillations", are characteristic of the strong-coupling [17].

3.4. Emission Spectrum in the Strong-Coupling Regime

There exists an alternative way to describe the coupling of a dipole to a lossy cavity, which is conceptually quite different from the ones presented in the previous sections. This model ([18], Chapter 1, Complement 1A) treats the spontaneous emission of an atom coupled to a bounded continuum of electromagnetic modes, with a bandwidth γ_c. As previously, the atom is modeled as a two-level system with transition frequency ω_0, and the continuum is assumed to have a "Lorentzian" density of states (modes) centered on a frequency ω_c and with a bandwidth expressed through the Full Width Half Maximum (FWHM) and from now on taken to be equal to γ_c. In particular, while conceptually very different, this model predicts the same temporal behavior as the previous ones. Its interest is that it predicts the distribution in energy of the emitted photons in the continuum which is an observable that one can measure in practice: the so-called vacuum Rabi splitting.

This model is developed in appendix (Supplementary Material), where we show that, in the highly strong-coupling regime, the probability of emitting a photon in mode j, denoted $P_{\mathrm{emit,j}}(t \to +\infty) \equiv |\beta_{\mathrm{j}}(t \to +\infty)|^2$ obeys

$$P_{\mathrm{emit,j}}(t \to +\infty) = \frac{1}{4}\frac{|g_{\mathrm{j}}|^2}{[(\omega_{\mathrm{j}} - \omega_0) + g]^2 + \left(\frac{\gamma_c}{4}\right)^2} + \frac{1}{4}\frac{|g_{\mathrm{j}}|^2}{[(\omega_{\mathrm{j}} - \omega_0) - g]^2 + \left(\frac{\gamma_c}{4}\right)^2} + \text{C.T.} \tag{21}$$

where the cross-term C.T. is given by:

$$\text{C.T.} = \frac{|g_j|^2}{2} \frac{(\omega_j - \omega_0)^2 - g^2 + \left(\frac{\gamma_c}{4}\right)^2}{\left[(\omega_j - \omega_0)^2 - g^2 + \left(\frac{\gamma_c}{4}\right)^2\right]^2 + 4\left(\frac{\gamma_c}{4}\right)^2 g^2} \tag{22}$$

As seen from Equation (21), in the strong-coupling regime $g > \gamma_c$, the distribution of emitted photons features two peaks separated by $2g$, and of FWHM$= 2 \times \gamma_c/4 = \gamma_c/2$. Therefore, an "order of magnitude" condition to be able to distinguish the two peaks is:

$$2g > \frac{\gamma_c}{2} \quad \Rightarrow \quad \boxed{g > \frac{\gamma_c}{4}} \tag{23}$$

When this condition is fulfilled, strong-coupling is achieved and the emission spectrum consists of two non-overlapping Lorentzian distributions respectively centered around $\omega_0 - g$ and $\omega_0 + g$, which is the Rabi splitting previously described in Equations (5) and (6).

3.5. Studying Poincaré Recurrences with a Discrete Model of Evolution

As we show now, the weak- to strong-coupling transition can also be interpreted in terms of Poincaré recurrences, in the framework of a discrete model which can be tackled numerically. We have already considered this model in the past, in Refs. [3,19] where we focused on energy conservation, and also showed its good agreement with the Wigner-Weiskopff model [20]. In this model, one considers a single atom coupled to N states j with a "door" distribution centered on the atomic frequency ω_0 and of variable bandwidth γ_c. They represent the distribution of the e-m modes in the cavity. One can then express the evolution equation in a matrix form:

$$i\hbar \frac{\partial}{\partial t} \begin{pmatrix} \alpha(t) \\ \beta_1(t) \\ \vdots \\ \beta_N(t) \end{pmatrix} = \hbar \underbrace{\begin{pmatrix} \omega_0 & g_1^*(\mathbf{r_0}) & \cdots & g_N^*(\mathbf{r_0}) \\ g_1(\mathbf{r_0}) & \omega_1 & & \\ \vdots & & \ddots & 0 \\ g_N(\mathbf{r_0}) & 0 & & \omega_N \end{pmatrix}}_{M} \cdot \begin{pmatrix} \alpha(t) \\ \beta_1(t) \\ \vdots \\ \beta_N(t) \end{pmatrix}, \tag{24}$$

Moreover, one assumes equal and real coupling constants: $g_j(\mathbf{r_0}) \equiv \mathbf{g}$ for all modes j.

The square matrix M can be numerically diagonalised. The program gives back the eigenvalues κ_n and eigenvectors $|\kappa_n\rangle$ of M, which can be used to solve $\alpha(t)$ and $\beta_j(t)$, using the general expression of their solution

$$\begin{pmatrix} \alpha(t) \\ \beta_1(t) \\ \vdots \\ \beta_N(t) \end{pmatrix} = \sum_{n=1}^{N+1} c_n |\kappa_n\rangle e^{-i\kappa_n t}. \tag{25}$$

where the c_n are given by the initial conditions:

$$\alpha(t=0) = 1 \tag{26}$$

$$\beta_j(t=0) = 0 \tag{27}$$

In order to better understand the implications of our toy model, we plotted the survival probability of the initially excited atom/fluorophore in function of the coupling to the cavity, varying the parameters of the model. These parameters are: $\rho = 1/\delta\omega$ which is the density of states in the comb (with $\delta\omega$ equal to the difference $\omega_i - \omega_{i-1}$ for $i \geq 1$); N is the number of modes and λ the coupling between the "atom" and the "cavity". $N \cdot \delta\omega$ is thus equal to

the "continuum" bandwidth γ_c, while the theoretical value of the gamma factor obtained by applying the Fermi golden rule is denoted γ. It is equal to $2\pi\lambda^2\rho$.

In Figure 2, we plot the survival probability $P_{\text{surv}}(t) = |\alpha(t)|^2$ obtained with this numerical method in the weak coupling regime, for two values of the density of modes, adjusting, however, the coupling constant in order to keep constant the theoretical value of the gamma factor obtained by applying the Fermi golden rule. Exponential decay is well observed, in agreement with the Fermi golden rule, but for very long times there appear large "revival" peaks which are an artefact peculiar to the discretization [3]. It is a manifestation of partial Poincaré recurrence due to the fact that when the Hilbert space of the quantum system is of finite dimension, the Poincaré recurrence time is finite (and its value is the smallest common multiple of all the eigenfrequencies of the Hamiltonian in Equation (24)). The Poincaré recurrence time increases when the density of modes increases as we can check comparing the red and blue recurrences, illustrating that, at least in the weak-coupling regime, the Poincaré recurrence goes to infinity in the continuum's limit.

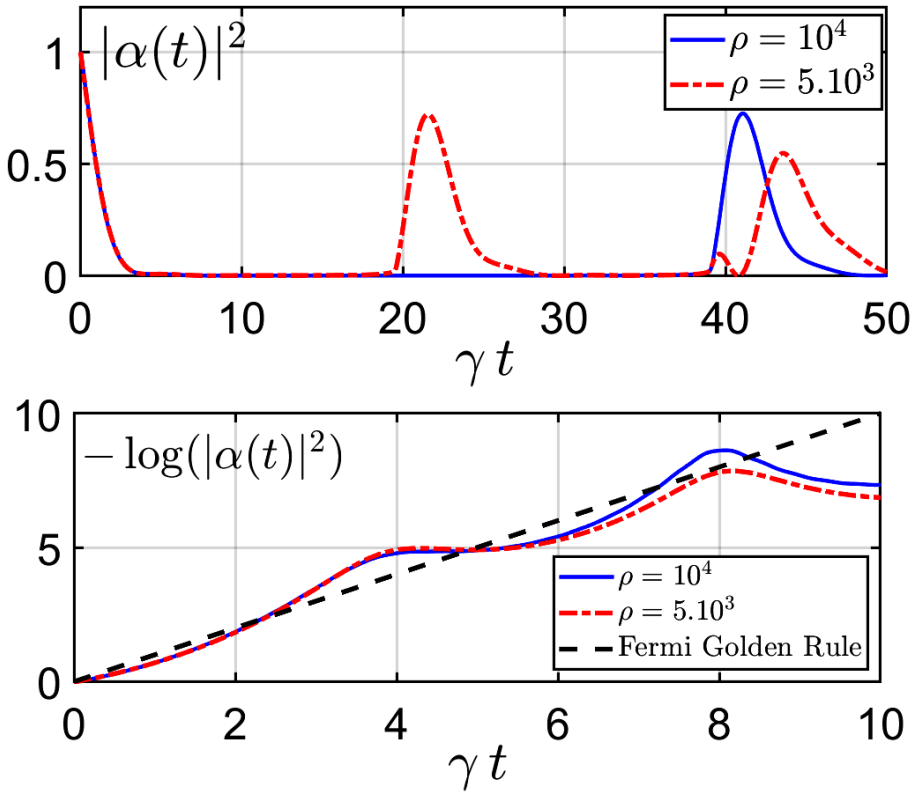


Figure 2. Survival probability in function of time in the weak coupling regime: linear–linear plot (above) and log–linear plot (below) for two values of the mode density ρ, respecting the scaling constraint $2\pi\rho \cdot \lambda^2 = \gamma$ =constant (where γ is the decay factor obtained from the Fermi golden rule and γt the rescaled time).

As can be seen in Figure 3, when we vary the bandwidth, keeping constant the spacing between the states in the comb, as well as the gamma factor obtained by applying the Fermi golden rule, the Poincaré recurrence time is constant. This effect is easy to explain in the weak-coupling regime because "active" resonant modes are then confined in an interval of width Γ around the resonant frequency in agreement with time-energy uncertainties; therefore, in the broad spectrum regime ($N \cdot \delta\omega >> 2\pi\gamma$), the physics of the system is unchanged when we vary the bandwidth.

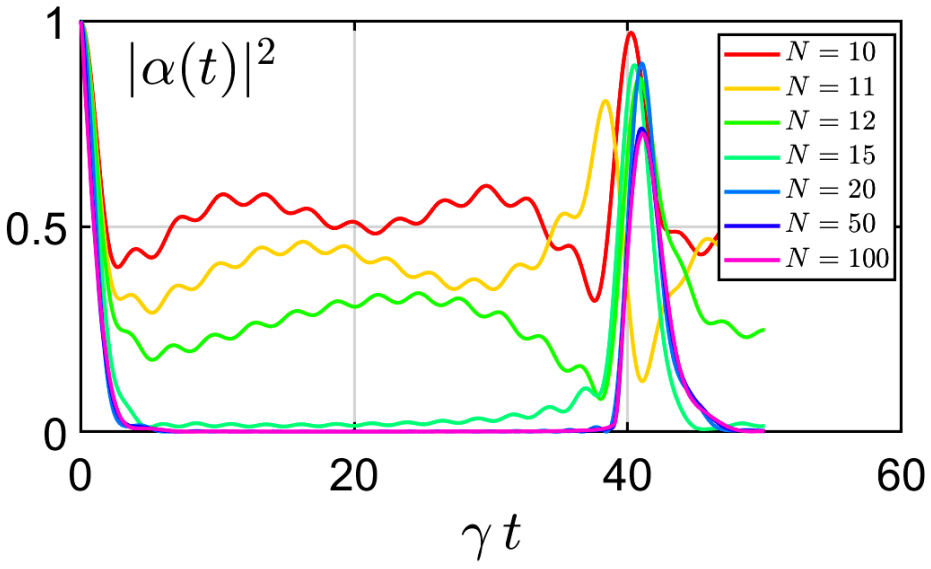


Figure 3. Survival probability in function of time respecting the scaling constraint $\rho \cdot \lambda^2 = \gamma_F =$ constant but varying the number of modes N.

This is no longer true however if we keep the number of modes constant, even when we vary the bandwidth (respecting the scaling constraint $\rho \cdot \lambda^2 =$ constant), as already seen in Figure 2.

When the number of modes is small enough, new fractional Poincaré recurrences appear, announcing the Rabi oscillations of Figure 4, typical of the strong coupling regime.

As can be seen from Figure 4, fractional Poincaré recurrences appear at the weak–strong transition ($N \cdot \delta\omega/\gamma = \gamma_c/\gamma > 2\pi$). In the strong-coupling regimes the revivals become indistinguishable from Rabi oscillations. The nature of Poincaré recurrences is clearly different in the weak- and strong-coupling regimes: in the weak-coupling regime they are an artefact of the discretization; in the strong-coupling regime, (fractional) Poincaré recurrences correspond to Rabi oscillations.

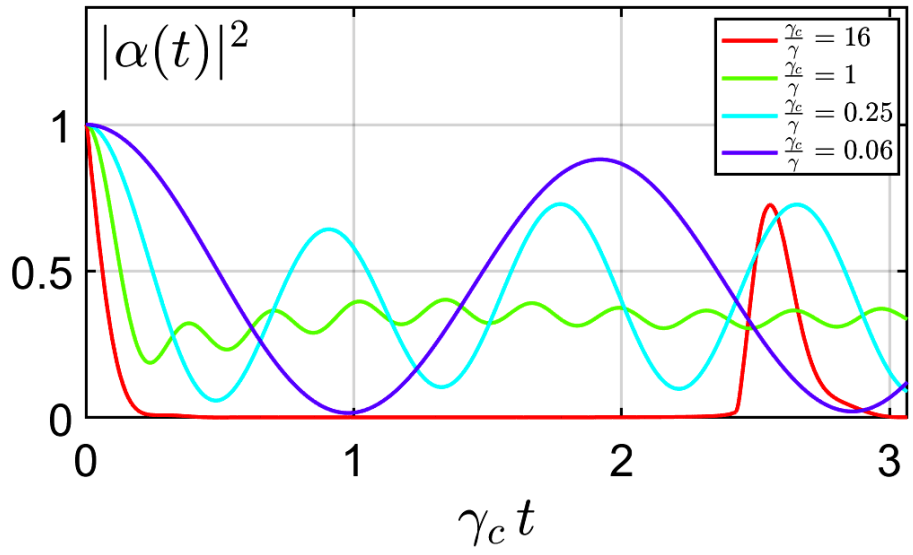


Figure 4. Survival probability in function of time for various values of γ_c/γ. In the weak-coupling regime, the Poincaré recurrence is an artefact of discretization, whereas in the strong-coupling regime Poincaré recurrences become indistinguishable from Rabi oscillations, typical of a system consisting of two coupled modes.

4. Experimental Study

4.1. Experimental Protocol

In order to perform the strong-coupling between nanoprobe and the cavity, we fabricated the plasmonic cavity by combining thermal-sputtering (for metal/Al deposition), and spin coating (for controlling the thickness of the cavity and for embedding nanoprobes into the cavity). The obtained cavity has a quality factor of around 70. Later we dissolved perovskite fluorophores (commercially available), at the concentration of 0.1 nM. The schematic structure of perovskite is presented in Figure 5.

Subsequently, 10 microliters of the perovskite solution (dissolved in toluen) were transferred into polymer solution (polystyrene(PS), volume 2 mL) used for spin coating in order to place the nanoprobe inside a cavity. The thickness of the cavity was adjusted to achieve resonance ($\delta = \omega_c - \omega_0$ close to zero, where ω_0 represents the Bohr frequency of the fluorophores in free space).

The details concerning cavity design, sample preparation, and quality factor estimation are described in Supplementary Materials.

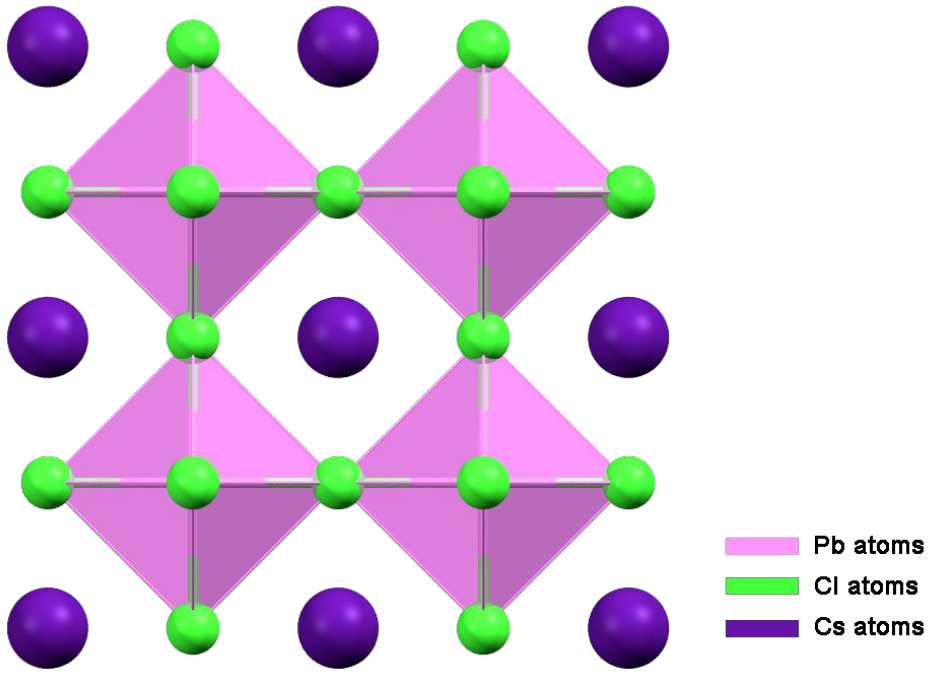


Figure 5. Structure of $CsPbCl_3$ perovskite is based on crystal structure from ICSD database 201250 [21].

4.2. Results

First, we investigate the fluorescence response of the perovskite outside the cavity. Figure 6 shows the fluorescence response of the perovskite probes in solution. The excitation wavelength used for fluorescence measurement was 440 nm. The observed emission spectrum is relatively narrow (for organic and metalorganic compounds), with the maximum around 530 nm and full width half maximum (FWHM) approximately 25 nm.

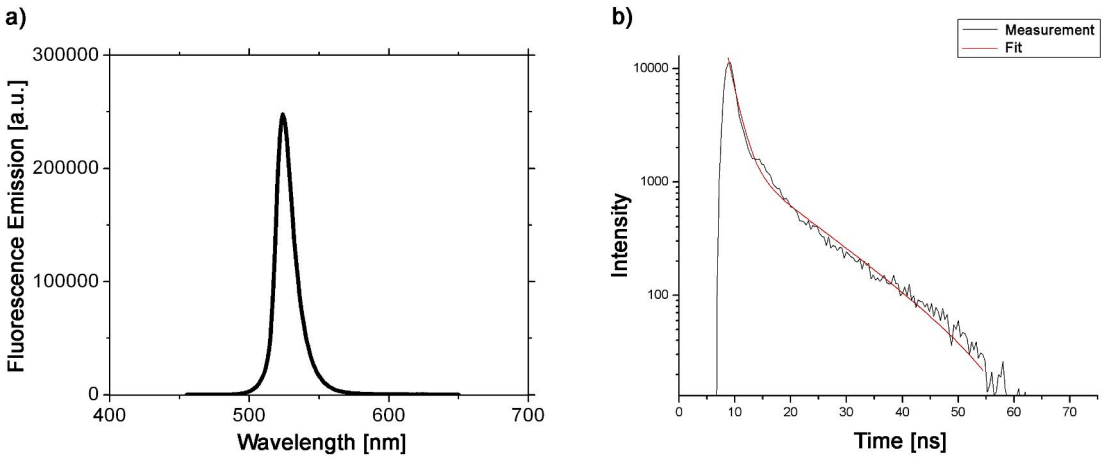


Figure 6. (**a**) Fluorescence steady state spectrum of perovskite in solution; (**b**) Fluorescence decay time response of the perovskite in solution fitted with a double exponential function.

In order to understand better the radiative response, we performed time-resolved measurements of the emitted fluorescence intensity (Figure 6b). The best fits of experimental results are obtained with a double exponential function that gave rise to a long decay time (of ca. 12.2 ns) that is related to the actual lifetime of the probe in this particular environment, and a short decay time (of ca. 1.6 ns), is associated with different nonradiative processes that affect the radiative dynamics of the dye. After that, we perform the steady-state investigation of the perovskite embedded into the plasmonic cavity at two different temperatures (room temperature 298 K and 10K). The sample was excited from outside the cavity; the excess energy $\delta\omega$ is necessary for creating a complex metastable excited state that will firstly follow a complicated non-radiative decay process before arriving at the radiative excited dipole state $|e, 0_c\rangle$ considered in Section 3. The steady-state response of the perovskite within the cavity is presented in Figure 7 and shows the signature of Rabi splitting that confirms that strong coupling between cavity and probe is achieved. As can be seen from Figure 7b, the splitting remains observable at room temperature, even though the height of the peaks diminished by then due to various sources of decoherence that increase with increasing temperature of the sample. Figure 7a exhibits the typical response of a Fabry–Pérot cavity.

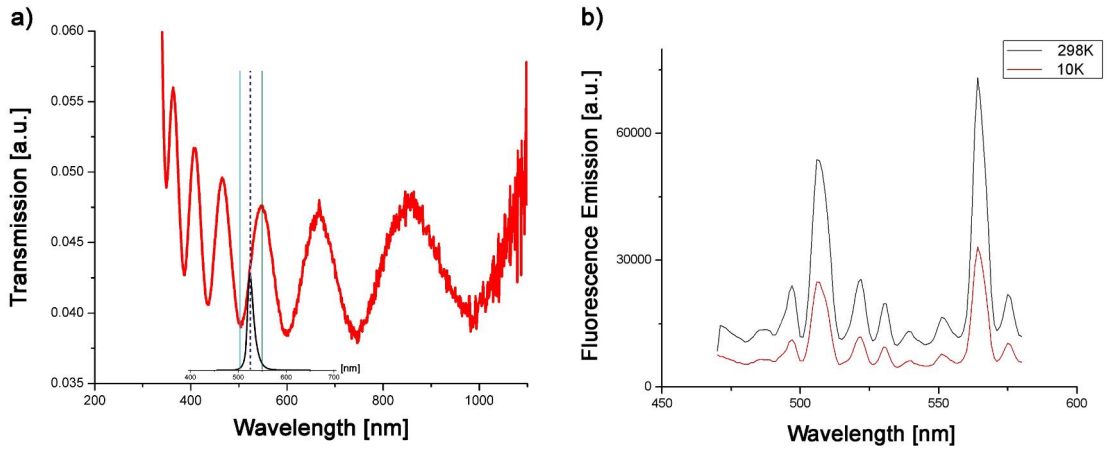


Figure 7. (**a**) Optical response of the cavity with emission spectrum from perovskite fluorophores in solution (inset); (**b**) emission spectrum from perovskite fluorophores in cavity—signature of Rabi splitting.

After a steady-state fluorescence study that shows the signature of the strong-coupling through Rabi splitting, the fluorescence time-resolved study reveals the effect of the strong coupling on the dynamics of the excited state. The theoretical decay time of the cavity is comparable, in the strong-coupling regime, to the survival time of the excited state $|e, 0_c\rangle$. It can be estimated by measuring the width of one of the Lorentzian peaks of Figure 7. By so doing, we estimate the lifetime of the cavity to be in the picosecond range. The distance between the two peaks makes it possible to estimate the value of the coupling constant g from which the ratio g/γ_c is thus predicted to be equal to 5.9, which confirms once more that we are well in the strong-coupling regime. Results of the measurement show that, as in the case of the probe in solution, the perovskite radiation dynamics within the cavity are best fitted with the double exponential functions. Like the energy splitting, the two decay signatures survive at room temperature (as can be seen from Figure 8. At room temperature (298 K), the perovskite within the cavity gave rise to a long decay time (of ca. 7.7 ns) that is related to the actual lifetime of the probe within the cavity and a short decay time (of ca. 0.87 ns) that is associated with different nonradiative processes that affect the radiative dynamics of the dye. The probe's lifetime within the cavity is significantly shorter (37%) compared to the lifetime in solution (decay rate increases). Decreasing temperature causes the increase of the lifetime of the probe to the value of 8.1 ns (5%), while the short decay stays unchanged, indicating that non-radiative processes within the cavity are not so strongly affected by the decrease in temperature.

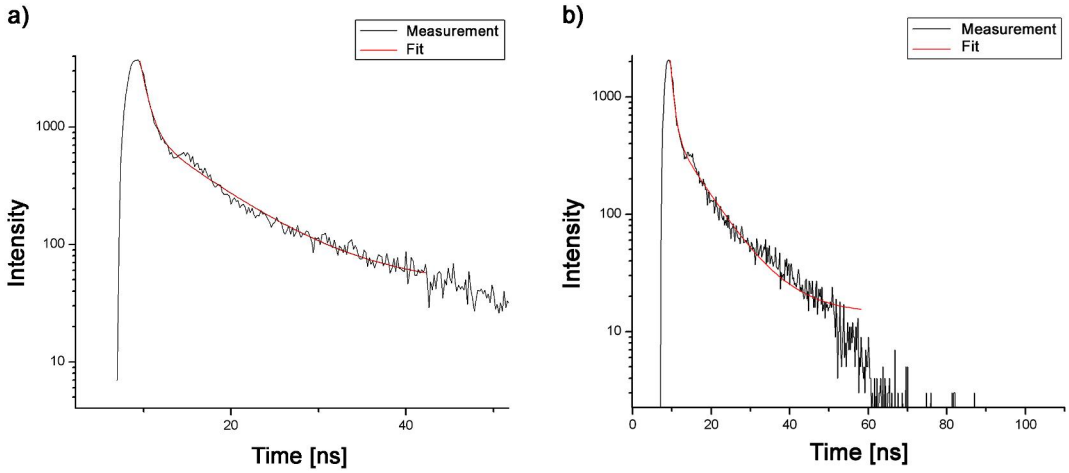


Figure 8. Fluorescence time-resolved measurements of the perovoskite within plasmonic cavity at two temperatures: (**a**) 298 K, and (**b**) 10 K.

The duration of the radiative process, estimated by measuring the width of the Lorentzian emission curve, is quite smaller than the duration of the non-radiative part of the decay process. Among other consequences, the probability that two photons will be emitted at the same time goes to zero, and we are thus always operating in the single photon regime. Due to the coexistence of the (long) fluorescence timescale and of the (short) timescale of the photon emission process, it is impossible for us to put into evidence specific signatures of the strong-coupling such as Rabi oscillations, without speaking about the entanglement between the dipole and the field inside the cavity. However, frequency splitting is directly observable with our device. It constitutes an authentic signature of the quantum strong-coupling, which offers promising perspectives regarding tracing and marking as we shall explain now.

5. Tracing and Marking in the Strong-Coupling Regime

Fluorophores are widely used for tracing and marking [2,22–24], but it is uncommon to let them operate in the strong-coupling regime. Recently, strong-coupling has been exploited for potential quantum chip applications using fluorophores attached to oligonu-

cleotide strands and embedded into the cavity [25]. These DNA or RNA oligonucleotide strands offer the possibility of putting the probe in a particular position within the cavity, and/or to link it with a plasmonic nanoobject (for instance a golden nanosphere) playing the same role as an external cavity [26–28], but this advantage comes with the relatively high cost of design and purification of oligonucleotides associated with the aging problem (stability of oligonucleotide probes within the cavity). In our approach, combining cavity design, spin coating, and specifically chosen fluorophores, we reach the strong-coupling regime without resorting to DNA strands. Another advantage of this regime is that it increases the signal-to-noise ratio, due to the fact that the frequency of the emitted photons differs from the resonance frequency of the cavity, and from the excitation frequency of the laser as well, which makes it easy to filter out the noise at those frequencies, by using well-chosen frequency filters (as we described in the previous section). The use of a resonant cavity also grandly amplifies the signal, which is a well-known manifestation of the Purcell effect [15]. In summary, our approach reduces noise and increases the signal, directly benefiting the signal-to-noise ratio.

6. Conclusions

In order to prevent counterfeiting, and to be able to authenticate their own manufactured goods, certain brands hide specific DNA branes in their products (clothes for instance), since they are difficult to imitate and can be revealed through DNA sequencing. We propose to use fluorophores in the strong-coupling regime described in the previous sections to realize the same goal. The present manuscript describes the quantum foundation of the strong-coupling and the experimental study of radiation dynamics in the strong-coupling regime. It also highlights how these dynamics can be harnessed in tracing and authentication, due to their unique response and simple detection requirements. The specific signature of strong-coupling is difficult to counterfeit (it also requires good overlap between the cavity resonance and absorption/emission spectrum of the probe), and it is easy to reveal because it needs a basic fluorescence device, is widely commercialized, and is versatile and fast to operate compared to DNA sequencing, for instance. It should be emphasized that instead of using expensive lithography techniques or time-consuming self-assembly processes, the new PUF that we propose here is solely based on the light–matter interaction. It constitutes a compromise between quantum encryption, *à la* Wiesner [11], and classical encryption. This approach opens a large field of potential applications.

Supplementary Materials: The following supporting information can be downloaded at: https://www.mdpi.com/article/10.3390/app12189238/s1, Figure S1: Two-level system in a cavity.

Author Contributions: Conceptualization: T.D.; Theoretical study: T.D., M.H. and E.L. Experimental study: D.M., B.B. and B.K.; Writing—original draft: T.D. and B.K.; Discussion: all authors; Writing—review & editing: all authors. All authors have read and agreed to the published version of the manuscript.

Funding: Biological and bioinspired structures for multispectral surveillance, funded by NATO SPS (NATO Science for Peace and Security), the Office of Naval Research Global through the Research Grant N62902-22-1-2024, the John Templeton foundation (grant 60230, Non-Linearity and Quantum Mechanics: Limits of the No-Signaling Condition, 2016–2019).

Institutional Review Board Statement: Not applicable.

Informed Consent Statement: The authors declare no conflict of interest. The funders had no role in the design of the study; in the collection, analyses, or interpretation of data; in the writing of the manuscript, or in the decision to publish the results.

Data Availability Statement: Not applicable.

Acknowledgments: All authors acknowledge the support of Sylvain Desprez-Materia Nova regarding metal deposition. B.K. acknowledge support of the project *Biological and bioinspired structures for multispectral surveillance*, funded by NATO SPS (NATO Science for Peace and Security) 2019–2022. B.B. and B.K. acknowledge funding provided by the Institute of Physics Belgrade, through the institutional

funding by the Ministry of Education, Science, and Technological Development of the Republic of Serbia. D.M., B.B. and B.K. acknowledge the support of the Office of Naval Research Global through the Research Grant N62902-22-1-2024. Additionally, B.K. acknowledges support from F.R.S.-FNRS Belgium. E.L. acknowledges support from Ecole Doctorale 352, Aix-Marseille. M.H. acknowledges support from the John Templeton foundation (grant 60230, Non-Linearity and Quantum Mechanics: Limits of the No-Signaling Condition, 2016–2019).

Conflicts of Interest: The authors declare no conflict of interest.

References

1. Sengupta, P.; Khanra, K.; Chowdhury, A.R.; Datta, P. Lab-on-a-chip sensing devices for biomedical applications. In *Bioelectronics and Medical Devices from Materials to Devices—Fabrication, Applications and Reliability*, 1st ed.; Pal, K., Kraatz, H.-B., Khasnobish, A., Bag, S., Banerjee, I., Kuruganti, U., Eds.; Woodhead Publishing: Sawston, UK, 2019; pp. 47–95.
2. Lakowicz, J.R. *Principles of Fluorescence Spectroscopy*, 3rd ed.; Springer: New York, NY, USA, 2006; pp. 623–740.
3. Kolaric, B.; Maes, B.; Clays, K.; Durt, T.; Caudano, Y. Strong Light-Matter Coupling as a New Tool for Molecular and Material Engineering: Quantum Approach. *Adv. Quantum Technol.* **2018**, *1*, 1800001. [CrossRef]
4. Shalabney, A.; George, J.; Hiura, H.; Hutchison, J.A.; Genet, C.; Hellwig, P.; Ebbesen, T.W. Enhanced Raman Scattering from Vibro-Polariton Hybrid States. *Angew. Chem. Int. Ed.* **2015**, *54*, 7971–7975. [CrossRef]
5. Orgiu, E.; George, J.; Hutchison, J.A.; Devaux, E.; Dayen, J.F.; Doudin, B.; Stellacci, F.; Genet, C.; Schachenmayer, J.; Genes, C.; et al. Conductivity in organic semiconductors hybridized with the vacuum field. *Nat. Mater.* **2015**, *14*, 1123–1129. [CrossRef] [PubMed]
6. Vergauwe, R.M.A.; George, J.; Chervy, T.; Hutchison, J.A.; Shalabney, A.; Torbeev, V.Y.; Ebbesen, T.W. Quantum Strong Coupling with Protein Vibrational Modes. *J. Phys. Chem. Lett.* **2016**, *7*, 4159. [CrossRef]
7. Ramezani, M.; Berghuis, M.; Gómez Rivas, J. Strong light–matter coupling and exciton-polariton condensation in lattices of plasmonic nanoparticles (Review). *J. Opt. Soc. Am. B Opt. Phys.* **2019**, *36*, E88–E103. [CrossRef]
8. Pelton, M.; Storm, S.D.; Leng, H. Strong coupling of emitters to single plasmonic nanoparticles: Exciton-induced transparency and Rabi splitting. *Nanoscale* **2019**, *11*, 14540–14552. [CrossRef]
9. Pappu, R.; Recht, B.; Taylor, R.; Gershenfeld, N. Physical One-Way Functions. *Science* **2002**, *297*, 2026–2030. [CrossRef] [PubMed]
10. Pavlović, D.; Rabasović, M.D.; Krmpot, A.J.; Lazović, V.; Ćurčić, S.; Stojanović, D.V.; Jelenković, B.; Zhang, W.; Zhang, D.; Vukmirović, N.; et al. Naturally safe: Cellular noise for document security. *J. Biophotonics* **2019**, *12*, e201900218. [CrossRef]
11. Wiesner Quantum Money. Available online: https://wiki.veriqloud.fr/index.php?title=WiesnerQuantumMoney,seealsohttp://users.cms.caltech.edu/~vidick/teaching/120qcrypto/wiesner.pdf (accessed on 1 September 2022).
12. Jaynes, E.T.; Cummings, F.W. Comparison of Quantum and Semiclassical Radiation Theories with Application to the Beam Maser. *Proc. IEEE* **1963**, *51*, 89–109. [CrossRef]
13. Bina, M. The coherent interaction between matter and radiation. *Eur. Phys. J. Spec. Top.* **2012**, *203*, 163–183. [CrossRef]
14. Haroche, S.; Raimond, J.M. *Exploring the Quantum—Atoms, Cavities and Photons*; Oxford University Press: Oxford, UK, 2007.
15. Carminati, R.; Greffet, J.J.; Henkel, C.; Vigoureux, J. Radiative and non-radiative decay of a single molecule close to a metallic nanoparticle. *Opt. Commun.* **2006**, *261*, 368–375. [CrossRef]
16. Lassalle, E. Environment Induced Modifications of Spontaneous Quantum Emissions. Ph.D. Thesis, University of Marseille, Marseille, France, 2019.
17. Dutra, S.M. *Cavity Quantum Electrodynamics: The Strange Theory of Light in a Box*, 1st ed.; John Wiley & Sons: Hoboken, NJ, USA, 2005.
18. Grynberg, G.; Aspect, A.; Fabre, C. *Introduction to Quantum Optics: From the Semi-Classical Approach to Quantized Light*, 1st ed.; Cambridge University Press: Cambridge, UK, 2010.
19. Debierre, V.; Goessens, I.; Brainis, E.; Durt, T. Fermi's golden rule beyond the zeno regime. *Phys. Rev. A* **2015**, *92*, 023825. [CrossRef]
20. Weisskopf, V.; Wigner, E. Berechnung der natürlichen linienbreite auf grund der diracschen lichttheorie. *Z. Für Phys.* **1930**, *63*, 54–73. [CrossRef]
21. Hunton, J.; Nelmes, R.J.; Moyer, G.M.; Eriksson, V.R. High resolution study of cubic perovskites by elastic neutron diffraction: $CsPbCl_3$. *J. Phys. C Solid State Phys.* **1979**, *12*, 5393.
22. Cowen, E.A.; Ward, K.B. Chemical Plume Tracing. *Environ. Fluid Mech.* **2002**, *2*, 1–7. [CrossRef]
23. *Anti-Counterfeiting Technology Guide*; European Union Intellectual Property Office: Alicante, Spain, 2021.
24. *Trace Chemical Sensing of Explosives*, 1st ed.; Woodfin, R.L., Ed.; Wiley: Hoboken, NJ, USA, 2006.
25. Chan, W.P.; Chen, J.H.; Chou, W.L.; Chen, W.Y.; Liu, H.Y.; Hu, H.C.; Jeng, C.C.; Li, J.R.; Chen, C.; Chen, S.Y. Efficient DNA-Driven Nanocavities for Approaching Quasi-Deterministic Strong Coupling to a Few Fluorophores. *ACS Nano* **2021** , *15*, 13085–13093. [CrossRef] [PubMed]
26. Punj, D.; Regmi, R.; Devilez, A.; Plauchu, R.; Moparthi, S.B.; Stout, B.; Bonod, N.; Rigneault, H.; Wenger, J. Self-Assembled Nanoparticle Dimer Antennas for Plasmonic-Enhanced Single-Molecule Fluorescence Detection at Micromolar Concentrations. *ACS Photonics* **2025**, *2*, 1099–1107. [CrossRef]

27. Busson, M.; Rolly, B.; Stout, B.; Bonod, N.; Bidault, S. Accelerated single photon emission from dye molecule-driven nanoantennas assembled on DNA. *Nat. Commun.* **2012**, *3*, 962. [CrossRef] [PubMed]
28. Busson, M.P.; Rolly, B.; Stout, B.; Bonod, N.; Wenger, J.; Bidault, S. Photonic Engineering of Hybrid Metal—Organic Chromophores. *Angew. Chem. Int. Ed.* **2012**, *51*, 44, 11083–11087. [CrossRef] [PubMed]

Journal of Luminescence 254 (2023) 119490

Contents lists available at ScienceDirect

Journal of Luminescence

journal homepage: www.elsevier.com/locate/jlumin

Full Length Article

Revealing natural fluorescence in transparent insect wings by linear and nonlinear optical techniques

Sébastien R. Mouchet [a,b,1,*], Charlotte Verstraete [c,1], Bojana Bokic [d], Dimitrije Mara [c,e,f], Louis Dellieu [b], Albert G. Orr [g], Olivier Deparis [b], Rik Van Deun [e], Thierry Verbiest [c], Pete Vukusic [a,**], Branko Kolaric [d,h]

[a] School of Physics, University of Exeter, Stocker Road, Exeter, EX4 4QL United Kingdom
[b] Department of Physics & Namur Institute of Structured Matter (NISM), University of Namur, Rue de Bruxelles 61, 5000 Namur, Belgium
[c] Molecular Imaging and Photonics, Department of Chemistry, KU Leuven, Celestijnenlaan 200D, 3001 Heverlee, Belgium
[d] Center for Photonics, Institute of Physics, University of Belgrade, Pregrevica 118, 11080 Belgrade, Serbia
[e] L^3 – Luminescent Lanthanide Lab, Department of Chemistry, Ghent University, Krijgslaan 281-S3, 9000 Ghent, Belgium
[f] Institute of General and Physical Chemistry, Studentski trg 12/V, 11158 Belgrade, Serbia
[g] Environmental Futures Centre, Griffith University, Nathan, QLD 4111, Australia
[h] Micro- and Nanophotonic Materials Group, University of Mons, Place du Parc 20, 7000 Mons, Belgium

ARTICLE INFO

Keywords:
Fluorescence
Nonlinear optics
Two-photon fluorescence
SHG
Insect
Cicada
Resilin

ABSTRACT

For most natural organisms, the physical, chemical and biological aspects of fluorescence emission are poorly understood. For example, to the best of our knowledge, fluorescence from the transparent wings of any of the 3000 known species of cicadas has never been reported in the literature. These wings are known to exhibit anti-reflective properties arising from quasi-periodic arrays of nipples. Our study, using linear and nonlinear optical techniques, including spectrofluorimetry, two-photon fluorescence spectroscopy and Second Harmonic Generation (SHG), reveals the fluorescence properties in the wings the grey and the common cicadas (*Cicada orni* and *Lyristes (Tibicen) plebejus*, respectively), as well as the broad-bordered bee hawk-moth (*Hemaris fuciformis*). The study suggests that fluorescence would be more widespread in transparent insect wings than what was previously believed. Comparing this result to the fluorescence emission from the wings of the Bornean damselfly (*Vestalis amabilis*), we inferred that this emission probably arises from resilin, a protein reported to enhance wing flexibility. Moreover, the nonlinear optical investigation of the insects' wings provided further insight into wing structure, indicating that multiphoton techniques add valuable information for the analysis of insect integuments. The strong SHG signal detected from the wing veins implies that these veins are materially organised in a non-centrosymmetric and hence non-random fashion.

1. Introduction

Fluorescence emission takes place in the integument of several natural organisms including species from the animal classes Insecta, Aves, Amphibia, Reptilia and Mammalia as well as the plant kingdom [1–21]. This emission of light has been shown to play a role in visual communication of some organisms, facilitating species recognition, mate selection, prey detection, camouflage and agonistic behaviour [7,11]. Fluorescence results from the presence of fluorophores, such as papiliochrome II, biopterin, psittacofulvin, or green fluorescent protein (GFP) within the biological integuments. Following the absorption of incident light (typically in the UV or the shorter-wavelength part of the visible range), these molecules emit light at a longer wavelength (usually in the visible), resulting from transitions between their electron states. In spite of the crucial role that it is believed to play in nature, fluorescence in natural organisms remains under-investigated from optical, chemical and biological perspectives. One example is the transparent wings of certain insects of the order Hemiptera. For example, in

* Corresponding author. School of Physics, University of Exeter, Stocker Road, Exeter EX4 4QL, United Kingdom.
** Corresponding author. School of Physics, University of Exeter, Stocker Road, Exeter EX4 4QL, United Kingdom.
E-mail addresses: s.mouchet@exeter.ac.uk (S.R. Mouchet), P.Vukusic@exeter.ac.uk (P. Vukusic).
[1] Co-shared first authorship.

https://doi.org/10.1016/j.jlumin.2022.119490
Received 2 June 2022; Received in revised form 25 October 2022; Accepted 1 November 2022
Available online 11 November 2022
0022-2313/© 2022 Published by Elsevier B.V.

both males and females of many cicadas, both pairs of wings are known for their anti-reflective properties [21–26] arising from electromagnetic impedance matching between the air and the wing material covered by quasi-periodic arrays of hexagonally close-packed protrusions, often referred to as nipples (Fig. 1a and b). Similar structures also cover parts of the integument in other organisms such as the wings of several moths and butterflies (Order Lepidoptera), dragonflies and damselflies (Order Odonata) (Fig. 1c–f) [21,25,27–35] and the corneas of some insect eyes [36,37]. In all these examples, the basic building material of the insect tissues is chitin, a polysaccharide, overlaid by a thin epicuticle of wax. In cicadas, transmittance spectra of their wings have been measured to reach more than 90% and to peak at up to 98% over the range from 500 to 2500 nm [22,23]. These anti-reflective properties are thought to be involved as part of the insects' strategy for crypsis and the nano-structured protrusions have been mimicked for the development of anti-reflective coatings for a full range of applications such as solar cells, screens, anti-glare glasses, light-sensitive detectors, telescopes and camera lenses [21,38–40]. In addition to this optical property, the transparent wings of insects are known to be hydrophobic [23–25, 41–44] and some exhibit anti-bacterial properties [44–48]. In the case of cicadas, the surface morphology was found to influence jointly the hydrophobic and anti-reflective properties (Fig. 1) [24,25]. The protrusions on the wing surface can be modelled as truncated cones covered by hemispheres. The cone shape affects the transparency and the hemispheres enhance the wing's hydrophobicity. Despite these properties, which are relevant in many scientific fields ranging from physics and material science to chemistry and biology, to the best of our knowledge fluorescence emission has so far not been reported, to the best of our knowledge, in any of the 3000 described species of the superfamily Cicadoidea. The phenomenon has however been investigated in several butterfly and moth species, in which the coloured wing scales are known to embed fluorophores such as papiliochrome II [3,6,49–52].

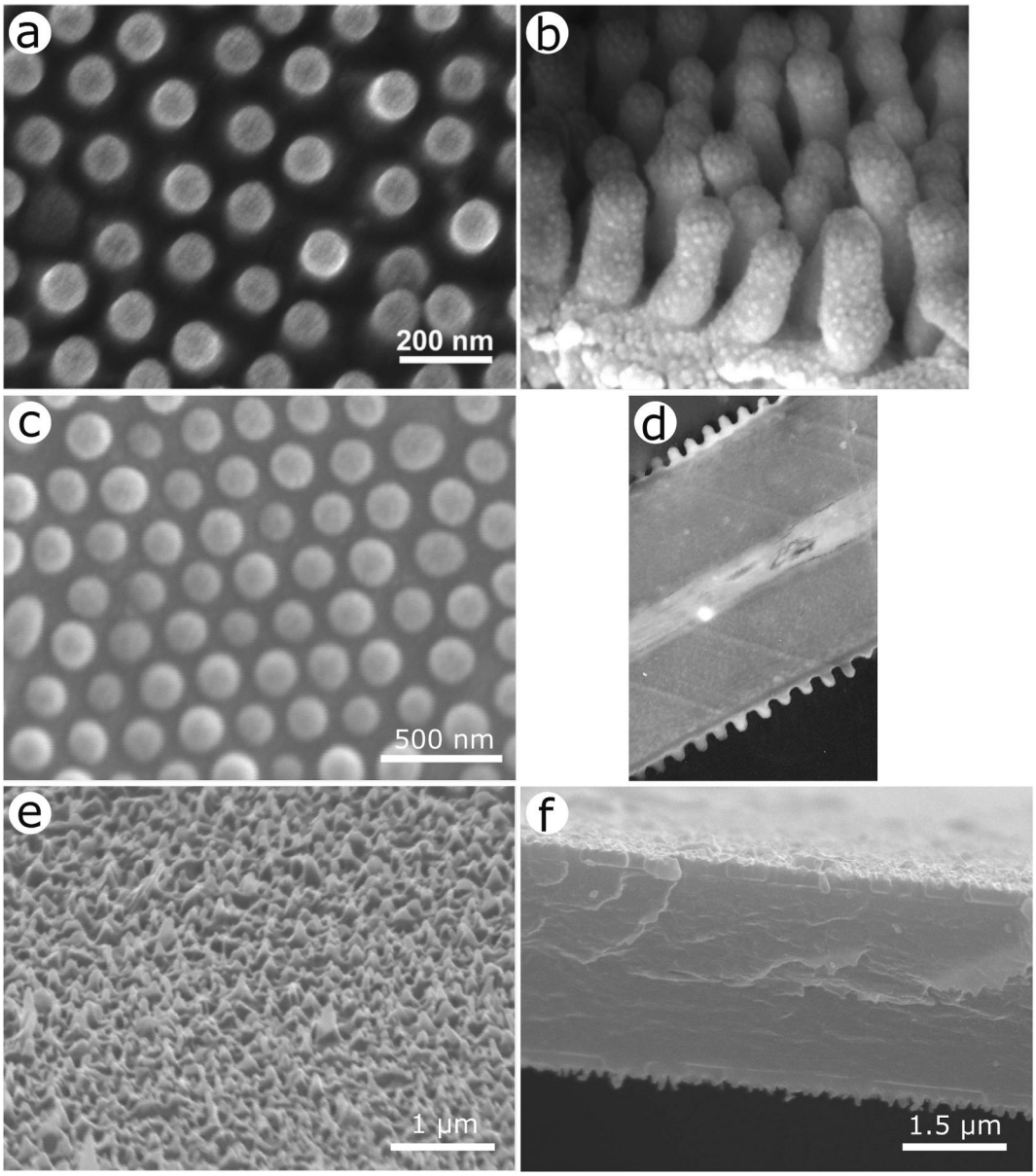


Fig. 1. The transparent parts of the wings of insects including the grey cicada Cicada*orni*(a,b), the broad-bordered bee hawk-moth*Hemaris fuciformis*(c,d) and the dragonfly blue hawker*Aeshna cyanea*(e,f) are covered by arrays of protrusions. These protrusions are sometimes displayed along a quasi-periodic hexagonally close-packed array such as on the wings of *C. orni* (a,b) and *H. fuciformis* (c) or a disordered pattern such as in the case of *A. cyanea* (e), as observed here by scanning electron microscopy (a-c,e-f) and transmission electron microscopy (d) with top views (a,c), oblique views (b,e) and views of cross-sections (d,f). Figures (a,b) and (d) were reproduced (a,b) from Ref. [24] with permission from AIP publishing and (d) from Ref. [30] with permission from Springer Nature.

Photonic structures present in these scales sometimes mediate the associated light emission [53–55]. Fluorescence has also been described in the vein joints and the membrane of the transparent wings of damselflies and dragonflies [56–59]. This emission was attributed to the presence of autofluorescent proteins such as resilin. Resilin proteins emit blue light (at about 400 nm) under incident UV light and were reported to decrease in concentration toward the distal regions of the wings (on both sides) [56,57]. They give rise to low stiffness and high strain in biological tissues, allowing passive wing deformations [60,61]. We note that resilin fluorescence may often be incidental with little or no semiotic function. However, in the case of males of the red-winged damselfly *Mnesarete pudica* (Hagen in Selys, 1853), fluorescence emission from resilin-containing wings was demonstrated to have a role in signalling (e.g., in courtship and territorial behaviour) in combination with pigments and UV reflection, by modulating the visual appearance of the insect according to sex and age [62].

In this article, we characterised the fluorescence emission from the transparent wings of two species of cicadas, the grey cicada Cicada *orni* (Linnaeus, 1758) (Fig. 2a) and the common cicada *Lyristes (Tibicen) plebejus* (Scopoli, 1763), using both linear and nonlinear optical methods. We compared their properties with the fluorescence emission from two other insects exhibiting transparent wings, namely, *Hemaris fuciformis* (Linnaeus, 1758) commonly known as the broad-bordered bee hawk-moth (Fig. 2b) and the Bornean damselfly *Vestalis amabilis* (Lieftinck, 1965) (Fig. 2c). These fluorescent properties were optically characterised by one- and multi-photon microscopy and spectrometry. The one-photon fluorescence techniques allowed us to explain the previously measured high absorption in the range 300–400 nm [24] and to infer the biological role of the fluorophores in the visual perception of insects. Multi-photon techniques enabled us to highlight the symmetry properties of the material within the wings.

2. Materials and methods

2.1. Sample collection

Adult specimens of *C. orni* and *L. plebejus* were collected in Fournès in the Gard Department (France) on the June 22, 2014 (by S.R. Mouchet and L. Dellieu), and *V. amabilis* was collected in swamp forest in Belait Division (Brunei Darussalam) in 1994 (by A.G. Orr). Adult specimens of *H. fuciformis* were bought from licensed vendors. *V. amabilis* was immersed for 24 h in acetone and air-dried. Other specimens were air-dried. No further sample preparation was necessary for the microscopy and spectrofluorimetry observations. All analyses were performed on the insects' wings.

2.2. Optical and fluorescence microscopy

The sample wings were analysed using two different configurations of the microscope: a reflection mode (illumination with visible light and observation in the visible range) and a fluorescence mode (illumination with ultraviolet light and observation in the visible range). Optical microscopy analysis was performed using an Olympus BX61 (Tokyo, Japan) microscope, an Olympus XC50 camera and an Olympus BX-UCB visible light source (in reflection mode) or a Lumen Dynamics X-cite Series 120 PCQ (Mississauga, Ontario, Canada) UV-lamp (in fluorescence mode).

2.3. Spectrofluorimetry

One-photon fluorescence (1 PF) emission spectra were recorded using a 450 W xenon lamp as steady state excitation source. The incident light formed a 45° angle with the normal direction to the sample surface and emitted light was detected at a 45° angle on the other side of the normal direction. The sample was excited at different excitation wavelengths: 320 nm, 340 nm, 360 nm, 380 nm, 400 nm, 420 nm, and 440 nm. Time-resolved measurements of fluoresence emission were performed using a microF920H xenon Flashlamp light source operating at a frequency of 100 Hz with a pulse width of 4 μs and excitation wavelengths equal to 340 nm and 360 nm. These time-resolved measurements were performed at the wavelengths of the maximum of emission peak intensity. They were fitted to double exponential functions. These best fits allowed us to assess the decay time of the fluorescence emission.

2.4. Multiphoton microscopy

Multiphoton microscopy experiments were carried out with an Olympus BX61 WI-FV1200-M (Münster, Germany) system. The laser was a Spectra-Physics (Santa Clara, CA, USA) InSight DS+ laser (82-MHz repetition rate, 120-fs pulse width, *p*-polarised) at 800 nm, 900 nm, 1000 nm, and 1100 nm fundamental wavelengths. The incident laser power was controlled by an achromatic half-wave plate and a *s*-oriented polariser directly after the laser. The laser beam was focused on the sample via either a 15× LMV objective (NA 0.3) or a 50× SLMPlan N objective (NA 0.35). The resulting signal was detected non-descanned in backwards reflection via a Hamamatsu R3896 photomultiplier tube. Different detection optics were used, depending on the excitation wavelength, in order to separate the two-photon fluorescence (2 PF) and the Second Harmonic Generation (SHG) signal. At 1000 nm, a 525 LPXR dichroic mirror was used to remove the SHG from the 2 PF, and an additional 500/10 bandpass filter cleared the SHG signal further. Similar filters were used for the other three fundamental wavelengths. The signal at each pixel was depicted in the micrographs as different intensities in false green (SHG) or false red (2 PF) colours. A routine providing an extended depth field allowed us to obtain in-focus micrographs from multiple images recorded at different depths in steps of 4 μm. Samples were observed over several minutes of time, in order to assess the photostability.

2.5. Electron microscopy

Apart from two scanning electron microscopy (SEM) images taken

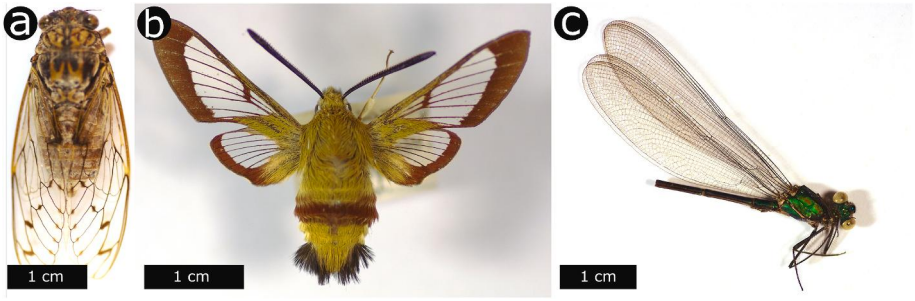


Fig. 2. The wings of the grey cicada*C. orni*(a), the broad-bordered bee hawk-moth*H. fuciformis*(b) and the damselfly*V. amabilis*(c) exhibit transparent wings.

from the literature [24], SEM observations were performed with a FEI (Hillsboro, OR) Nova 600 NanoLab Dual-Beam FIB/SEM microscope on small transparent regions of the wing membranes of *H. fuciformis* and *A. cyanea*. These samples were mounted onto SEM stubs with electrically conducting epoxy resin and sputter-coated with ca. 8 nm of gold palladium.

Transmission electron microscopy (TEM) imaging was carried on with cross-sections of transparent regions of *H. fuciformis*'s wings using a JEOL (Tokyo, Japan) 100S TEM instrument. The figure was previously published in Ref. [30]. The samples were fixed in 3% glutaraldehyde at 21°C for 2 h and consequently rinsed in sodium cacodylate buffer before being fixed in 1% osmic acid in buffer for 1 h. The samples were then block-stained in 2% aqueous uranyl acetate for 1 h, dehydrated through an acetone series (ending in 100% acetone) and embedded in Spurr resin [63]. After microtoming, cross-sections were stained with lead citrate.

3. Results and discussion

Both *C. orni* and *L. plebejus* cicada species have brown-grey bodies and transparent wings (Fig. 2) with very low light reflection [21–26]. The bodies and wings are approximately 25 mm and 30–35 mm long, respectively. Like most insects including moths and damselflies, the wings of cicadas are divided by veins (Fig. 3a–d) appearing as darker structures forming the structurally flexible frame supporting of the wing membranes, while the transparent parts are membranes that form the main aerodynamic surface of the wing [60,64].

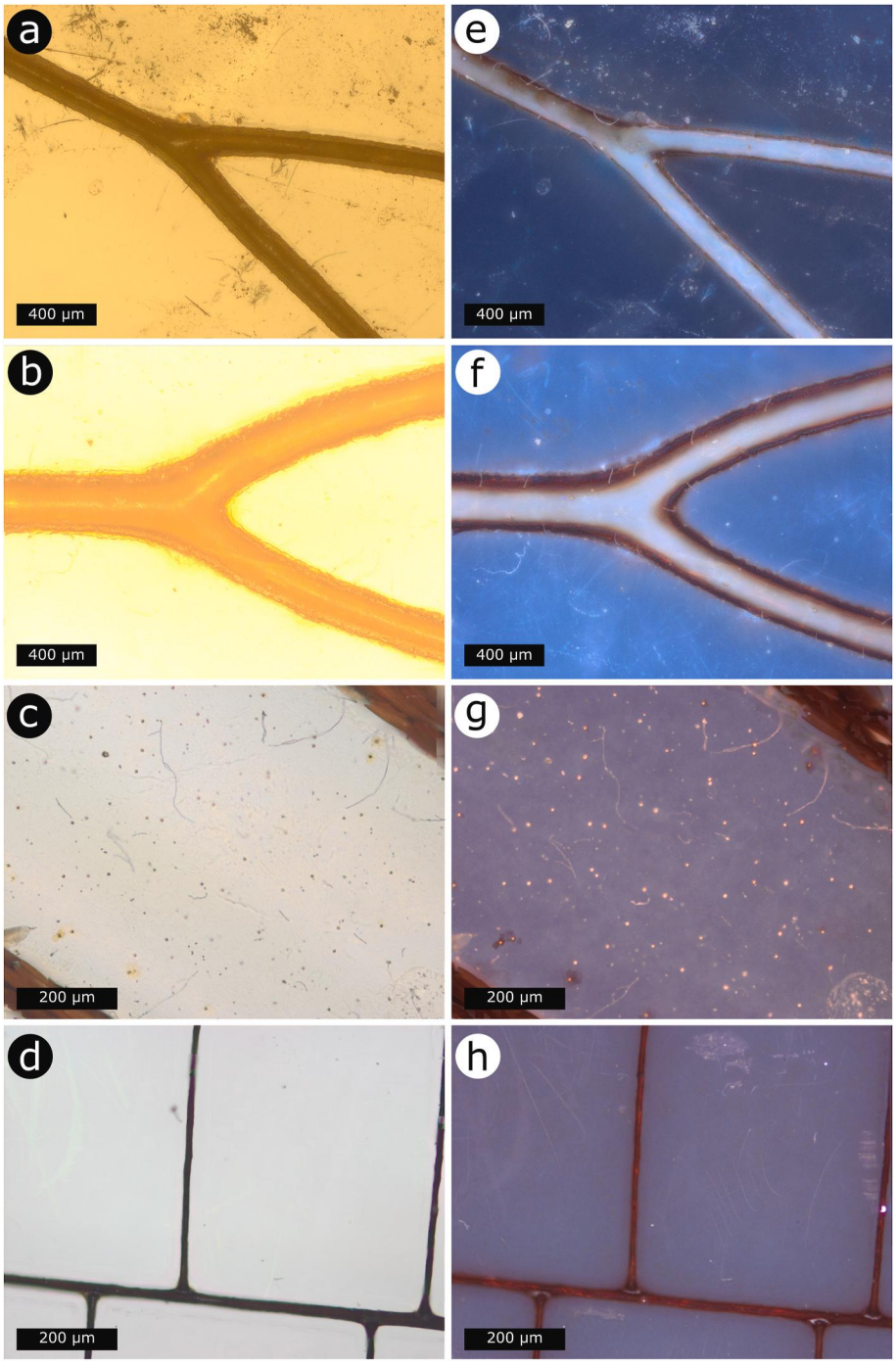


Fig. 3. The membranes and the veins of the transparent wings of the grey cicada (*C. orni*), the common cicada (*L. plebejus*), the broad-bordered bee hawk-moth (*H. fuciformis*) and *V. amabilis* damselfly emit light by fluorescence under UV irradiation. The transparent wings of *C. orni* (a), *L. plebejus* (b), *H. fuciformis* (c) and *V. amabilis* (d) are divided by brown veins. Both their transparent membranes and the veins of the wings emit visible light under UV incident light (e–h). The 1 PF signal from the veins of the cicada species (e,f) is especially intense.

Fluorescent microscopy observations indicate that both the transparent membrane and the veins of the wings fluoresce (Fig. 3). The latter are clearly brighter in the two investigated cicada species (Fig. 3e and f), indicating that they might contain many more fluorescent molecules than the membrane. Chitin is known to give rise to autofluorescence, with a very low quantum yield [65]. In addition, autofluorescent proteins such as resilin are known to be at the origin of blue hue fluorescence emission from damselfly and dragonfly species [56–58,62]. Hence both chitin and resilin are likely to play a role in the fluorescence emission observed from investigated cicada and moth species (Fig. 3e–g). It was previously reported that the extinction coefficient κ -namely, the imaginary part of the complex refractive index- of the wing material of *C. orni* exhibits a double peak in the UV range 200–300 nm, reaching ca. $\kappa = 2.5 \times 10^{-2}$ and $\kappa = 1.5 \times 10^{-2}$, with a non-negligible component in the range 300–400 nm [24]. Similarly, Azofeifa et al. measured peaks at 280 nm and 325 nm in the extinction coefficient for chitin samples from the exoskeleton of fresh Pacific white shrimps *Litopenaeus* (formerly *Penaeus*) *vannamei* (Boone, 1931) [66].

Our results show that light absorption in the wings of insects such as cicadas within the range 300–400 nm gives rise to fluorescence emission. In all four investigated insect wings, fluorescence emission single peaks were measured upon excitation with wavelengths ranging from 320 nm to 440 nm (Fig. 4). For instance, the measured emission spectra display peaks at about 410–420 nm with a 360-nm excitation wavelength. In addition, a 340-nm excitation wavelength appears to give rise to the most intense emission. The presence of a single peak in the emission spectra suggests that there is likely only a single type of fluorophore within the insect wings. The presence of mixtures of several fluorophores is less likely as this would imply emission spectra with multiple peaks. The measured emission peaks for all four insect wings are similar to the fluorescence emission measured by Chuang et al. from the wings of the damselfly *Ischnura senegalensis* (Rambur, 1842) [59]. Despite the fact that our observations are significantly different from the fluorescence response from the male neotropical damselfly *M. pudica* (i.e., emission at ca. 650 nm upon excitation at 405 nm) [62], the wings of which are known to contain resilin, the emission peaks that we measured are in agreement with the emission band of resilin located at ca. 415 nm [58,67].

In addition, the emission peak widths and positions strongly depend on the excitation wavelength (Fig. 4). The peak position shifts from ca. 380 nm to ca. 490 nm as the excitation wavelength is increased from 320 nm to 440 nm. This dependence is similar to the previously reported one for males of the beetle *Hoplia coerulea* (Drury, 1773) [14]. It suggests that the fluorophores could exhibit complex dynamics with several excited states. In complex organic fluorophores, several excited states are likely related to exciton resonances (i.e., energy transfers between different donor and acceptor groups within the same molecule) [14,68,69].

In order to understand better the radiative response in the linear regime, we performed time-resolved measurement of the emitted fluorescence intensity (Fig. 5).

In all cases (Table 1), the best fits to double exponential functions gave rise to a long decay time (of ca. 7–8 ns) and a short decay time (of ca. 1.1–1.3 ns), whatever the excitation and detection wavelengths were. This also suggests that only one type of fluorophores is present in the wings of each insect. The long decay time is related to the radiative decay of the fluorophores, whereas the short one is related to non-radiative decay [70]. If we assume that measured fluorescent signals originate from the same molecule (namely, resilin), the discrepancy observed in the emission spectra and decay time among the investigated samples could be attributed to differences in the chemical environment among the various species.

In addition, both *C. orni* and *L. plebejus* were probed at fundamental wavelengths ranging from 800 nm to 1100 nm, and showed significant SHG and 2 PF signal response over all this wavelength range (see Fig. 6 at a 1000-nm wavelength). At any of these selected fundamental wavelengths, the veins clearly appear in both SHG and 2 PF observations. The difference in signals between the veins and the membrane (in 1 PF, 2 PF, and SHG) is likely due to the significant difference in composition [56,57,64]: the veins of cicadas would show a much higher

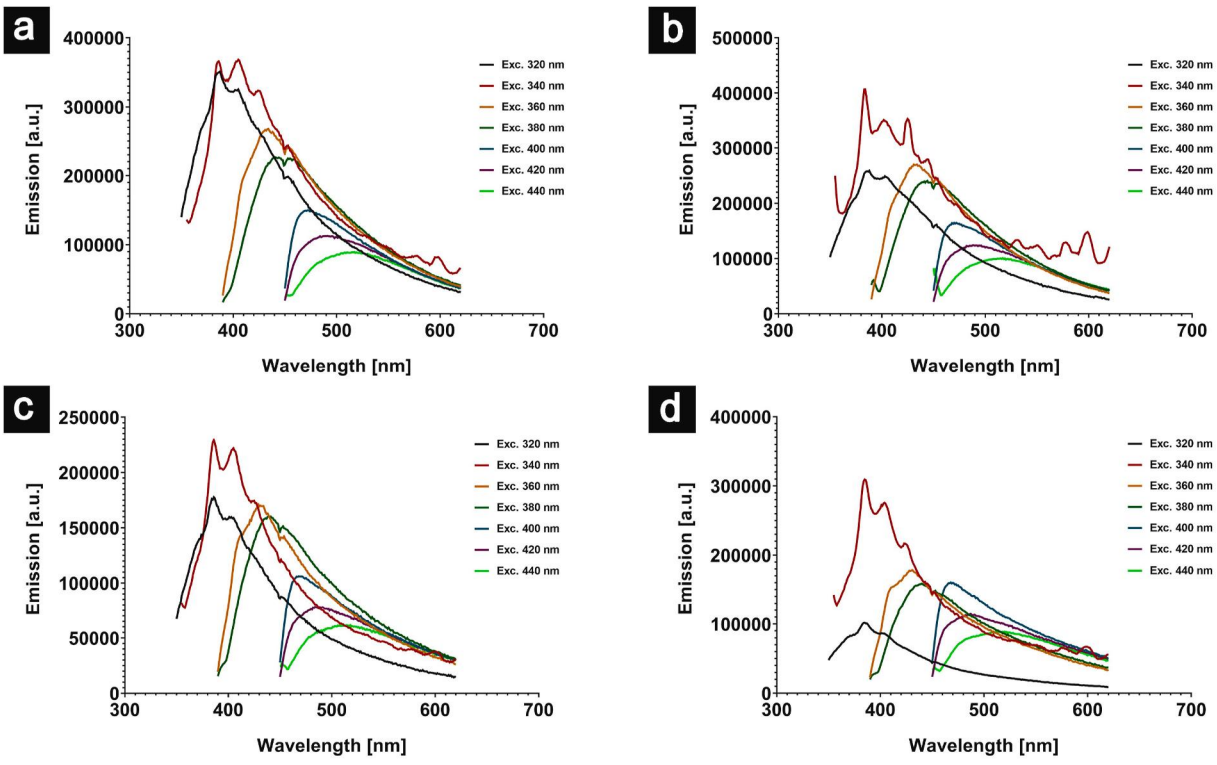


Fig. 4. Fluorescence emission from the transparent wings of a) *C. orni*, b) *L. plebejus*, c) *H. fuciformis*, d) *V. amabilis*. The emission peak widths, intensities and positions strongly depend on the excitation wavelength and are in agreement with the narrow emission band of resilin reported in the literature [67].

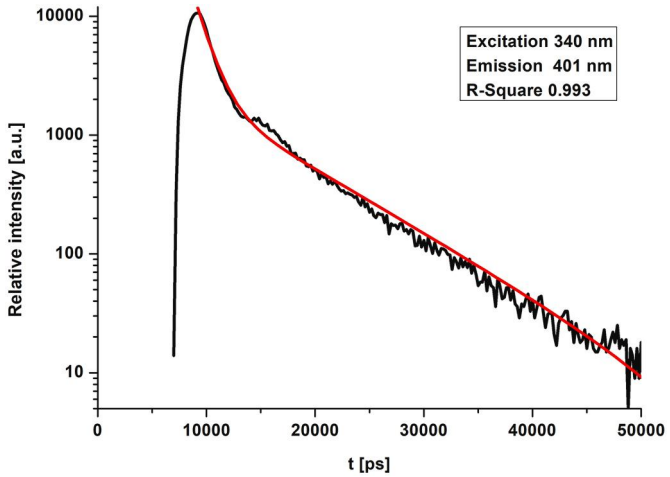


Fig. 5. Time-resolved measurement of the emission intensity of the fluorophores embedded in the wings of *H. fuciformis* (black curve). The measurements were performed with an excitation wavelength at 340 nm and an emission wavelength at 401 nm. The best fit to the decay is a double exponential function (red curve).

Table 1
Decay times of the fluorophores embedded within the transparent wings of *C. orni*, *L. plebejus*, *H. fuciformis* and *V. amabilis*. Measurements were performed at excitation wavelengths equal to 340 nm and 360 nm, and emission wavelengths lying within the emission peaks.

Species	Excitation Wavelength [nm]	Emission Wavelength [nm]	Decay time [ps]
Cicada orni	340	385	$t_1 = 1271.23$ $t_2 = 8933.32$
	340	403	$t_1 = 1309.57$ $t_2 = 9272.42$
	360	388	$t_1 = 1192.96$ $t_2 = 8508.55$
	360	406	$t_1 = 1237.31$ $t_2 = 8831.80$
Lyristes (Tibicen) plebejus	340	384	$t_1 = 1372.48$ $t_2 = 8288.30$
	340	402	$t_1 = 1184.63$ $t_2 = 7688.22$
	360	387	$t_1 = 1107.87$ $t_2 = 7708.26$
	360	406	$t_1 = 1328.55$ $t_2 = 8299.55$
Hemaris fuciformis	340	384	$t_1 = 1322.55$ $t_2 = 8249.07$
	340	401	$t_1 = 1278.86$ $t_2 = 8149.58$
	340	425	$t_1 = 1313.99$ $t_2 = 8491.21$
	360	406	$t_1 = 1298.20$ $t_2 = 7997.02$
	360	424	$t_1 = 1284.24$ $t_2 = 8262.70$
	360	451	$t_1 = 1245.23$ $t_2 = 8126.60$
Vestalis amabilis	340	384	$t_1 = 1235.50$ $t_2 = 7578.67$
	340	402	$t_1 = 1374.48$ $t_2 = 8060.57$
	340	425	$t_1 = 1338.49$ $t_2 = 8220.30$
	360	387	$t_1 = 1326.02$ $t_2 = 8226.46$
	360	406	$t_1 = 1203.75$ $t_2 = 7596.25$
	360	450	$t_1 = 1119.60$ $t_2 = 7841.73$

concentration in chitin and the fluorescent compounds. The former is known to give rise to an SHG signal [71]. Additionally, the veins are much thicker than the membrane, leading to an increased amount of material. Optical second-order behaviours such as SHG are known to take place exclusively in non-centrosymmetric media [72]. The detected SHG signal implies that the veins are materially organised in a non-centrosymmetric (and hence non-random) way.

From a visual point of view, the biological significance of fluorescence emission in the transparent wings of insects depends on the total number of photons emitted or scattered from the wings and transmitted through the wings from their backgrounds. Many cicadas are known to be mainly active during the hottest hours of summer days, when sunlight is very intense (but may also be active at twilight and at night). Although the measured fluorescence emission ranges match the range of both scotopic and photopic photoreceptors of many insects [73–76], it is hard to conclude that the measured 1 PF signal plays any role in cicadas' behaviour since the quantum yield of natural fluorophores are generally low [4,5,12], especially that of chitin [65], and the ratio of UV light in both sun- and moonlight is very limited with respect to that of visible light (for instance, ca. 6% of sunlight at sea level lies in the UV range, whereas about 50% is visible) [77]. The role of this fluorescence emission may possibly be a by-product of another biological function such as photoprotection due to the increased absorption of UV by the fluorophores (for example, when the wings are at rest over the insect's body in the case of cicadas) and incidental property of resilin that enhances wing flexibility.

4. Conclusion

Transparent wings of two cicada species, namely *C. orni*, *L. plebejus*, as well as the broad-bordered bee hawk-moth *H. fuciformis*, were demonstrated to emit light under incident UV light by fluorescence decay. All of them showed similar 1 PF properties, as their wings were excited in the 320–440 nm range and emitted in the range 380–490 nm. They were compared to the transparent wings of the damselfly *V. amabilis*, which showed similar fluorescent behaviours. Damselflies fluorescence emission is reported to arise from substances such as resilin embedded in their tissues. Additionally, the wings of both cicada species and more specifically their veins showed strong SHG and 2 PF signals, which are possibly due to the higher concentration of resilin or chitin in the veins with respect to the membrane that makes up most of the wing. The nonlinear optical characterisation of the cicadas' wings gives us more insight into the wing structure, indicating that multiphoton techniques add valuable information while characterising biological samples.

Author statement

Sébastien R. Mouchet: Conceptualisation, Methodology, Investigation, Resources, Data Curation, Writing - Original Draft, Writing - Review & Editing, Visualisation, Project administration; Charlotte Verstraete: Investigation, Data Curation, Writing - Original Draft, Writing - Review & Editing, Visualisation, Project administration, Funding acquisition; Bojana Bokic: Investigation, Writing - Review & Editing, Visualisation, Funding acquisition; Dimitrije Mara: Investigation, Data Curation, Writing - Review & Editing, Visualisation, Funding acquisition; Louis Dellieu: Resources, Writing - Review & Editing; Albert G. Orr: Resources, Writing - Review & Editing; Olivier Deparis: Writing - Review & Editing, Rik Van Deun: Writing - Review & Editing, Thierry Verbiest: Writing - Review & Editing, Supervision, Funding acquisition; Pete Vukusic: Conceptualisation, Investigation, Resources, Writing - Review & Editing; and Branko Kolaric: Conceptualisation, Methodology, Writing - Review & Editing, Project administration, Funding acquisition

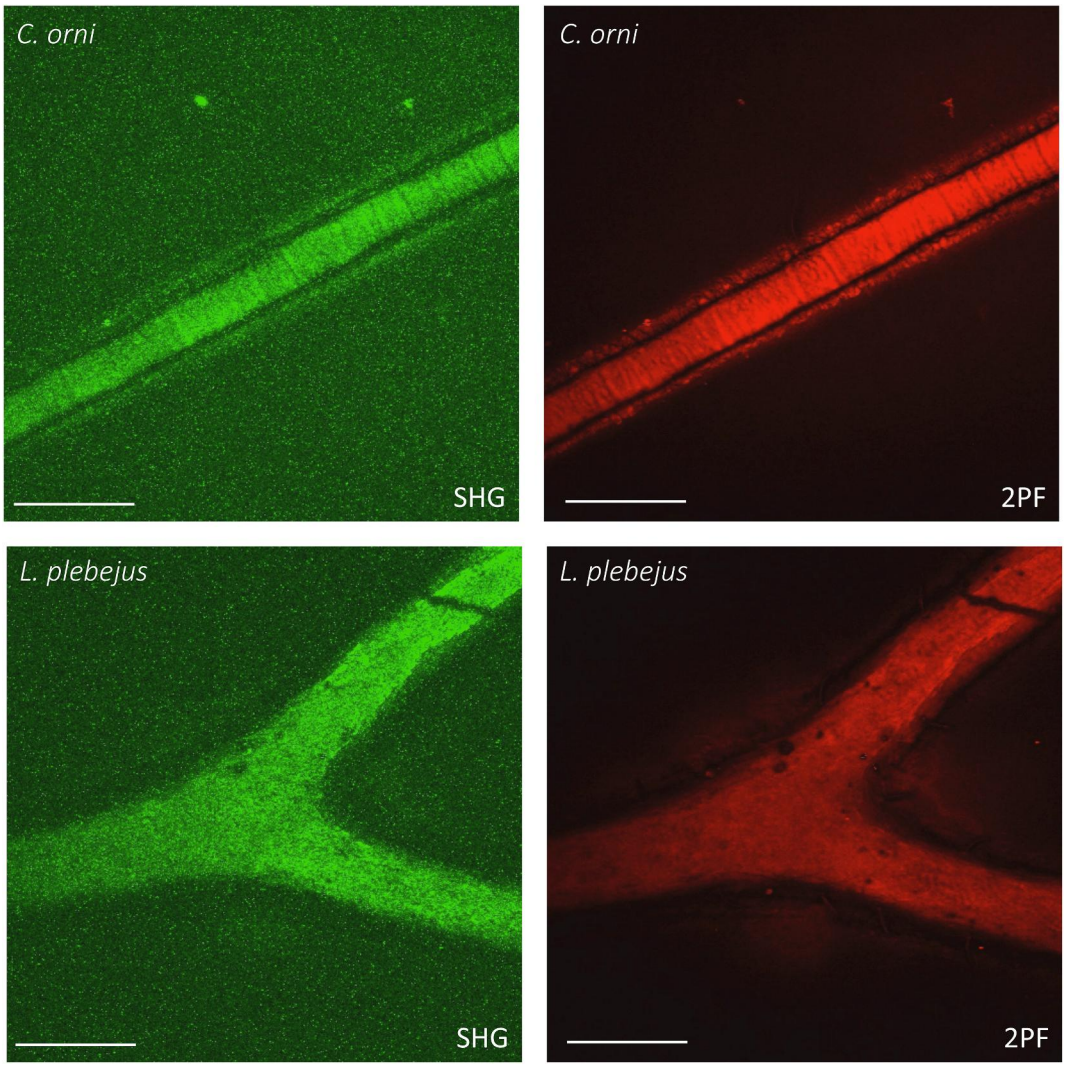


Fig. 6. Strong SHG and 2 PF signals are observed from the veins of the wings. Multiphoton micrographs of *C. orni* (top) and *L. plebejus* (bottom) at a fundamental wavelength of 1000 nm. Left: SHG response. Right: 2 PF response. Laser power: 200 mW (*C. orni*) and 80 mW (*L. plebejus*). Scale bars: 200 μm.

Declaration of competing interest

The authors declare that they have no known competing financial interests or personal relationships that could have appeared to influence the work reported in this paper.

Data availability

Data will be made available on request.

Acknowledgments

SRM was supported by the Belgian National Fund for Scientific Research (FRS-FNRS) (91400/1.B.309.18F), the Maturation Fund of the Walloon Region, and a BEWARE Fellowship (Convention n°2110034) of the Walloon Region (Marie Skłodowska-Curie Actions of the European Union - COFUND - contract 847587), as a Postdoctoral Researcher. DM acknowledges KU Leuven Postdoctoral Mandate Internal Funds (PDM) for a Postdoctoral fellowship (PDM/20/092). TV acknowledges financial support from the Hercules Foundation. BK and BB acknowledge financial support of the Ministry of Education, Science and Technological Development of the Republic of Serbia (grant III 45016). BK, BB and DM acknowledge the support of the Office of Naval Research Global through the Research Grant N62902-22-1-2024. In addition, BK acknowledges support from FRS-FNRS. This research used resources of the Lasers, Optics & Spectroscopies (LOS) Technology Platform (https://platforms.unamur.be/los) of UNamur.

References

[1] M. Pavan, M. Vachon, Sur l'existence d'une substance fluorescente dans les téguments des scorpions (Arachnides), C. R. Acad. Sci. 239 (1954) 1700–1702.
[2] K. Tani, F. Watari, M. Uo, M. Morita, Fluorescent properties of porcelain-restored teeth and their discrimination, Mater. Trans. 45 (2004) 1010–1014.
[3] P. Vukusic, I. Hooper, Directionally controlled fluorescence emission in butterflies, Science 310 (2005) 1151.
[4] A. Iriel, M.G. Lagorio, Is the flower fluorescence relevant in biocommunication? Naturwissenschaften 97 (10) (2010) 915–924.
[5] A. Iriel, M.G. Lagorio, Implications of reflectance and fluorescence of *Rhododendron indicum* flowers in biosignaling, Photochem. Photobiol. Sci. 9 (2010) 342–348.
[6] V.L. Welch, E. Van Hooijdonk, N. Intrater, J.-P. Vigneron, Fluorescence in insects, Proc. SPIE 8480 (2012), 848004.
[7] M.G. Lagorio, G.B. Cordon, A. Iriel, Reviewing the relevance of fluorescence in biological systems, Photochem. Photobiol. Sci. 14 (2015) 1538–1559.
[8] D.F. Gruber, J.P. Gaffney, S. Mehr, R. DeSalle, J.S. Sparks, J. Platisa, V. A. Pieribone, Adaptive evolution of eel fluorescent proteins from fatty acid binding proteins produces bright fluorescence in the marine environment, PLoS One 10 (11) (2015) e0140972.
[9] D.F. Gruber, E.R. Loew, D.D. Deheyn, D. Akkaynak, J.P. Gaffney, W.L. Smith, M. P. Davis, J.H. Stern, V.A. Pieribone, J.S. Sparks, Biofluorescence in catsharks (Scyliorhinidae): fundamental description and relevance for elasmobranch visual ecology, Sci. Rep. 6 (24751) (2016) 1–16.

[10] S.R. Mouchet, M. Lobet, B. Kolaric, A.M. Kaczmarek, R. Van Deun, P. Vukusic, O. Deparis, E. Van Hooijdonk, Controlled fluorescence in a beetle's photonic structure and its sensitivity to environmentally induced changes, Proc. R. Soc. Lond. B Biol. Sci. 283 (1845) (2016).

[11] J. Marshall, S. Johnsen, Fluorescence as a means of colour signal enhancement, Philos. Trans. R. Soc. Lond. B Biol. Sci. 372 (1724) (2017).

[12] C. Taboada, A.E. Brunetti, F.N. Pedron, F. Carnevale Neto, D.A. Estrin, S.E. Bari, L. B. Chemes, N. Peporine Lopes, M.G. Lagorio, J. Faivovich, Naturally occurring fluorescence in frogs, Proc. Natl. Acad. Sci. USA 114 (14) (2017) 3672–3677.

[13] P. Deschepper, B. Jonckheere, J. Matthys, A light in the dark: the discovery of another fluorescent frog in the Costa Rican rainforests, Wilderness Environ. Med. 29 (3) (2018) 421–422.

[14] S.R. Mouchet, A.M. Kaczmarek, D. Mara, R. Van Deun, P. Vukusic, Colour and fluorescence emission of *Euchroea auripigmenta* beetle, Proc. SPIE 10965 (2019) 72–82.

[15] M. Ladouce, T. Barakat, B.-L. Su, O. Deparis, S.R. Mouchet, Scattering of ultraviolet light by avian eggshells, Faraday Discuss. 223 (2020) 63–80.

[16] M. Ladouce, T. Barakat, B.-L. Su, O. Deparis, S.R. Mouchet, UV scattering by pores in avian eggshells, Proc. SPIE 11481 (2020) 101–109.

[17] M. Mohd Top, C.L. Puan, M.-F. Chuang, S.N. Othman, A. Borzée, First record of ultraviolet fluorescence in the bent-toed gecko *Cyrtodactylus quadrivirgatus* taylor, 1962 (Gekkonidae: Sauria), Herpetol. Notes 13 (2020) 211–212.

[18] A.C. Croce, Light and autofluorescence, multitasking features in living organisms, Photochemistry 1 (2) (2021) 67–124.

[19] L. Reinhold, Mammals with fluorescent fur: observations from the wet tropics, North Queensl. Nat. 51 (2021) 1–8.

[20] S.L.D. Toussaint, J. Ponstein, M. Thoury, R. Métivier, D.C. Kalthoff, B. Habermeyer, R. Guilard, S. Bock, P. Mortensen, S. Sandberg, P. Gueriau, E. Amson, Fur glowing under ultraviolet: *in situ* analysis of porphyrin accumulation in the skin appendages of mammals, Integr. Zool. 0 (2021) 1–12.

[21] S.R. Mouchet, O. Deparis, Natural Photonics and Bioinspiration, Artech House, 2021.

[22] P.R. Stoddart, P.J. Cadusch, T.M. Boyce, R.M. Erasmus, J.D. Comins, Optical properties of chitin: surface-enhanced Raman scattering substrates based on antireflection structures on cicada wings, Nanotechnology 17 (3) (2006) 680.

[23] M. Sun, A. Liang, Y. Zheng, G.S. Watson, J.A. Watson, A study of the anti-reflection efficiency of natural nano-arrays of varying sizes, Bioinspiration Biomimetics 6 (2) (2011), 026003.

[24] L. Dellieu, M. Sarrazin, P. Simonis, O. Deparis, J.-P. Vigneron, A two-in-one superhydrophobic and anti-reflective nanodevice in the grey cicada *Cicada orni* (Hemiptera), J. Appl. Phys. 116 (2) (2014), 024701.

[25] O. Deparis, S.R. Mouchet, L. Dellieu, J.-F. Colomer, M. Sarrazin, Nanostructured surfaces: bioinspiration for transparency, coloration and wettability, Mater. Today Proc. 1S (2014) 122–129.

[26] C. Verstraete, S.R. Mouchet, T. Verbiest, B. Kolaric, Linear and nonlinear optical effects in biophotonic structures using classical and nonclassical light, J. Biophot. (2019), e201800262.

[27] A. Yoshida, M. Motoyama, A. Kosaku, K. Miyamoto, Nanoprotuberance array in the transparent wing of a hawkmoth, *Cephonodes hylas*, Zool. Sci. 13 (4) (1996) 525–526.

[28] A. Yoshida, M. Motoyama, A. Kosaku, K. Miyamoto, Antireflective nanoprotuberance array in the transparent wing of a hawkmoth, *Cephonodes hylas*, Zool. Sci. 14 (5) (1997) 737–741.

[29] A. Yoshida, Antireflection of the butterfly and moth wings through microstructure, Forma 17 (2) (2002) 75–89.

[30] P. Vukusic, J.R. Sambles, Photonic structures in biology, Nature 424 (6950) (2003) 852–855.

[31] I.R. Hooper, P. Vukusic, R.J. Wootton, Detailed optical study of the transparent wing membranes of the dragonfly *Aeshna cyanea*, Opt Express 14 (11) (2006) 4891–4897.

[32] O. Deparis, N. Khuzayim, A. Parker, J.-P. Vigneron, Assessment of the antireflection property of moth wings by three-dimensional transfer-matrix optical simulations, Phys. Rev. E 79 (2009), 041910.

[33] D.G. Stavenga, Thin film and multilayer optics cause structural colors of many insects and birds, Mater. Today Proc. 1S (2014) 109–121.

[34] R. Siddique, G. Gomard, H. Hölscher, The role of random nanostructures for the omnidirectional anti-reflection properties of the glasswing butterfly, Nat. Commun. 6 (2015) 6909.

[35] S.R. Mouchet, C. Verstraete, D. Mara, S.V. Cleuvenbergen, E.D. Finlayson, R. Van Deun, O. Deparis, T. Verbiest, B. Maes, P. Vukusic, B. Kolaric, Nonlinear optical spectroscopy and two-photon excited fluorescence spectroscopy reveal the excited states of fluorophores embedded in a beetle's elytra, Interface Focus 9 (1) (2019), 20180052.

[36] C.G. Bernhard, The insect corneal nipple array. a biological, broad-band impedance transformer that acts as an antireflection coating, Acta Physiol. Scand. 63 (243) (1965) 1–79.

[37] D.G. Stavenga, S. Foletti, G. Palasantzas, K. Arikawa, Light on the moth-eye corneal nipple array of butterflies, Proc. R. Soc. Lond. B Biol. Sci. 273 (1587) (2006) 661–667.

[38] G. Xie, G. Zhang, F. Lin, J. Zhang, Z. Liu, S. Mu, The fabrication of subwavelength anti-reflective nanostructures using a bio-template, Nanotechnology 19 (9) (2008), 095605.

[39] Z. Han, Z. Wang, X. Feng, B. Li, Z. Mu, J. Zhang, S. Niun, L. Ren, Antireflective surface inspired from biology: a review, Biosurf. Biotribol. 2 (2016) 137–150.

[40] I. Zada, W. Zhang, P. Sun, M. Imtiaz, W. Abbas, D. Zhang, Multifunctional, angle dependent antireflection, and hydrophilic properties of SiO_2 inspired by nano-scale structures of cicada wings, Appl. Phys. Lett. 111 (15) (2017), 153701.

[41] G. Zhang, J. Zhang, G. Xie, Z. Liu, H. Shao, Cicada wings: a stamp from nature for nanoimprint lithography, Small 2 (12) (2006) 1440–1443.

[42] M. Sun, G.S. Watson, Y. Zheng, J.A. Watson, A. Liang, Wetting properties on nanostructured surfaces of cicada wings, J. Exp. Biol. 212 (19) (2009) 3148–3155.

[43] K.M. Wisdom, J.A. Watson, X. Qu, F. Liu, G.S. Watson, C.-H. Chen, Self-cleaning of superhydrophobic surfaces by self-propelled jumping condensate, Proc. Natl. Acad. Sci. USA 110 (20) (2013) 7992–7997.

[44] J. Román-Kustas, J.B. Hoffman, J.H. Reed, A.E. Gonsalves, J. Oh, L. Li, S. Hong, K. D. Jo, C.E. Dana, N. Miljkovic, D.M. Cropek, M. Alleyne, Molecular and topographical organization: influence on cicada wing wettability and bactericidal properties, Adv. Mater. Interfac. 7 (10) (2020), 2000112.

[45] E.P. Ivanova, J. Hasan, H.K. Webb, V.K. Truong, G.S. Watson, J.A. Watson, V. A. Baulin, S. Pogodin, J.Y. Wang, M.J. Tobin, C. Löbbe, R.J. Crawford, Natural bactericidal surfaces: mechanical rupture of *Pseudomonas aeruginosa* cells by cicada wings, Small 8 (16) (2012) 2489–2494.

[46] E.P. Ivanova, J. Hasan, H.K. Webb, G. Gervinskas, S. Juodkazis, V.K. Truong, A. H. Wu, R.N. Lamb, V.A. Baulin, G.S. Watson, J.A. Watson, D.E. Mainwaring, R. J. Crawford, Bactericidal activity of black silicon, Nat. Commun. 4 (2013) 2838.

[47] T. Diu, N. Faruqui, T. Sjoöström, B. Lamarre, H.F. Jenkinson, B. Su, M.G. Ryadnov, Cicada-inspired cell-instructive nanopatterned arrays, Sci. Rep. 4 (2014) 7122.

[48] S.M. Kelleher, O. Habimana, J. Lawler, B. O'Reilly, S. Daniels, E. Casey, A. Cowley, Cicada wing surface topography: an investigation into the bactericidal properties of nanostructural features, ACS Appl. Mater. Interfaces 8 (24) (2016) 14966–14974.

[49] E. Cockayne, I. The distribution of fluorescent pigments in Lepidoptera, Trans. R. Entomol. Soc. Lond. 72 (1–2) (1924) 1–19.

[50] K. Kumazawa, S. Tanaka, K. Negita, H. Tabata, Fluorescence from wing of *Morpho sulkowskyi* butterfly, Jpn. J. Appl. Phys. 33 (1;4A) (1994) 2119–2122.

[51] T.M. Trzeciak, B.D. Wilts, D.G. Stavenga, P. Vukusic, Variable multilayer reflection together with long-pass filtering pigment determines the wing coloration of papilionid butterflies of the *nireus* group, Opt. Express 20 (8) (2012) 8877–8890.

[52] B.D. Wilts, T.M. Trzeciak, P. Vukusic, D.G. Stavenga, Papiliochrome II pigment reduces the angle dependency of structural wing colouration in *nireus* group papilionids, J. Exp. Biol. 215 (5) (2012) 796–805.

[53] J.-P. Vigneron, K. Kertész, Z. Vértesy, M. Rassart, V. Lousse, Z. Bálint, L.P. Biró, Correlated diffraction and fluorescence in the backscattering iridescence of the male butterfly *Troides magellanus* (Papilionidae), Phys. Rev. E 78 (2008), 021903.

[54] E. Van Hooijdonk, C. Barthou, J.-P. Vigneron, S. Berthier, Detailed experimental analysis of the structural fluorescence in the butterfly *Morpho sulkowskyi* (Nymphalidae), J. Nanophotonics 5 (1) (2011), 053525.

[55] E. Van Hooijdonk, C. Barthou, J.-P. Vigneron, S. Berthier, Angular dependence of structural fluorescent emission from the scales of the male butterfly *Troïdes magellanus* (Papilionidae), J. Opt. Soc. Am. B 29 (5) (2012) 1104–1111.

[56] S.N. Gorb, Serial elastic elements in the damselfly wing: mobile vein joints contain resilin, Naturwissenschaften 86 (11) (1999) 552–555.

[57] E. Appel, S.N. Gorb, Resilin-bearing wing vein joints in the dragonfly *Epiophlebia superstes*, Bioinspiration Biomimetics 6 (4) (2011), 046006.

[58] E. Appel, L. Heepe, C.-P. Lin, S.N. Gorb, Ultrastructure of dragonfly wing veins: composite structure of fibrous material supplemented by resilin, J. Anat. 227 (4) (2015) 561–582.

[59] C.-J. Chuang, C.-D. Liu, R.A. Patil, C.-C. Wu, Y.-C. Chang, C.-W. Peng, T.-K. Chao, J.-W. Liou, Y. Liou, Y.-R. Ma, Impact of cuticle photoluminescence on the color morphism of a male damselfly *Ischnura senegalensis* (Rambur, 1842), Sci. Rep. 6 (2016), 38051.

[60] C.M. Elvin, A.G. Carr, M.G. Huson, J.M. Maxwell, R.D. Pearson, T. Vuocolo, N. E. Liyou, D.C.C. Wong, D.J. Merritt, N.E. Dixon, Synthesis and properties of crosslinked recombinant pro-resilin, Nature 437 (2005) 999–1002.

[61] M. Burrows, S.R. Shaw, G.P. Sutton, Resilin and chitinous cuticle form a composite structure for energy storage in jumping by froghopper insects, BMC Biol. 6 (41) (2008) 1–16.

[62] R. Guillermo-Ferreira, E.M. Therézio, M.H. Gehlen, P.C. Bispo, A. Marletta, The role of wing pigmentation, UV and fluorescence as signals in a neotropical damselfly, J. Insect Behav. 27 (1) (2014) 67–80.

[63] A.R. Spurr, A low-viscosity epoxy resin embedding medium for electron microscopy, J. Ultra. Res. 26 (1) (1969) 31–43.

[64] J.D. Gullion, T. Gullion, Solid-state NMR study of the cicada wing, J. Phys. Chem. B 121 (32) (2017) 7646–7651.

[65] T.A.P. Hai, R. Sugimoto, Fluorescence control of chitin and chitosan fabricated via surface functionalization using direct oxidative polymerization, RSC Adv. 8 (2018) 7005–7013.

[66] D.E. Azofeifa, H.J. Arguedas, W.E. Vargas, Optical properties of chitin and chitosan biopolymers with application to structural color analysis, Opt. Mater. 35 (2012) 175–183.

[67] S.O. Andersen, Characterization of a new type of cross-linkage in resilin, a rubber-like protein, Biochim. Biophys. Acta 69 (1963) 249–262.

[68] J. Lakowicz, Principles of Fluorescence Spectroscopy, Kluwer Academic/Plenum Publishers, New York, NY, 1999.

[69] C. Ramanan, C. Hoon Kim, T.J. Marks, M.R. Wasielewski, Excitation energy transfer within covalent tetrahedral perylenediimide tetramers and their intermolecular aggregates, J. Phys. Chem. C 118 (2014) 16941–16950.

[70] B. Kolaric, R.A.L. Vallée, Dynamics and stability of DNA mechano-nanostructures: energy-transfer investigations, J. Phys. Chem. C 114 (3) (2010) 1430–1435.

[71] M.D. Rabasović, D.V. Pantelić, B.M. Jelenković, S.B. Ćurčić, M.S. Rabasović, M. D. Vrbica, V.M. Lazović, B.P. Ćurčić, A.J. Krmpot, Nonlinear microscopy of chitin and chitinous structures: a case study of two cave-dwelling insects, J. Biomed. Opt. 20 (1) (2015), 016010.
[72] T. Verbiest, K. Clays, V. Rodriguez, Second-order Nonlinear Optical Characterization Techniques: an Introduction, CRC press, 2009.
[73] D. Peitsch, A. Fietz, H. Hertel, J. de Souza, D.F. Ventura, R. Menzel, The spectral input systems of hymenopteran insects and their receptor-based colour vision, J. Comp. Physiol. 170 (1) (1992) 23–40.
[74] D.G. Stavenga, Colour in the eyes of insects, J. Comp. Physiol. 188 (5) (2002) 337–348.
[75] D.G. Stavenga, Surface colors of insects: wings and eyes, in: Functional Surfaces in Biology: Little Structures with Big Effects, 1, Springer Netherlands, Dordrecht, 2009, pp. 285–306.
[76] K. Lunau, Visual ecology of flies with particular reference to colour vision and colour preferences, J. Comp. Physiol. 200 (6) (2014) 497–512.
[77] J. Moan, Visible light and UV radiation, in: A. Brune, R. Hellborg, B. Persson, R. Pääkkönen (Eds.), Radiation at Home, Outdoors and in the Workplace, Oslo), Scandinavian Science Publisher, 2001, pp. 69–85.

symmetry

MDPI

Perspective

Structured Light from Classical to Quantum Perspectives

Bojana Bokić [1], Yovan de Coene [2], Maria Antonietta Ferrara [3], Thierry Verbiest [2], Yves Caudano [4] and Branko Kolaric [1,5,*]

1 Nanophotonics Laboratory, Photonics Center, Institute of Physics, University of Belgrade, Pregrevica 118, 11080 Belgrade, Serbia; bojana@ipb.ac.rs
2 Molecular Imaging and Photonics, Department of Chemistry, KU Leuven, Celestijnenlaan 200 D, Box 2425, B-3001 Leuven, Belgium; yovan.decoene@kuleuven.be (Y.d.C.); thierry.verbiest@kuleuven.be (T.V.)
3 Institute of Applied Sciences and Intelligent Systems, Unit of Naples, National Research Council, Via Pietro Castellino 111, 80131 Naples, Italy; antonella.ferrara@na.isasi.cnr.it
4 Department of Physics & Namur Institute of Structured Matter (NISM) and Namur Institute for Complex Systems (naXys), University of Namur, Rue de Bruxelles 61, B-5000 Namur, Belgium; yves.caudano@unamur.be
5 Micro- and Nano-Photonics Materials Group, University of Mons, Avenue Maistriau 19, B-7000 Mons, Belgium
* Correspondence: branko.kolaric@umons.ac.be

Abstract: Most optical phenomena result from the interaction of electromagnetic waves with matter. However, the light structure can be eminently more complex than plane waves, with many degrees of freedom and dimensions involved, yielding intricate configurations. Light transcends the conventional landscape of electromagnetism, offering the possibility to tailor light in three dimensions (intermixing all three electric field components), in four-dimensional spacetime (for fields manifesting both temporal and spatial patterns), and, beyond that, to make structured quantum light, tuning its characteristics at an unprecedented new level of control. This article addresses the physical foundations of structured light, its interactions with matter, including the nonlinear regime and probing chirality, its classical benefits with holography as a specific highlight, and quantum mechanical applications. It describes the various applications connecting structured light with material physics, quantum information, and technology. Notably, we discuss weak measurements with structured light acting as the meter with connections to probing structured-light beam shifts at interfaces. Ultimately, revealing the interplay between structured light and matter opens attractive avenues for different new technologies and applications, covering both the classical and the quantum realms.

Keywords: structured light; chirality; holography; weak measurements; quantum applications

check for updates

Citation: Bokić, B.; de Coene, Y.; Ferrara, M.A.; Verbiest, T.; Caudano, Y.; Kolaric, B. Structured Light from Classical to Quantum Perspectives. *Symmetry* **2024**, *16*, 1053. https://doi.org/10.3390/sym16081053

Academic Editor: Alberto Ruiz Jimeno

Received: 17 May 2024
Revised: 1 July 2024
Accepted: 12 July 2024
Published: 15 August 2024

Copyright: © 2024 by the authors. Licensee MDPI, Basel, Switzerland. This article is an open access article distributed under the terms and conditions of the Creative Commons Attribution (CC BY) license (https://creativecommons.org/licenses/by/4.0/).

1. Introduction

The new science that was born at the beginning of the 20th century aims to describe a microscopic reality that cannot be sufficiently and correctly described by classical physics. New ideas, such as the postulate of quantization of energy and the concept of the photon (carrier of the energy of the electromagnetic field), were introduced and led to the development of the new theory known today as Quantum Mechanics. Through the concept of the photon [1], as a quantum of oscillating electromagnetic field, the new physics of light emerged, connecting the corpuscular and electromagnetic wave nature of light in a single unity. Also, with the development of new physics, topology has become not only a fundamental branch of mathematics but also a tool that connects advanced mathematical concepts of space and its transformations with the physics and dynamics of physical systems. In this account, we are especially interested in describing the link between the shape and geometry of electromagnetic waves with their properties [2,3]. Complex structured light shows great potential in that regard [4,5]. That makes ideas issued from the field of topology relevant to other disciplines, such as chaos, continuum mechanics, nonlinear

dynamics, electromagnetism, quantum physics, mathematical biology, and physics of communication, to give a few examples. It should be emphasized that the vector nature of light (polarization, vector potential, vectorial fields, etc.) is indispensable in describing light-matter interactions in various systems and controls numerous phenomena, such as diffraction, scattering, nonlinear processes, and polarization-sensitive interactions [6]. Now, we acquired the capability to design and shape the polarization of optical beams from high to low intensities, down to the single-photon level. Subsequently, that enabled the study of topological phenomena. These advancements also went along increased control of phase and polarization singularities, as well as of orbital angular momentum (OAM) of light and spin angular momentum (SAM) [2,7], including spin-orbit coupling. It also spurred progress in areas as diverse as optical sensors and spectroscopy, holography, ellipsometry, nonlinear optics, and super-resolution imaging. Furthermore, vectorial light fields provide us with more informational resources than homogeneously polarized plane waves. Indeed, while classical, these fields exhibit nonseparable properties, evidenced through correlations reminiscent of quantum entanglement. In addition to applications, the concept of structured light uniquely connects the shape and geometry of light waves with matter [8].

In this account, we first briefly introduce structured light with a detailed description of a few attractive beams (diffracting and nondiffracting) for photonics and material applications, focusing mainly on the applications of structured light in spectroscopy, chirality, and quantum studies. Subsequently, we also summarized structural light in prominent applications such as linear and nonlinear photonics and holography. In the end, we present the applications of structured light from the quantum perspective, highlighting the power of structured light for fundamental quantum studies and applications relevant to quantum technologies, including the context of quantum weak measurements. This article is aimed at the broad community of physicists, quantum researchers, and physical chemists, with the goal of attracting attention to structured light and its applications in material and quantum science. It serves as a first step in enlightening these communities about the unusual properties of electromagnetic waves, which differ significantly from simple plane waves, and their vast potential for fundamental control of light-matter interaction, as well as applications in material and communication sciences. With that respect, we highlighted original applications, which we believe are of particular interest for these communities, and which were not the focus of previous reviews on structured light (such as probing chirality, holographic applications, and quantum weak measurements, to cite a few).

2. Structured Light: Nondiffracting and Accelerating Beams

Commonly, electromagnetic wave fields undergo diffraction during propagation, resulting in a transverse spreading of the field distribution. However, there are beam classes that maintain their profile along propagation. Such beams became famous as diffraction-free or nondiffracting beams [9]. Nondiffracting beams were first introduced by Durnin in 1987 [10], as monochromatic optical fields with propagation-invariant transverse intensity distributions. Mathematically, they are particular solutions of the Helmholtz equation

$$\partial_t^2 U(x,y) + k_t^2 U(x,y) = 0. \quad (1)$$

in different coordinate systems: Cartesian, circular cylindrical, elliptical cylindrical, and parabolic cylindrical coordinates [11,12]. Such coordinate systems give rise to a certain type of nondiffracting beam: discrete (plane wave and their superpositions) [11], Bessel [13], Mathieu [14], and Parabolic beams [15], respectively.

Nondiffracting beams have been studied in different configurations. Two-dimensional periodic intensity patterns can be generated as a superposition of multiple plane waves [11], but a quasiperiodic pattern such as a Penrose lattice is generated as a superposition of five plane waves [16]. Bessel beams are obtained by solving the Helmholtz equation in circular cylindrical coordinates and their transverse intensity distributions are characterized by concentric rings; Figure 1a depicts a Bessel beam. They possess a whole class of higher-order modes, which are typically indicated by one integer. Additionally, their higher-

order modes carry optical orbital angular momentum (OAM) along their propagation axis, which can be transferred to trapped particles. Bessel beams can be easily generated with conical lenses, so-called axicons, and they are the most investigated [17]. In recent studies, Bessel beams have been used to induce periodic photonic lattices [12], and even Fibonacci photonic lattices [18]. Bessel beams are already well described and reviewed as the simplest form of light with OAM after the Laguerre–Gauss beams. In this highlight, we focus more on other types of structured beams (Airy, Matthieu, and Laguerre–Gauss) and their applications in spectroscopic and quantum studies that could be exploited in various optical and quantum technologies. A third family of nondiffracting beams, so-called Mathieu beams, are solutions of the Helmholtz equation in elliptical symmetry. The transverse intensity distribution of Mathieu beams consists of discrete spots along elliptic or hyperbolic paths; one example is shown in Figure 1b. Their generation is more complicated, compared to Bessel beam generation as there are no commercially available simple refractive devices. One option for their realization is the holographic generation with spatial light modulators (SLM). A nondiffracting beam that is distorted by an obstacle within the beam path reconstructs its original transverse shape after a distinct propagation length. This feature makes nondiffracting beams highly suited for three-dimensional applications. Moreover, helical Mathieu beams that are superpositions of even and odd modes of Mathieu beams, provide continuous phase variations, so they have been used to investigate the transfer of orbital angular momentum to particles in optical micromanipulation [9,19].

Parabolic beams are the fourth family of nondiffracting beams, they are a solution of the Helmholtz equation in the parabolic cylindrical coordinate system and might be interesting for further applications in optical micromanipulation. One intensity distribution of the Parabolic beam is depicted in Figure 1c.

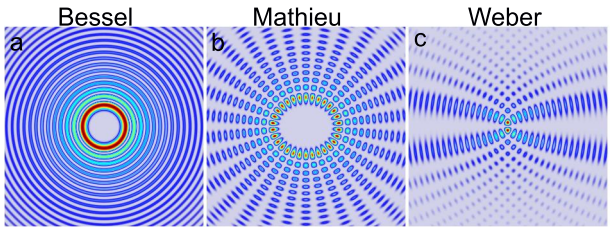


Figure 1. Typical examples of nondiffracting beams: transverse field distributions of selected (**a**) Bessel, (**b**) Mathieu, and (**c**) Weber beams.

Nondiffracting beams with finite energy are bounded by the homogeneously transmitting aperture of finite dimensions or by the Gaussian aperture, and they are known as pseudo-nondiffracting beams. Experimental and numerical investigations show that the nondiffracting and pseudo-nondiffracting beams have δ-like angular spectrum, represented by a circle in the Fourier plane, that confirms their propagation-invariant character making such beams useful in optical micromanipulation, wireless communication and nonlinear optics [20,21].

Apart from eliminating diffraction, additional properties of such beams are observed, that make them useful for potential applications. One of them is the robustness of the nondiffracting beams: they show resistance against both amplitude and phase distortions, and they are able to regenerate themselves to the original form in the free propagation behind a nontransparent obstacle [22,23]. Nondiffracting beams also possess a self-reconstruction ability [24]. Well-known methods of generating nondiffracting beams require the use of the computer-generated holograms [25], the axicon [26] or the programmable spatial light modulators [27].

2.1. Applications of Accelerating Beams

Since their revelation by Berry and Balazs, the appealing class of Airy beams has attracted vast interest in different fields of physics. Originally, Airy beams were introduced as wave functions, solving the one-dimensional Schrödinger equation for free particles. Their probability density exceptionally stays non-spreading under time evolution, while

being transversely accelerated to follow a parabolic trajectory [28]. Due to the formal equivalence between the Schrödinger equation in quantum mechanics and the paraxial equation of diffraction in optics, the concepts and solutions can be exploited within the field of optics, where Airy beams can be directly observed and revealed in experiments [29,30].

They are invariant along parabolic trajectories and attract enormous attention because of their unique properties. Contrary to the previously mentioned straight nondiffracting beams, they belong to the class of accelerating nondiffracting beams and propagate on curved trajectories. Figure 2 shows the transverse (a) and longitudinal (b) intensity distribution of a two-dimensional Airy beam.

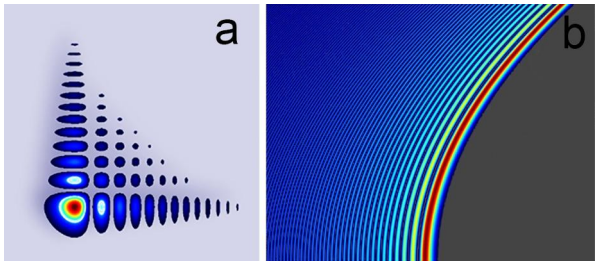


Figure 2. Two-dimensional Airy beam: Numerical simulation of (**a**) transverse intensity distribution, and (**b**) the intensity distribution along the propagation.

Their transverse self-acceleration [31,32] and nondiffraction [33,34] features make them useful for various applications ranging from laser micromachining (Figure 3a) [35], ultra-fast self-accelerating pulses [36] to dynamically routing surface plasmon polaritons (Figure 3b) [37,38], self-bending plasma channels (Figure 3c) [39], and frequency generation [40]. In optical micromanipulation, they have been proposed as an "optical snowblower" (Figure 3d) due to their ability of two-dimensional particle transport [20]. Their special self-healing properties and self-reconstruction after passing small obstacles have been demonstrated theoretically and experimentally [41].

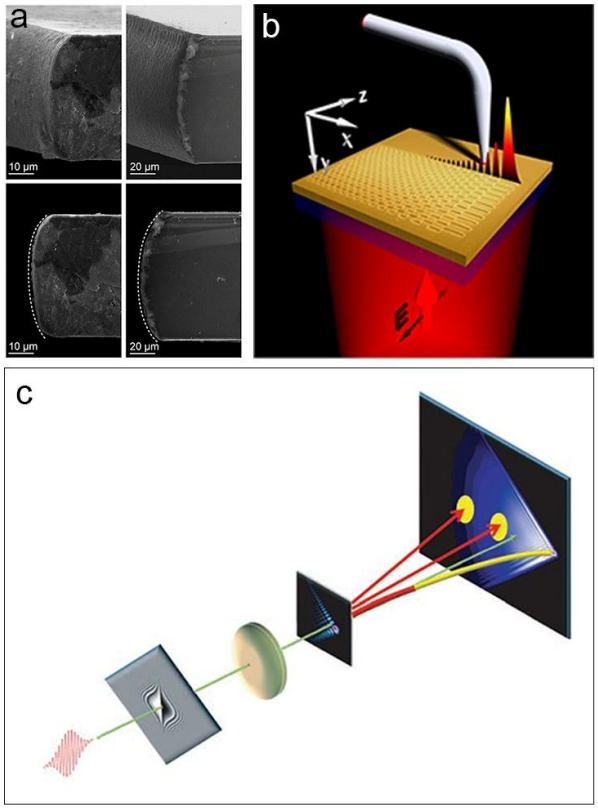


Figure 3. *Cont.*

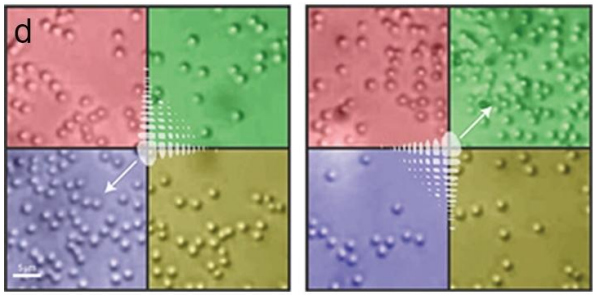


Figure 3. Applications with Airy beams: (**a**) Femtosecond laser micromachining with accelerating beams in diamond (left) and silicon (right), top row represents 3D view images of the samples while bottom row shows the same samples but with a profile orientation—Reprinted from [35], with the permission of AIP Publishing, (**b**) generation of Airy plasmons (scheme of the experimental set-up)—Reprinted figure with permission from [38], ©2011 by the American Physical Society, (**c**) curved plasma channel generation (scheme of the experimental set-up) From [39]—Reprinted with permission from AAAS, and (**d**) optically mediated particle clearing, micrographs of the colloids exposed to the Airy beam with two different rotations (left and right) of the beam [20]—Reproduced with permission from SNCSC.

2.2. *Applications of Nondiffracting Beams*

The science of nondiffracting beams carries great potential and is well-recognized for advancing many fields, especially in discrete and nonlinear photonics [42–44]. Some examples considering Airy beams are the influence of photonic lattice or refractive index gradient to control or compensate the Airy beam self-acceleration and design the beam caustics itself [42–47], as well as using two-dimensional Airy beams to optically induce light-guiding structures for various applications such as optical signal routing and switching [48].

The effects of nonlinearity on Airy beam propagation have been investigated in many theoretical and experimental studies [49–51]. Nonlinearity added a new degree of freedom to the system leading to interesting effects and phenomena. One of the well-known and most fundamental effects in nonlinear systems is the existence of spatial solitons—localized structures that preserve their shape owing to the balance between diffraction and nonlinear self-focusing. Arising from the interaction of multiple two-dimensional Airy beams in a nonlinear medium, a new type of soliton formation has been demonstrated [52]. Depending on different phase configurations of such synthesized beams (in phase or out of phase), either one solitary solution (Figure 4a) or a pair (Figure 4b) is observed that propagates almost stable with small intensity modulations (breathing).

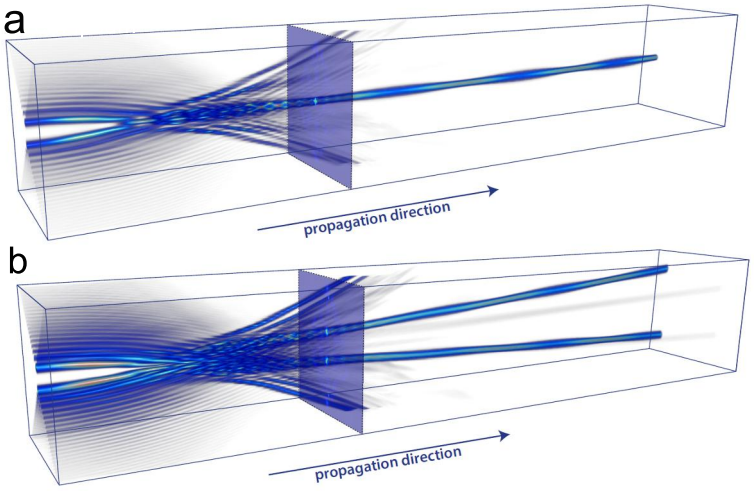


Figure 4. Formation of solitary states from the interaction of two Airy beams: (**a**) in-phase, and (**b**) out-of-phase. Reprinted with permission from [52] © Optica Publishing Group.

Another class of nondiffracting beams, Mathieu beams, are mostly used as lattice-writing light to fabricate discrete waveguide structures and investigate their nonlinear self-action, which lead to the morphing of the discrete diffraction [53]. It is linked to linear discrete diffraction with nonlinear self-effects and demonstrates a gradual transition from one to two dimensions (Figure 5). Discrete diffraction similar to the typical one observed in 1D waveguide arrays is demonstrated with Mathieu beams of zeroth order propagating in nonlinear media (Figure 5a). With higher-order Mathieu beams, discrete diffraction is observed along each layer.

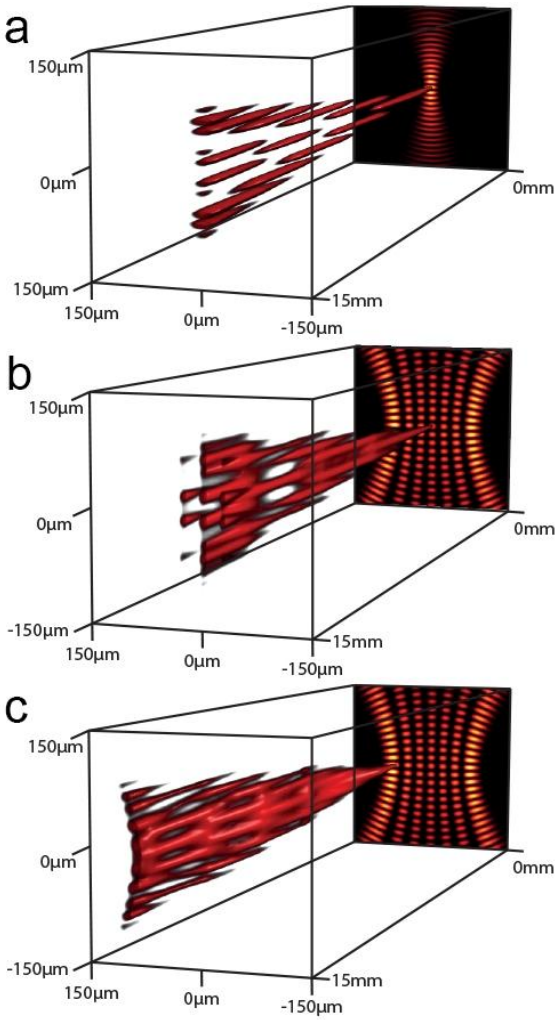


Figure 5. Gaussian probe beam propagation in Mathieu lattices: (**a**) 0th order Mathieu lattice; (**b**) 6th order Mathieu lattice, central; (**c**) 6th order Mathieu lattice, outer. Reprinted with permission from [53] © Optica Publishing Group.

Nonlinear self-action of elliptic Mathieu beams leads to the formation of high-intensity filaments, which rotated in the direction determined by the energy flow, forming chiral Mathieu photonic structures [54]. The formation of chiral Mathieu lattices is observed only in a limited regime with proper parameters for the nonlinearity and structure size (Figure 6). An investigation of chirality with other classes of beams (diffracting Laguerre–Gaussian beams) is described thoroughly in the next section.

Two-dimensional Fibonacci photonic structures are optically induced, which are supposed to be among the most ordered realizations of deterministic aperiodic patterns [18]. For their generation, nondiffracting Bessel beams are used as waveguide formation entities (Figure 7). It is constructed as an experimental system for the realization of disordered lattices by a single optical induction process in parallel using nondiffracting beams

and numerically precalculated disordered patterns with adjustable disorder degrees [55] (Figure 8).

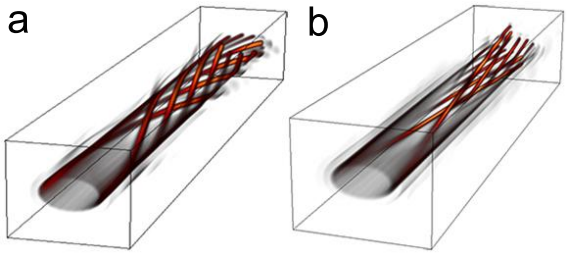


Figure 6. Chiral Mathieu photonic lattices made with Mathieu beam structure size of (**a**) 15 μm, and (**b**) 25 μm [54].

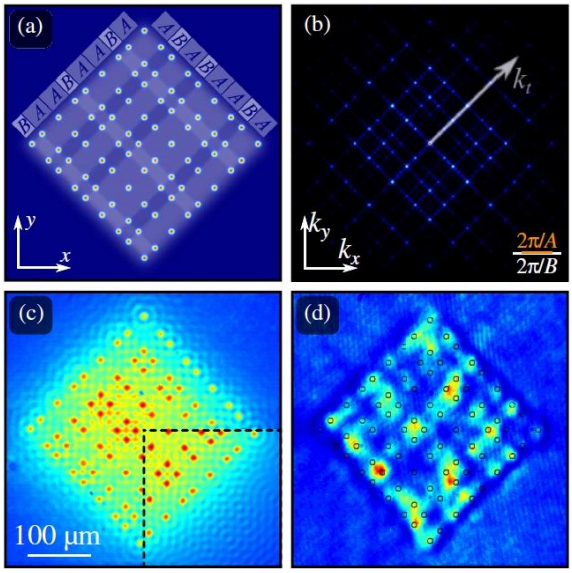


Figure 7. Optical induction of photonic lattice in photorefractive crystal SBN: Fibonacci photonic lattice generated with Bessel beams. (**a**) Fibonacci lattice with lattice spacing following Fibonacci words (indicated alongside), (**b**) spatial spectrum $S(k_x, k_y)$ according to lattice shown in (**a**), (**c**) measured effective intensity with Bessel beam lattice sites taken by multiple-shot illumination at the back face of the crystal. The bottom right quadrant shows according to numerical simulation, and (**d**) experimental output for plane-wave probing (contours indicate waveguide positions). Reprinted with permission from [18] © Optica Publishing Group.

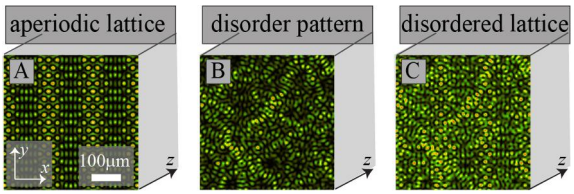


Figure 8. Optical induction of aperiodic and disordered aperiodic Mathieu photonic lattice in photorefractive crystal SBN: (**A**) aperiodic lattice, (**B**) disordered pattern, and (**C**) disordered lattice. Reprinted with permission from [55] © Optica Publishing Group.

3. Structured Light: Probing Chirality in Molecular Systems Using Diffracting Laguerre–Gaussian Beams

Although the optical properties of a material can be understood using the more-than-150-year-old Maxwell's equations, the fundamental structure–property relationship between light and matter remains very relevant. Particularly interesting are the optical properties of chiral materials (different interactions with left and right circularly polarized

light), a class of materials that is of fundamental importance in all scientific fields, especially in life sciences because all biological entities are mostly composed of chiral molecules. Chiral molecules are not superimposable on their mirror image and occur in two different forms, called enantiomers. Chiral materials have unique optical properties. For example, they have a different interaction with left- and right-hand circularly-polarized light, termed optical activity, allowing optical interrogation of each enantiomeric form. Experimental methods to study chiral materials and discriminate between enantiomers mostly rely on circular dichroism (CD), and optical rotation (OR). These optical activity effects can be explained by interferences between electric-dipole (ED) and magnetic-dipole (MD) contributions to the optical response. Electric-quadrupole (EQ) interactions can also contribute, but in isotropic systems, they average to zero and therefore EQ contributions are rarely invoked to explain CD and OR [56].

Apart from linear momentum along its trajectory, light can carry a nonzero angular momentum. When light is circularly polarized and in the paraxial regime, the photons carry a spin angular momentum (SAM) of $\sigma\hbar$ where σ can either be $+1$ (for LCP) or -1 (for RCP). Hence, optical activity effects such as CD and OR originate from the interaction of chiral materials with the SAM of light. In 1992, Allen et al. [57] showed that photons can carry an additional orbital angular momentum (OAM) apart from spin. The total angular momentum is thus the sum of a spin part depending on polarization, and an orbital part with a certain spatial distribution of the momentum vector. If we consider a plane wave, where electric field $\vec{E}$ and magnetic field $\vec{B}$ are transverse with respect to the direction of propagation, the cross-product results in the energy flux vector (Poynting vector) parallel to the direction of propagation. This means that in free space the direction of momentum flow is parallel to the direction of light propagation. To attain a helical phase front (carrying OAM), $\vec{E}$ and $\vec{B}$ are transverse to the phase fronts, but not to the propagation direction. This results in a momentum flow not only in the z direction but around the beam axis as well. Within the paraxial approximation, we can say that a photon in a helical phase front carries a momentum of $\ell\hbar$ where $\ell \in \mathbb{Z}$ is the topological charge representing the multiplicity (the number of twists within a wavelength) with the sign representing the twisting direction of the helical wavefront. If one were to look towards such a Laguerre–Gaussian (LG) beam, it would appear doughnut-shaped due to the phase singularity at the middle of the phase cross-section (Figure 9).

Up to now, Laguerre–Gaussian light has been used for various applications, and many excellent reviews are available on this topic [58,59]. However, in this paragraph, we would like to focus on the electronic interaction of Laguerre–Gaussian light with chiral matter as a new spectroscopy method. Indeed, a central question regarding their interaction with matter in the spectroscopic framework remains still unanswered. In theory, ℓ can go up to infinity but since infinitely large beam sizes do not exist, the topological charge is limited by the aperture size. The optical vortex thus propagates with a helical phase defined as $e^{i\ell\phi}$, where the gradient of the azimuthal phase results in the OAM.

A central question remains how the OAM of such a vortex beam can engage with chiral matter other than in merely exerting mechanical torque, acting as an optical spanner [60]. It seems rather intuitive that, because the spin part of angular momentum can infer optical activity in chiral materials, OAM can do it as well. However, the scientific community has been divided on the physical mechanism through which this occurs. Initial theoretical work showed that the helicity of optical vortices cannot engage with the chirality of a molecular system [61–63]. In that work, the authors considered the classical electric-dipole and magnetic-dipole interactions to the optical response, as is usually performed to describe the interaction of chiral materials with SAM. However, they did not exclude the possibility of interaction through an EQ mechanism. The first experimental investigations were initiated by Araoka et al and Löffler et al. The former investigated solutions of an enantiomerically pure helicene bisquinone derivative, the latter focused on a cholesteric polymer [64,65]. Both studies showed that OAM is not specific in its interaction with chiral matter. Only circular polarization, associated with SAM, can engage with materials chirality. However,

it was not until many years later that it was demonstrated that the OAM of light can indeed electronically interact with chiral matter [66]. They showed that light with OAM of $+l_z$ and $-l_z$ interacts differently with the enantiomers of chiral systems. The observed difference effect was dependent on the topological charge and was termed helical dichroism. The material used in these experiments was a hybrid layered material consisting of chiral organic molecules and plasmonic and superparamagnetic nanoparticles [66]. The authors showed that one needs to invoke electric-quadrupole contributions to describe the optical interaction with OAM. Later theoretical work indeed confirmed that EQ interactions are crucial in describing the interaction of OAM with chiral matter [7,67,68].

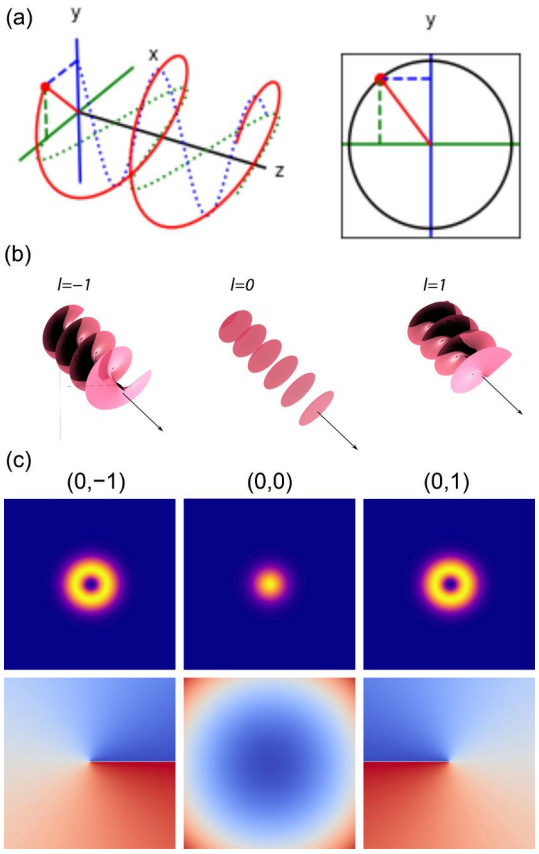


Figure 9. (**a**) Electric field propagation of circularly polarized light (in a Gaussian beam), carrying spin angular momentum. (**b**) Stylistic representation of wave-front propagation of Gaussian beam with OAM quantum number of zero and Laguerre–Gaussian beams with OAM quantum number of 1 and −1. (**c**) Two-dimensional representation of intensity and phase according to the beams represented in (**b**).

Since then, helical dichroism has been observed in other systems, but mostly in nano or microstructures—systems that are not purely molecular in nature. For example, extremely strong helical dichroism that changed with the sign and magnitude of the topological charge was observed by Ni et al. in two-dimensional chiral nanostructures [69]. The same authors observed very strong vortical differential scattering, i.e., a different scattering efficiency for opposite topological charges, in chiral (helical) microstructures and showed that the chiro-optical response can be carefully tuned by the geometry of the structures [70,71]. Indeed, by matching the structural dimensions with the dimensions of the vortex beam, they were able to optimize the vortical differential scattering geometry. Furthermore, adsorbing chiral molecules (L-and D-phenylalanine) on the microstructures allowed them to discriminate between the enantiomers. Recently, it was demonstrated that helical dichroism can even be observed in purely molecular systems by exploiting nonlinear optical processes such as multi-photon absorption. Isotropic chiral solutions of simple organic molecules were

shown to exhibit helicity-dependent nonlinear absorption [72]. The authors also stressed the importance of quadrupole contributions that occur due to laser-induced orientational effects in the solution.

From the above, it is clear that the study of the interaction of vortex beams with chiral matter is still in its infancy. However, recent experiments have shown that chiro-optical techniques based on OAM can be an extremely valuable addition to the portfolio of currently available chiro-optical spectroscopies. One of the main advantages of OAM is that the momentum values are not limited to $\pm\hbar$ as is the case for SAM but can in principle take on any integer value. This yields an additional degree of freedom to explore the interesting properties of chiral molecules. Furthermore, chiro-optical techniques based on OAM need not to be limited to linear optical processes such as absorption, transmission, or scattering. Multi-photon techniques such as two-photon absorption, two-photon fluorescence, or second-harmonic generation may in fact be much more sensitive to probe helical dichroism.

4. Structured Light: Holographic Applications

Since Gabor's first hologram [73], the holographic technique has largely grown and is widely used in different fields, such as security [74], data storage [75], cultural heritage [76], as well as imaging and medicine [77]. Basically, holography is an interferometric technique: an interference pattern (i.e., the hologram) is generated by superimposing two coherent beams, named the object and reference beam. The hologram can be recorded on a photo-sensitive medium or, in the case of digital holography (DH), on a CCD. The original object wavefront can be obtained by illuminating the hologram with the only reference beam; in DH, this operation is numerically performed to retrieve the whole complex object beam.

Holography has been used to generate and detect structured light beams [78]. However, this section aims to report on how structured light can improve the performance of holographic techniques. Therefore, with this goal in mind, the following aspects will be examined: phase shifting and resolution enhancement, memory and high-security encryption, 3D communications, and nonlinear and quantum holography.

In in-line DH, where the object and reference waves are overlapped, the reconstruction of the object image is difficult due to real and virtual images overlapping. In order to overcome this drawback, an off-axis configuration or phase-shifting approach can be implemented [79]. However, a high-quality off-axis hologram is difficult to record due to the limited bandwidth of the off-axis system which is feckless with respect to the space-bandwidth product of the optical image amplitude [80]. Phase-shifting DH allows for reconstruction of high-resolution images making full use of the bandwidth of the optical detector; however, it generally requires multi-exposure holographic recording while shifting the phase of reference field by an integer fraction of 2π [81]. In 2004, the use of an optical vortex (OV) beam as the reference wave for phase-shifting holographic recording was proposed [82]. The required phase shifts were obtained by generating four different angled optical vortices; this optical vortex phase-shifting holography could offer a new perspective in research on the dynamics of the OV in linear or nonlinear materials.

For high-throughput dynamic imaging, single-shot phase-shifting DH is highly desirable. In this context, illumination with structured light could offer a new approach. Zhang et al. proposed to use an OV beam with different eccentricity and topological charge as the reference beam into a modified Michelson interferometer with two different 4f-telescopes [83]. A cosine grating is positioned in the object path allowing to produce at once two-copy images of the measured object beam in the other beam path, leading to their interference with the vortex reference wave in one single exposure (see Figure 10a). Parts of the reference beam can be used to remove zero-order terms in the reconstruction process. The reported experimental results are in good agreement with the theoretical analysis. The same authors reported a Mach-Zehnder interferometer with a vortex beam (amplitude-only Fermat-spiral sieve) as the reference signal and a splitting grating in the object arm [84] which splits the object wave into four parts positioned in the four quadrants of the vor-

tex reference wave. This scheme, shown in Figure 10b, gives rise to a single-exposure interference pattern that contains the four frames of phase-shifting holography.

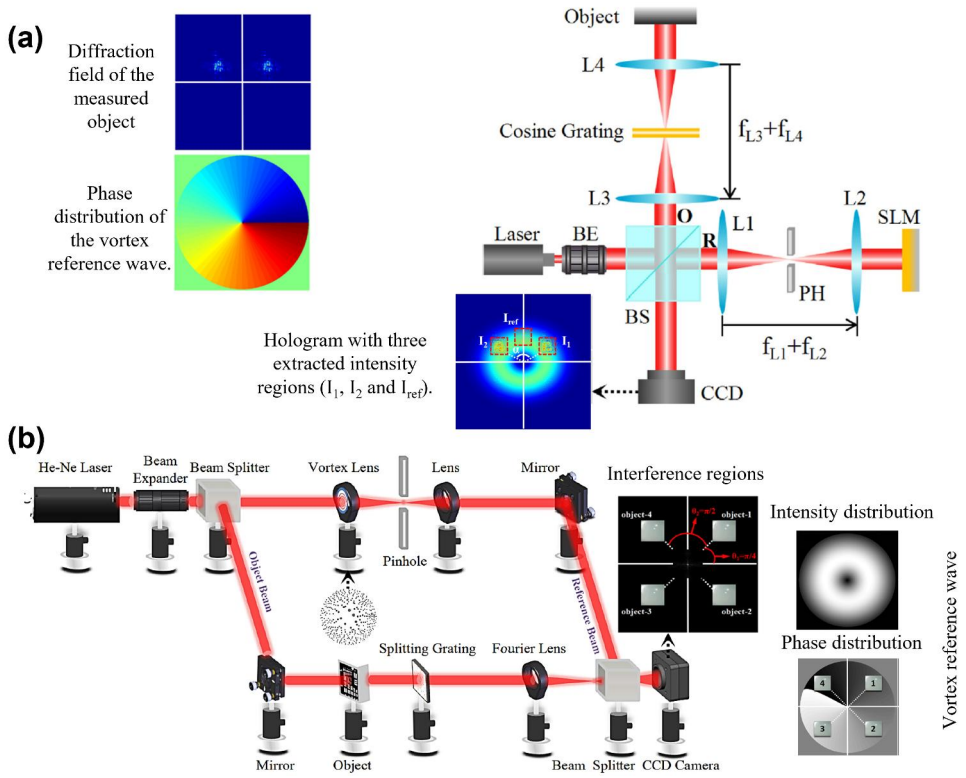


Figure 10. Phase-shifting digital holography set-ups with vortex beam in one single exposure. (**a**) Two interference patterns. Laser: He-Ne laser; BE: beam expander; BS: beam splitter; O: object wave; R: reference wave; L1-L4: condenser lens; PH: pinhole. Reprinted from [83] with permission from Elsevier. (**b**) Four interference patterns [84]. ©Astro Ltd. Reproduced by permission of IOP Publishing Ltd. All rights reserved.

By combining DH with optical microscopy, digital holographic microscopy (DHM) can be implemented to image semi-transparent and transparent objects. Generally, DHM spatial resolution is limited by the wavelength (λ) and the numerical aperture (NA) of the imaging system [85]. In order to improve the resolution of intensity images, structured illumination microscopy (SIM) has shown high potential [86]. Since 2010, when super-resolution in holograph was demonstrated using structured illumination [87], this research field has attracted increasing interest. In 2013, Gao and co-workers reported an improvement of the resolution thanks to the use of structured light generated by a spatial light modulator (SLM) which illuminates the object projecting fringes with different orientations and phase shifts without mechanical motion [88]. Autofocusing has been also achieved for both amplitude and phase objects by detecting the minimal difference between the reconstructed images related to different diffraction orders of the structured illuminations. Alternatively, fringe patterns can be generated by a digital micromirror device (DMD) and, when applied as illumination of the object in DHM, 3D refractive index tomographic images of samples have been retrieved [89].

Structured illumination generated by a sequence of differently oriented sinusoidal gratings onto an SLM has been directed to a Mirau microscope objective in DHM, forming its image on the sample and leading to a resolution enhancement of 35% with respect to standard DHM [90]. One-dimensional gratings with different orientations can be replaced by single 2D gratings, allowing increased resolution in multiple directions. Moreover, deep learning has been recently proposed to further enhance the reconstruction efficiency and the accuracy of DHM imaging based on structured illumination [91].

Among its different applications, holography is considered a crucial platform for optical encryption and data storage. Despite the possibility of holograms reaching nanometre-scale resolution thanks to recent progress in metasurface technologies, the hologram bandwidth is still too low for practical applications. This drawback has been recently addressed by storing information in the orbital angular momentum (OAM) of light: basically, the incident OAM beam is the key to unlocking the specific information. Multi-bit OAM-multiplexing holograms can be obtained by high-order OAM beams allowing an all-optical holographic encryption with a high level of security. The basic principle of OAM holography is reported in Figure 11. Starting from 2019, Fang and colleagues firstly demonstrated a multiplex information of four channels based on a meta-hologram consisting of GaN nanopillars with discrete spatial frequency distribution (see Figure 11a) [92]. Then, in 2020, they reported an OAM holography technology able to multiplex up to 200 independent OAM channels and realized by a polymer-based metasurface [93]. Finally, the same research group reached an ultra-high-capacity holographic information system able to have up to 2^{10} OAM-specific holographic images [94]. This goal has been achieved by engineering a sampling array period in order to match the spatial-frequency distribution of a precise incident OAM beam. The design approach of the 10-bit OAM-encoded hologram as well as the OAM code chart are shown in Figure 11b,c.

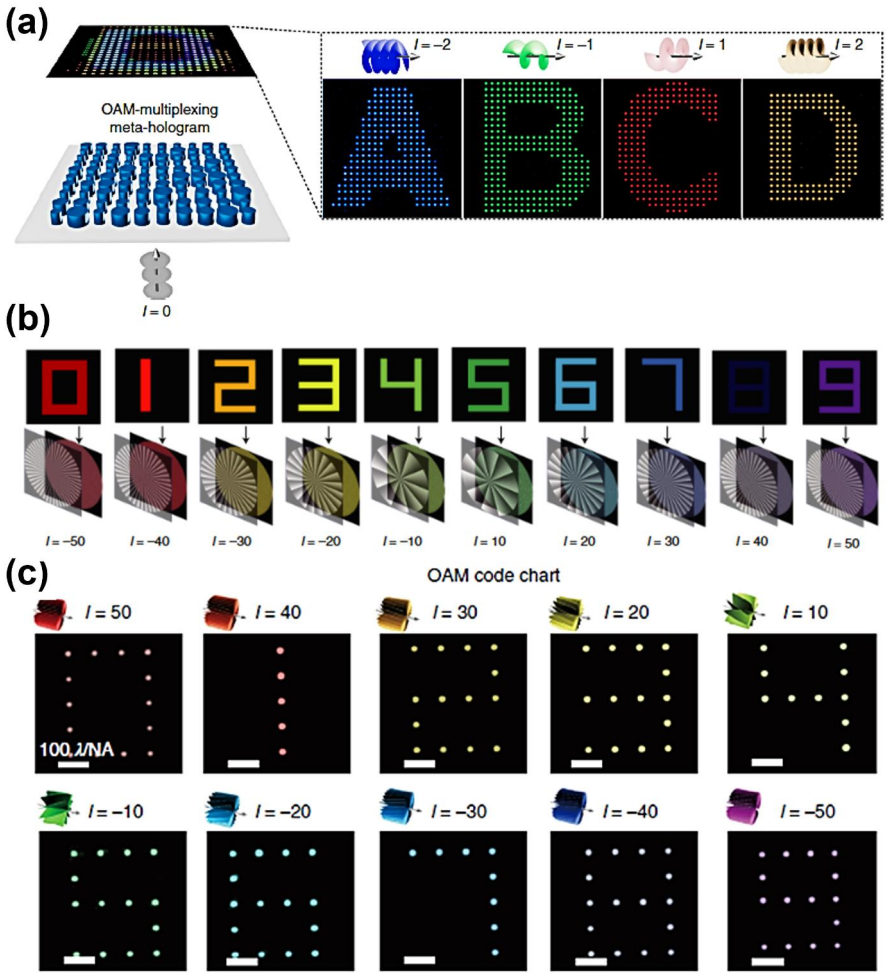


Figure 11. (**a**) Schematic of an OAM-multiplexing meta-hologram: multiple OAM-dependent holographic images can be reconstructed [92]; (**b**) design approach for a 10-bit OAM-multiplexing hologram for high-security holographic encryption [94] , reproduced with permission from SNCSC; (**c**) OAM code chart: 10 high-order OAM modes are used to reconstruct the 10 OAM-dependent digits based on the OAM-multiplexing hologram [94], reproduced with permission from SNCSC.

High-security holographic encryption has been also obtained by using an all-dielectric birefringent metasurface for holographic encryption: the OAM selective holographic information can be retrieved only if the incident beam has the right topological charge and polarization state [95].

The holographic technique has been traditionally applied in the linear optical regime; however, in the recent past, the concept of nonlinear holography has been introduced to shape the wavefront of the light emitted by nonlinear optical process [96]. In this context, the use of OAM multiplexing nonlinear holography has been experimentally demonstrated to overcome the crucial restriction of wave coupling in nonlinear optical process [97]. This approach, demonstrated in a type-II second harmonic generation (SHG) process, allows wavelength-multiplexing nonlinear holography (WMNH) and can be also enhanced by encoding multiple patterns for each wavelength leading to an increase in information channels, thus proving for the first time the multichannel nonlinear holography (MCNH). The basic principles of both WMNH and MCNH applied in type-II SHG are reported in Figure 12.

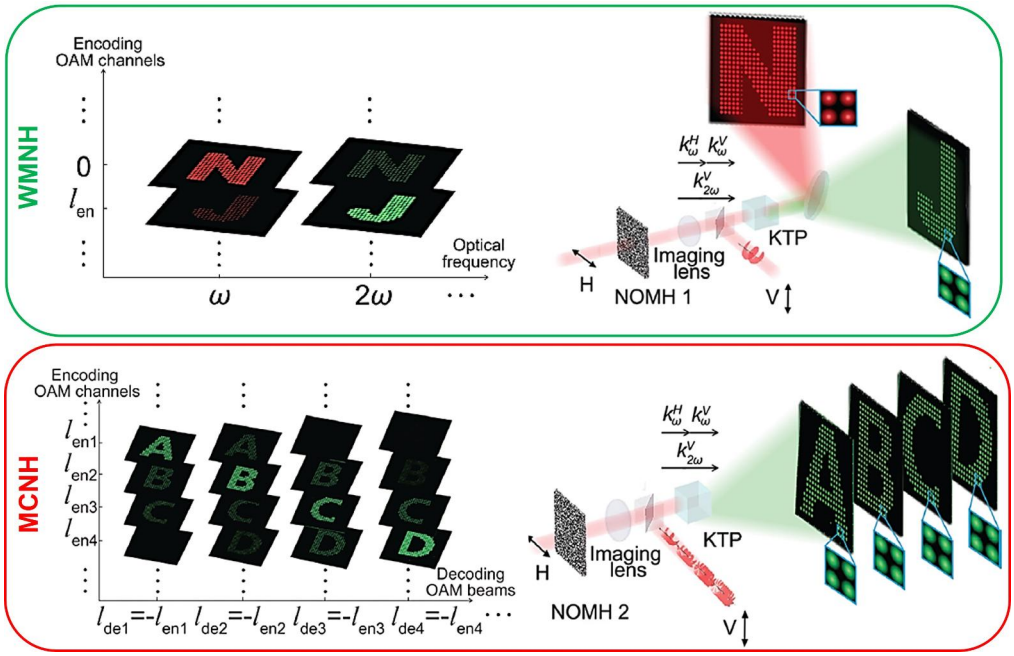


Figure 12. Concepts of WMNH (up) and MCNH (down). NOMH: nonlinear OAM-multiplexing hologram; KTP: nonlinear material ($KTiOPO_4$). In the SHG process there are two incident fundamental beams (k_ω^H and k_ω^V, H and V are the horizontal and vertical polarizations, respectively) and the output is the second-harmonic beam ($k_{2\omega}^V$, vertically polarized). WMNH in a type-II SHG process allows to separately reconstruct letters N and J in forward wave and SHG wave, respectively; MCNH in a type-II SHG process permits to reconstruct letters A, B, C, and D in SHG wave [97].

Taking advantage of quantum interference in a nonlinear interferometer between correlated signal and idler photon pairs generated by spontaneous parametric downconversion (SPDC), Töpfer et al. overcame the limited detection for wavelengths outside the visible range [**?**]. In detail, they designed a phase-shifting holography with nonclassical states of light and demonstrated that both the amplitude and phase of the photons transmitted/reflected from the object can be reconstructed, hence obtaining an image of the object even if the same photons are never detected. With such a configuration, the reference for holography corresponds to one of the photons of the pair.

Another interesting and widely used application of the holography technique is 3D imaging and display technologies, useful for 3D communication. On this line of arguments, a potential solution to telepresence in the metaverse has been proposed by developing a real-time 3D system integrating the detection, hologram generation, transmission, and

visualization [99]. This system is based on a structured light camera (slower, with a higher resolution and depth accuracy with respect to a CCD) and a light field camera (with a high frame rate) that acquired the 3D scene; then, phase-only holograms are computer-generated by an algorithm based on rendered depth images and shading images (layer-based angular spectrum method), as sketched in Figure 13a. A 4K SLM is used to dynamically reconstruct the phase-only holograms. A 3D model of a human body has been captured and rendered into videos by rotating 360° around the central axis (see Figure 13b), showing the abilities of this system for 3D communication in the near future.

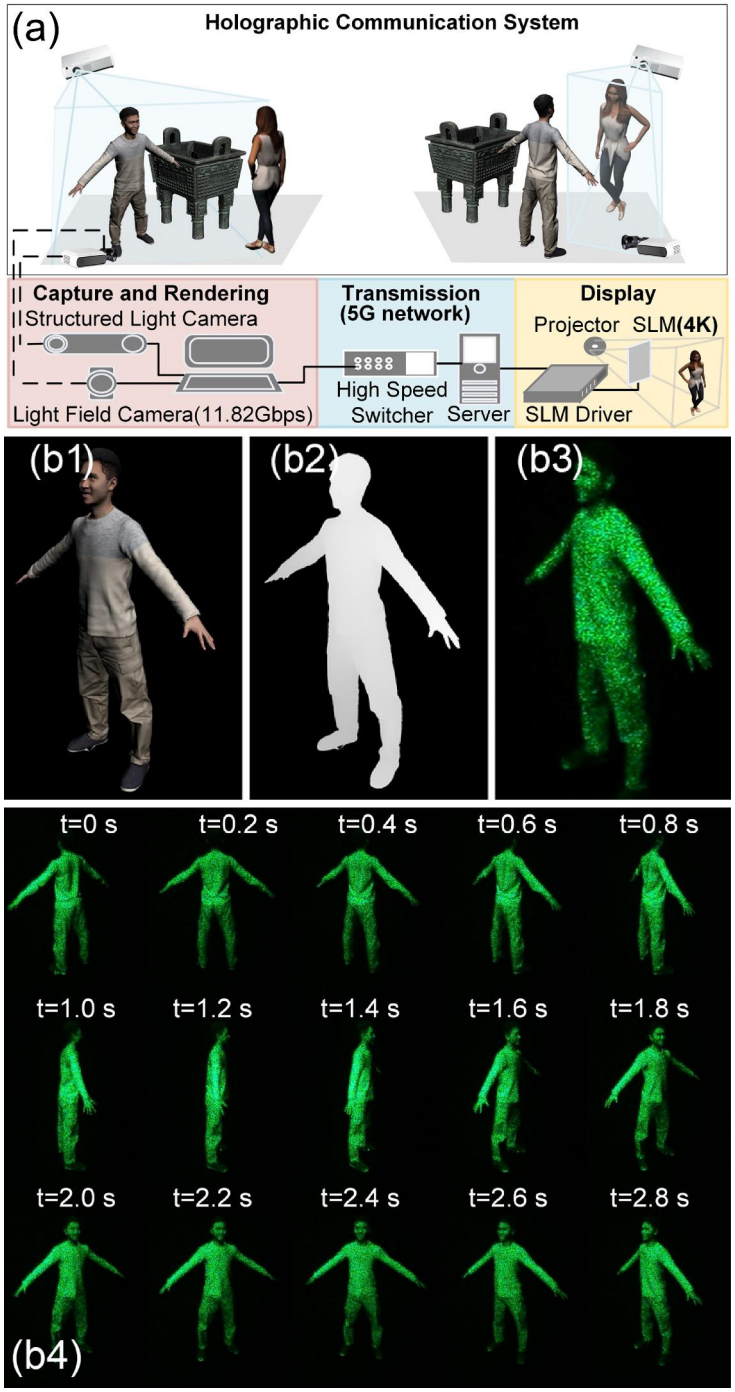


Figure 13. (**a**) Holographic communication system; (**b**) experimental results: (**b1**) color maps of target objects, (**b2**) depth maps of target objects, (**b3**) reconstructions of the objects, (**b4**) dynamic holographic 3D display. Reprinted from [99] with permission from Elsevier.

The significant research efforts, partly reported in this section, highlight that in the last few years structured light beams have become an important tool for holography technique to strongly enhance its performance, open up new perspectives, and pave the way for a wide range of its potential applications.

5. Structured Light: Quantum Viewpoint and Applications

Many of the remarkable properties of structured light beams originate from classical electromagnetism, a world fundamentally ruled by Maxwell's equations and wave physics. However, when the light intensity reaches extremely low values, the beams exhibit discrete behaviors that conform to the quantized rules of optics and light–matter interactions. In quantum optics, photons become the building blocks of structured beams. In a simple picture, photons carry not only a discrete quantum of energy but linear and angular momentum as well. The classical beam qualities emerge thus from the individual properties of photons, with classical interferences arising from quantum superpositions. Nevertheless, to describe the beam granularity, especially when correlations are involved, we must refer to the quantum formalism. Indeed, the main conservation laws of physics affecting classical optics, including phase matching in nonlinear optics, may produce entanglement in energy, momentum, and angular momentum at the quantum level. Entanglement is associated to nonseparable quantum states of composite systems. Multi-photon entanglement enables the fundamental testing of nonlocality in quantum mechanics through the violation of Bell inequalities. Interestingly, many structured light beams already exhibit nonseparable, local correlations of their degrees of freedom in the classical description of the beam [100,101]. Structured light concepts often overlap the quantum–classical boundary. This section briefly reviews the properties of structured light beams from a quantum perspective, highlighting the usefulness of structured light beams for fundamental quantum studies, as well as a few applications relevant to quantum technologies.

Without considering the temporal structure of the wavepacket, the quantum state of a photon from a paraxial beam propagating along the z axis can typically be written as

$$\sum_{i=0}^{\infty}\sum_{j=0}^{\infty}\left(c_H^{ij}|H\rangle\otimes\left|\mathcal{M}_{ij}\right\rangle+c_V^{ij}|V\rangle\otimes\left|\mathcal{M}_{ij}\right\rangle\right)e^{ik_z z}. \tag{2}$$

The kets $|H\rangle$ and $|V\rangle$ form the basis of the polarization degree of freedom (here, the horizontal and vertical polarization states). The indices i and j label the various orthogonal transverse modes $\left|\mathcal{M}_{ij}(\vec{r}_\perp,z)\right\rangle$, since the spatial mode structure is conserved at the single-photon level. The pair of indices arises from different mode families, which depend, in particular, on the associated coordinate system (among them, the Hermite–Gauss modes in Cartesian coordinates, the Laguerre–Gauss modes in cylindrical coordinates, or the Mathieu–Gauss modes in elliptic cylindrical coordinates, for example). The complex amplitudes c_H^{ij} and c_V^{ij} weigh the contributions of the different polarization and spatial modes to the quantum state, as well as set their relative phases. Often, one will work with a reduced set of modes, so that only a few coefficients may contribute to the structured light beam, if not a single one. When the coefficients are factorizable, i.e., if we can write $c_H^{ij}=m_{ij}C_H$ and $c_V^{ij}=m_{ij}C_V$, the polarization and the spatial structures of the light are decoupled. In that case, the state is separable: it can be expressed as a single tensor product

$$(c_H|H\rangle+c_V|V\rangle)\otimes\sum_{i=0}^{\infty}\sum_{j=0}^{\infty}m_{ij}\left|\mathcal{M}_{ij}\right\rangle e^{ik_z z}. \tag{3}$$

Otherwise, the polarization and the spatial degrees of freedom are correlated, with a quantum state (2) appearing formally as entangled, even though a single photon is involved.

One of the significant benefits of structured light beams as quantum resources is their ability to carry orbital angular momentum (OAM). The spin angular momentum (SAM) of light, i.e., its polarization, corresponds to a two-level quantum system, known as a

quantum bit, or qubit. Polarization qubits are widely used in quantum optical studies. Geometrically, their pure states correspond to the full surface of a sphere (Figure 14), called the Bloch sphere in the context of quantum physics, or the Poincaré sphere in the context of classical polarization optics [102] (actually, a representation of $\mathbb{C}\mathrm{P}^1$, the complex projective line [103]). Left and right circularly polarized photons carry $S_z = \pm 1\hbar$ of angular momentum. However, OAM states are associated to integer quanta $L_z = \ell\hbar$ of orbital angular momentum. OAM orthogonal modes can thus build higher-dimensional quantum spaces, defining qudits. OAM qudits benefit experimentally from the light's advantage of interacting very little with its environment, avoiding decoherence, and thus preserving quantum superpositions and entanglement over long distances. Unfortunately, the complicated geometry of the qudit state space prevents a simple generalization of the Bloch sphere representation [103], even in the three-dimensional, qutrit case [104]. Nevertheless, transpositions of the polarization Poincaré sphere describe two-dimensional subspaces of OAM modes [105] (Figure 14), as well as higher-order Poincaré spheres depict the polarization structure of vortex beams in terms of the total angular momentum [106], along with their associated Pancharatnam-Berry geometric phase acquired under parametric evolution on this sphere [107]. For example, structured light can acquire a geometric phase when propagating in helical fibers [108]. Representations of generalized Hermite–Laguerre–Gauss modes exist now in terms of Jones vectors [109], rays [110], and the Majorana stellar representation of the modes [111]. A synthetic approach in terms of SU(2) coherent states [112] englobes these prior descriptions [113]. We note in passing that the so-called fractional angular momentum vortex beam actually consists of a quantum superposition of many integer OAM states [114,115], generating high-dimensional spatial entanglement in twin photons [116].

High angular momentum states are advantageous for quantum communications, including quantum key distribution [117] (commonly referred to as QKD) because qudits carry more information than qubits and are theoretically more secure (for example, they are harder to clone optimally [118]). Atmospheric turbulence generally degrades the beam spatial profile in practice [119], including for vector beams [120] (although they confer an enhancement [121]). Nevertheless, it is possible to avoid the consequences of distortions, notably by using structured states invariant under turbulence [122] (the latter are not based on OAM, though), or to improve pattern recognition at detection by exploiting machine learning [123]. Entanglement is a key concept in many quantum information processing tasks. Early on, it was realized that spontaneous parametric down-conversion (SPDC) in nonlinear crystals, with a Gaussian pump, produced pairs of photons entangled in OAM (each photon carrying opposite values, considering a pump photon with no OAM) [124]. More explicitly, the conservation of angular momentum can yield entangled states of the modes of twin photons, such as

$$|\psi_{AB}\rangle = c_{\ell,-\ell}|\ell\rangle \otimes |\ell_p - \ell\rangle + c_{-\ell,\ell}|\ell_p - \ell\rangle \otimes |\ell\rangle, \tag{4}$$

for a pump photon of angular momentum ℓ_p, assuming that only two modes are produced, of angular momentum $\ell\hbar$ and $(\ell_p - \ell)\hbar$. Here, the tensor product involves the states of different photons, meaning correlations can become nonlocal, contrary to the single-photon correlations described by Equation (2). SPDC involving structured light [125–127] is thus at the heart of many sources of photon pairs entangled in OAM. Interestingly, spin to OAM coupling may occur in nonlinear conversion processes [128], going beyond the simple phenomenon illustrated by (4). For the interested reader, a recent review [129] brings into focus the specificity of nonlinear optics with structured light propagating in bulk crystals. SPDC provides heralded single photons as well, that can be tailored to specified beam shapes using standard structured light technologies (such as spatial light modulators and holographic plates): for example, Airy single photons put in shape after SPDC [130] (actually, the entanglement resulting from SPDC can even produce correlated Airy photons [131] or correlated Airy-non-Airy photons [132]). This technology enabled the creation of entangled photon pairs in high dimensions and confirmed their entanglement through

the measurement of a Bell inequality violation. For example, structured beams of entangled photons demonstrated quantum cryptography with qutrits [133], as well as quantum key distribution implemented in a 7-dimensional basis [134] or using mutually unbiased bases encoded in OAM [135]. Over the years, structured light technology has substantially pushed the boundaries of achievable entanglement: notably, by entangling high quantum numbers of OAM [136,137]; by using hybrid entanglement schemes involving several degrees of freedom of photons, such as coupling spin and orbital angular momentum in single photons [138] or in entangled photon pairs [139]; by entangling more than two degrees of freedom [140], such as mixing polarization, OAM, and time-frequency modes [141], degree of polarization [142,143], paths [144], or wavelength [145]; by increasing the number of photons entangled in OAM [146,147] (the last example involves six photonic qutrits); and by increasing the amount of entanglement using high-dimensional spaces, for example involving many spatial (Laguerre–Gauss) modes of entangled photons [148]. For a review of hyper-entanglement schemes (involving N photons entangled in $d-$dimensional qudits), we suggest [149]. Recently, the spatial dependence of both classical and quantum manifestations of entanglement were resolved in photon and biphoton vector modes [150,151], indicating that entanglement must not necessarily be a global property. Storing and converting OAM information is also crucial for quantum communication purposes. Memories were notably realized using electromagnetically induced transparency in cold atomic ensembles (for a recent long-lived qutrit memory [152]), with doped crystals [153], or with paths [154]. In order to develop technologies for quantum key distribution networks, entanglement was successfully transferred from free-space OAM modes to energy-time entanglement in fibres [155], and OAM transmission in fibres was demonstrated [156]. Entangled photons of structured beams may also be useful for quantum metrology and imaging, for example in generalizations of quantum ghost imaging techniques [157] or for sparse sensing [158].

OAM impacts light beam interactions with matter at the quantum level, as total angular momentum exchanges occur in integer values of $\hbar$. However, total angular momentum conservation in these interactions does not preserve a priori SAM and OAM individually, affecting selection rules in spectroscopy [159]. Even in a Gaussian beam, photons may contribute OAM to complete a transition [160], since orbital angular momentum can be defined with respect to an arbitrary off-axis origin. Transfers of photon OAM to matter were observed for bound electrons in trapped ions [161] and evaluated theoretically for atoms [162], while light vortices might produce rare superkicks to atoms [163,164]. Interactions of structured light with matter can leave the matter in a desired quantum state, making it useful for applications, such as acting as an entangling gate for two atomic qubits [165], or generating vortices in quantum matter (for example, imprinting the OAM on the spin texture in semiconductors [166], producing coherent atomic vortices in Bose-Einstein condensates [167,168], or storing OAM information from ultra-short pulses in the rotational coherences of molecules in the gas phase [169]). Structured light beams affect the selection rules of atomic transitions in a position-dependent way [170]. Conversely, light–matter interactions may probe the OAM structure, for example through atomic photoionization [171]. The interplay between chirality, optical activity, and OAM is discussed in more detail in Section 3 of this paper. Subtly, a quantum study of the atomic emission [172] and absorption [173] processes in the close vicinity of the vortex of an OAM-carrying beam enables probing how the classical phase singularity becomes blurred at the quantum level, due to the quantum uncertainty and the quantum vacuum. In particular, absorption near the vortex line defines a quantum core where absorption produces predominantly a spinning motion of the atom around its center of mass, contrary to absorption occurring in the coherent, classical field far from the vortex [173], which causes negligible spinning of the atom. Let us note in passing that the rotations of atoms, molecules, and small objects that are induced by the classical mechanical torque associated to OAM beams are of considerable interest, including for studying quantum effects. Structured light beams can act as optical spanners, where the beam total angular momentum, combining both SAM and OAM, contributes to the induced rotational motion of the particle [174,175]. For a particle

located off-axis, the different mechanical actions of SAM and OAM transfer can be tracked experimentally, as SAM induces spinning of the particle around its own axis, while OAM transfer makes it rotate around the beam axis [176–179]. The mechanical motion of atoms in structured light was extensively reviewed [180]. Structured light enables optical trapping and microparticle manipulation [181–183] (there is a nice earlier account of field [184] in addition to the recent reviews [182,183]). The in-depth study of particle rotations promises many quantum applications [185], such as probing the collapse of macroscopic quantum superpositions by tracking orientational quantum revivals in nanorotors [186], or evidencing quantum friction [187] and rotation-induced quantum phases [188]. Mechanical rotations probe the complex structure of vortex beams as well, such as in this study of beams evidencing transverse (instead of longitudinal) phase singularities and transverse OAM [189]. To conclude this part on structured-light–matter interactions, let us add that new material developments are crucial to efficiently tailor the structured light properties at the single-photon level, notably through the use of metasurfaces [190–192].

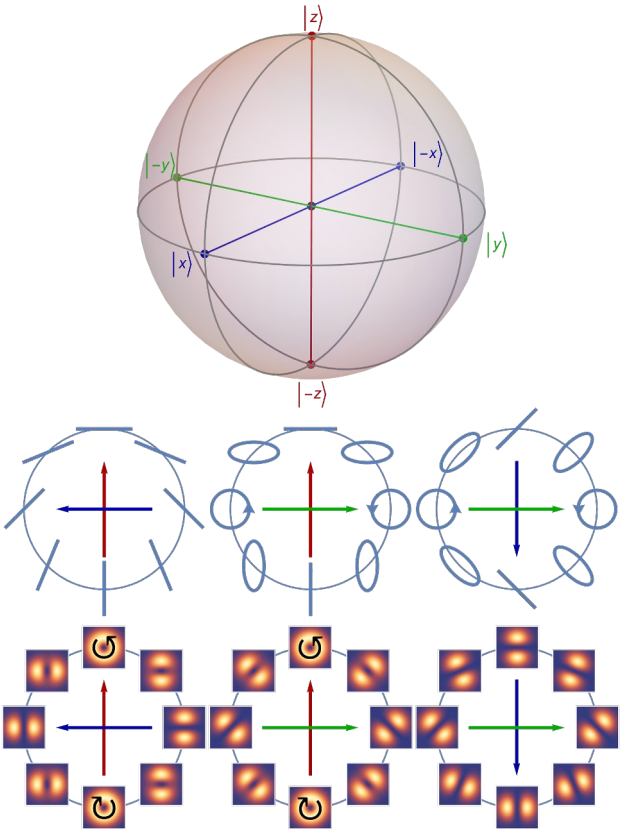


Figure 14. Top: Bloch sphere representation of a two-level quantum system. Any pure quantum state can be represented as a coherent superposition $\cos(\theta/2)|z\rangle + \sin(\theta/2)e^{i\varphi}|-z\rangle$ of the two basis states $|\pm z\rangle$, with θ and ϕ corresponding the usual spherical coordinates of points on the unit sphere. Mixed states correspond to points inside the sphere. They can be described with density operators as $\hat{\rho} = (1+p)/2|\theta,\phi\rangle\langle\theta,\phi| + (1-p)/2|\pi-\theta,-\phi\rangle\langle\pi-\theta,-\phi|$ with $p \in [0,1]$ linked to the state purity. First row: Polarization ellipses for a polarization qubit with $|z\rangle = |H\rangle$ (horizontal), $|-z\rangle = |V\rangle$ (vertical), $|x\rangle = |D\rangle$ (diagonal), $|-x\rangle = |A\rangle$ (anti-diagonal), $|y\rangle = |R\rangle$ (circular right), $|-y\rangle = |L\rangle$ (circular left), along the zx, zy, and xy great circles, respectively. The red arrow indicates the z axis, the green arrow, the y axis, and the blue arrow, the x axis. Second row: Intensity profiles of beams generated by the coherent superpositions of the Laguerre–Gauss beams $LG_0^{\pm 1}$ with $|z\rangle$ representing the LG_0^1 mode and $|-z\rangle$ representing the LG_0^{-1} mode, also along the zx, zy, and xy great circles, respectively. We can observe that the superposition generate the Hermite–Gauss modes HG_{10} for $|x\rangle$ and HG_{01} for $|-x\rangle$. Equivalent representations also exist for two-level systems based on coupled degrees of freedom (for example with $|z\rangle = |R\rangle \otimes \left|LG_0^{-1}\right\rangle$ and $|-z\rangle = |L\rangle \otimes \left|LG_0^{+1}\right\rangle$).

At low intensities, structured light beams exhibit photon shot noise that can be detrimental to highly sensitive applications. With reduced quantum noise, sources of squeezed structured light [193,194] can improve detection, imaging, and laser position measurements (Figure 15). Thus, a quantized theoretical description of the fields and their observables is necessary to describe the various quantum statistics, for polarization [195] and vortex modes [196,197], including for phase [198], intensity, position, and angular measurements. It can be obtained from the raising and lowering operators of quantum harmonic oscillators associated to the classical electromagnetic modes, typically in the paraxial approximation, but considering the photon wavefunction [199] is also fruitful to provide the appropriate photon quantum numbers [200] and Stokes parameters [201]. An approach emphasizing symmetry at the photon level sheds light on the essential features of the quantized field operators and their associated quantum uncertainties relevant for light–matter interactions [197]. Additionally, the raising and lowering operators for OAM can be constructed from Schwinger's representation of angular momentum using pseudo-oscillators [110]. The algebraic formalism of the quantum raising and lowering operators can notably relate the mode families of purely classical paraxial beams [202], such as Hermite–Gauss or Laguerre–Gauss modes. Certain complex beams can even be described at the theoretical level with quasiparticles, such as skyrmions and hopfions [203,204], as well as effective bosonic particles [205]. One practical question is whether structured light beams preserve their useful classical properties down to the photon level. This has been shown, for example, for the self-healing properties of heralded single photons of Airy [206] (Figure 16) and Bessel [207] beams, and for the healing of entanglement in entangled Bessel beams [208]. OAM-entangled Airy biphotons were shown theoretically to be more resilient against underwater turbulences than Laguerre–Gauss beams [209]. Perhaps counter-intuitively, the photon group velocity is slower than c for a beam propagating in free space [210,211]: a simplified argument links this to the projection, on the beam axis, of the twisting movement in a beam carrying OAM, which reduces the average propagation along the axis. This effect was described in a quantum formalism using a Dirac-like equation, in which the photon acquires an effective mass [212] and in terms of bosonic quasiparticles [205]. Thus, the advent of structured light forces us to reconsider the nature of photons beyond the simple plane wave or standing wave models. Conversely, the nonseparability of many properties of photons in classical, structured light beams, as illustrated in (2), makes us revisit the notion of entanglement in a classical context [213], such as nonseparability of polarization and position or of ray-wave duality [214]. Nonseparability of classical space-time wave packets, such as in the flying doughnut, has also been studied using the tools of quantum information theory, such as fidelity, entanglement of formation, and concurrence [215], while a quantum formulation of space-time wave packets has also been developed [196]. Another point of interest for the statistical quantum description is the study of phase singularities in the global biphoton states, that manifest themselves in the detection coincidences, i.e., in the quantum correlations [216].

We wish to highlight the importance of structured light beams for fundamental studies of quantum mechanics. As an alternative to polarization qubits, OAM modes allow us to investigate higher-dimensional quantum spaces with the advantages of low decoherence. Many archetypal quantum experiments were carried out with OAM, such as Young's two-slit experiment [217,218], the verification of Heisenberg's uncertainty relations for angular position and OAM [219] (recently performed with entangled photons to test Popper's conjecture [220]), the demonstration of a delayed choice quantum eraser based on OAM and SAM [221], the realization of entanglement swapping and/or teleportation [222,223], including the teleportation multiple degrees of freedom [224] (operations that are also very relevant for quantum information processing tasks useful for quantum technologies), and performing Hong-Ou-Mandel interferences [225] to produce high-dimensional entanglement. The azimuthal phase of vortex beams affects the Wigner phase time in quantum tunnelling, effectively controlling the Hartman effect [226]. OAM modes enable the testing of local realism through the violation of Bell [227] or Leggett [228] inequalities, including

for high-dimensional systems [229] and for local degrees of freedom [230], but also of contextuality [231,232]. In addition, a nonlocal game exploiting quantum correlations to win with certainty [233], quantum correlations in optical-angle-OAM [234], and quantum steering in a set-up closing the detection loophole using hybrid OAM-polarization entanglement [235] have all been demonstrated. Bell-like inequalities for continuous variables expressed in terms of Wigner functions were violated for Laguerre–Gauss beams [236] and studied theoretically for Ince-Gauss beams [237] (which include Hermite-Gauss and Laguerre–Gauss modes as limits of their ellipticity parameter). Experimental tests of quantum mechanics and quantum technologies require generating specific quantum states such as Dicke [238], GHZ-like [213] and GHZ (entangled qutrits actually) [239] states, as well as W states. Processing these states necessitates implementing mutually unbiased bases (MUB) [135] and Bell basis [240,241], as well as building sets of quantum gates for single-photon OAM states [242–244] and two-qubit SWAP gates [245]. For additional information on the quantum aspects of structured light in high dimensions, we refer the reader to a recent tutorial [246]. Light beams carrying OAM demonstrated quantum sensing of three-dimensional rotations with parameter estimation near the optimal Cramer-Rao bound [247]. In addition, structured light beam concepts inspire applications in other fields, such as atom optics with Bose-Einstein condensates [248].

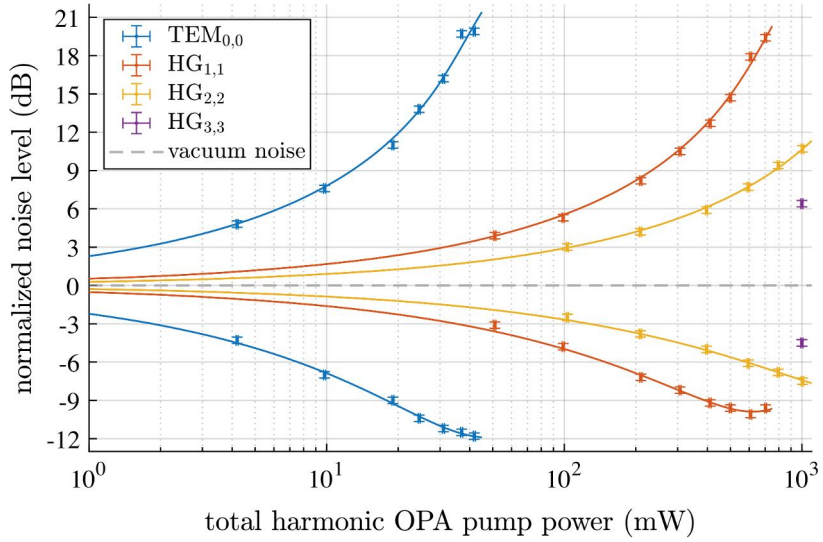


Figure 15. Noise reduction and amplification obtained for squeezed and anti-squeezed structured light, respectively (the solid line corresponds to the theoretical model). The noise reduction reaches up to 10 db for the Hermite-Gauss modes. Using higher-order spatial modes could mitigate the effect of thermal noise in advanced interferometers. Reproduced from APS under CC4.0 license [194].

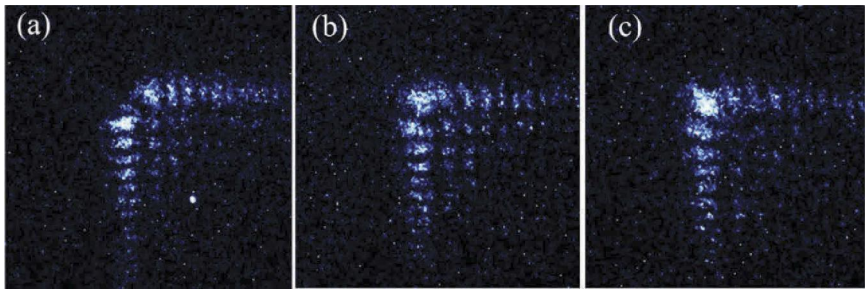


Figure 16. Self-healing of Airy photons with the main lobe blocked (the lobe is located in the top-left corner of the beam). (**a**) Intensity profile in the plane $z = 0$, (**b**) $z = 5$ mm, (**c**) $z = 10$ mm. The main lobe reappears upon the beam propagation, evidencing self-healing at the photon level. The images correspond to the accumulation of 3500 heralded single photons. Reprinted with permission from [206] © Optica Publishing Group.

A salient feature of light beams is their practical connection to quantum weak measurements, at the very boundary between classical and quantum optics. Weak measurements were introduced in 1988 by Y. Aharonov et al. to study foundational issues in quantum mechanics [249]. Since then, however, weak measurements found their way into many applications, especially because they enabled the detection of tiny physical phenomena, through what is called weak value amplification [250]. A typical weak measurement of a quantum system involves three successive steps: a pre-selection, which corresponds to setting the initial state $|\psi_i\rangle$ of the probed system; a weak unitary interaction involving the property of interest, that entangles slightly the probed quantum system with an ancilla system (also called the pointer) that will act as a quantum measuring device; and the measurement of the ancilla's final state conditioned on the successful post-selection of the system on a predefined final state $|\phi_f\rangle$ (this can be accomplished by performing a projective measurement on the system, followed by a filtering of the results of the system-ancilla joint measurement). A classic weak measurement set-up involves the light's polarization as the probed system and the transverse position of the beam center as a pointer [249] (see Figure 17). Let us note as an illustration that a usual quantum measurement of the OAM of a structured light beam involves post-selection, performed by combining a specific OAM-to-Gaussian mode converter followed by a Gaussian single-mode fibre [251]. Interestingly, the results of a weak measurement of an observable $\hat{A}$ depend on the real and imaginary parts of a complex number called the weak value

$$\langle A \rangle_w = \frac{\left\langle \phi_f | \hat{A} | \psi_i \right\rangle}{\left\langle \phi_f | \psi_i \right\rangle}, \tag{5}$$

an expression that bears some resemblance to a generalized conditional quantum average. Weak measurements are well-suited to probe fundamental issues of quantum mechanics because, as the coupling becomes weak, the ensuing perturbation of the quantum state due to measurement becomes negligible. This has allowed probing quantum paradoxes, such as the three-box paradox [252] and quantum Cheshire cat [253] (which could be performed using OAM as suggested here [254]), and to determine average photon trajectories in superposed Gaussian beams in a model of the two-slit experiment [255], where both interferences and trajectories are observed. The correspondence between paraxial optics and Schrödinger's equation for a massive particle in two dimensions [202] make such experiments even more interesting from a fundamental point of view. Structured light is inviting to probe more complex structures of the quantum probability flux [256,257], although interpreting the optical current may be complicated [258]. In particular, a phenomenon corresponding to quantum backflow [259] is observed for OAM, whereby the interference of two light beams carrying negative orbital angular momentum results in locally occurring regions of positive angular momentum [260].

By exploiting the complex nature of weak values, weak measurements enable direct measurement of the wavefunction [261], avoiding the state reconstruction procedures of the usual quantum tomography, which become demanding in large dimensions. Structured light beams were exploited to demonstrate the reconstruction of a photon state in 27 OAM dimensions [262] (Figure 18) and of a transverse beam profile [263] (actually, structured light was also featured in direct methods [264] going beyond the standard weak measurement paradigm, such as when using strong measurements [265,266], or in combination with a wavefront restoring algorithm [267]). However, in addition to their exploitation as high-dimensional quantum systems, structured light beams connect naturally with weak measurements. Indeed, in the paradigmatic weak measurement experiment, the system is played by light polarization, while the ancilla corresponds to the spatial profile of a Gaussian beam [250] (Figure 17). Therefore, structured light is bound to play the role of advanced pointer states in the transverse position or momentum spaces. Indeed, weak measurements were demonstrated with Laguerre–Gauss and Hermite-Gauss beam pointers and modeled theoretically [268,269]. Neatly, using a Laguerre–Gauss beam as a pointer

enables the direct observation of the stereographic projection of the polarization quantum state in the pointer final position [270] (Figure 19), including the case of density matrices describing partially polarized states [270]. This method measures the concurrence of entangled qubits [271] as well. With Hermite-Gauss beam pointers, higher modes provide increased sensitivity compared to Gaussian profiles [272] and improve the estimation of small parameters [273]. Using structured-light pointers, weak measurements exploiting amplification determined extremely small rotations with high sensitivity [272,274]. Weak value amplification occurs for nearly orthogonal pre- and post-selected states, as the weak value (5) becomes very large then (the weak value denominator is the state overlap); accordingly, the observed pointer shift becomes large as well. The small rotation measured in [272] is nicely mapped to a large, amplified rotation of the spatial profile of the pointer, shaped as a small angular sector in this case. Weak measurements with Laguerre–Gauss beams offer the advantage of allowing the measurement of joint observables (without a nonlinear Hamiltonian) [275–277] and of higher moments of single particle observables [278], which is not possible with Gaussian beams. Interestingly, the imaginary part of the weak value under amplification conditions can be determined from the spatial profile of a pointer carrying OAM [278], while, with Gaussian beams, only the transverse wavevector profile can provide this information through the pointer conjugate variable [250]. Conversely, we can also weakly measure the OAM of a beam [279,280] and visualize it directly on the beam profile (interestingly, the result is linked to the argument of the weak value [281–283], a fact that does not seem to have been pointed out explicitly, to our knowledge). Actually, weak measurements can identify both indices of Laguerre–Gauss beams [284,285]. An alternative procedure exploiting optical differentiation in combination with weak measurements [286] was recently used to determine the OAM of Laguerre–Gauss beams from the post-selected beam profile [287] (i.e., without averaging the meter observable).

The connection between weak measurements and structured light formally goes deeper, on both sides of the quantum–classical frontier. Indeed, the reflection of light beams at interfaces exhibit tiny deviations from the laws of geometrical optics, when naively applying these laws to the beam axis: both angular and spatial deviations appear, known as Goos-Hänchen shifts (for longitudinal deviations, in the incidence plane) and Imbert-Fedorov shifts (for transverse deviations) [288]. In transmission, the spin Hall effect of light occurs [289], where opposite circular polarizations of light propagate slightly shifted from one another, following conservation of angular momentum. These effects are typically of the order of the wavelength or less and are thus not immediately observable. However, in a pre- and post-selected measurement, these shifts can be evidenced by weak value amplification [290–293] (with a formal analogy pointed out by Dennis and Götte [294]). Thus, the intricacies of the reflection and refraction of structured light beams [295–297] can be probed by weak measurements of the polarization for the four spatial and angular Goos-Hänchen and Imbert-Fedorov shifts [277,296,298,299], as well as for the spin Hall effect of light [300,301]. Here, the weak system–pointer interaction comes from the weak coupling linking the photon polarization and wavevectors in connection to the amplitude and phase of the reflection and transmission coefficients [288,294,302]. These effects can also be described in terms of geometric phases (of the Pancharatnam-Berry type) [288,289,303]. We note that weak value amplification is not a cure-all miracle, as the price to pay is vanishing post-selection success. However, the amplification advantages remain when facing technical limitations [250,304]. Such weak measurements of light beams and photons have a dual description [288,294,302] that can be useful to explore the quantum to classical transition. Beyond fundamental quantum optical aspects, the interaction of structured light at interfaces may be useful for metrology and sensing as it is very sensitive to the refractive index [305–309], with further improvements in sensitivity to expect from exploiting higher-order modes of structured light [272,273,277,296,298–301].

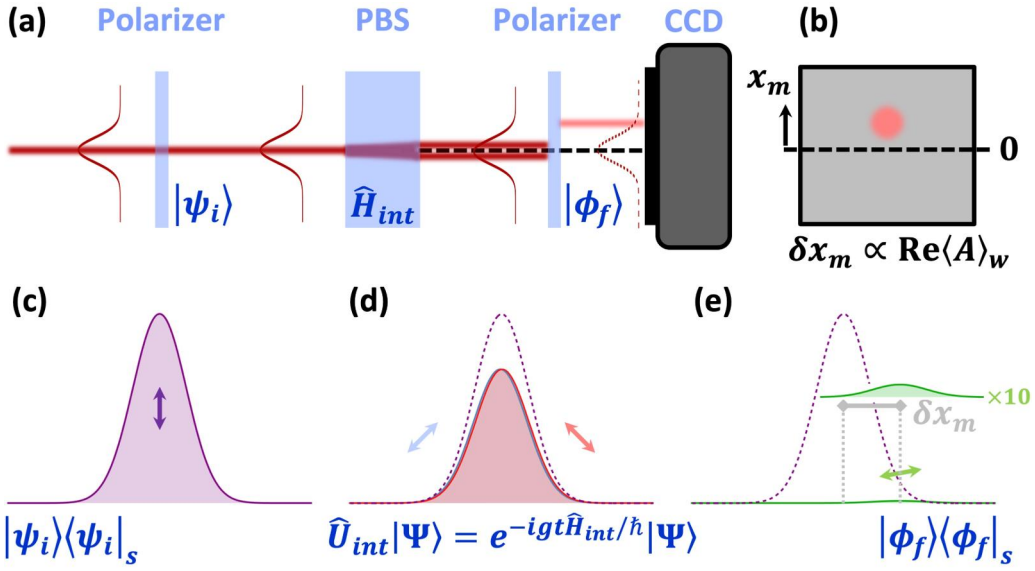


Figure 17. Principles of a weak measurement. (**a**,**c**) The measured quantum system, here the photon polarization, is pre-selected in the state $|\psi_i\rangle$ by a projective measurement $|\psi_i\rangle\langle\psi_i|_s$ applied on the system, using a polarizer. The quantum meter, here the transverse profile of the photon wavepacket, is initially in a spatial Gaussian mode $|G(x)\rangle$ centered on 0. The center of the meter profile propagates along the red line. The full quantum state of system–meter pair is $|\Psi\rangle = |\psi_i\rangle \otimes |G(x)\rangle$. (**a**,**d**) The photon passes through a birefringent plate (PBS) that, for a very short time t, weakly couples the photon propagation direction to its polarization through the interaction Hamiltonian $\hat{H}_{int} = g\hbar\hat{A}_s \otimes \hat{p}_m$, where $\hat{p}_m$ is the meter momentum, while $\hat{A}_s$ is the polarization observable weakly measured and g represents the small coupling constant. For example, we could choose $|\psi_i\rangle = |V\rangle$ as the initial state and the Pauli operator $\hat{\sigma}_x$ as the weakly measured polarization observable. The unitary evolution $\hat{U}_{int} \approx 1 - igt\hat{A}_s \otimes \hat{p}_m$ entangles the polarization and the transverse profile of the beam. As the coupling is weak ($gt \ll 1$), the two orthogonal polarizations (in our example, $|D\rangle$ and $|A\rangle$, the eigenvectors of $\hat{\sigma}_x$) are very slightly shifted—imperceptibly—in position; however, the two associated Gaussian profiles cannot interfere as their polarizations are orthogonal. (**a**,**e**) Then, we proceed to the post-selection of the system, performing a projective measurement $\left|\phi_f\right\rangle\left\langle\phi_f\right|_s$ with the last polarizer. Often, one chooses $\left\langle\phi_f|\psi_i\right\rangle \approx \epsilon$ with $\epsilon \ll 1$, so that the weak value (5) is amplified by the small parameter ϵ in the denominator (corresponding to a nearly horizontal polarization in our example $\left|\phi_f\right\rangle = |H + \epsilon\rangle$). In return, the post-selection success probability decreases as ϵ^2. After the post-selection projection, the shifted Gaussian profiles can interfere and the remaining beam centroid is shifted by a quantity related to the weak value (5): the shift is proportional to the real part of the weak value if we measure the meter position $\hat{x}_m$ and to the imaginary part if we measure the meter momentum $\hat{p}_m$. The observed shift δx_m can become anomalously large (pink direction of propagation: **a**,**b**), as the weak value can become much larger than the eigenvalues of the weakly measured observable $\hat{A}_s$. The weak value appears as a consequence of the linearization of the unitary $\hat{U}_{int}$ in the weak coupling approximation.

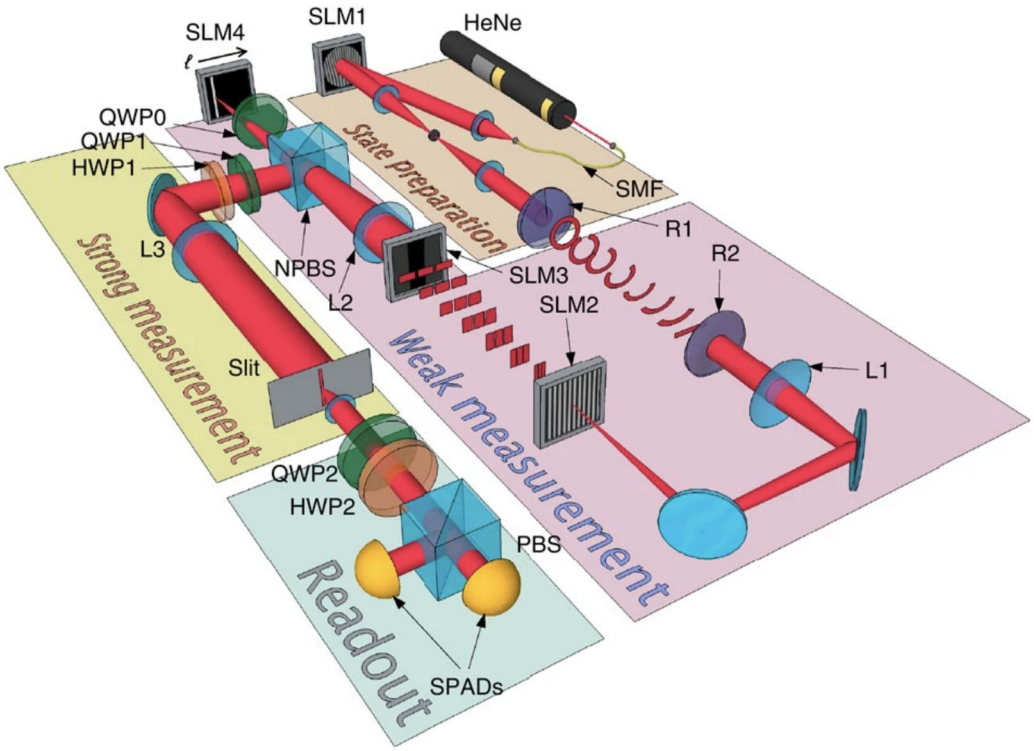


Figure 18. Experimental set-up enabling the direct measurement of a 27-dimensional OAM quantum state of photons from an attenuated HeNe beam. The state preparation generates an OAM state $|\psi_i\rangle = \sum_\ell c_\ell |\ell\rangle$ ($|\ell| \leq 13$) of vertical polarization $|V\rangle$, using a spatial light modulator (SLM1) after spatial filtering (SMF). The beam polarization corresponds to the meter. The system state is expressible in terms of weak values of projectors $\hat{\pi}_\ell = |\ell\rangle\langle\ell|$ on angular momentum basis states: $|\psi_i\rangle = k \sum_\ell \langle \pi_\ell \rangle_w |\ell\rangle$, where $k = \langle\theta_0|\psi_i\rangle / \langle\theta_0|\ell\rangle$ is a normalization constant. The post-selected state $\left|\phi_f\right\rangle = |\theta_0\rangle$ is the angular position basis state $\theta_0 = 0$ (the $|\ell\rangle$ and $|\theta\rangle$ are mutually unbiased bases, ensuring that k does not depend on ℓ for $\theta_0 = 0$). To perform the weak measurements of the projectors $\hat{\pi}_\ell$, the OAM modes with azimuthal phase $e^{i\ell\varphi}$ are first transformed to momentum modes with spatial phase $e^{i\ell x/a}$ using two custom refractive elements (R1 and R2). These different momentum modes are focused on different x positions on SLM4. SLM2 and SLM3 improve the mode resolution obtained on SLM4 (SLM2 is a fan-out element that diffracts three copies of each momentum mode, while SLM3 performs a relative-phase correction between the copies). A projector $\hat{\pi}_\ell$ is weakly probed by rotating the polarization of the associated OAM mode by a small angle α (using SLM4 and the quarter-wave plate QWP0). Post-selection on $|\theta_0\rangle$ is performed by passing the beam through a 10 µm slit placed in the Fourier plane of the lens L3 (as SLM4 and the slit are in conjugated planes, the positions x in those planes represent $|\ell\rangle$ and $|\theta\rangle$, respectively). Finally, the meter is read out by counting the photons at the two exits of a polarizing beamsplitter (PBS) using single-photon avalanche detectors (SPAD). If we note the final meter state $\left|\mu_f\right\rangle$, then measuring the polarization in the $\{|D\rangle, |A\rangle\}$ diagonal basis gives the real part of the OAM weak value, while measuring it in the circular polarization basis $\{|R\rangle, |L\rangle\}$ provides the imaginary part because $\left\langle \mu_f | \hat{\sigma}_x - i\hat{\sigma}_y | \mu_f \right\rangle = \sin\alpha \langle \pi_\ell \rangle_w$ at the end of the post-selected weak measurement [262]. Reproduced with permission from SNCSC.

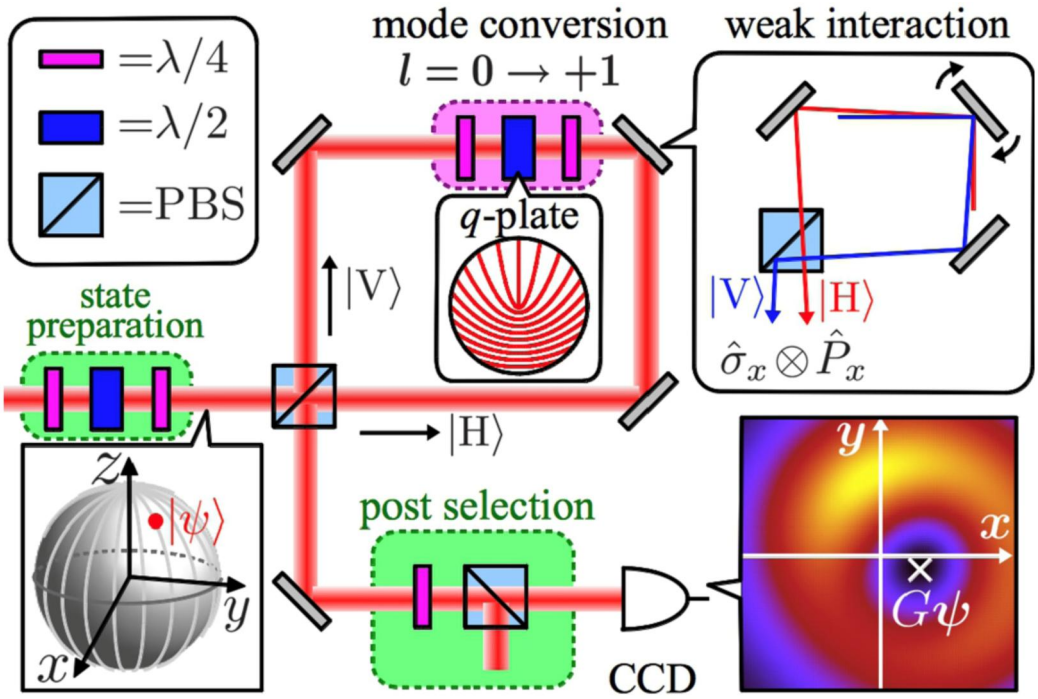


Figure 19. Stereographic visualization of a polarization state using weak measurements with a vortex beam [270]. An arbitrary polarization state $|\psi\rangle = \cos(\theta/2)|H\rangle + \sin(\theta/2)e^{i\varphi}|V\rangle$ of a Gaussian beam is pre-selected. Then, a Sagnac interferometer with a q-plate converts the Gaussian mode to a Laguerre–Gauss mode ($\ell = 1$), without affecting the beam polarization when optimally aligned. The $|H\rangle$ and $|V\rangle$ components of the beam rotate in opposite directions due to the polarizing beamsplitter (PBS) at the entrance of the interferometer. A small rotation of a mirror detunes slightly the interferometer so that the $\hat{\sigma}_x$ polarization observable couples weakly to the Gaussian beam momentum $\hat{p}_x$. After exiting the interferometer, the beam polarization is post-selected on $|V\rangle$. The weak value equals $\langle\hat{\sigma}_x\rangle_w = \langle H|\hat{\sigma}_x|\psi\rangle / \langle H|\psi\rangle = \tan(\theta/2)e^{i\varphi} = \cot\theta' e^{i\varphi}$, where θ' is now the angle seen from the pole of the sphere (between the z axis and the line joining the north pole to the state on the Bloch sphere). The weak value is thus the stereographic projection of the state on the complex plane $z = 0$ (with x corresponding to the real axis and y the imaginary axis). The position of the beam vortex after successful post-selection is shifted proportionally to the real part of the weak value along the x axis and to the imaginary part of the weak value along the y axis, enabling the visualization of the stereographic projection of the initial, arbitrary polarization state. Reprinted figure with permission from [270] ©2014 by the American Physical Society.

6. Conclusions

In this perspective article, we present the theoretical background of structured light and the properties of a few beams interesting for broad and conceivable applications in photonics, sensing, chirality, holography, and quantum technology. Structured light profoundly connects the topology of light with matter and its responses, and uniquely interconnects fundamental physics with quantum information science. The essential elements of structured light are not only their exceptional topology (quite different from the plane waves) or their nondiffraction capability but also the presence of nonseparable local correlations. We discussed in detail the importance of structured light, including in the presence of entanglement (nonseparable correlations of their degrees of freedom), for various classical and quantum applications. The opportunity to design and control different topologies of light on command will lead to a new scientific and technological revolution. It can improve quantum measurements, impacting optics and quantum physics at both the fundamental and applied levels. It can help the design and study of original complex materials, such as chiral and topological super- and semiconductors. It can steer chemical and biological dynamics and affect chemical reactivity, with remarkable control, just by shaping the light

topology. Furthermore, engineering and controlling structured light will rapidly lead to new surface optics, nanoscale optics, and photonics breakthroughs. Even though, at the moment, the interaction of structured light with matter is still under rapid development, this highlight aims primarily to capture the attention of the wider physical and quantum science community for structured light and its power. Ultimately, the structured light unifies many ideas and perspectives in physics and material science and uniquely connects geometry with physics. Harnessing the power of structured light is essential for future scientific and technological advancement.

Author Contributions: Conceptualization: B.K.; project administration: B.B. and B.K.; original draft preparation: B.B., Y.d.C., M.A.F., T.V., Y.C. and B.K.; writing—review and editing: B.B., Y.d.C., M.A.F., T.V., Y.C. and B.K.; visualization: B.B.; funding acquisition: B.B., Y.d.C., M.A.F., T.V., Y.C. and B.K. All authors have read and agreed to the published version of the manuscript.

Funding: BB and BK acknowledge funding provided by the Institute of Physics Belgrade, through the institutional funding by the Ministry of Science, Technological Development and Innovations of the Republic of Serbia, and the support of the Office of Naval Research Global through the Research Grant N62902-22-1-2024. YdC acknowledges the fund for scientific research—Flanders for a junior post-doc position (nr 1234222N). MAF acknowledges financial support from ESA MAP Project (4000129503/20/NL/PG/pt): Wound Healing In Space: Key challenges towards Intelligent and Enabling Sensing platforms (WHISKIES). TV acknowledges financial support from KULeuven. This work was supported by the Action de Recherche Concertée WeaM at the University of Namur (19/23-001). BB, MAF, TV, YC, and BK acknowledge the support of the EU: the EIC Pathfinder Challenges 2022 call through the Research Grant 101115149 (project ARTEMIS).

Data Availability Statement: The data that supports the findings of this study are available within the article.

Acknowledgments: All authors warmly acknowledge fruitful discussion and contribution of Dragana Jović Savić from the Institute of Physics Belgrade and Dejan Timotijević from the Institute of Multidisciplinary Research Belgrade regarding the physics of nondiffracting beams. BB and BK acknowledge funding provided by the Institute of Physics Belgrade, through the institutional funding by the Ministry of Science, Technological Development and Innovations of the Republic of Serbia, and the support of the Office of Naval Research Global through the Research Grant N62902-22-1-2024. Additionally, BK acknowledges support from F.R.S.-FNRS. YdC acknowledges the fund for scientific research-Flanders for a junior post-doc position (nr 1234222N). MAF acknowledges financial support from ESA MAP Project (4000129503/20/NL/PG/pt): Wound Healing In Space: Key challenges towards Intelligent and Enabling Sensing platforms (WHISKIES). TV acknowledges financial support from KULeuven. YC is a Research Associate of the Fund for Scientific Research F.R.S.-FNRS. This work was supported by the Action de Recherche Concertée WeaM at the University of Namur (19/23-001). BB, MAF, TV, YC, and BK acknowledge the support of the EU: the EIC Pathfinder Challenges 2022 call through the Research Grant 101115149 (project ARTEMIS). The content reflects only the authors' views, and the European Commission is not responsible for any use that may be made of the information it contains.

Conflicts of Interest: The authors declare no conflicts of interest.

References

1. Haroche, S.; Raimond, J.-M. *Exploring the Quantum: Atoms, Cavities and Photons*; Oxford University Press: Oxford, UK, 2006.
2. Secor, J.; Alfano, R.; Ashrafi, S. *Complex Light*; IOP: Bristol, UK, 2017. [CrossRef]
3. Zangwill, A. *Modern Elecromagnetism*; Cambridge University Press: Cambridge, UK, 2013. [CrossRef]
4. Rubinsztein-Dunlop, H.; Forbes, A.; Berry, M.V.; Dennis, M.R.; Andrews, D.L.; Mansuripur, M.; Denz, C.; Alpmann, C.; Banzer, P.; Bauer, T.; et al. Roadmap on structured light. *J. Opt.* **2017**, *19*, 013001. [CrossRef]
5. Bliokh, K.Y.; Karimi, E.; Padgett, M.J.; Alonso, M.A.; Dennis, M.R.; Dudley, A.; Forbes, A.; Zahedpour, S.; Hancock, S.W.; Milchberg, H.M.; et al. Roadmap on structured waves. *J. Opt.* **2023**, *25*, 103001. [CrossRef]
6. Wang, J.; Castellucci, F.; Franke-Arnold, S. Vectorial light-matter interaction: Exploring spatially structured complex light fields. *AVS Quantum Sci.* **2020**, *2*, 031702. [CrossRef]
7. Forbes, A.K.; Andrews, D.L. Orbital angular momentum of twisted light: Chirality and optical activity. *J. Phys. Photonics* **2021**, *3*, 022007. [CrossRef]
8. Frankel, T. *The Geometry of Physics*; Cambridge University Press: Cambridge, UK, 2004. [CrossRef]

9. Durnin, J.; Miceli, J.J.; Eberly, J.H. Diffraction-free beams. *Phys. Rev. Lett.* **1987**, *58*, 1499–1501. [CrossRef] [PubMed]
10. Durnin, J. Exact solutions for nondiffracting beams. I. The scalar theory. *J. Opt. Soc. Am. A* **1987**, *4*, 651–654. [CrossRef]
11. Boguslawski, M.; Rose, P.; Denz, C. Increasing the structural variety of discrete nondiffracting wave fields. *Phys. Rev. A* **2011**, *84*, 013832. [CrossRef]
12. Rose, P.; Boguslawski, M.; Denz, C. Nonlinear lattice structures based on families of complex nondiffracting beams. *New J. Phys.* **2012**, *14*, 033018. [CrossRef]
13. McQueen, C.; Arlt, J.; Dholakia, K. An experiment to study a "nondiffracting" light beam. *Am. J. Phys.* **1999**, *67*, 912–915. [CrossRef]
14. Gutiérrez-Vega, J.C.; Iturbe-Castillo, M.D.; Chávez-Cerda, S. Alternative formulation for invariant optical fields: Mathieu beams. *Opt. Lett.* **2000**, *25*, 1493–1495. [CrossRef]
15. Bandres, M.A.; Gutiérrez-Vega, J.C.; Chávez-Cerda, S. Parabolic nondiffracting optical wave fields. *Opt. Lett.* **2004**, *29*, 44–46. [CrossRef]
16. Freedman, B.; Bartal, G.; Segev, M.; Lifshitz, R.; Christodoulides, D.N.; Fleischer, J.W. Wave and defect dynamics in nonlinear photonic quasicrystals. *Nature* **2006**, *440*, 04722. [CrossRef]
17. Vicente, O.C.; Caloz, C. Bessel beams: A unified and extended perspective. *Optica* **2021**, *8*, 2334–2536. [CrossRef]
18. Boguslawski, M.; Lučić, N.M.; Diebel, F.; Timotijević, D.V.; Denz, C.; Savić, D.M.J. Light localization in optically induced deterministic aperiodic Fibonacci lattices. *Optica* **2016**, *3*, 711–717. [CrossRef]
19. Lóxpez-Mariscal, C.; Gutiérrez-Vega, J.C.; Milne, G.; Dholakia, K. Orbital angular momentum transfer in helical Mathieu beams. *Opt. Express* **2006**, *14*, 4182–4187. [CrossRef] [PubMed]
20. Baumgartl, J.; Mazilu, M.; Dholakia, K. Optically mediated particle clearing using Airy wavepackets. *Nat. Photonics* **2008**, *2*, 675–678. [CrossRef]
21. Fleischer, J.; Segev, M.; Efremidis, N.; Christodoulides, D. Observation of two-dimensional discrete solitons in optically induced nonlinear photonic lattices. *Nature* **2003**, *422*, 147. [CrossRef]
22. Sogomonian, S.; Klewitz, S.; Herminghaus, S. Self-reconstruction of a Bessel beam in a nonlinear medium. *Opt. Commun.* **1997**, *139*, 313–319. [CrossRef]
23. Bouchal, Z.; Wagner, J.; Chlup, M. Self-reconstruction of a distorted nondiffracting beam. *Opt. Commun.* **1998**, *151*, 207–211. [CrossRef]
24. Chávez-Cerda, S.; Meneses-Nava, M.A.; Hickmann, J.M. Interference of traveling nondiffracting beams. *Opt. Lett.* **1998**, *23*, 1871–1873. [CrossRef]
25. Vasara, A.; Turunen, J.; Friberg, A.T. Realization of general nondiffracting beams with computer-generated holograms. *J. Opt. Soc. Am. A* **1989**, *6*, 1748–1754. [CrossRef] [PubMed]
26. Scott, G.; McArdle, N. Efficient generation of nearly diffraction-free beams using an axicon. *Opt. Eng.* **1992**, *31*, 2640. [CrossRef]
27. Chattrapiban, N.; Rogers, E.A.; Cofield, D.; Wendell, T.; Hill, I.; Roy, R. Generation of nondiffracting Bessel beams by use of a spatial light modulator. *Opt. Lett.* **2003**, *28*, 2183–2185. [CrossRef] [PubMed]
28. Berry, M.V.; Balazs, N.L. Nonspreading wave packets. *Am. J. Phys.* **1979**, *47*, 264. [CrossRef]
29. Siviloglou, G.A.; Christodoulides, D.N. Accelerating finite energy Airy beams. *Opt. Lett.* **2007**, *32*, 979–981. [CrossRef]
30. Siviloglou, G.A.; Broky, J.; Dogariu, A.; Christodoulides, D.N. Observation of Accelerating Airy Beams. *Phys. Rev. Lett.* **2007**, *99*, 213901. [CrossRef] [PubMed]
31. Siviloglou, G.A.; Broky, J.; Dogariu, A.; Christodoulides, D.N. Ballistic dynamics of Airy beams. *Opt. Lett.* **2008**, *33*, 207–209. [CrossRef] [PubMed]
32. Bandres, M.A.; Kaminer, I.; Mills, M.; Rodríguez-Lara, B.; Greenfield, E.; Segev, M.; Christodoulides, D.N. Accelerating Optical Beam. *Opt. Photonics News* **2013**, *24*, 30–37. [CrossRef]
33. Besieris, I.M.; Shaarawi, A.M. A note on an accelerating finite energy Airy beam. *Opt. Lett.* **2007**, *32*, 2447–2449. [CrossRef]
34. Novitsky, A.V.; Novitsky, D.V. Nonparaxial Airy beams: Role of evanescent waves. *Opt. Lett.* **2009**, *34*, 3430–3432. [CrossRef]
35. Mathis, A.; Courvoisier, F.; Froehly, L.; Furfaro, L.; Jacquot, M.; Lacourt, P.A.; Dudley, J.M. Micromachining along a curve: Femtosecond laser micromachining of curved profiles in diamond and silicon using accelerating beams. *Appl. Phys. Lett.* **2012**, *101*, 071110. [CrossRef]
36. Chong, A.; Renninger, W.H.; Christodoulides, D.N.; Wise, F.W. Airy-Bessel wave packets as versatile linear light bullets. *Nat. Photonics* **2010**, *4*, 103–106. [CrossRef]
37. Zhang, P.; Wang, S.; Liu, Y.; Yin, X.; Lu, C.; Chen, Z.; Zhang, X. Plasmonic Airy beams with dynamically controlled trajectories. *Opt. Lett.* **2011**, *36*, 3191–3193. [CrossRef] [PubMed]
38. Minovich, A.; Klein, A.E.; Janunts, N.; Pertsch, T.; Neshev, D.N.; Kivshar, Y.S. Generation and Near-Field Imaging of Airy Surface Plasmons. *Phys. Rev. Lett.* **2011**, *107*, 116802. [CrossRef]
39. Polynkin, P.; Kolesik, M.; Moloney, J.V.; Siviloglou, G.A.; Christodoulides, D.N. Curved Plasma Channel Generation Using Ultraintense Airy Beams. *Science* **2009**, *324*, 229–232. [CrossRef]
40. Ellenbogen, T.; Voloch-Bloch, N.; Ganany-Padowicz, A.; Arie, A. Nonlinear generation and manipulation of Airy beams. *Nat. Photon.* **2009**, *3*, 395–398. [CrossRef]
41. Broky, J.; Siviloglou, G.A.; Dogariu, A.; Christodoulides, D.N. Self-healing properties of optical Airy beams. *Opt. Express* **2008**, *16*, 12880–12891. [CrossRef]

42. Efremidis, N.K. Airy trajectory engineering in dynamic linear index potentials. *Opt. Lett.* **2011**, *36*, 3006–3008. [CrossRef] [PubMed]
43. Efremidis, N.K. Accelerating beam propagation in refractive-index potentials. *Phys. Rev. A* **2014**, *89*, 023841. [CrossRef]
44. Makris, K.G.; Kaminer, I.; El-Ganainy, R.; Efremidis, N.K.; Chen, Z.; Segev, M.; Christodoulides, D.N. Accelerating diffraction-free beams in photonic lattices. *Opt. Lett.* **2014**, *39*, 2129–2132. [CrossRef]
45. Chávez-Cerda, S.; Ruiz, U.; Arrizón, V.; Moya-Cessa, H.M. Generation of Airy solitary-like wave beams by acceleration control in inhomogeneous media. *Opt. Express* **2011**, *19*, 16448–16454. [CrossRef]
46. Lučić, N.M.; Bokić, B.M.; Grujić, D.i.c.v.; Pantelić, D.V.; Jelenković, B.M.; Piper, A.; Jović, D.M.; Timotijević, D.V. Defect-guided Airy beams in optically induced waveguide arrays. *Phys. Rev. A* **2013**, *88*, 063815. [CrossRef]
47. Diebel, F.; Bokić, B.M.; Boguslawski, M.; Piper, A.; Timotijević, D.V.; Jović, D.M.; Denz, C. Control of Airy-beam self-acceleration by photonic lattices. *Phys. Rev. A* **2014**, *90*, 033802. [CrossRef]
48. Rose, P.; Diebel, F.; Boguslawski, M.; Denz, C. Airy beam induced optical routing. *Appl. Phys. Lett.* **2013**, *102*, 101101. [CrossRef]
49. Bekenstein, R.; Segev, M. Self-accelerating optical beams in highly nonlocal nonlinear media. *Opt. Express* **2011**, *19*, 23706–23715. [CrossRef]
50. Hu, Y.; Huang, S.; Zhang, P.; Lou, C.; Xu, J.; Chen, Z. Persistence and breakdown of Airy beams driven by an initial nonlinearity. *Opt. Lett.* **2010**, *35*, 3952–3954. [CrossRef]
51. Driben, R.; Konotop, V.V.; Meier, T. Coupled Airy breathers. *Opt. Lett.* **2014**, *39*, 5523–5526. [CrossRef] [PubMed]
52. Diebel, F.; Bokić, B.M.; Timotijević, D.V.; Savić, D.M.J.; Denz, C. Soliton formation by decelerating interacting Airy beams. *Opt. Express* **2015**, *23*, 24351–24361. [CrossRef]
53. Zannotti, A.; Vasiljević, J.M.; Timotijević, D.V.; Savić, D.M.J.; Denz, C. Morphing discrete diffraction in nonlinear Mathieu lattices. *Opt. Lett.* **2019**, *44*, 1592–1595. [CrossRef]
54. Zannotti, A.; Vasiljević, J.M.; Timotijević, D.V.; Jović Savić, D.M.; Denz, C. Visualizing the Energy Flow of Tailored Light. *Adv. Opt. Mater.* **2018,** *6*, 1701355. [CrossRef]
55. Vasiljević, J.M.; Zannotti, A.; Timotijević, D.V.; Denz, C.; Savić, D.M.J. Light transport and localization in disordered aperiodic Mathieu lattices. *Opt. Lett.* **2022**, *47*, 702–705. [CrossRef] [PubMed]
56. Lakhtakia, A. (Ed.) *Selected Papers on Natural Optical Activity*; SPIE: Bellingham, WA, USA, 1990; Volume MS15.
57. Allen, L.; Beijersbergen, M.W.; Spreeuw, R.J.C.; WoerdmanDurnin, J.P. Orbital angular momentum of light and the transformation of Laguerre-Gaussian laser modes. *Phys. Rev. A.* **1992**, *45*, 8185–8189. [CrossRef] [PubMed]
58. Rosales-Guzman, C.; Ndagano, B.; Forbes, A. A review of complex vector light fields and their applications. *J. Opt.* **2018**, *20*, 123001. [CrossRef]
59. Dholakia, K.; Lee, W.M. Optical trapping takes shape: The use of structured light fields. *Adv. At. Mol. Opt. Phys.* **2008**, *56*, 261–337. [CrossRef]
60. Piccirillo, B.; Toscano, C.; Vetrano, F.; Santamato, E. Orbital and Spin Photon Angular Momentum Transfer in Liquid Crystals. *Phys. Rev. Lett.* **2001**, *86*, 2285–2288. [CrossRef] [PubMed]
61. Babiker, M.; Bennett, C.; Andrews, D.L.; Dávila Romero, L.C. Orbital Angular Momentum Exchange in the Interaction of Twisted Light with Molecules. *Phys. Rev. Lett.* **2002**, *89*, 143601. [CrossRef] [PubMed]
62. Andrews, D.L.; Dávila Romero, L.C.; Babiker, M. On optical vortex interactions with chiral matter. *Opt. Commun.* **2004**, *237*, 133–139. [CrossRef]
63. Coles, M.; Andrews, D.L. Chirality and angular momentum in optical radiation. *Phys. Rev. A* **2012**, *85*, 063810. [CrossRef]
64. Araoka, F.; Verbiest, T.; Clays, K.; Persoons, A. Interactions of twisted light with chiral molecules: An experimental investigation. *Phys. Rev. A* **2005**, *71*, 055401. [CrossRef]
65. Loeffler, W.; Broer, J.D.; Woerdman, P.J. Circular dichroism of cholesteric polymers and the orbital angular momentum of light. *Phys. Rev. A* **2011**, *83*, 065801. [CrossRef]
66. Brullot, W.; Vanbel, K.M.; Swusten, T.; Verbiest, T. Resolving enantiomers using the optical angular momentum of twisted light. *Sci. Adv.* **2016**, *2*, e1501349. [CrossRef] [PubMed]
67. Forbes, A.K.; Andrews, D.L. Optical orbital angular momentum: Twisted light and chirality. *Opt. Lett.* **2018**, *43*, 435–438. [CrossRef]
68. Forbes, A.K.; Andrews, D.L. Spin-orbit interactions and chiroptical effects engaging orbital angular momentum of twisted light in chiral and achiral media. *Phys. Rev. A* **2019**, *99*, 023837. [CrossRef]
69. Ni, J.; Liu, S.; Hu, G.; Hu, Y.; Lao, Z.; Li, J.; Zhang, Q.; Wu, D.; Dong, S.; Chu, J.; et al. Giant helical dichroism of single chiral nanostructures with photonic orbital angular momentum. *ACS Nano* **2021**, *15*, 2893–2900. [CrossRef]
70. Ni, J.; Liu, S.; Lao, Z.; Wang, Z.; Huang, K.; Ji, S.; Li, J.; Huang, Z.; Xiong, Q.; Hu, Y.; et al. Gigantic vortical differential scattering as a monochromatic probe for multiscale chiral structures. *Proc. Natl. Acad. Sci. USA* **2021**, *118*, e2020055118. [CrossRef]
71. Liu, S.; Ni, J.; Zhang, C.; Wang, X.; Cao, Y.; Wang, D.; Ji, S.; Pan, D.; Li, R.; Wu, H.; et al. Tailoring Optical Vortical Dichroism with Stereometamaterials. *Laser Photonics Rev.* **2022**, *16*, 2100518. [CrossRef]
72. Begin, J.L.; Jain, A.; Parks, A.; Hufnagel, F.; Corkum, P.; Karimi, E.; Brabec, T.; Bhardwaj, R. Nonlinear helical dichroism in chiral and achiral molecules. *Nat. Photonics* **2023**, *17*, 82–88. [CrossRef]
73. Gabor, D. A New Microscopic Principle. *Nature* **1948**, *161*, 777–778. [CrossRef]

74. Ruffato, G.; Rossi, R.; Massari, M.; Mafakheri, E.; Capaldo, P.; Romanato, F. Design, fabrication and characterization of Computer Generated Holograms for anti-counterfeiting applications using OAM beams as light decoders. *Sci. Rep.* **2017**, *7*, 18011. [CrossRef]
75. Ashley, J.; Bernal, M.P.; Burr, G.W.; Coufal, H.; Guenther, H.; Hoffnagle, J.A.; Jefferson, C.M.; Marcus, B.; MacFarlane, R.M.; Shelby, R.M.; et al. Holographic Data Storage Technology. *IBM J. Res. Dev.* **2000**, *44*, 341–368. [CrossRef]
76. Kosma, K.; Andrianakis, M.; Hatzigiannakis, K.; Tornari, V. Digital holographic interferometry for cultural heritage structural diagnostics: A coherent and a low-coherence optical set-up for the study of a marquetry sample. *Strain* **2018**, *54*, e12263. [CrossRef]
77. Coppola, G.; Zito, G.; Luca, A.C.D.; Ferrara, M.A. Polarized Digital Holography as Valuable Analytical Tool in Biological and Medical Research. In *Proceedings of the Digital Holography and Three-Dimensional Imaging 2019*; Paper Th4A.5; Optica Publishing Group: Washington, DC, USA, 2019. [CrossRef]
78. Wang, J.; Liang, Y. Generation and Detection of Structured Light: A Review. *Front. Phys.* **2021**, *9*, 688284. [CrossRef]
79. Hariharan, P. *Basics of Holography*; Cambridge University Press: Cambridge, UK, 2002. [CrossRef]
80. Stoykova, E.; Kang, H.; Park, J. Twin-image problem in digital holography-a survey (Invited Paper). *Chin. Opt. Lett.* **2014**, *12*, 060013. [CrossRef]
81. Tahara, T.; Lee, Y.; Ito, Y.; Xia, P.; Shimozato, Y.; Takahashi, Y.; Awatsuji, Y.; Nishio, K.; Ura, S.; Kubota, T.; et al. Superresolution of interference fringes in parallel four-step phase-shifting digital holography. *Opt. Lett.* **2014**, *39*, 1673–1676. [CrossRef] [PubMed]
82. Guo, C.S.; Cheng, X.; Ren, X.Y.; Ding, J.P.; Wang, H.T. Optical vortex phase-shifting digital holography. *Opt. Express* **2004**, *12*, 5166–5171. [CrossRef]
83. Zhang, X.; Zhang, J.; Li, Y.; Zhou, S.; Liu, D.; Zhu, J. Phase-shifting digital holography with vortex beam in one single exposure. *Optik* **2019**, *185*, 1024–1029. [CrossRef]
84. Zhang, X.; Zhang, J.; Zhou, S.; Liu, D.; Zhu, J. Single-shot phase-shifting digital holography with amplitude-only Fermat-spiral sieves. *Laser Phys. Lett.* **2019**, *16*, 025002. [CrossRef]
85. Born, M.; Wolf, E.; Bhatia, A.B.; Clemmow, P.C.; Gabor, D.; Stokes, A.R.; Taylor, A.M.; Wayman, P.A.; Wilcock, W.L. *Principles of Optics: Electromagnetic Theory of Propagation, Interference and Diffraction of Light*, 7th ed.; Cambridge University Press: Cambridge, UK, 1999. [CrossRef]
86. Gustafsson, M.G.L. Surpassing the lateral resolution limit by a factor of two using structured illumination microscopy. *J. Microsc.* **2001**, *198*, 82–87. [CrossRef]
87. Mudassar, A.A.; Hussain, A. Super-resolution of active spatial frequency heterodyning using holographic approach. *Appl. Opt.* **2010**, *49*, 3434–3441. [CrossRef]
88. Gao, P.; Pedrini, G.; Osten, W. Structured illumination for resolution enhancement and autofocusing in digital holographic microscopy. *Opt. Lett.* **2013**, *38*, 1328–1330. [CrossRef] [PubMed]
89. Shin, S.; Kim, K.; Yoon, J.; Park, Y. Active illumination using a digital micromirror device for quantitative phase imaging. *Opt. Lett.* **2015**, *40*, 5407–5410. [CrossRef] [PubMed]
90. Ganjkhani, Y.; Charsooghi, M.A.; Akhlaghi, E.A.; Moradi, A.R. Super-resolved Mirau digital holography by structured illumination. *Opt. Commun.* **2017**, *404*, 110–117. [CrossRef]
91. Meng, Z.; Pedrini, G.; Lv, X.; Ma, J.; Nie, S.; Yuan, C. DL-SI-DHM: A deep network generating the high-resolution phase and amplitude images from wide-field images. *Opt. Express* **2021**, *29*, 19247–19261. [CrossRef] [PubMed]
92. Ren, H.; Briere, G.; Fang, X.; Ni, P.; Sawant, R.; Héron, S.; Chenot, S.; Vézian, S.; Damilano, B.; Brändli, V.; et al. Metasurface orbital angular momentum holography. *Nat. Commun.* **2019**, *10*, 2986. [CrossRef] [PubMed]
93. Ren, H.; Fang, X.; Jang, J.; Bürger, J.; Rho, J.; Maier, S.A. Complex-amplitude metasurface-based orbital angular momentum holography in momentum space. *Nat. Nanotechnol.* **2020**, *15*, 948–955. [CrossRef] [PubMed]
94. Fang, X.; Ren, H.; Gu, M. Orbital angular momentum holography for high-security encryption. *Nat. Photonics* **2020**, *14*, 101–108. [CrossRef]
95. Zhou, H.; Sain, B.; Wang, Y.; Schlickriede, C.; Zhao, R.; Zhang, X.; Wei, Q.; Li, X.; Huang, L.; Zentgraf, T. Polarization-Encrypted Orbital Angular Momentum Multiplexed Metasurface Holography. *ACS Nano* **2020**, *14*, 5553–5559. [CrossRef] [PubMed]
96. Trajtenberg-Mills, S.; Juwiler, I.; Arie, A. On-axis shaping of second-harmonic beams. *Laser Photonics Rev.* **2015**, *9*, L40–L44. [CrossRef]
97. Fang, X.; Yang, H.; Yao, W.; Wang, T.; Zhang, Y.; Gu, M.; Xiao, M. High-dimensional orbital angular momentum multiplexing nonlinear holography. *Adv. Photonics* **2021**, *3*, 015001. [CrossRef]
98. Töpfer, S.; Basset, M.G.; Fuenzalida, J.; Steinlechner, F.; Torres, J.P.; Gräfe, M. Quantum holography with undetected light. *Sci. Adv.* **2022**, *8*, eabl4301. [CrossRef]
99. He, L.; Liu, K.; He, Z.; Cao, L. Three-dimensional holographic communication system for the metaverse. *Opt. Commun.* **2023**, *526*, 128894. [CrossRef]
100. Aiello, A.; Töppel, F.; Marquardt, C.; Giacobino, E.; Leuchs, G. Quantum-like nonseparable structures in optical beams. *New J. Phys.* **2015**, *17*, 043024. [CrossRef]
101. Forbes, A.; Aiello, A.; Ndagano, B. Classically entangled light. *Prog. Opt.* **2019**, *64*, 99–153. [CrossRef]
102. Goldstein, D. *Polarized Light, Revised and Expanded*, 2nd ed.; Marcel Dekker Inc.: New York, NY, USA, 2003. [CrossRef]
103. Bengtsson, I.; Zyczkowski, K. *Geometry of Quantum States*; Cambridge University Press: Cambridge, UK, 2009. [CrossRef]
104. Saito, S. Photonic quantum chromodynamics. *Front. Phys.* **2023**, *11*, 1225488. [CrossRef]

105. Padgett, M.J.; Courtial, J. Poincaré-sphere equivalent for light beams containing orbital angular momentum. *Opt. Lett.* **1999**, *24*, 430–432. [CrossRef]
106. Milione, G.; Sztul, H.I.; Nolan, D.A.; Alfano, R.R. Higher-order Poincaré sphere, Stokes parameters, and the angular momentum of light. *Phys. Rev. Lett.* **2011**, *107*, 053601. [CrossRef]
107. Milione, G.; Evans, S.; Nolan, D.A.; Alfano, R.R. Higher order Pancharatnam-Berry phase and the angular momentum of light. *Phys. Rev. Lett.* **2012**, *108*, 190401. [CrossRef]
108. Yang, L.P. Geometric phase for twisted light. *Opt. Express* **2023**, *31*, 10287–10296. [CrossRef]
109. Gutiérrez-Cuevas, R.; Dennis, M.R.; Alonso, M.A. Generalized Gaussian beams in terms of Jones vectors. *J. Opt.* **2019**, *21*, 084001. [CrossRef]
110. Dennis, M.R.; Alonso, M.A. Gaussian mode families from systems of rays. *J. Phys. Photonics* **2019**, *1*, 025003. [CrossRef]
111. Gutiérrez-Cuevas, R.; Wadood, S.A.; Vamivakas, A.N.; Alonso, M.A. Modal Majorana sphere and hidden symmetries of structured-Gaussian beams. *Phys. Rev. Lett.* **2020**, *125*, 123903. [CrossRef] [PubMed]
112. Shen, Y.; Wang, Z.; Fu, X.; Naidoo, D.; Forbes, A. SU(2) Poincaré sphere: A generalized representation for multidimensional structured light. *Phys. Rev. A* **2020**, *102*, 031501(R). [CrossRef]
113. Shen, Y. Rays, waves, SU(2) symmetry and geometry: Toolkits for structured light. *J. Opt.* **2021**, *23*, 124004. [CrossRef]
114. Zhang, H.; Zeng, J.; Lu, X.; Wang, Z.; Zhao, C.; Cai, Y. Review on fractional vortex beam. *Nanophotonics* **2022**, *11*, 241–273. [CrossRef]
115. Götte, J.B.; Franke-Arnold, S.; Zambrini, R.; Barnett, S.M. Quantum formulation of fractional orbital angular momentum. *J. Mod. Opt.* **2007**, *54*, 1723–1738. [CrossRef]
116. Oemrawsingh, S.S.R.; Ma, X.; Voigt, D.; Aiello, A.; Eliel, E.R.; 't Hooft, G.W.; Woerdman, J.P. Experimental demonstration of fractional orbital angular momentum Entanglement of two photons. *Phys. Rev. Lett.* **2005**, *95*, 240501. [CrossRef] [PubMed]
117. Sit, A.; Bouchard, F.; Fickler, R.; Gagnon-Bischoff, J.; Larocque, H.; Heshami, K.; Elser, D.; Peuntinger, C.; Günthner, K.; Heim, B.; et al. High-dimensional intracity quantum cryptography with structured photons. *Optica* **2017**, *4*, 1006–1010. [CrossRef]
118. Bouchard, F.; Fickler, R.; Boyd, R.W.; Karimi, E. High-dimensional quantum cloning and applications to quantum hacking. *Sci. Adv.* **2017**, *3*, e1601915. [CrossRef]
119. Ndagano, B.; Perez-Garcia, B.; Roux, F.S.; McLaren, M.; Rosales-Guzman, C.; Zhang, Y.; Mouane, O.; Hernandez-Aranda, R.I.; Konrad, T.; Forbes, A. Characterizing quantum channels with non-separable states of classical light. *Nat. Phys.* **2017**, *13*, 397–402. [CrossRef]
120. Nape, I.; Singh, K.; Klug, A.; Buono, W.; Rosales-Guzman, C.; McWilliam, A.; Franke-Arnold, S.; Kritzinger, A.; Forbes, P.; Dudley, A.; et al. Revealing the invariance of vectorial structured light in complex media. *Nat. Photonics* **2022**, *16*, 538–546. [CrossRef]
121. Sekga, C.; Mafu, M. Measurement device-independent quantum key distribution with vector vortex modes under diverse weather conditions. *Sci. Rep.* **2023**, *13*, 14931. [CrossRef] [PubMed]
122. Klug, A.; Peters, C.; Forbes, A. Robust structured light in atmospheric turbulence. *Adv. Photonics* **2023**, *5*, 016006. [CrossRef]
123. Bai, X.; Wang, Y.; Dai, K. Classification of 270 classes of vector vortex beams using Machine learning-based methods. *Optik* **2023**, *291*, 171362. [CrossRef]
124. Mair, A.; Vaziri, A.; Weihs, G.; Zeilinger, A. Entanglement of the orbital angular momentum states of photons. *Science* **2001**, *412*, 313–316. [CrossRef]
125. Khoury, A.Z.; Souto Ribeiro, P.H.; Dechoum, K. Transfer of angular spectrum in parametric down-conversion with structured light. *Phys. Rev. A* **2020**, *102*, 033708. [CrossRef]
126. Trajtenberg-Mills, S.; Karnieli, A.; Voloch-Bloch, N.; Megidish, E.; Eisenberg, H.S.; Arie, A. Simulating correlations of structured spontaneously down-converted photon pairs. *Laser Photonics Rev.* **2020**, *14*, 1900321. [CrossRef]
127. Rodrigues, R.B.; Alves, G.B.; Barros, R.F.; Souza, C.E.R.; Khoury, A.Z. Generalized orbital angular momentum symmetry in parametric amplification. *Phys. Rev. A* **2022**, *105*, 013510. [CrossRef]
128. Pinheiro da Silva, B.; Buono, W.T.; Pereira, L.J.; Tasca, D.S.; Dechoum, K.; Khoury, A.Z. Spin to orbital angular momentum transfer in frequency up-conversion. *Nanophotonics* **2022**, *11*, 771–778. [CrossRef]
129. Buono, W.T.; Forbes, A. Nonlinear optics with structured light. *Opto-Electron. Adv.* **2022**, *5*, 210174. [CrossRef]
130. Maruca, S.; Kumar, S.; Meng Sua, Y.; Chen, J.Y.; Shahverdi, A.; Huang, Y.P. Quantum Airy photons. *J. Phys. B At. Mol. Opt. Phys.* **2018**, *51*, 175501. [CrossRef]
131. Lib, O.; Bromberg, Y. Spatially entangled Airy photons. *Opt. Lett.* **2020**, *45*, 1399–1402. [CrossRef] [PubMed]
132. Pimenta, R.C.S.; Santos, G.H.d.; Barreto, A.B.; Celeri, L.C.; Ribeiro, P.H.S. Photonic entanglement with accelerated light. *Quantum* **2024**, *8*, 1317. [CrossRef]
133. Gröblacher, S.; Jennewein, T.; Vaziri, A.; Weihs, G.; Zeilinger, A. Experimental quantum cryptography with qutrits. *New J. Phys.* **2006**, *8*, 75. [CrossRef]
134. Mirhosseini, M.; Magaña-Loaiza, O.S.; O'Sullivan, M.N.; Rodenburg, B.; Malik, M.; Lavery, M.P.J.; Padgett, M.J.; Gauthier, D.J.; Boyd, R.W. High-dimensional quantum cryptography with twisted light. *New J. Phys.* **2015**, *17*, 033033. [CrossRef]
135. Mafu, M.; Dudley, A.; Goyal, S.; Giovannini, D.; McLaren, M.; Padgett, M.J.; Konrad, T.; Petruccione, F.; Lütkenhaus, N.; Forbes, A. Higher-dimensional orbital-angular-momentum-based quantum key distribution with mutually unbiased bases. *Phys. Rev. A* **2013**, *88*, 032305. [CrossRef]

136. Fickler, R.; Lapkiewicz, R.; Plick, W.N.; Krenn, M.; Schaeff, C.; Ramelow, S.; Zeilinger, A. Quantum Entanglement of High Angular Momenta. *Science* **2012**, *338*, 640–643. [CrossRef] [PubMed]
137. Fickler, R.; Campbell, G.; Buchlerd, B.; Lamd, P.K.; Zeilinger, A. Quantum entanglement of angular momentum states with quantum numbers up to 10,010. *Proc. Natl. Acad. Sci. USA* **2016**, *113*, 13642–13647. [CrossRef]
138. Stav, T.; Faerman, A.; Maguid, E.; Oren, D.; Kleiner, V.; Hasman, E.; Segev, M. Quantum entanglement of the spin and orbital angular momentum of photons using metamaterials. *Science* **2018**, *361*, 1101–1104. [CrossRef]
139. Nagali, E.; Sciarrino, F. Generation of hybrid polarization-orbital angular momentum entangled states. *Opt. Express* **2010**, *18*, 18243. [CrossRef]
140. Shen, Y.; Rosales-Guzmán, C. Nonseparable states of light: From quantum to classical. *Laser Photonics Rev.* **2022**, *16*, 2100533. [CrossRef]
141. Graffitti, F.; D'Ambrosio, V.; Proietti, M.; Ho, J.; Piccirillo, B.; de Lisio, C.; Marrucci, L.; Fedrizzi, A. Hyperentanglement in structured quantum light. *Phys. Rev. Res.* **2020**, *2*, 043350. [CrossRef]
142. Chen, J.; Qi, G.z.; Wu, Y.; Shi, Y.; Zhao, C.l.; Jin, S.z. Partially coherent twisted vector vortex beam enabling manipulation of high-dimensional classical entanglement. *Opt. Express* **2023**, *31*, 38305. [CrossRef] [PubMed]
143. Wang, J.; Tie, X.; Tan, Z.; Wang, X.; Lei, S.; Wu, P. Recognizing OAM Modes of Electromagnetic Laguerre-Gaussian Schell-Model Vortex Beams in Atmospheric Turbulence from Polarization. *Adv. Quantum Technol.* **2023**, *6*, 2300233. [CrossRef]
144. Hai, L.; Zhang, Z.; Liu, S.; Li, L.; Zhou, Z.; Wang, Q.; Gao, Y.; Gao, C.; Shen, Y.; Fu, S. Intra-Cavity Laser Manipulation of High-Dimensional Non-Separable States. *Laser Photonics Rev.* **2024**, *18*, 2300593. [CrossRef]
145. Kopf, L.; Barros, R.; Fickler, R. Correlating Space, Wavelength, and Polarization of Light: Spatiospectral Vector Beams. *ACS Photonics* **2024**, *11*, 241–246. [CrossRef]
146. Malik, M.; Erhard, M.; Huber, M.; Krenn, M.; Fickler, R.; Zeilinger, A. Multi-photon entanglement in high dimensions. *Nat. Photon.* **2016**, *10*, 248–252. [CrossRef]
147. Wang, X.L.; Luo, Y.H.; Huang, H.L.; Chen, M.C.; Su, Z.E.; Liu, C.; Chen, C.; Li, W.; Fang, Y.Q.; Jiang, X.; et al. 18-Qubit entanglement with six photons' three degrees of freedom. *Phys. Rev. Lett.* **2018**, *120*, 260502. [CrossRef] [PubMed]
148. Krenn, M.; Huber, M.; Fickler, R.; Lapkiewicz, R.; Ramelowa, S.; Zeilinger, A. Generation and confirmation of a (100 × 100)-dimensional entangled quantum system. *Proc. Natl. Acad. Sci. USA* **2014**, *111*, 6243–6247. [CrossRef] [PubMed]
149. Forbes, A.; Nape, I. Quantum mechanics with patterns of light: Progress in high dimensional and multidimensional entanglement with structured light. *AVS Quantum Sci.* **2019**, *1*, 011701. [CrossRef]
150. Gao, X.; Zhang, Y.; D'Errico, A.; Sit, A.; Heshami, K.; Karimi, E. Full Spatial Characterization of Entangled Structured Photons. *Phys. Rev. Lett.* **2024**, *132*, 063802. [CrossRef] [PubMed]
151. Peters, C.; Ornelas, P.; Nape, I.; Forbes, A. Spatially resolving classical and quantum entanglement with structured photons. *Phys. Rev. A* **2023**, *108*, 053502. [CrossRef]
152. Ye, Y.H.; Zeng, L.; Dong, M.X.; Zhang, W.H.; Li, E.Z.; Li, D.C.; Guo, G.C.; Ding, D.S.; Shi, B.S. Long-lived memory for orbital angular momentum quantum states. *Phys. Rev. Lett.* **2022**, *129*, 193601. [CrossRef]
153. Zhou, Z.Q.; Hua, Y.L.; Liu, X.; Chen, G.; Xu, J.S.; Han, Y.J.; Li, C.F.; Guo, G.C. Quantum storage of three-dimensional orbital-angular-momentum entanglement in a crystal. *Phys. Rev. Lett.* **2015**, *115*, 070502. [CrossRef]
154. Fickler, R.; Lapkiewicz, R.; Huber, M.; Lavery, M.P.J.; Padgett, M.J.; Zeilinger, A. Interface between path and orbital angular momentum entanglement for high-dimensional photonic quantum information. *Nat. Commun.* **2014**, *5*, 4502. [CrossRef]
155. Huang, Y.; Li, Y.; Qi, Z.; Feng, J.; Zheng, Y.; Chen, X. A two-way photonic quantum entanglement transfer interface. *Npj Quantum Inf.* **2022**, *8*, 8. [CrossRef]
156. Cozzolino, D.; Bacco, D.; Da Lio, B.; Ingerslev, K.; Ding, Y.; Dalgaard, K.; Kristensen, P.; Galili, M.; Rottwitt, K.; Ramachandran, S.; et al. Orbital angular momentum states enabling fiber-based high-dimensional quantum communication. *Phys. Rev. Appl.* **2019**, *11*, 064058. [CrossRef]
157. Qiu, X.; Zhang, D.; Zhang, W.; Chen, L. Structured-pump-enabled quantum pattern recognition. *Phys. Rev. Lett.* **2019**, *122*, 123901. [CrossRef]
158. Uribe-Patarroyo, N.; Fraine, A.; Simon, D.S.; Minaeva, O.; Sergienko, A.V. Object identification using correlated orbital angular momentum states. *Phys. Rev. Lett.* **2013**, *110*, 043601. [CrossRef]
159. Franke-Arnold, S. Optical angular momentum and atoms. *Philos. Trans. R. Soc. A* **2017**, *375*, 20150435. [CrossRef]
160. Barnett, S.M.; Speirits, F.C.; Babiker, M. Optical angular momentum in atomic transitions: A paradox. *J. Phys. A Math. Theor.* **2022**, *55*, 234008. [CrossRef]
161. Schmiegelow, C.T.; Schulz, J.; Kaufmann, H.; Ruster, T.; Poschinger, U.G.; Schmidt-Kaler, F. Transfer of optical orbital angular momentum to a bound electron. *Nat. Commun.* **2016**, *7*, 12998. [CrossRef]
162. Picón, A.; Benseny, A.; Mompart, J.; Vázquez de Aldana, J.R.; Plaja, L.; Calvo, G.F.; Roso, L. Transferring orbital and spin angular momenta of light to atoms. *New J. Phys.* **2010**, *12*, 083053. [CrossRef]
163. Barnett, S.M.; Berry, M.V. Superweak momentum transfer near optical vortices. *J. Opt.* **2013**, *15*, 125701. [CrossRef]
164. Afanasev, A.; Carlson, C.E.; Mukherjee, A. Superkicks and the photon angular and linear momentum density. *Phys. Rev. A* **2022**, *105*, L061503. [CrossRef]
165. Sola, I.R.; Malinovsky, V.S.; Ahn, J.; Shin, S.; Chang, B.Y. Two-qubit atomic gates: Spatio-temporal control of Rydberg interaction. *Nanoscale* **2023**, *15*, 4325. [CrossRef]

166. Ishihara, J.; Mori, T.; Suzuki, T.; Sato, S.; Morita, K.; Kohda, M.; Ohno, Y.; Miyajima, K. Imprinting spatial helicity structure of vector vortex beam on spin texture in semiconductors. *Phys. Rev. Lett.* **2023**, *130*, 126701. [CrossRef]
167. Andersen, M.F.; Ryu, C.; Cladé, P.; Natarajan, V.; Vaziri, A.; Helmerson, K.; Phillips, W.D. Quantized Rotation of Atoms from Photons with Orbital Angular Momentum. *Phys. Rev. Lett.* **2006**, *97*, 170406. [CrossRef]
168. Wright, K.C.; Leslie, L.S.; Bigelow, N.P. Optical control of the internal and external angular momentum of a Bose-Einstein condensate. *Phys. Rev. A* **2008**, *77*, 041601(R). [CrossRef]
169. Trawi, F.; Billard, F.; Faucher, O.; Béjot, P.; Hertz, E. Molecular Quantum Interface for Storing and Manipulating Ultrashort Optical Vortex. *Laser Photonics Rev.* **2023**, *17*, 2200525. [CrossRef]
170. Verde, M.; Schmiegelow, C.T.; Poschinger, U.; Schmidt-Kaler, F. Trapped atoms in spatially-structured vector light fields. *Sci. Rep.* **2023**, *13*, 21283. [CrossRef]
171. Chen, Y.; Zhou, Y.; Li, M.; Liu, K.; Ciappina, M.F.; Lu, P. Atomic photoionization by spatiotemporal optical vortex pulses. *Phys. Rev. A* **2023**, *107*, 033112. [CrossRef]
172. Berry, M.V.; Dennis, M.R. Quantum cores of optical phase singularities. *J. Opt. A Pure Appl. Opt.* **2004**, *6*, S178–S180. [CrossRef]
173. Barnett, S.M. On the quantum core of an optical vortex. *J. Mod. Opt.* **2014**, *55*, 2279–2292. [CrossRef]
174. Simpson, N.B.; Dholakia, K.; Allen, L.; Padgett, M.J. Mechanical equivalence of spin and orbital angular momentum of light: An optical spanner. *Opt. Lett.* **1997**, *22*, 52–54. [CrossRef] [PubMed]
175. Friese, M.E.J.; Enger, J.; Rubinsztein-Dunlop, H.; Heckenberg, N.R. Optical angular-momentum transfer to trapped absorbing particles. *Phys. Rev. A* **1996**, *54*, 1593–1596. [CrossRef]
176. O'Neil, A.T.; MacVicar, I.; Allen, L.; J, P.M. Intrinsic and Extrinsic Nature of the Orbital Angular Momentum of a Light Beam. *Phys. Rev. Lett.* **2002**, *88*, 053601. [CrossRef] [PubMed]
177. Curtis, J.; Grier, D. Structure of optical vortices. *Phys. Rev. Lett.* **2003**, *90*, 133901. [CrossRef] [PubMed]
178. Garcés-Chávez, V.; McGloin, D.; Padgett, M.J.; Dultz, W.; Schmitzer, H.; Dholakia, K. Observation of the Transfer of the Local Angular Momentum Density of a Multiringed Light Beam to an Optically Trapped Particle. *Phys. Rev. Lett.* **2003**, *91*, 103601. [CrossRef]
179. Li, M.; Yan, S.; Yao, B.; Liang, Y.; Zhang, P. Spinning and orbiting motion of particles in vortex beams with circular or radial polarizations. *Opt. Express* **2016**, *24*, 20604–20612. [CrossRef]
180. Babiker, M.; Andrews, D.L.; Lembessis, V.E. Atoms in complex twisted light. *J. Opt.* **2019**, *21*, 013001. [CrossRef]
181. Ng, J.; Lin, Z.; Chan, C.T. Theory of Optical Trapping by an Optical Vortex Beam. *Phys. Rev. Lett.* **2010**, *104*, 103601. [CrossRef] [PubMed]
182. Yang, Y.; Ren, Y.X.; Chen, M.; Arita, Y.; Rosales-Guzmán, C. Optical trapping with structured light: A review. *Adv. Photonics* **2021**, *3*, 034001. [CrossRef]
183. Li, M.; Yan, S.; Zhang, Y.; Zhou, Y.; Yao, B. Orbital angular momentum in optical manipulations. *J. Opt.* **2022**, *24*, 114001. [CrossRef]
184. Padgett, M.; Bowman, R. Tweezers with a twist. *Nat. Photonics* **2011**, *5*, 243–248. [CrossRef]
185. Stickler, B.A.; Hornberger, K.; Kim, M.S. Quantum rotations of nanoparticles. *Nat. Rev.* **2021**, *3*, 589–597. [CrossRef]
186. Stickler, B.A.; Papendell, B.; Kuhn, S.; Schrinski, B.; Millen, J.; Arndt, M.; Hornberger, K. Probing macroscopic quantum superpositions with nanorotors. *New J. Phys.* **2018**, *20*, 122001. [CrossRef]
187. Zhao, R.; Manjavacas, A.; García de Abajo, F.J.; Pendry, J.B. Rotational Quantum Friction. *Phys. Rev. Lett.* **2012**, *109*, 123604. [CrossRef]
188. Wood, A.A.; Hollenberg, L.C.L.; Scholten, R.E.; Martin, A.M. Observation of a Quantum Phase from Classical Rotation of a Single Spin. *Phys. Rev. Lett.* **2020**, *124*, 020401. [CrossRef] [PubMed]
189. Hu, Y.; Kingsley-Smith, J.J.; Nikkhou1, M.; Sabin, J.A.; Rodríguez-Fortuño, F.J.; Xu, X.; Millen, J. Structured transverse orbital angular momentum probed by a levitated optomechanical sensor. *Nat. Commun.* **2023**, *14*, 2638. [CrossRef]
190. Li, C.; Jang, J.; Badloe, T.; Yang, T.; Kim, J.; Kim, J.; Nguyen, M.; Maier, S.A.; Rho, J.; Ren, H.; et al. Arbitrarily structured quantum emission with a multifunctional metalens. *eLight* **2023**, *3*, 19. [CrossRef]
191. Liang, H.; Ahmed, H.; Tam, W.Y.; Chen, X.; Li, J. Continuous heralding control of vortex beams using quantum metasurface. *Commun. Phys.* **2023**, *6*, 140. [CrossRef]
192. Liu, X.; Kan, Y.; Kumar, S.; Kulikova, L.F.; Davydov, V.A.; Agafonov, V.N.; Zhao, C.; Bozhevolnyi, S.I. Ultracompact Single-Photon Sources of Linearly Polarized Vortex Beams. *Adv. Mater.* **2024**, *36*, 2304495. [CrossRef]
193. Li, Z.; Guo, H.; Liu, H.; Li, J.; Sun, H.; Yang, R.; Liu, K.; Gao, J. Higher-order spatially squeezed beam for enhanced spatial measurements. *Adv. Quantum Technol.* **2022**, *5*, 2200055. [CrossRef]
194. Heinze, J.; Willke, B.; Vahlbruch, H. Observation of squeezed states of light in higher-order Hermite-Gaussian modes with a quantum noise reduction of up to 10 dB. *Phys. Rev. Lett.* **2022**, *128*, 083606. [CrossRef]
195. Goldberg, A.Z.; de la Hoz, P.; Björk, G.; Klimov, A.B.; Grassl, M.; Leuchs, G.; Sánchez-Soto, L.L. Quantum concepts in optical polarization. *Adv. Opt. Photonics* **2021**, *13*, 1–73. [CrossRef]
196. Yang, L.P.; Jacob, Z. Non-classical photonic spin texture of quantum structured light. *Commun. Phys.* **2021**, *4*, 221. [CrossRef]
197. Andrews, D.L. Symmetry and quantum features in optical vortices. *Symmetry* **2021**, *13*, 1368. [CrossRef]
198. Williams, M.D.; Bradshaw, D.S.; Andrews, D.L. Quantum issues with structured light. *Proc. SPIE* **2016**, *9764*, 976407. [CrossRef]

199. Smith, B.J.; Raymer, M.G. Photon wave functions, wave-packet quantization of light, and coherence theory. *New J. Phys.* **2007**, *9*, 414. [CrossRef]
200. Bialynicki-Birula, I.; Bialynicka-Birula, Z. Quantum numbers and spectra of structured light. *Phys. Scr.* **2018**, *93*, 104005. [CrossRef]
201. Bialynicki-Birula, I. Helicity amplitudes, polarization of EM waves and Stokes parameters: Classical versus quantum theory. *J. Opt.* **2019**, *21*, 094002. [CrossRef]
202. Nienhuis, G. Analogies between optical and quantum mechanical angular momentum. *Philos. Trans. R. Soc. A* **2017**, *375*, 20150443. [CrossRef]
203. Sugic, D.; Droop, R.; Otte, E.; Ehrmanntraut, D.; Nori, F.; Ruostekoski, J.; Denz, C.; Dennis, M.R. Particle-like topologies in light. *Nat. Commun.* **2021**, *12*, 6785. [CrossRef] [PubMed]
204. Shen, Y.; Zhang, Q.; Shi, P.; Du, L.; Yuan, X.; Zayats, A.V. Optical skyrmions and other topological quasiparticles of light. *Nat. Photon.* **2024**, *18*, 15–25. [CrossRef]
205. Tamburini, F.; Thidé, B.; Licata, I.; Bouchard, F.; Karimi, E. Majorana bosonic quasiparticles from twisted photons in free space. *Phys. Rev. A* **2021**, *103*, 033505. [CrossRef]
206. Li, Z.X.; Ruan, Y.P.; Tang, J.; Liu, Y.; Liu, J.J.; Tang, J.S.; Zhang, H.; Xia, K.Y.; Lu, Y.Q. Self-healing of a heralded single-photon Airy beam. *Opt. Express* **2021**, *29*, 40187. [CrossRef]
207. Nape, I.; Otte, E.; Vallés, A.; Rosales-Guzmán, C.; Cardano, F.; Denz, C.; Forbes, A. Self-healing high-dimensional quantum key distribution using hybrid spin-orbit Bessel states. *Opt. Express* **2018**, *26*, 26946. [CrossRef]
208. McLaren, M.; Mhlanga, T.; Padgett, M.J.; Roux, F.S.; Forbes, A. Self-healing of quantum entanglement after an obstruction. *Nat. Commun.* **2014**, *5*, 3248. [CrossRef]
209. Yang, D.; Yu, Z.; Wang, W.; Hu, Z.D.; Zhu, Y. Underwater entanglement propagation of auto-focusing Airy beams. *Opt. Express* **2024**, *32*, 4887. [CrossRef]
210. Giovannini, D.; Romero, J.; Potoček, V.; Ferenczi, G.; Speirits, F.; Barnett, S.M.; Faccio, D.; Padgett, M.J. Spatially structured photons that travel in free space slower than the speed of light. *Science* **2015**, *347*, 857–860. [CrossRef]
211. Petrov, N.I. Speed of structured light pulses in free space. *Sci. Rep.* **2019**, *9*, 18332. [CrossRef]
212. Silenko, A.J.; Zhang, P.; Zou, L. Relativistic quantum-mechanical description of twisted paraxial electron and photon beams. *Phys. Rev. A* **2019**, *100*, 030101(R). [CrossRef]
213. Shen, Y.; Nape, I.; Yang, X.; Fu, X.; Gong, M.; Naidoo, D.; Forbes, A. Creation and control of high-dimensional multi-partite classically entangled light. *Light Sci. Appl.* **2021**, *10*, 50. [CrossRef] [PubMed]
214. Wan, Z.; Wang, Z.; Yang, X.; Shen, Y.; Fu, X. Digitally tailoring arbitrary structured light of generalized ray-wave duality. *Opt. Express* **2020**, *28*, 31043. [CrossRef] [PubMed]
215. Shen, Y.; Zdagkas, A.; Papasimakis, N.; Zheludev, N.I. Measures of space-time nonseparability of electromagnetic pulses. *Phys. Rev. Res.* **2021**, *3*, 013236. [CrossRef]
216. Gomes, R.M.; Salles, A.; Toscano, F.; Souto Ribeiro, P.H.; Walborn, S.P. Observation of a nonlocal optical vortex. *Phys. Rev. Lett.* **2009**, *103*, 033602. [CrossRef]
217. Qi, W.R.; Liu, R.; Kong, L.J.; Wang, Z.X.; Huang, S.Y.; Tu, C.; Li, Y.; Wang, H.T. Double-slit interference of single twisted photons. *Chin. Opt. Lett.* **2020**, *18*, 102601. [CrossRef]
218. Aili, M.; Liu, P.; Chen, X.X.; Wu, Q.Y.; Meng, Z.; Yang, J.Z.; Li, J.; Zhang, A.N. Double-slit experiment with multiple vortex beams. *Phys. Rev. A* **2024**, *109*, 013521. [CrossRef]
219. Franke-Arnold, S.; Barnett, S.M.; Yao, E.; Leach, J.; Courtial, J.; Padgett, M. Uncertainty principle for angular position and angular momentum. *New J. Phys.* **2004**, *6*, 103. [CrossRef]
220. Gounden, N.; Epstein, J.; Ornelas, P.; Beck, G.; Nape, I.; Forbes, A. Popper's conjecture with angular slits and twisted light. *Sci. Rep.* **2023**, *13*, 21701. [CrossRef]
221. Nape, I.; Ndagano, B.; Forbes, A. Erasing the orbital angular momentum information of a photon. *Phys. Rev. A* **2017**, *95*, 053859. [CrossRef]
222. Zhang, Y.; Agnew, M.; Roger, T.; Roux, F.S.; Konrad, T.; Faccio, D.; Leach, J.; Forbes, A. Simultaneous entanglement swapping of multiple orbital angular momentum states of light. *Nat. Commun.* **2017**, *8*, 632. [CrossRef]
223. Liu, S.; Lou, Y.; Jing, J. Orbital angular momentum multiplexed deterministic all-optical quantum teleportation. *Nat. Commun.* **2020**, *11*, 3875. [CrossRef]
224. Wang, X.L.; Cai, X.D.; Su, Z.E.; Chen, M.C.; Wu, D.; Li, L.; Liu, N.L.; Lu, C.Y.; Pan, J.W. Quantum teleportation of multiple degrees of freedom of a single photon. *Nature* **2015**, *518*, 516–519. [CrossRef] [PubMed]
225. Zhang, Y.; Roux, F.S.; Konrad, T.; Agnew, M.; Leach, J.; Forbes, A. Engineering two-photon high-dimensional states through quantum interference. *Sci. Adv.* **2016**, *2*, e1501165. [CrossRef]
226. Kevin, S.; Sahrai, M.; Asadpour, S.H. Controllable Hartman effect by vortex beam in a one dimensional photonic crystal doped by graphene quantum dots. *Sci. Rep.* **2023**, *13*, 2992. [CrossRef]
227. Leach, J.; Jack, B.; Romero, J.; Ritsch-Marte, M.; Boyd, R.W.; Jha, A.K.; Barnett, S.M.; Franke-Arnold, S.; Padgett, M.J. Violation of a Bell inequality in two-dimensional orbital angular momentum state-spaces. *Opt. Express* **2009**, *17*, 8287–8293. [CrossRef]
228. Romero, J.; Leach, J.; Jack, B.; Barnett, S.M.; Padgett, M.J.; Franke-Arnold, S. Violation of Leggett inequalities in orbital angular momentum subspaces. *New J. Phys.* **2010**, *12*, 123007. [CrossRef]

229. Dada, A.; Leach, J.; Buller, G.S.; Padgett, M.J.; Andersson, E. Experimental high-dimensional two-photon entanglement and violations of generalized Bell inequalities. *Nat. Phys.* **2011**, *7*, 677–680. [CrossRef]
230. Tang, Y.; Perrie, W.; Schille, J.; Loeschner, U.; Li, Q.; Liu, D.; Edwardson, S.P.; Forbes, A.; Dearden, G. High-quality vector vortex arrays by holographic and geometric phase control. *J. Phys. D Appl. Phys.* **2020**, *53*, 465101. [CrossRef]
231. Qi, W.R.; Zhou, J.; Kong, L.J.; Xu, Z.P.; Meng, H.X.; Liu, R.; Wang, Z.X.; Tu, C.; Li, Y.L.; Cabello, A.; et al. Stronger Hardy-like proof of quantum contextuality. *Photonics Res.* **2022**, *10*, 1582–1593. [CrossRef]
232. Karimi, E.; Leach, J.; Slussarenko, S.; Piccirillo, B.; Marrucci, L.; Chen, L.; She, W.; Franke-Arnold, S.; Padgett, M.J.; Santamato, E. Spin-orbit hybrid entanglement of photons and quantum contextuality. *Phys. Rev. A* **2010**, *82*, 022115. [CrossRef]
233. Xu, J.M.; Zhen, Y.Z.; Yang, Y.X.; Cheng, Z.M.; Ren, Z.C.; Chen, K.; Wang, X.L.; Wang, H.T. Experimental Demonstration of Quantum Pseudotelepathy. *Phys. Rev. Lett.* **2022**, *129*, 050402. [CrossRef]
234. Leach, J.; Jack, B.; Romero, J.; Jha, A.K.; Yao, A.M.; Franke-Arnold, S.; Ireland, D.G.; Boyd, R.W.; Barnett, S.M.; Padgett, M.J. Quantum correlations in optical angle-orbital angular momentum variables. *Science* **2010**, *329*, 662–665. [CrossRef] [PubMed]
235. Slussarenko, S.; Joch, D.J.; Tischler, N.; Ghafari, F.; Shalm, L.K.; Verma, V.B.; Nam, S.W.; Pryde, G.J. Quantum steering with vector vortex photon states with the detection loophole closed. *Npj Quantum Inf.* **2022**, *8*, 20. [CrossRef]
236. Stoklasa, B.; Motka, L.; Rehacek, J.; Hradil, Z.; Sánchez-Soto, L.L.; Agarwal, G.S. Experimental violation of a Bell-like inequality with optical vortex beams. *New J. Phys.* **2015**, *17*, 113046. [CrossRef]
237. González-Domínguez, M.A.; Piceno-Martínez, A.E.; Rosales-Zárate, L.E.C. Nonlocality and quantum correlations in Ince–Gauss structured light modes. *J. Opt. Soc. Am. B* **2023**, *40*, 881. [CrossRef]
238. Prevedel, R.; Cronenberg, G.; Tame, M.S.; Paternostro, M.; Walther, P.; Kim, M.S.; Zeilinger, A. Experimental realization of Dicke states of up to six qubits for multiparty quantum networking. *Phys. Rev. Lett.* **2009**, *103*, 020503. [CrossRef]
239. Erhard, M.; Malik, M.; Krenn, M.; Zeilinger, A. Experimental Greenberger-Horne-Zeilinger entanglement beyond qubits. *Nat. Photon* **2018**, *12*, 759–764. [CrossRef]
240. Wang, F.; Erhard, M.; Babazadeh, A.; Malik, M.; Krenn, M.; Zeilinger, A. Generation of the complete four-dimensional Bell basis. *Optica* **2017**, *4*, 1462. [CrossRef]
241. Kong, L.J.; Li, Y.; Liu, R.; Qi, W.R.; Wang, Q.; Wang, Z.X.; Huang, S.Y.; Si, Y.; Tu, C.; Hu, W.; et al. Complete measurement and multiplexing of orbital angular momentum Bell states. *Phys. Rev. A* **2019**, *100*, 023822. [CrossRef]
242. Wang, Y.; Ru, S.; Wang, F.; Zhang, P.; Li, F. Experimental demonstration of efficient high-dimensional quantum gates with orbital angular momentum. *Quantum Sci. Technol.* **2022**, *7*, 015016. [CrossRef]
243. Babazadeh, A.; Erhard, M.; Wang, F.; Malik, M.; Nouroozi, R.; Krenn, M.; Zeilinger, A. High-dimensional single-photon quantum gates: Concepts and experiments. *Phys. Rev. Lett.* **2017**, *119*, 180510. [CrossRef] [PubMed]
244. Vashukevich, E.A.; Bashmakova, E.N.; Golubeva, T.Y.; Golubev, Y.M. High-fidelity quantum gates for OAM single qudits on quantum memory. *Laser Phys. Lett.* **2022**, *19*, 025202. [CrossRef]
245. Bashmakova, E.N.; Vashukevich, E.A.; Golubeva, T.Y. Parallel multi-two-qubit swap gate via quantum nondemolition interaction of orbital-angular-momentum light and an atomic ensemble. *Phys. Rev. A* **2024**, *109*, 012428. [CrossRef]
246. Nape, I.; Sephton, B.; Ornelas, P.; Moodley, C.; Forbes, A. Quantum structured light in high dimensions. *APL Photonics* **2023**, *8*, 051101. [CrossRef]
247. Eriksson, M.; Goldberg, A.; Hiekkamäki, M.; Bouchard, F.; Rehacek, J.; Hradil, Z.; Leuchs, G.; Fickler, R.; Sánchez-Soto, L. Sensing Rotations with Multiplane Light Conversion. *Phys. Rev. Appl.* **2023**, *20*, 024052. [CrossRef]
248. Jayaseelan, M.; Murphree, J.D.; Schultz, J.T.; Ruostekoski, J.; Bigelow, N.P. Topological atom optics and beyond with knotted quantum wavefunctions. *Commun Phys* **2024**, *7*, 7. [CrossRef]
249. Aharonov, Y.; Albert, D.Z.; Vaidman, L. How the result of a measurement of a component of the spin of a spin-1/2 particle can turn out to be 100. *Phys. Rev. Lett.* **1988**, *60*, 1351–1354. [CrossRef]
250. Dressel, J.; Malik, M.; Miatto, F.M.; Jordan, A.N.; Boyd, R.W. Colloquium: Understanding quantum weak values: Basics and applications. *Rev. Mod. Phys.* **2013**, *86*, 307–316. [CrossRef]
251. Forbes, A. Structured light from lasers. *Laser Photonics Rev.* **2019**, *13*, 1900140. [CrossRef]
252. Resch, K.J.; Lundeen, J.S.; Steinberg, A.M. Experimental realization of the quantum box problem. *Phys. Lett.* **2004**, *324*, 125–131. [CrossRef]
253. Ashby, J.M.; Schwarz, P.D.; Schlosshauer, M. Observation of the quantum paradox of separation of a single photon from one of its properties. *Phys. Rev. A* **2016**, *94*, 012102. [CrossRef]
254. Kumar Pan, A. Disembodiment of arbitrary number of properties in quantum Cheshire cat experiment. *Eur. Phys. J. D* **2020**, *74*, 151. [CrossRef]
255. Kocsis, S.; Braverman, B.; Ravets, S.; Stevens, M.J.; Mirin, R.P.; Shalm, L.K.; Steinberg, A.M. Observing the average trajectories of single photons in a two-slit interferometer. *Science* **2011**, *332*, 1170–1173. [CrossRef]
256. Bliokh, K.Y.; Bekshaev, A.Y.; Kofman, A.G.; Nori, F. Photon trajectories, anomalous velocities and weak measurements: A classical interpretation. *New J. Phys.* **2013**, *15*, 073022. [CrossRef]
257. Li, Y.; Ren, Z.C.; Kong, L.J.; Tu, C.; Wang, H.T. Trajectory-based unveiling of the angular momentum of photons. *Phys. Rev. A* **2017**, *95*, 043830. [CrossRef]
258. Berry, M.V. Optical currents. *J. Opt. A: Pure Appl. Opt.* **2009**, *11*, 094001. [CrossRef]

259. Berry, M.V. Quantum backflow, negative kinetic energy, and optical retro-propagation. *J. Phys. A Math. Theor.* **2010**, *43*, 415302. [CrossRef]
260. Ghosh, B.; Daniel, A.; Gorzkowski, B.; Lapkiewicz, R. Azimuthal backflow in light carrying orbital angular momentum. *Optica* **2023**, *10*, 1217. [CrossRef]
261. Lundeen, J.S.; Sutherland, B.; Patel, A.; Stewart, C.; Bamber, C. Direct measurement of the quantum wavefunction. *Nature* **2011**, *474*, 188–191. [CrossRef] [PubMed]
262. Malik, M.; Mirhosseini, M.; Lavery, M.P.J.; Leach, J.; Padgett, M.J.; Boyd, R.W. Direct measurement of a 27-dimensional orbital-angular-momentum state vector. *Nat. Commun.* **2014**, *5*, 3115. [CrossRef]
263. Shi, Z.; Mirhosseini, M.; Margiewicz, J.; Malik, M.; Rivera, F.; Zhu, Z.; Boyd, R.W. Scan-free direct measurement of an extremely high-dimensional photonic state. *Optica* **2015**, *2*, 388–392. [CrossRef]
264. Mirhosseini, M.; Lundeen, J.S.; Boyd, R.W. Direct measurement of the photon's spatial wave function. In *Quantum Photonics: Pioneering Advances and Emerging Applications*; Springer Nature Switzerland AG: Cham, Switzerland, 2019; pp. 25–49. [CrossRef]
265. Zhang, C.R.; Hu, M.J.; Hou, Z.B.; Tang, J.F.; Zhu, J.; Xiang, G.Y.; Li, C.F.; Guo, G.C.; Zhang, Y.S. Direct measurement of the two-dimensional spatial quantum wave function via strong measurements. *Phys. Rev. A* **2020**, *101*, 012119. [CrossRef]
266. Zhang, C.R.; Hu, M.J.; Xiang, G.Y.; Zhang, Y.S.; Li, C.F.; Guo, G.C. Direct strong measurement of a high-dimensional quantum state. *Chin. Phys. Lett.* **2020**, *37*, 080301. [CrossRef]
267. Yang, M.; Xiao, Y.; Liao, Y.W.; Liu, Z.H.; Xu, X.Y.; Xu, J.S.; Li, C.F.; Guo, G.C. Zonal reconstruction of photonic wavefunction via momentum weak measurement. *Laser Photonics Rev.* **2020**, *14*, 1900251. [CrossRef]
268. de Lima Bernardo, B.; Azevedo, S.; Rosas, A. Simplified algebraic description of weak measurements with Hermite-Gaussian and Laguerre-Gaussian pointer states. *Opt. Commun.* **2014**, *331*, 194–197. [CrossRef]
269. Turek, Y.; Kobayashi, H.; Akutsu, T.; Sun, C.P.; Shikano, Y. Post-selected von Neumann measurement with Hermite-Gaussian and Laguerre-Gaussian pointer states. *New J. Phys.* **2015**, *17*, 083029. [CrossRef]
270. Kobayashi, H.; Nonaka, K.; Shikano, Y. Stereographical visualization of a polarization state using weak measurements with an optical-vortex beam. *Phys. Rev. A* **2014**, *89*, 053816. [CrossRef]
271. Tukiainen, M.; Kobayashi, H.; Shikano, Y. Quantification of concurrence via weak measurement. *Phys. Rev. A* **2017**, *95*, 052301. [CrossRef]
272. Xia, B.; Huang, J.; Li, H.; Liu, M.; Xiao, T.; Chen, F.; Zeng, G. Ultrasensitive measurement of angular rotations via a Hermite-Gaussian pointer. *Photonics Res.* **2022**, *10*, 2816–2827. [CrossRef]
273. Xia, B.; Huang, J.; Fang, C.; Li, H.; Zeng, G. High-precision multiparameter weak measurement with Hermite-Gaussian pointer. *Phys. Rev. Appl.* **2020**, *13*, 034023. [CrossRef]
274. Magaña-Loaiza, O.S.; Mirhosseini, M.; Rodenburg, B.; Boyd, R.W. Amplification of angular rotations using weak measurements. *Phys. Rev. Lett.* **2014**, *112*, 200401. [CrossRef]
275. Resch, K.J.; Steinberg, A.M. Extracting joint weak values with local, single-particle measurements. *Phys. Rev. Lett.* **2004**, *92*, 130402. [CrossRef]
276. Kobayashi, H.; Puentes, G.; Shikano, Y. Extracting joint weak values from two-dimensional spatial displacements. *Phys. Rev. A* **2012**, *86*, 053805. [CrossRef]
277. Zhu, W.; Zhang, S.; Liang, X.; Zheng, H.; Zhong, Y.; Yu, J.; Chen, Z.; Zhang, L. Joint spatial weak measurement with higher-order Laguerre-Gaussian point states. *Opt. Express* **2022**, *30*, 17848–17857. [CrossRef]
278. Puentes, G.; Hermosa, N.; Torres, J.P. Weak measurements with orbital-angular-momentum pointer states. *Phys. Rev. Lett.* **2012**, *109*, 040401. [CrossRef]
279. Qiu, J.; Ren, C.; Zhang, Z. Precisely measuring the orbital angular momentum of beams via weak measurement. *Phys. Rev. A* **2016**, *93*, 063841. [CrossRef]
280. Zhu, J.; Zhang, P.; Li, Q.; Wang, F.; Wang, C.; Zhou, Y.; Wang, J.; Gao, H.; Kwek, L.C.; Li, F. Measuring the topological charge of orbital angular momentum beams by utilizing weak measurement principle. *Sci. Rep.* **2019**, *9*, 7993. [CrossRef] [PubMed]
281. Cormann, M.; Caudano, Y. Geometric description of modular and weak values in discrete quantum systems using the Majorana representation. *J. Phys. A Math. Theor.* **2017**, *50*, 305302. [CrossRef]
282. Ballesteros Ferraz, L.; Lambert, D.L.; Caudano, Y. Geometrical interpretation of the argument of weak values of general observables in N-level quantum systems. *Quantum Sci. Technol.* **2022**, *7*, 045028. [CrossRef]
283. Cormann, M.; Remy, M.; Kolaric, B.; Caudano, Y. Revealing geometric phases in modular and weak values with a quantum eraser. *Phys. Rev. A* **2016**, *93*, 042124. [CrossRef]
284. Wang, B.; Li, P.; Chen, T.; Zhang, X. Accurately identifying mode indices of Laguerre-Gaussian beams via weak measurements. *J. Opt.* **2017**, *19*, 055603. [CrossRef]
285. Zhu, J.; Zhang, P.; Wang, F.; Wang, Y.; Li, Q.; Liu, R.; Wang, J.; Gao, H.; Li, F. Experimentally measuring the mode indices of Laguerre-Gaussian beams by weak measurement. *Opt. Express* **2021**, *29*, 5419–5426. [CrossRef]
286. Wang, A.; Zhu, J.; Luo, L.; Liu, X.; Ye, L.; Zhang, Z.; Du, J. Optical differentiation based on weak measurements. *Opt. Lett.* **2022**, *47*, 3880. [CrossRef]
287. Fang, L.; Luo, L.; Zhao, R.; Liu, B. Measuring the Orbital Angular Momentum of Light Based on Optical Differentiation. *IEEE Photonics J.* **2023**, *15*, 1–7. [CrossRef]
288. Bliokh, Y.K.; Aiello, A. Goos-Hänchen and Imbert-Fedorov beam shifts: An overview. *J. Opt.* **2013**, *15*, 014001. [CrossRef]

289. Hosten, O.; Kwiat, P. Observation of the spin Hall effect of light via weak measurements. *Science* **2008**, *319*, 787–790. [CrossRef]
290. Jayaswal, G.; Mistura, G.; Merano, M. Weak measurement of the Goos–Hänchen shift. *Opt. Lett.* **2013**, *38*, 1232–1234. [CrossRef]
291. Jayaswal, G.; Mistura, G.; Merano, M. Observing angular deviations in light-beam reflection via weak measurements. *Opt. Lett.* **2014**, *39*, 6257–6260. [CrossRef]
292. Goswami, S.; Pal, M.; Nandi, A.; Panigrahi, P.K.; Ghosh, N. Simultaneous weak value amplification of angular Goos-Hänchen and Imbert-Fedorov shifts in partial reflection. *Opt. Lett.* **2014**, *39*, 6229–6232. [CrossRef]
293. Prajapati, C.; Viswanathan, N.K. Simultaneous weak measurement of angular and spatial Goos-Hänchen and Imbert-Fedorov shifts. *J. Opt.* **2017**, *19*, 105611. [CrossRef]
294. Dennis, M.R.; Götte, J.B. The analogy between optical beam shifts and quantum weak measurements. *New J. Phys.* **2012**, *14*, 073013. [CrossRef]
295. Dennis, M.R.; Götte, J.B. Beam shifts to reflected light beams and their axial structure. *Proc. SPIE* **2014**, *9441*, 94410M. [CrossRef]
296. Merano, M.; Hermosa, N.; Woerdman, J.P.; Aiello, A. How orbital angular momentum affects beam shifts in optical reflection. *Phys. Rev. A* **2010**, *82*, 023817. [CrossRef]
297. Zhang, X.; Wang, S.; Liu, J.; Wu, J.; Li, J. Spin-Hall Effect of Cylindrical Vector Vortex Beams. *Photonics* **2023**, *10*, 1356. [CrossRef]
298. Long, W.; Pan, J.; Guo, X.; Liu, X.; Lin, H.; Zheng, H.; Yu, J.; Guan, H.; Lu, H.; Zhong, Y.; et al. Optimized weak measurement of orbital angular momentum-induced beam shifts in optical reflection. *Photonics Res.* **2019**, *7*, 1273–1278. [CrossRef]
299. Mandal, S.; Das, A.; Pradhan, M. Weak measurement of the Goos–Hänchen shift for a Hermite–Gaussian laser beam. *J. Opt.* **2024**, *26*, 045403. [CrossRef]
300. Prajapati, C.; Viswanathan, N.K. Enhancement of weak spin-Hall shift using higher-order helical-wavefront beams. *OSA Contin.* **2018**, *1*, 872–881. [CrossRef]
301. Xie, S.; Zhu, J.; Wang, A.; Wang, Y.; Huang, Y.; Zhang, Z. Super amplification enabled by orbital angular momentum in weak measurement. *Opt. Express* **2024**, *32*, 11794. [CrossRef]
302. Töppel, F.; Ornigotti, M.; Aiello, A. Goos-Hänchen and Imbert-Fedorov shifts from a quantum-mechanical perspective. *New J. Phys.* **2013**, *15*, 113059. [CrossRef]
303. Shi, L.k.; Song, J.C.W. Shift vector as the geometric origin of beam shifts. *Phys. Rev. B* **2019**, *100*, 201405(R). [CrossRef]
304. Xu, L.; Liu, Z.; Datta, A.; Knee, G.C.; Lundeen, J.S.; Lu, Y.Q.; Zhang, L. Approaching quantum-limited metrology with imperfect detectors by using weak-value amplification. *Phys. Rev. Lett.* **2020**, *125*, 080501. [CrossRef]
305. Yin, X.; Hesselink, L. Goos-Hänchen shift surface plasmon resonance sensor. *Appl. Phys. Lett.* **2006**, *89*, 261108. [CrossRef]
306. Wang, X.; Yin, C.; Sun, J.; Li, H.; Wang, Y.; Ran, M.; Cao, Z. High-sensitivity temperature sensor using the ultrahigh order mode-enhanced Goos-Hänchen effect. *Opt. Express* **2013**, *11*, 13380. [CrossRef]
307. Xu, L.; Luo, L.; Wu, H.; Luo, Z.; Zhang, Z.; Shi, H.; Chang, T.; Wu, P.; Du, C.; Cui, H.L. Measurement of chiral molecular parameters based on a combination of surface plasmon resonance and weak value amplification. *ACS Sens.* **2020**, *5*, 2398–2407. [CrossRef] [PubMed]
308. Tang, T.; Shen, K.; Li, J.; Liang, X.; Tang, Y.; Li, C.; He, Y. Optimal weak measurement scheme for chiral molecular detection based on photonic spin Hall effect. *Opt. Express* **2023**, *31*, 40308. [CrossRef]
309. Wang, Y.; Yang, S.; Zhang, Q.; Chen, Y.; Hu, X.; Zhang, H.; Zhang, Z. Complete chiroptical signal detection using weak measurement with intensity-contrast-ratio pointers. *APL Photonics* **2023**, *8*, 126102. [CrossRef]

Disclaimer/Publisher's Note: The statements, opinions and data contained in all publications are solely those of the individual author(s) and contributor(s) and not of MDPI and/or the editor(s). MDPI and/or the editor(s) disclaim responsibility for any injury to people or property resulting from any ideas, methods, instructions or products referred to in the content.

IOP Publishing Bioinspir. Biomim. 20 (2025) 024001 https://doi.org/10.1088/1748-3190/adb6e8

Bioinspiration & Biomimetics



RECEIVED
12 November 2024

REVISED
10 February 2025

ACCEPTED FOR PUBLICATION
17 February 2025

PUBLISHED
5 March 2025

NOTE

Thermophoretic effect in natural photonics: holographic study

Marina Simovic Pavlovic[1,2,*], Dusan Grujic[1], Maja Pagnacco[3], Bojana Bokic[1], Darko Vasiljevic[1], Thierry Verbiest[4] and Branko Kolaric[1,5]

[1] Nanophotonics Lab, Photonics Center, Institute of Physics, University of Belgrade, Pregrevica 118, 11080 Belgrade, Serbia
[2] Faculty of Mechanical Engineering, University of Belgrade, Kraljice Marije 16, 11000 Belgrade, Serbia
[3] Center for Catalysis and Chemical Engineering, Institute of Chemistry, Technology and Metallurgy, University of Belgrade, Njegoševa 12, 11000 Belgrade, Serbia
[4] Laboratory of Molecular Imaging and Photonics, KULeuven, Belgium
[5] Micro- and Nanophotonic Materials Group, University of Mons, Place du Parc 20, 7000 Mons, Belgium
[*] Author to whom any correspondence should be addressed.

E-mail: simovicmarina99@gmail.com

Keywords: thermophoretic effect, natural photonics, holography, biomimetics, nanostructured materials

Abstract

Natural photonic structures allow us to reveal and mold the thermophoretic effect at the nanoscale within condensed matter systems. In this paper, for the first time, holography has been exploited to disclose conditions that determine the strength and dynamics of the thermophoretic effect. We experimentally revealed the link between geometry and nano-corrugation of biological structures that shapes the power of thermophoresis. The presented study opens enormous possibilities for harnessing the thermophoretic effect in various bioinspired sensing applications, uniquely merging the fields of photonics and mechanics.

1. Introduction

Fresnel and Crooks first spotted the mechanical displacement caused by the temperature gradient, known as the thermophoretic effect [1]. Later on, this phenomenon has been thoroughly investigated for years by many groups [2–4]. The same effect could be produced by light irradiation, and the term photophoresis describes it [5]. As it is the same phenomenon, and as photophoresis is only a specific case of thermophoresis in which a sufficient amount of light causes the thermal effect, the more general term—thermophoretic effect—will be used below. In the Bogolepov paper [6], an investigation of the various parameters that control the magnitude of the thermophoretic force on aerosol particles has been elaborated on and published elsewhere. Passian *et al* [7, 8] have also pioneered the field of thermophoresis by demonstrating that a heated cantilever near a surface will sense a force. Various papers [5, 9, 10] discuss the theoretical framework and experimental measurements of photophoretic/thermophoretic force. Many experiments have exploited the thermophoretic effect to discover or confirm other nano phenomena [11, 12]. For example, revealing the protein-protein interactions responsible for different medical pathologies exploits complex, timely, and costly methods. Microscale thermophoresis offers significant advantages [11]. Additionally, the thermophoretic behavior of oil droplets in solvent was analyzed using opto-thermophoretic tweezers [12]. The oil droplets move to areas with higher temperatures by the photothermal conversion of light. This fact allows us to study the arrangement of the droplets (dynamics) and the interfacial behavior of water *in situ*.

The effect itself has not been thoroughly investigated within the condensed matter systems, i.e. natural photonic structures. This research aims to reveal the dynamics of natural photonic structures as a function of laser light wavelength in order to exploit the sensitivity of dynamic response for various sensing applications. Natural structures could serve as excellent models for generating various technical solutions that can lead to the development of new advanced materials [13]. Thermophoresis offers a unique way to connect the system's dynamics with light-matter interaction. This coupling has huge potential in the

© 2025 IOP Publishing Ltd. All rights, including for text and data mining, AI training, and similar technologies, are reserved.

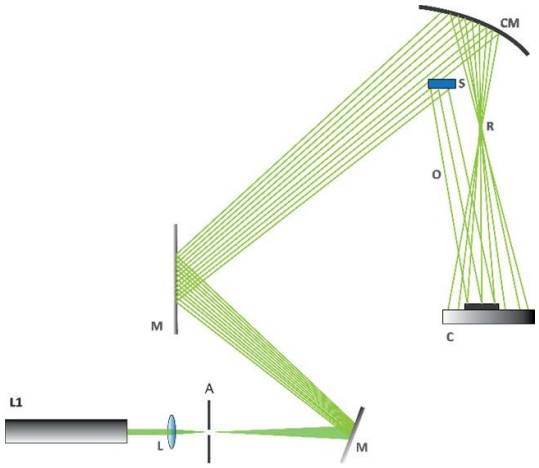


Figure 1. The scheme of the holographic setup (L1-laser, L-lens, M-Mirrors, CM-Concave mirrors, O-Object beam, R-Reference beam, S-Sample, C-CMOS camera). Reproduced with permission from [16]. Copyright © 2025 MyJoVE Corporation. All rights reserved.

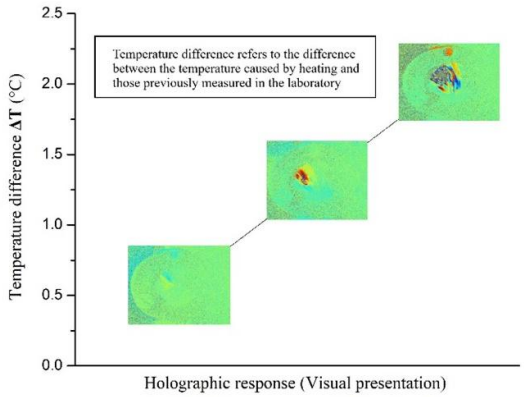


Figure 2. Holographic response as a function of temperature: images on the diagram represents holographic reconstructions. Holographic recording is explained in detail in [16].

area of sensing as well as in the fundamental study of corrugated (nanostructure) biological and non-biological materials.

Since the effect is related to observation of nanoscopic, thermally/photo-induced displacements, we choose holographic interferometry as an ideal method to reveal the origins and dynamics of thermophoresis within the condensed matter systems. In this way, bio-inspired artificial structures with exceptional characteristics can be proposed [14].

2. Experimental

The thermophoretic effect occurs in structures in which dimensions (at least one) match the mean free path of the molecule. Digital holographic interferometry is an appropriate tool to gain more precise measurements in the experiment, where the state of the object changes as a result of a displacement, and the interference pattern changes too. Holographic interferometry allows the comparison of wavefronts recorded at different times and has been used for the vibration measurements for a long time [15]. The holographic setup used in the experiment is shown in figure 1 and described in the paper [16].

The already known sensing feature of butterfly wings drew attention to this particular species [17].

The experiment started with examination of samples, certain parts of the wing, originating from eight different types of butterfly species: *Morpho didius* (Fabricius, 1807), *Morpho peleides* (Kollar, 1850), *Morpho portis* (Hubner, 1821), *Apatura iris* (Linnaeus, 1758), *Pieris rapae* (Linnaeus, 1758), *Calophrys rubi* (Linnaeus, 1758), *Issoria lathonia* (Linnaeus, 1758) and *Polyommatus icarus* (Latreille, 1804).

Additionally, all samples were investigated by the scanning electron microscopy (SEM) [18].

Each sample has been initiated by laser light with four different wavelengths: 450, 532, 660 and 980 nm. The laser power in our experiment was set to 1 mW. Tested samples responded well to initiation by mentioned wavelengths.

In addition to holographic imaging, the experiment was followed by a thermal camera 'FLIR A65' (640 × 512 pixel, thermal resolution 50 mK, focal length 13 mm, field of view angle 45 × 37°) and photographic camera Cannon EOS 50D [16].

3. Results and discussion

3.1. Holographic response as a function of nanostructure and temperature

Heating of the sample causes a thermophoretic effect that manifests as the displacement of the structures. In the case of elastic deformation, theory predicts that the intensity of elastic response increases linearly in the narrow (ambient) temperature range [19]. This observation scales nicely with linear temperature increase measured with a thermal camera. The holographic response that records the system's vibrations increases with temperature, as shown in figure 2. By means of the holographic reconstructions one could directly visualize the temperature differences.

A butterfly's wing consists of a biopolymer known as chitin [20]. It is a polysaccharide, a basic building block of natural photonic structures. In the case of natural photonic structures, the presence of pigments embedded in elytra is also considered. At first glance, it is possible to assume that the presence of pigments would influence the effect. However, the pigments of the examined species absorb light of wavelengths much smaller than those used in the experiment. Due

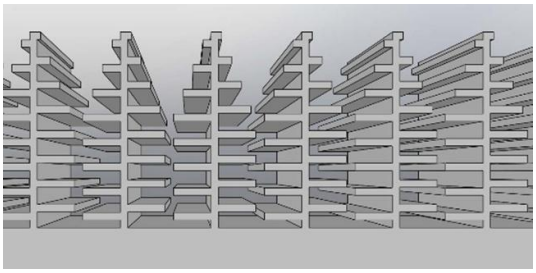


Figure 3. Representation of the herringbone structure.

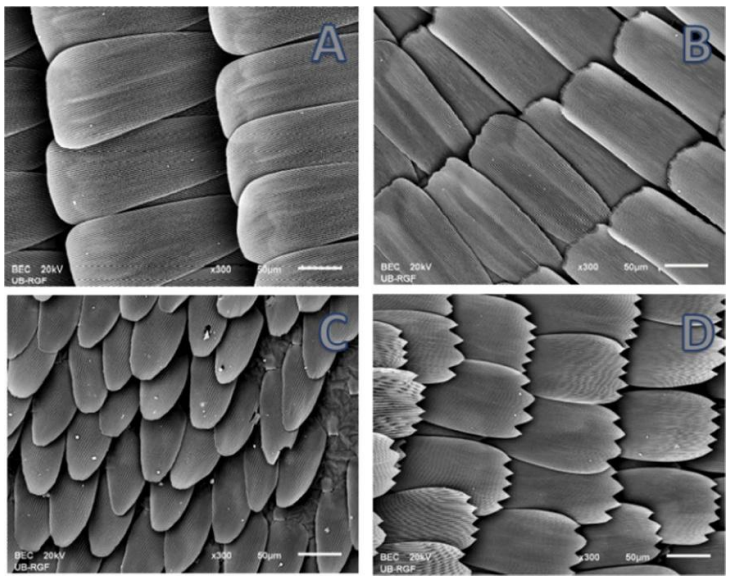


Figure 4. Microscopic images of the *Apatura iris* butterfly wing: side 1 (A) and side 2 (B), and *Morpho didius* butterfly wing: side 1 (C) and side 2 (D). Magnification 300x.

to the above reasons, the pigments found in the biophotonic structure do not have a significant, measurable influence on the dynamics of the thermophoretic response. It should be noted that the effect of temperature on holographic response has not been recorded in the case of planar chitin film.

After testing the eight listed species, corrugation proved to be the principal factor that shaped the strength of the thermophoretic effect. For further detailed testing, two types of butterflies were chosen, which are representatives of the herringbone type of structure (figure 3).

The morphology of the surface of the wing samples of two butterfly species is characterized by SEM and shown in the following figure 4.

Based on the comparison of the size of the wing structure's elements, three wing structure elements are distinguished. Among these elements, scales are the largest and consist of the so-called *Christmas trees* with a certain number of microconsole pairs.

After it is proved that structural corrugation governs the strength of the thermophoretic effect, we continued the investigation to reveal the other parameters that determine the power of thermophoretic response.

3.2. Effect of the lightwave and phase on thermophoretic response

Biophotonic structures are photonic structures that exibit periodic changes in refractive index and modify the propagation of electromagnetic waves. This periodic dielectric profile leads to the appearance of a photonic band-gap, i.e. 'forbidden zones', precisely, a zone in which certain wavelengths cannot propagate [21]. The propagation of light at different wavelengths differs, and therefore the influence of wavelengths on heating, i.e. deformation of the structure, is expected. The influence of the wavelength of laser light on the heating of the sample is shown in figure 5.

The non-linear dependence of the temperature, as a function of the wavelength is observed. The observed disproportionality directly indicates the influence of the photonic structure on the degree of heating. The investigated structures show the strongest response at specific wavelengths (450,

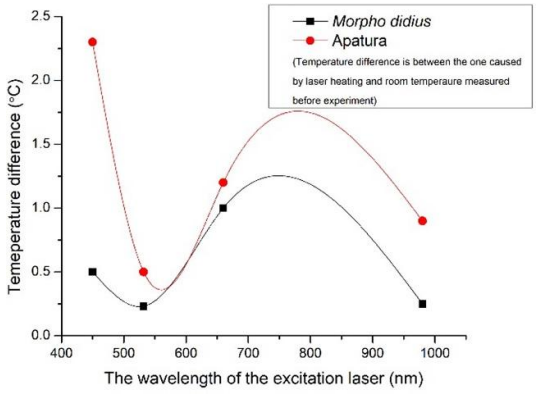


Figure 5. Diagram representing the dependence of the sample's heating on the wavelength of incidental light.

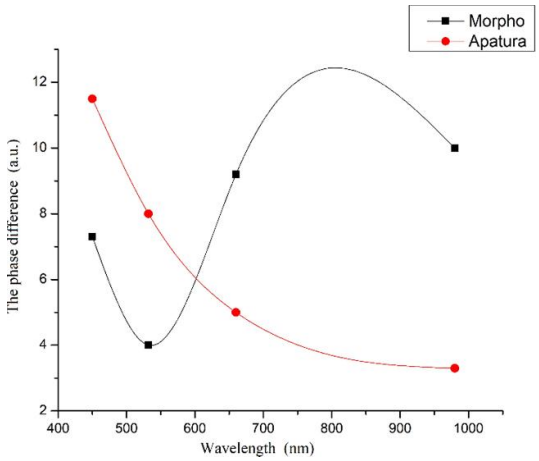


Figure 6. The maxima of the phase profile diagram.

660 nm). Therefore, it can be assumed that, due to interference effects within the periodic photonic structure and the existence of the so-called 'photonic forbidden zones'—the transmission of the mentioned wavelengths through the given structure is partially impeded [21]. Additionally, since the natural photonic structures cannot create a perfect (full) band gap, some light will pass through the forbidden zone and be trapped inside a structure. Due to the increase in the interaction time, temperature will rise.

This presented research is significant because it shows the influence of light wavelength on nanostructure dynamics, visualized through the measurement of the temperature gradient. Furthermore, the advantage of holography is that it allows obtaining the phase information. Specifically, for this study, the part of the energy of the light wave, that is transmitted through the examined structure and causes deformation (structure displacement), is important, which is , essentially, the subject of this observation and analysis. As an essential parameter for displacement characterization, the phase of light is calculated by home-built C++ software based on Fresnel approximation, which takes into account the reconstructions of recorded holograms [22, 23].

The maximums of the phase profile for both types of butterfly samples, calculated for the four measured wavelengths, are shown in figure 6. Due to the laser's polarization, which makes its phase undetermined, the observed phase is relative. The utterly different phase response as a function of wavelength (observed for different butterflies) nicely matches the fact that both butterflies have slightly different nanostructure architectures.

Additionally, the phase difference ($\Delta\psi$) can be expressed as being proportionate to the changes of the refractive index (n). The unique power of holographic measurements is the possibility of relating changes in the estimated phase difference to relative changes in refractive index,

$$\Delta\psi = k \cdot x - \omega_t \approx n. \quad (1)$$

The refractive index is a function of composition of the system as well as the function of the corrugation if the corrugation exists. Since chitin is the dominant building block of photonic structures for both butterflies, the difference in corrugation determines the effective refractive index.

We conclude that corrugation plays a dominant role in determining the effective refractive index. Changes in the value of the refractive index as a function of temperature are observed as a phase shift in holographic experiments.

The dynamics of the phase as a function of time is fitted with an exponential function and time dependence graphs of the same type are obtained for each wavelength. A comparative presentation of the data obtained by fitting analog diagrams for four wavelengths, when analyzing two different species of butterflies, is tabulated in table 1.

A relatively slow relaxation of the system is observed. Considering the relaxation time, it could be assumed that the measured relaxation represents the cumulative effect of coupling of multiple parts within the same nanostructures. In a mechanical sense, it can be said that the object of observation is a large number of oscillators with different phase values at the same moment.

3.3. Perspectives

Applications of the thermophoretic effect cover various areas, from medicine to materials science and technology. The most inspiring use of some variation of this effect in medicine and pharmacy relates to the challenging issue of drug delivery [24]. Furthermore, the thermophoretic effect, in combination with holography and similar techniques [25], offers way to manipulate and control the position of microparticles on command. Numerous electronic and mechatronic systems consisting of MEMS/NEMS subsystems exploit thermophoretic and similar nanoeffects

Table 1. Table of calculated phases' relaxation times.

Wavelength (nm)	Apatura		Morpho didius	
	Phase lifetime (ms)	Standard deviation (ms)	Phase lifetime (ms)	Standard deviation (ms)
450	79	3	89	2
532	125	2	56	1
660	59	2	30	2
980	138	9	71	2

exploiting optical tweezers [26]. Therefore, the potential of utilization of the thermophoretic effect in future technology is obvious.

3.4. Highlights

This work showed the uniqueness of natural photonic structures and the specificity of their response. It has been demonstrated that corrugation, i.e. the geometry of the structure, most influences the thermophoretic effect. Equally important, the power of holography is highlighted as a method for studying the dynamics of nanostructures *in situ*. We mentioned potential applications to promote the scientific community's interest in future studies of the thermophoretic effect and its applications.

4. Conclusion

This paper presents the results obtained by experimental examination of thermophoretic effect. The holographic recording of several butterfly species exposed to laser heating reveals essential properties of the thermophoretic effect.

The sensitivity of holography to determine changes in refractive index value as a function of temperature has been exploited.

This research could be used to select an ideal bioinspired structure that perfectly responds to the thermophoretic effect. Further research will propose an artificial structure based on the investigated butterfly as a potential solution for new infrared detection elements.

Data availability statement

All data that support the findings of this study are included within the article (and any supplementary files).

Acknowledgment

B. K., D. V., B. B., D. G., and M. S. P. acknowledge funding provided by the Institute of Physics Belgrade, through the institutional funding by the Ministry of Education, Science, and Technological Development of the Republic of Serbia. Additionally, B. K. acknowledges support from F R S—FNRS. M. P. acknowledges support from the Ministry of Education, Science and Technological Development of the Republic of Serbia, Contract number 451-03-9/2021-14/200026. D. V., M. S. P., D. G., M. P., B. B., and B. K. acknowledge the support of the Office of Naval Research Global through the Research Grant N62902-22-1-2024. M. S. P., M. P., B. B., D. V. and B. K. acknowledge the support of the EU: the EIC Pathfinder Challenges 2022 call through the Research Grant 101115149(project ARTEMIS).

ORCID iDs

Marina Simovic Pavlovic https://orcid.org/0000-0003-0766-059X
Maja Pagnacco https://orcid.org/0000-0002-1299-7974
Branko Kolaric https://orcid.org/0000-0003-0203-7897

References

[1] Crookes W 1873 *Phil. Trans.* **164** 81
[2] Simovic Pavlovic M, Pagnacco M, Radulovic A, Sencanski J and Markovic M 2023 *Kemija u Industriji: Casopis kemicara I kemijskih inzenjera Hrvatske* **72** 693
[3] Oh S, Figgis B W and Rashkeev S 2020 *Sol. Energy* **211** 412
[4] Liu W, Wang J, Xia G and Li Z 2023 *Phys. Fluids* **35** 083316
[5] Horvath H 2014 *KONA Powder Part. J.* **31** 181
[6] Bogolepov A I 1991 *J. Aerosol Sci.* **22** 439
[7] Passian A, Wig A, Meriaudeau F, Ferrell T L and Thundat T 2002 *J. Appl. Phys.* **10** 6326
[8] Passian A, Warmack R J, Ferrell T L and Thundat T 2003 *Phys. Rev. Lett.* **12** 124503
[9] Wieben F and Block D 2018 *Phys. Plasmas* **25** 123705
[10] Gallis M A, Rader D J and Torczynski J R 2004 *Aerosol Sci. Technol.* **38** 692–706
[11] Magnez R, Bailly C and Thuru X 2022 *Int. J. Mol. Sci.* **23** 7672
[12] Kim Y, Ding H and Zheng Y 2022 *Nat. Commun.* **13** 3742
[13] Simovic Pavlovic M, Bokic B, Vasiljevic D and Kolaric B 2022 *Appl. Sci.* **12** 905
[14] Grujić D, Vasiljević D, Pantelić D, Tomić L, Stamenković Z and Jelenković B 2018 *Opt. Express* **26** 14143
[15] Pedrini G, Osten W and Gusev M E 2006 *Appl. Opt.* **45** 3456
[16] Simovic Pavlovic M, Pagnaco M C, Grujic D, Bokic B, Vasiljevic D, Mouchet S, Verbiest T and Kolaric B 2022 *J. Vis. Exp.* **181** E63676
[17] Qingsong L, Qi Z, Lei S, Xiaohua Z and Ke-Qin Z 2016 *J. Mater. Chem.* C **4** 1752
[18] Kishimoto S, Wang Q, Xie H and Zhao Y 2007 *Appl. Opt.* **46** 7026
[19] Alasfar R H, Ahzi S, Barth N, Kochkodan V, Khraisheh M and Koc M 2022 *Polymers* **14** 360
[20] Mouchet S and Deparis O 2021 *Natural Photonics and Bioinspiration* (Artech House)

[21] Gonzalez-Urbina L, Baert K, Kolaric B, Perez-Moreno J and Clays K 2012 *Chem. Rev.* **112** 2268–85
[22] Shimobaba T and Ito T 2019 *Computer Holography: Acceleration Algorithms and Hardware Implementations* (CRC Press)
[23] Shimobaba T, Weng J, Sakurai T, Okada N, Nishitsuji T, Takada N, Shiraki A, Masuda N and Ito T 2012 *Comput. Phys. Commun.* **183** 1124–38
[24] Morales-Bonilla S, Mota-Diaz I I, Douda J, Gonzalez-Vargas C R, Villalpando I and Torres-Torres C 2021 *Optik* **245** 167738
[25] Li F, Wei J, Qin X, Chen X, Chen D, Zhang W, Han J, Yuan L and Deng H 2024 *Microsyst. Nanoeng.* **10** 123
[26] Wang D, Ping T, Du Z, Liu X and Zhang Y 2025 *Nano-Micro Lett.* **17** 100

THE JOURNAL OF PHYSICAL CHEMISTRY C
A JOURNAL OF THE AMERICAN CHEMICAL SOCIETY

pubs.acs.org/JPCC

Article

Stochastic Phase Transition Dynamics in Nonequilibrium System: Holographic Study

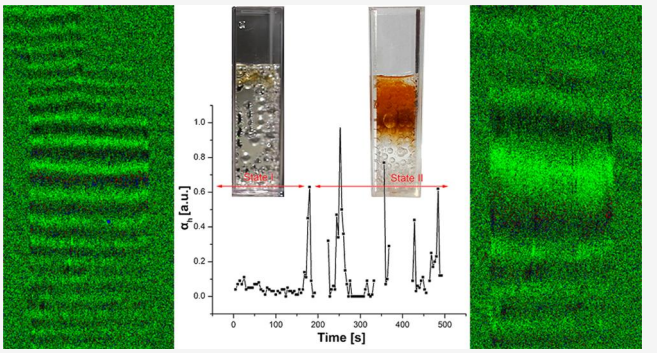
Maja C. Pagnacco,* Marina Simović-Pavlović, Dušan Ž. Grujić, Darko M. Vasiljević, Bojana Bokic, Sébastien R. Mouchet, Thierry Verbiest, Yves Caudano, and Branko Kolaric*

Cite This: https://doi.org/10.1021/acs.jpcc.3c01831

Read Online

ACCESS | Metrics & More | Article Recommendations

ABSTRACT: This paper presents a holographic study of the phase transition that occurs in a nonequilibrium system. The chosen model is a unique Briggs−Rauscher oscillatory reaction that, first, follows a deterministic pattern (namely, an oscillatory behavior) and, later, exhibits a phase transition occurring randomly and without any known link with the previous deterministic state. The presented research opens up a new way to reveal complex chemical phenomena and dynamics in situ, without disturbing significantly the nonequilibrium system and its pathways. Simultaneously, it unfolds a new route for applications of interferometric methods in different areas of materials science. Under the applied conditions, we show that the holographic method is more sensitive to the phase transition dynamics than the commonly used potentiometric method.



Downloaded via Branko Kolaric on May 25, 2023 at 17:41:32 (UTC).
See https://pubs.acs.org/sharingguidelines for options on how to legitimately share published articles.

INTRODUCTION

Patterns, from biological origin or not, are everywhere around us, with various complexities and shapes.[1−3] From a fundamental point of view, natural patterns emerge as a consequence of a local decrease of entropy within an open system. The buildup of coherence among the components of the system is responsible for self-organization processes and structures that build complex patterns in both organic and inorganic worlds, including living organisms and ecosystems.[2,3]

So far, considerable effort has been made to understand pattern formation and chemical reactivity in open systems using thermodynamics and chemical kinetics.[2] However, only a limited number of self-assembly processes and systems have been completely investigated. Beyond the phenomenological description, only a few quantitative models have been proposed within the framework of nonequilibrium thermodynamics and statistical physics.[2−6]

Due to their so-called sensitivity to initial conditions and external factors, nonequilibrium systems can emerge through various pathways so that full control of their dynamics is practically impossible.[7−9] Additionally, monitoring the nonequilibrium process without disturbing the system is a challenging task as well.

Oscillatory reactions are nonequilibrium systems that exhibit unique behavior and rich kinetic patterns.[2,7,9] Still, many intrinsic informations need to be discovered, related to the kinetics of the oscillatory reaction, and the dynamics of the pattern formation. Currently, the lack of fast, sensitive, unambiguous, and nondisturbing techniques is one of the major obstacles to understanding the nano- and macroscale dynamics in a nonequilibrium system. Therefore, it is crucial to develop methods that offer new insight into the physics of oscillatory reactions, the pattern formations at the nanoscale, and their links with macroscopic behavior. In this article, we analyzed a nonequilibrium chemical system, an oscillatory Briggs−Rauscher (BR) reaction accompanied with phase transition, i.e., solid iodine formation.[7,10] Under the applied experimental conditions, after the BR oscillatory period, two states are observed: State I (low iodide and iodine concentration) and State II (high iodide and iodine concentration, with solid iodine formation). A sudden transition from State I to State II, so-called *crazy-clock behavior*, is accompanied by a liquid−solid iodine phase transition.[7,10,11] This process proved to be an ideal model for implementing a new holographic approach. In addition to holographic observations, potentiometric measurements are performed, as a comparison to assess the performance of our method.

Received: March 18, 2023
Revised: May 10, 2023

ACS Publications

© XXXX American Chemical Society

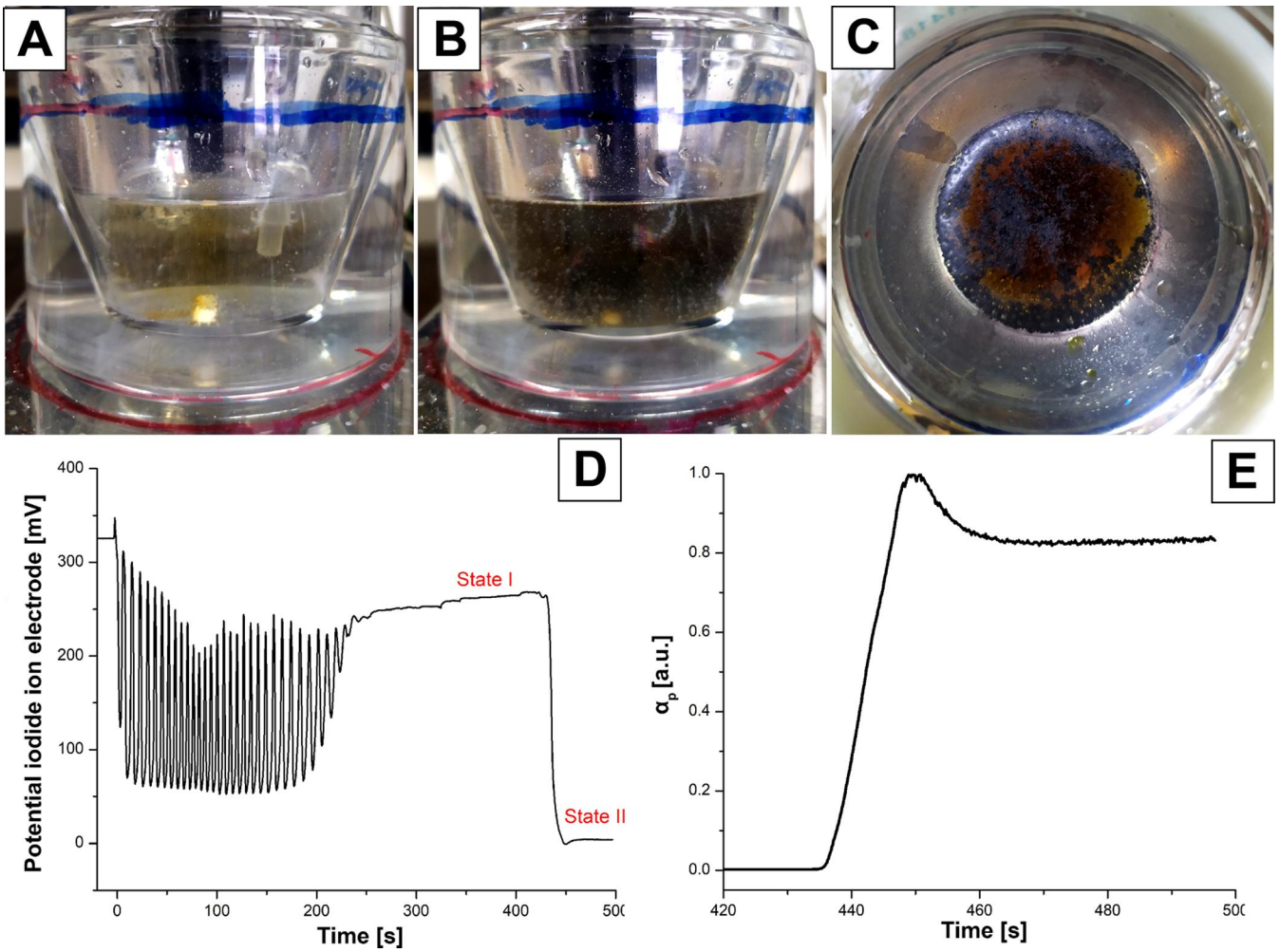


Figure 1. BR oscillatory dynamics preceding the crazy-clock transition. Photographs of the State I → State II transition: side view of the beginning of transition, high iodide and iodine concentration (A), side view of the end of transition characterized by solid iodine formation (B), top view of the end of iodine phase transition, the formation of iodine film (C), BR dynamics including oscillatory period, State I and State II obtained by potentiometric method (D), and State I → State II transition (α_p electrochemical is defined in page 6) (E).

MATERIALS AND METHODS

Holographic Study of Briggs−Rauscher Reaction. Holographic method relies on the recording of an interference fringe pattern as a function of time.[12−15] Unlike other optical methods such as spectroscopy or photography, holography deciphers, at the same time, information about the phase and amplitude of light after its interaction with the sample. The BR reaction is examined with the *triple rec* method.[14]

The formula $\alpha_h(t) = \frac{\lambda_{min} - \lambda(t)}{\lambda_{min} - \lambda_{max}}$ normalizes the observed wavelengths of the holographic fringes to the interval [0,1]. The wavelength of the fringe pattern reflects its spatial periodicity, corresponding to the average interfringe distance of a pattern, where $\lambda(t)$ is the wavelength of the fringe pattern at time t during the transition, λ_{min} is the wavelength of the narrowest fringe pattern obtained during the transition, and λ_{max} is the maximal measured wavelength. The α_h parameter was measured as a function of time. The data were interpolated every 0.1 s using a spline method and numerically derivated with respect to time.

The phase transition from State I to State II was monitored in a cuvette at an ambient temperature with initial concentrations of reactants $[CH_2(COOH)_2]_0 = 0.0789$ mol dm^{-3}, $[MnSO_4]_0 = 0.0075$ mol dm^{-3}, $[HClO_4]_0 = 0.03$ mol dm^{-3}, $[KIO_3]_0 = 0.0752$ mol dm^{-3} and $[H_2O_2]_0 = 1.269$ mol dm^{-3}. The total volume was 2.5 mL.

Potentiometric Study of the Briggs−Rauscher Reaction. The initial concentrations of reactants are identical to those in the cuvette for the holographic measurements (described above). However, the reaction volume is 10 times larger (25 mL). The experiments took place in a closed reactor without stirring, thermostated at 25 °C (the study regarding the impact of different factors on this phase transition (State I to State II) is described elsewhere[7]). A thermometer with an accuracy of 0.1 °C monitored the temperature of the BR reaction. When the temperature and potential were stabilized, the BR reaction was initiated with the addition of H_2O_2 (3 mL, 9.8 M). The beginning of the BR reaction ($t = 0$ s) corresponded to the moment when hydrogen peroxide was added to the vessel. The time evolution of the BR reaction is followed potentiometrically, by using an electrochemical device (PCMultilab EH4 16-bit analog-to-digital converter) coupled to a personal computer. The working and reference electrodes were an iodide ion-selective electrode (ISE) and a double-junction Ag/AgCl electrode, respectively. The potentiometric response obtained with ISE is converted to an iodide concentration−time curve, by

https://doi.org/10.1021/acs.jpcc.3c01831
J. Phys. Chem. C XXXX, XXX, XXX−XXX

transforming the logarithmic dependence of the ISE potential as a function of concentration to an iodide concentration as a function of time at a given temperature,[16] namely, T = 25 °C. The concentration is normalized to the interval [0,1] by defining $\alpha_p(t) = \frac{C_0 - C(t)}{C_0 - C_{max}}$, where C_0 is the initial concentration of iodide when the State I → State II transition starts; $C(t)$ is the iodide concentration during the transition at time t; and C_{max} is the maximal iodide concentration. As in the case of the holographic measurements, $\alpha_p(t)$ is interpolated every 0.1 s with a spline method and numerically derivated, with respect to time. In addition, the resulting data was smooth using a Savitzky−Golay polynomial filter[17] of order 3 and with a frame size equal to 55.

As shown previously,[7] strong stirring postponed State I to State II transition (for more hours), or transition does not occur at all. In our experiment, a holographic and potentiometric study of BR dynamics, hydrogen peroxide is added 3 min (and 10 min in the case of electrochemical measurements) after other reactants, and the BR reaction is naturally stirred by the expressive production of oxygen bubbles formed in the first part of the reaction (starting immediately after hydrogen peroxide addition) without additional mixing of the solution. Due to the practical difficulties related to the long-time holographic recording, the authors avoided time-consuming experiments.

RESULTS AND DISCUSSION

Nonlinear systems are highly sensitive to the concentration of reactants, the geometries of the reaction vessel, mixing conditions, and external influences like light and temperature.[7,9−18] Up to now, the time evolution of nonlinear chemical systems has been successfully monitored by potentiometric methods.[18−21] However, the electrodes immersed in the solution could give rise to additional effects like catalytic effect, "dead volume" effect (i.e., when diffusion of chemical species is a controlling factor for the reaction), and a lot of other processes highly dependent on the nature of the working electrode.[10,19] Furthermore, the main reactant, hydrogen peroxide, could be decomposed on the platinum electrode, which is widely used in potentiometric measurements of oscillatory reactions. In addition, many details of a complex redox system are not fully understood.[19] Therefore, the iodide ISE electrode is used as a working electrode to measure the State I to State II transition by potentiometric method (Figure 1). The oscillogram in Figure 1 is obtained without mixing, at 25 °C.

As previously published,[7,10,14] the State I → State II transition is essentially irreproducible in time (as its "crazy-clock" name indicates). Surprisingly, this crazy-clock behavior is preceded by a strongly reproducible oscillatory dynamics (at 25 °C, the oscillatory period lasts 240 s, with 33 oscillations), which happens before solid iodine formation, i.e., before the State I → State II transition.

Holography relies on the recording of the interference patterns in the form of fringes. Although the complete State I → State II phase transition could be observed with the naked eye (a change in coloration), the emergence of it could be determined at the nanoscale resolution using the holographic method (the scheme of the used setup is presented elsewhere[14]). The wavelength of the incident light (532 nm) overlaps slightly with the tail of the absorbance spectrum of iodine (λ_{max} at 460 nm), so the effect related to the absorption is very low.

Due to its stochastic behavior, the exact moment of the transition is very difficult to determine, bearing in mind that the time of transition from State I → State II is essentially irreproducible and strongly related to the particular kinetic run. Due to the stochastic behavior, the presented results are based on a rather large number of measurements (more than 30). The change in the fringe pattern (Figure 2B) is recorded at the moment the transition from State I → State II occurs. In Figure 2C, the time dynamics of the transition obtained from holographic measurements is presented.

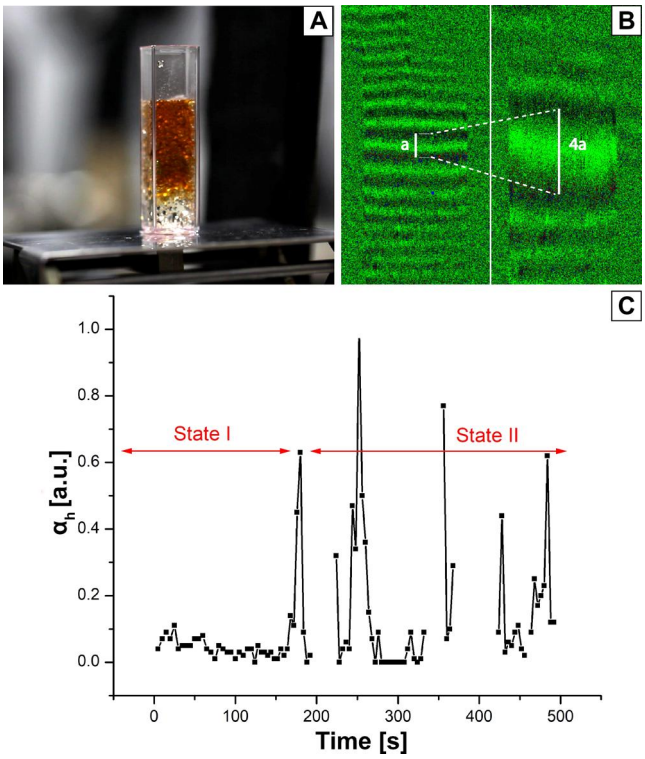


Figure 2. Holographic measurements: an example of the iodide sample (A), changes in the interference pattern, before (left) and at the moment of the reaction (right) (B), and time dynamics of the transition obtained from holographic measurement (C).

The observed interference signature in Figure 2B is a consequence of transition dynamics being changed with time, and it is assigned to State I (happened after hydrogen peroxide). The observed pattern fluctuations over time are related to the density fluctuations that occur during the State I to State II transition. At the moment of transition, the wavelength drastically increases (4 times), indicating the merging of different dissipative structures into a new single phase (Figure 2B). The presented values in the holographic pattern are relative and normalized for the wavelength of the laser used in our experiment. Due to the weak interaction between photons and matter (in the case of low or no absorption), interferometric techniques allow monitoring of the dynamics of nonequilibrium systems with minimum disturbance. Drastic changes in the intensity of the interference signal occur during the entire period of the process (Figure 2C), indicating the possibility of distinguishing different density fluctuations within the system by the holographic method. Dynamics of the pattern is observed during the transition from State I to State II, see Figure 2C. Additionally, the benefit of holography is clear when the dynamics of the phase transition monitored by holography as a function of time is compared to the same dynamics observed by the potentiometric method (Figure 3). The transition rates are

https://doi.org/10.1021/acs.jpcc.3c01831
J. Phys. Chem. C XXXX, XXX, XXX−XXX

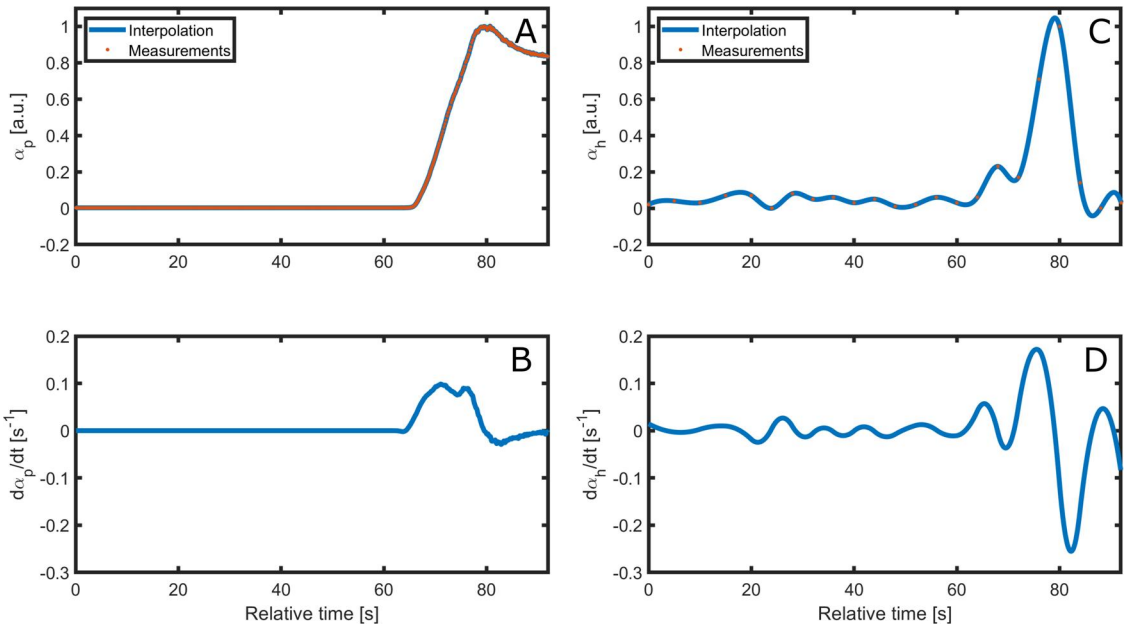


Figure 3. Holography approach (C, D) is more sensitive to the process than the potentiometry approach (A, B). The normalized holographic and potentiometric parameters, $\alpha_h(t)$ and $\alpha_p(t)$, were measured as functions of time (A, C). The maximum of the derivative of the holographic (D) curve is higher than the maximum of the potentiometric curve (D). *X*-axes correspond to the relative time. The moment of the detected phase transition was chosen to be at around 65 s.

determined using the first numerical derivative from both curves.

The maximum of the first derivative of the normalized holographic $\alpha_h(t)$ parameter is higher than the maximum of the derivative of $\alpha_p(t)$ measured by potentiometry: ca. 0.17 s^{-1} versus ca. 0.12 s^{-1}. This indicates that under the applied experimental conditions, holography is more sensitive to the process than potentiometry. Holography detects the rise of the transition directly, and it is not limited by various physicochemical processes that are involved in the electrochemical response, such as adsorption, diffusion, oxidation, reduction, etc.[19]

CONCLUSIONS

This holographic study opens up many new questions worth investigating, including the type of dissipative structures that are monitored by the holographic method, and the link between the temporary dissipative dynamics and the final structure after the transition. Also, it is still an open question whether the holographic and potentiometric methods monitor the concentration and dynamics of the same reaction species or not.

Finally, this study unveils the complex chemical dynamics in the BR system and, simultaneously, opens a new route for applications of interferometric methods in different areas of chemical and materials science.[22] The large deviation of individual kinetics run within nonequilibrium systems should not be alleviated or eliminated using the holographic method which minimally (or does not at all) disturbs the chemical system. In addition, this research discloses an advantage of holography in terms of detection sensitivity and possibility to reveal pattern formation at the nanoscale. The presented study also opens the possibility for the integration of holography with other optical methods and microscopy[23] in fundamental and applied research.

AUTHOR INFORMATION

Corresponding Authors

Maja C. Pagnacco − *Center for Catalysis and Chemical Engineering, Institute of Chemistry, Technology and Metallurgy, University of Belgrade, 11000 Belgrade, Serbia;* orcid.org/0000-0002-1299-7974; Email: maja.pagnacco@nanosys.ihtm.bg.ac.rs

Branko Kolaric − *Center for Photonics, Institute of Physics, University of Belgrade, 11080 Belgrade, Serbia; Micro- and Nanophotonic Materials Group, University of Mons, 7000 Mons, Belgium;* orcid.org/0000-0003-0203-7897; Email: branko.kolaric@umons.ac.be

Authors

Marina Simović-Pavlović − *Center for Photonics, Institute of Physics, University of Belgrade, 11080 Belgrade, Serbia; Faculty of Mechanical Engineering, University of Belgrade, 11120 Belgrade, Serbia*

Dušan Ž. Grujić − *Center for Photonics, Institute of Physics, University of Belgrade, 11080 Belgrade, Serbia*

Darko M. Vasiljević − *Center for Photonics, Institute of Physics, University of Belgrade, 11080 Belgrade, Serbia*

Bojana Bokic − *Center for Photonics, Institute of Physics, University of Belgrade, 11080 Belgrade, Serbia*

Sébastien R. Mouchet − *Department of Physics & Namur Institute of Structured Matter (NISM), University of Namur, 5000 Namur, Belgium; School of Physics, University of Exeter, Exeter EX4 4QL, U.K.;* orcid.org/0000-0001-6611-3794

Thierry Verbiest − *Molecular Imaging and Photonics, Department of Chemistry, KU Leuven, 3001 Heverlee, Belgium*

Yves Caudano − *Department of Physics & Namur Institute of Structured Matter (NISM), University of Namur, 5000 Namur, Belgium; Namur Institute for Complex Systems (naXys), University of Namur, 5000 Namur, Belgium*

Complete contact information is available at: https://pubs.acs.org/10.1021/acs.jpcc.3c01831

https://doi.org/10.1021/acs.jpcc.3c01831
J. Phys. Chem. C XXXX, XXX, XXX−XXX

Notes

The authors declare no competing financial interest.
The authors declare no conflict of interest. The funders had no role in the design of the study; in the collection, analyses, or interpretation of data; in the writing of the manuscript; or in the decision to publish the results.

■ ACKNOWLEDGMENTS

M.S.P., D.Ž.G., D.V., and B.K. acknowledge support of the project Biological and bioinspired structures for multispectral surveillance, funded by NATO SPS (NATO Science for Peace and Security) 2019−2022. B.K., D.V., B.B., D.Ž.G., and M.S.-P. acknowledge funding provided by the Institute of Physics Belgrade, through the institutional funding by the Ministry of Education, Science, and Technological Development of the Republic of Serbia. Y.C. is a research associate of the Fund for Scientific Research F.R.S.-FNRS. Additionally, B.K. acknowledges support from F.R.S.-FNRS. M.C.P. acknowledges support from the Ministry of Education, Science and Technological Development of the Republic of Serbia, Contract number 451-03-9/2021-14/200026. S.R.M. was supported by a BEWARE Fellowship (Convention no. 2110034) of the Walloon Region (Marie Skłodowska-Curie Actions of the European Union - COFUND - contract 847587), as a postdoctoral researcher. T.V. acknowledges financial support from the Hercules Foundation. D.V., M.S.P., D.Ž.G., M.P., B.B., and B.K. acknowledge the support of the Office of Naval Research Global through the Research Grant N62902-22-1-2024.

■ REFERENCES

(1) Smits, J.; Stoof, H. T. C.; Straten, P. V. D. Spontaneous Symmetry Breaking in a Driven-Dissipative System. *Phys. Rev. A* **2021**, *104*, No. 023318.
(2) Prigogine, I. *Self-Organization in Nonequilibrium Systems*, 1st ed.; Willey: New York, 1977.
(3) Misbah, C. *Complex Dynamics and Morphogenesis*, 1st ed.; Springer: Cham, Switzerland, 2016.
(4) Valkai, L.; Cseko, G.; Horvath, A. K. Initial Inhomogeneity-Induced Crazy-Clock Behavior in the Iodate-Arsenous Acid Reaction in a Buffered Medium under Stirred Batch Conditions. *Phys. Chem. Chem. Phys.* **2015**, *17*, 22187−22194.
(5) Turing, A. M. The Chemical Basis of Morphogenesis. *Philos. Trans. R. Soc. London, Ser. B* **1952**, *237*, 37−72.
(6) Prigogine, I.; Nicolis, G. On Symmetry-Breaking Instabilities in Dissipative Systems. *J. Chem. Phys.* **1967**, *46*, 3542−3550.
(7) Pagnacco, M. C.; Maksimović, J. P.; Potkonjak, N. I.; Božić, BĐ.; Horvath, A. K. Transition from Low to High Iodide and Iodine Concentration States in the Briggs−Rauscher Reaction: Evidence on Crazy Clock Behavior. *J. Phys. Chem. A* **2018**, *122*, 482−491.
(8) Genz, H. Symmetry and Symmetry Breaking in Nature. *Interdiscip. Sci. Rev.* **1999**, *24*, 129−138.
(9) Ruoff, P. Excitability in a Closed Stirred Belousov—Zhabotinskii System. *Chem. Phys. Lett.* **1982**, *90*, 76−80.
(10) Pagnacco, M. C.; Maksimović, J. P.; Daković, M.; Bokic, B.; Mouchet, S. R.; Verbiest, T.; Caudano, Y.; Kolaric, B. Spontaneous Symmetry Breaking: The Case of Crazy Clock and Beyond. *Symmetry* **2022**, *14*, No. 413.
(11) Horváth, A. K.; Nagypál, I. Classification of Clock Reactions. *ChemPhysChem* **2014**, *16*, 588−594.
(12) Gabor, D. A New Microscopic Principle. *Nature* **1948**, *161*, 777−778.
(13) Gabor, D. Microscopy by Reconstructed Wave-Fronts. *Proc. R. Soc. Lond. A* **1949**, *197*, 454−487. 1949.
(14) Simovic-Pavlovic, M.; Pagnacco, M. C.; Grujic, D.; Bokic, B.; Vasiljevic, D.; Mouchet, S.; Verbiest, T.; Kolaric, B. Uncovering Hidden Dynamics of Natural Photonic Structures using Holographic Imaging. *J. Vis. Exp.* **2022**, No. e63676.
(15) Harihan, P. *Basics of Holography*, 1st ed.; Cambridge University Press: Cambridge, 2002.
(16) Pagnacco, M. C.; Maksimovic, J. P.; Jankovic, B. Z. Analysis of Transition from Low to High Iodide and Iodine State in the Briggs−Rauscher Oscillatory Reaction Containing Malonic Acid Using Kolmogorov−Johnson−Mehl−Avrami (KJMA) Theory. *React. Kinet., Mech. Catal.* **2018**, *123*, 61−80.
(17) Savitzky, A.; Golay, M. J. E. Smoothing and Differentation of Data by Simplified Least Squares Procedures. *Anal. Chem.* **1964**, *36*, 1627−1639.
(18) Valkai, L.; Horváth, A. K. Imperfect Mixing as a Dominant Factor Leading to Stochastic Behavior: A New System Exhibiting Crazy Clock Behavior. *Phys. Chem. Chem. Phys.* **2018**, *20*, 14145−14154.
(19) Holló, G.; Kály-Kullai, K.; Lawson, T. B.; Noszticzius, Z.; Wittmann, M.; Muntean, N.; Furrow, S. D.; Schmitz, G. Platinum as a HOI/I_2 Redox Electrode and Its Mixed Potential in the Oscillatory Briggs−Rauscher Reaction. *J. Phys. Chem. A* **2017**, *1212*, 429−439.
(20) Maksimović, J. P.; Tosovic, J.; Pagnacco, M. C. Insight into the Origin of Pyrocatechol Inhibition on Oscillating Bray-Liebhafsky Reaction: Combined Experimental and Theoretical Study. *Bull. Chem. Soc. Jpn.* **2020**, *93*, 676−684.
(21) Cervellati, R.; Höner, K.; Furrow, S. D.; Neddens, C.; Costa, S. The Briggs-Rauscher Reaction as a Test to Measure the Activity of Antioxidants. *Helv. Chim. Acta* **2001**, *84*, 3533−3547.
(22) Yetisen, A. K.; Naydenova, I.; da Cruz Vasconcellos, F.; Blyth, J.; Lowe, C. R. Holographic Sensors: Three-Dimensional Analyte-Sensitive Nanostructures and Their Applications. *Chem. Rev.* **2014**, *114*, 10654−10696.
(23) Verstraete, C.; Mouchet, S. R.; Verbiest, T.; Kolaric, B. Linear and Nonlinear Optical Effects in Biophotonic Structures Using Classical and Nonclassical Light. *J. Biophotonics* **2019**, *12*, No. e201800262.

https://doi.org/10.1021/acs.jpcc.3c01831
J. Phys. Chem. C XXXX, XXX, XXX−XXX

Journal of the Serbian Chemical Society
JSCS-info@shd.org.rs • www.shd.org.rs/JSCS
J. Serb. Chem. Soc. *88* (11) 1119–1123 (2023)
JSCS–5684
Note
Published 11 November 2023

NOTE

Thermal investigation of material derived from the species *Apatura iris*

MARINA SIMOVIĆ PAVLOVIĆ[1]*, MAJA PAGNACCO[2], DIMITRIJE MARA[3], ALEKSANDRA RADULOVIĆ[3], BOJANA BOKIĆ[4], DARKO VASILJEVIĆ[4] and BRANKO KOLARIĆ[4,5]

[1]*Faculty of Mechanical Engineering, University of Belgrade, Kraljice Marije 16, Belgrade, Serbia,* [2]*Institute of Chemistry, Technology and Metallurgy, University of Belgrade, Njegoševa 12, Belgrade, Serbia,* [3]*Institute of General and Physical Chemistry, Studentski trg 12/V, Belgrade, Serbia,* [4]*Photonics Center, Institute of Physics, University of Belgrade, Pregrevica 118, Belgrade, Serbia and* [5]*Micro- and Nanophotonic Materials Group, University of Mons, Place du Parc 20, 7000 Mons, Belgium*

(Received 27 March, revised 20 April, accepted 21 July 2023)

Abstract: The material's size and shape influence its physical, chemical and mechanical properties. This study describes an investigation of natural photonic structure of the butterfly's wing, mainly composed of chitin. The effect of corrugations at the nanoscale on material's optical response is unambiguously revealed in the presented thermal measurements. Furthermore, the presented study shows the possibility of exploiting holography to monitor dynamics *in situ*.

Keywords: *Apatura iris* butterfly; biopolymer chitin; sensing dynamics *in situ*.

INTRODUCTION

Apatura iris butterfly's wing used for this study is shown in Fig. 1.[1–3] Butterfly wings are made of the biopolymer chitin,[4] with general formula $(C_8H_{13}O_5N)_n$. The chitin composition of different parts of the butterfly's body is described elsewhere.[5] The paper revealed that chitins from different parts are chemically very similar, but with significant differences in their surface morphologies.

In this study the surface morphology is characterized by JEOL JSM 6610 LV (Japan), scanning electron microscope (SEM) in conjunction with the energy dispersive spectroscopy (EDS) detector model X-Max large area analytical silicon drift connected with INCA Energy 350 Microanalysis (detection of elements $Z \geq 5$, detection limit: ~ 0.1 mas. %, resolution, 126 eV).

* Corresponding author. E-mail: simovicmarina99@gmail.com
https://doi.org/10.2298/JSC230327042P

Available on line at www.shd.org.rs/JSCS/
(CC) 2023 SCS.

Micro-elemental (EDS) analysis of *A. iris* butterfly's wing in two selected points, scale cell and the wing membrane, given in Fig. 2, showed the presence of carbon (C), oxygen (O) and nitrogen (N) originated from chitin. As it can be seen, the content of C, N and O slightly differs in scale cell and the wing membrane, indicating different chitin compositions in different surface structures. The presence of gold (Au) originates from the sample preparation for SEM/EDS analysis.

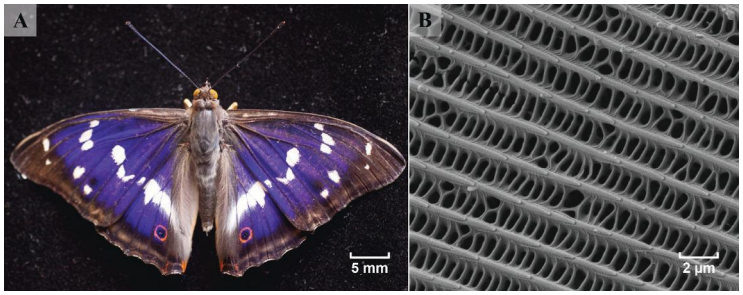


Fig. 1. *Apatura iris* butterfly: A) an optical image of the whole butterfly; B) SEM image of a ground scale of the wing.

Thermal camera "FLIR A65" (640×512 pixel, thermal resolution 50 mK, focal length 13 mm, field of view angle 45°×37°) is used to measure the temperature of the sample after the irradiation with laser. Later, holographic method will be used to characterize the interaction of the photonic structure with light.[6,7] A scheme of the holographic setup that is going to be used in the experiment is described elsewhere.[8] The setup will allow the simultaneous recording of deformation and temperature.

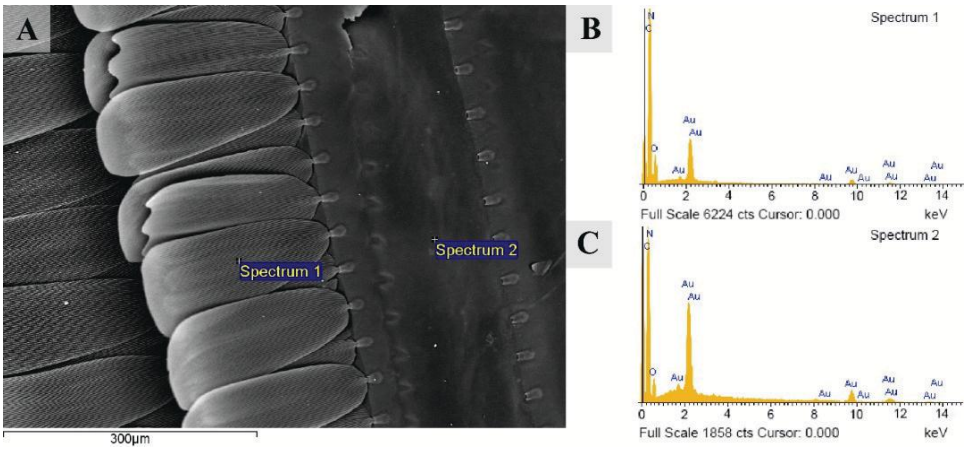


Fig. 2. A) SEM image of the scale cells and the wing membrane of *Apatura iris* butterfly's wing; B) EDS analysis of the wing at the scale cell (Spectrum 1); C) EDS analysis of the wing at the wing membrane (Spectrum 2).

(CC) 2023 SCS.

RESULTS AND DISCUSSION

Six samples are individually irradiated by external lasers operating at four different wavelengths (450, 532, 660 and 980 nm) keeping the power and illuminated spot diameter constant at 1 mW and 1 mm, respectively. The thermal measurement is made over the period that includes the time before the start of heating (interaction with laser), during the heating itself, and after the irradiation stopped, more precisely the cooling of the sample.

The difference in temperature due to heating by laser at various wavelengths has been observed. The highest temperature is caused by the interaction with 450 nm light, while the lowest is recorded for the wavelength of 532 nm. However, the complete reversible cooling (reaching the initial state) has not been observed for the wavelengths of 450 and 980 nm. A complete return to the initial state is observed for the wavelengths of 532 and 660 nm.

Analyzing data in depth is vital to link thermal measurement with the reflectance spectrum[9] (Fig. 3A) and the heating/cooling process as a function of time. Fig. 3B is showing the change in temperature over time, as a function of wavelengths.

Finally, the thermal measurements match the reflectance pattern and the heating/cooling dynamics as a function of time. It is evident that the temperature maximum in Fig. 3B at 450 nm corresponds to the reflectance maximum. The maximum value recorded at 450 nm is followed by 660 nm, while the reflectance is at minimum around 532 nm.

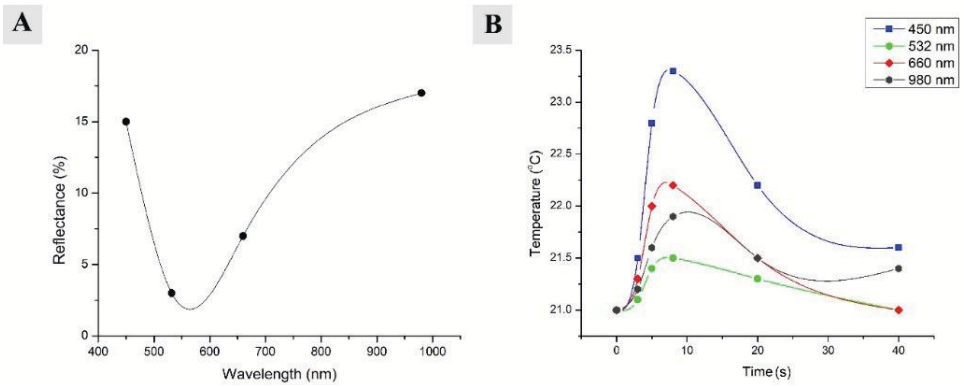


Fig. 3. A) *Apatura iris* reflectance spectrum; B) cooling dynamics as a function of time after the irradiation with four different wavelengths. The lasers have been switched on at 2nd s and switched off at 9th s in order to record heating/cooling dynamics. (Reflectance spectrum is taken from the reference 9).

The only observed discrepancy refers to the wavelength which does not belong to the visible part of the spectrum and for which completely different rules apply. The photon at 980 nm carries the energy that cannot cause any elec-

(CC) 2023 SCS.

tronic transitions but can affect the vibrational one within the system as well as thermal management by vibrational relaxation.

The observed asymmetric heating/cooling response scales perfectly with the measured reflectance response.

CONCLUSION

This paper presents an investigation of *Apatura iris*'s natural photonic structures under the light irradiation at different wavelengths. The correlation between the reflectance at different wavelengths and thermal response is revealed.

Acknowledgements. B.K., D.V., and B.B. acknowledge funding provided by the Institute of Physics Belgrade, through the institutional funding by the Ministry of Education, Science and Technological Development of the Republic of Serbia. Additionally, B.K. acknowledges support from F.R.S.-FNRS. M.P. acknowledges support from the Ministry of Education, Science and Technological Development of the Republic of Serbia (Grant No. 451-03-47/2023--01/200026). D.M. and A.R. acknowledges support from Ministry of Science, Technological Development and Innovation of the Republic of Serbia Contract number: 451-03-47/2023-01/ /200051. All authors acknowledge the support of the Office of Naval Research Global through the Research Grant N62902-22-1-2024.

ИЗВОД

ТЕРМАЛНО ИСПИТИВАЊЕ МАТЕРИЈАЛА ИЗ ЛЕПТИРА *Apatura iris*

МАРИНА СИМОВИЋ ПАВЛОВИЋ[1], МАЈА ПАЊАКО[2], ДИМИТРИЈЕ МАРА[3], АЛЕКСАНДРА РАДУЛОВИЋ[3], БОЈАНА БОКИЋ[4], ДАРКО ВАСИЉЕВИЋ[4] и БРАНКО КОЛАРИЋ[4,5]

[1]Машински факултет – Универзитет у Београду, Краљице Марије 16, Београд, [2]Институт за хемију, технологију и металургију, Универзитет у Београду, Његошева 12, Београд, [3]Институт за општу и физичку хемију, Студентски трг 12/V, Београд, [4]Центар за фотонику, Институт за физику, Универзитет у Београду, Прегревица 118, Београд и [5] Micro- and Nanophotonic Materials Group, University of Mons, Place du Parc 20, 7000 Mons, Belgium

Облик и величина материјала утичу на његове физичке, хемијске и механичке особине. Ова студија описује проучавање природних фотонских структура, крила лептира која се претежно састоје од полимера хитина. Ефекат нано коругације на оптички одговор материјала је презентован кроз термална мерења. Такође је представљена могућност примене холографске методе за праћење динамике *in situ*.

(Примљено 27. марта, ревидирано 20. априла, прихваћено 21. јула 2023)

REFERENCES

1. S.R. Mouchet, P. Vukusic, *Adv. Insect Physiol.* **54** (2018) 1 (https://doi.org/10.1016/bs.aiip.2017.11.002)
2. D. Mara, B. Bokic, T. Verbiest, S. R. Mouchet, B. Kolaric, *Biomimetics* **7** (2022) 153 (https://doi.org/10.3390/biomimetics7040153)
3. Z. Han, L. Wu, Z. Qiu, H. Guan, L. Ren, *J. Bionic Eng.* **5** (2008) 14 (https://doi.org/10.1016/S1672-6529(08)60066-9)
4. H.I. Leertouwer, B. D. Wilts, D. G. Stavenga, *Opt. Express* **19** (2011) 24061 (https://doi.org/10.1364/OE.19.024061)

(CC) 2023 SCS.

5. M. Kaya, B. Bitim, M. Mujtaba, T. Koyuncu, *Int. J. Biol. Macromol.* **81** (2015) 443 (https://doi.org/10.1016/j.ijbiomac.2015.08.021)
6. D. Pantelić, D. Grujić, D. Vasiljević, *J. Biomed. Opt.* **19** (2014) 127005 (https://doi.org/10.1117/1.JBO.19.12.127005)
7. J. Liu, W. Kuang, J. Liu, Z. Gao, S. Rohani, J. Gong, *J. Chem. Eng.* **438** (2022) 135554 (https://doi.org/10.1016/j.cej.2022.135554)
8. M. Simovic-Pavlovic, M.C. Pagnacco, D. Grujic, B. Bokic, D. Vasiljevic, S. Mouchet, T. Verbiest, B. Kolaric, *J. Vis. Exp.* (2022) e63676 (https://dx.doi.org/10.3791/63676)
9. D. Pantelić, S. Ćurčić, S. Savić-Šević, A. Korać, A. Kovačević, B. Ćurčić, B. Bokić, *Optics Express* **19** (2011) 5817 (https://opg.optica.org/oe/fulltext.cfm?uri=oe-19-7-5817#:~:text=https%3A//doi.org/10.1364/OE.19.005817).

(CC) 2023 SCS.

optics

MDPI

Article

Morphological and Optical Modification of Melanosomes in Fish Integuments upon Oxidation

Sébastien R. Mouchet [1,2,3,*,†], Fabio Cortesi [3,4,†], Bojana Bokic [5,†], Vladimir Lazovic [5], Pete Vukusic [1], N. Justin Marshall [3] and Branko Kolaric [5,6,*]

1 School of Physics, University of Exeter, Stocker Road, Exeter EX4 4QL, UK; p.vukusic@exeter.ac.uk
2 Department of Physics, Namur Institute of Structured Matter (NISM), Institute of Life, Earth and Environment (ILEE), University of Namur, Rue de Bruxelles 61, 5000 Namur, Belgium
3 Queensland Brain Institute, The University of Queensland, Brisbane, QLD 4072, Australia; f.cortesi@uq.edu.au (F.C.); justin.marshall@uq.edu.au (N.J.M.)
4 School of the Environment, The University of Queensland, Brisbane, QLD 4072, Australia
5 Center for Photonics, Institute of Physics, University of Belgrade, Pregrevica 118, 11080 Belgrade, Serbia; bojana@ipb.ac.rs (B.B.); lazovicv@ipb.ac.rs (V.L.)
6 Micro- and Nanophotonic Materials Group, University of Mons, Place du Parc 20, 7000 Mons, Belgium
* Correspondence: s.mouchet@exeter.ac.uk (S.R.M.); branko.kolaric@umons.ac.be (B.K.)
† These authors contributed equally to this work.

Abstract: Reactive oxygen species (ROS) such as superoxide radicals O_2^-, hydroxyl radicals OH^-, and hydrogen peroxide H_2O_2 may have detrimental effects on marine organisms, including their integuments and visual appearances. Although some studies have described the impact of ROS on marine ecosystems and species ecology, the influence on the optical response of the integuments of marine species and on their visual appearances remains unknown. In this article, we used histology and optical characterisation to show, for the first time, that skin melanophores (melanin-containing chromophores) of the coral reef fish, *Stegastes apicalis*, change their shapes and fluorescent proprieties upon oxidation with H_2O_2 radicals. Our observations also suggest that pheomelanosomes may occur in fish integuments, where, previously, it was thought that fish melanosomes only contain eumelanin. This investigation relied on light and electron microscopy and steady-state fluorimetry, as well as time-resolved streak imaging systems. We suggest that the changes in the morphological and spectral characteristics of melanophores can be used as a marker of physiological stress induced by environmental factors such as ROS. Moreover, *S. apicalis* may be used as a potential model for studying the interaction between the surrounding environment and natural organisms in biologically diverse ecosystems, such as the Great Barrier Reef in Australia.

Keywords: water contamination; marine pollution; clean water; water quality; ecosystem protection; coastal biodiversity; marine biodiversity; reactive oxygen species; coral reef fish; gregory; *Stegastes apicalis*; melanophores; melanosomes

check for updates

Citation: Mouchet, S.R.; Cortesi, F.; Bokic, B.; Lazovic, V.; Vukusic, P.; Marshall, N.J.; Kolaric, B. Morphological and Optical Modification of Melanosomes in Fish Integuments upon Oxidation. *Optics* **2023**, *4*, 563–572. https://doi.org/10.3390/opt4040041

Academic Editor: Manuel Jesús Hermoso-Orzáez

Received: 30 June 2023
Revised: 25 October 2023
Accepted: 30 October 2023
Published: 1 November 2023

Copyright: © 2023 by the authors. Licensee MDPI, Basel, Switzerland. This article is an open access article distributed under the terms and conditions of the Creative Commons Attribution (CC BY) license (https://creativecommons.org/licenses/by/4.0/).

1. Introduction

Colors in nature play an essential role in various biological phenomena such as visual communication, camouflage, and aposematism [1–3]. Their origin may be either pigmentary or structural. In fishes, colors originate from different cells in the skin, chromatophores (i.e., containing pigments), leucophores (i.e., comprising light scatterers), and iridophores (containing photonic structures), and from the structure of the scales covering a fish's body [1,3–7]. In addition to pigments, fish integuments can also emit light at different wavelengths by fluorescence decay [8–10]. Fishes use colors and patterns, amongst others, for social communication, mimicry, or camouflage and background adaptation [11–14].

Reactive oxygen species (ROS) such as superoxide radicals (O_2^-), hydroxyl radicals (OH^-), and non-radical hydrogen peroxide (H_2O_2) significantly impact sea organisms [15–18], including their integuments. ROS can be produced in seawater via various

abiotic and biotic processes, leading to the ionisation of organic or inorganic compounds, including the metabolisms of phytoplankton [19]; photolysis of water molecules; or radiolysis arising, e.g., from cosmic rays or ^{40}K decay [15,16]. In addition, climate changes and anthropogenic marine pollution appear to increase the concentration of ROS in seawater, especially in surface layers [18,20,21].

Despite the observed effect of ROS on marine organisms [15–18], how ROS affect the visual appearance and the optical proprieties of animal skin had not yet been described. In this study, we investigated the influence of ROS on the skin melanophores occurring in a marine fish, namely *Stegastes apicalis* (De Vis, 1885), through histological and optical characterization. This damselfish species of the family Pomacentridae, commonly known as the Australian gregory or the yellowtip gregory, lives on the Great Barrier Reef off the Australian East coast, in depths of 1–5 m. *S. apicalis* has a dark brown body coloration, with yellow, orange, or red margins on the dorsal fin and the tip of the upper lobe of the caudal fin (Figure 1a) [22]. Melanophores are cells that appear black or dark brown, as they contain vesicles of melanin called melanosomes within the cytoplasm [23,24]. This research allowed us to get insights into the naturally occurring interactions between the surrounding environment and the visual appearances of marine animals, by tracking the physical and optical properties of the fish melanophores upon oxidation with H_2O_2 [25], akin to oxidation with ROS within the marine environment. The goal of our study was to highlight the potential effects of oxidation on the visual appearance and optical properties of the integuments of a marine species. Since this study is a new topic of research, we aim at setting a baseline upon which future research using more naturalistic scenarios can build. In addition, microscope-based observations of the integuments unveiled the likely presence of pheomelanosomes, contradicting the common assumption that fish melanophores purely consist of eumelansosomes [23]. Finally, the changes that we found in this study can serve as an indicator of environmentally induced physiological stress. Hence, *S. apicalis* emerges as a potential model to study the effects of ROS and similar stressors on the reef.

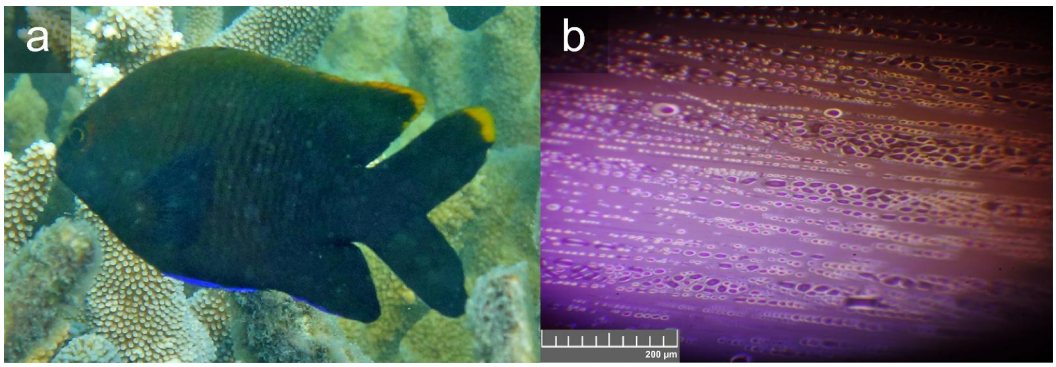


Figure 1. (**a**) *Stegastes apicalis* displays a brown color in daylight with yellow, orange, or red margins on its dorsal fin and the tip of the upper lobe of its caudal fin. (**b**) The brown color is due to melanophores occurring in the integuments of the fish; (**a**) was reproduced from Dr Anne Hoggett, https://commons.wikimedia.org/wiki/File:StegastApicalAnneHoggett.jpg, accessed on 26 June 2023.

2. Materials and Methods

2.1. Sample Preparation and Treatment

Specimens ($n = 4$) of *S. apicalis* were collected (GBRMPA permit number G17/381601; fishery permit number 180731) off the coast of Lizard Island, Queensland, Australia (S 14°41′16.5″, E 145°27′09.6″), at depth of 1–4 m in August 2018. All four dorsal fins were fixed overnight in a 0.01 M phosphate buffer solution (PBS) containing 4% paraformaldehyde (PFA) and 2.5% glutaraldehyde (GA) before being transferred to a PBS solution with a pH ranging from 7.2 to 7.4. Such fixation protocols are widespread in the scientific literature for histological observations of melanosomes in biological organisms, including fish [26–30]. Ideally, our study should have been carried out with fresh or living tissues. However, in this pioneering study, practical feasibility left us with no choice but to fix the

samples. Small areas of the dorsal fins were sampled using a scalpel and tweezers that are typically used for atomic force and electron microscopy following a standard procedure for the integuments of other biological organisms [31,32]. The tools were cleaned with 99.9999% isopropyl alcohol (IPA) prior to dissection. To assess the effect of the oxidative agent on the fluorescence emission from the integuments, some samples were incubated for 5 h in a 10% H_2O_2 weak-acid solution (pH between 4.5 and 5.0).

2.2. Light Microscopy

The instrument is based on a modified JENAVAL microscopic frame (manufactured by Carl Zeiss, Munich, Germany). The sample was placed on the existing mechanical stage, which was powered by a stepper motor, moving the sample vertically, with a 0.3-µm resolution. The removable prism deflected the beam and enabled the capture of bright field images on a Canon EOS 50D (Tokyo, Japan) digital camera. The images were recorded in reflection mode with a $40 \times \backslash 0.65$ objective.

2.3. Scanning Electron Microscopy

The histological observations were performed using a Tescan MIRA3 (Brno, Czech Republic) high-resolution field emission scanning electron microscope (FEG-SEM) with an accelerating voltage lower than 29 kV. Prior to any observation, the surface of samples was coated with a 2–3-nm-thin gold layer using a Quorum Technologies SC7620 Mini (Lewes, United Kingdom) sputter coater to prevent charging effects.

2.4. Time-Resolved and Steady-State Fluorimetry

The fluorimetry analysis was conducted using a pulsed light beam produced by a tunable Nd:YAG laser system (duration of 5 ns and repetition rate of 10 Hz) and by an FLSP920 UV–Vis–NIR spectrometer device (manufactured by Edinburgh Instruments, Livingston, UK). In the latter case, time-resolved measurements were recorded using a 60-W xenon lamp operating at a frequency of 100 Hz, and a Hamamatsu R928P (Hamamatsu City, Japan) photomultiplier tube was used to detect the emission signal in the visible region. In the former case, an optical parametric oscillator (OPO) was pumped by the fourth harmonic of the laser at 266 nm. The output of the OPO could be continuously tuned over a spectral range from 320 nm to 475 nm, and served as excitation beam. A time-resolved streak imaging system acquired the fluorescence steady-state emission spectra from the samples as a function of time. Full widths at half maximum (FWHM) were estimated using Origin 8.5.0 software, assuming a Gaussian function. The time-resolved streak imaging system used a Princeton Instruments SpectraPro 2300i (Trenton, NJ, USA) spectrograph, a Hamamatsu C4334-01 streak camera system, and the High-Performance Digital Temporal Analyzer Streak Camera Control software. The fundamental advantage of the streak camera is its two-dimensional nature that enables the acquisition of the temporal evolution of laser-induced phenomena. The camera was equipped with an image intensifier so that single photons could be detected, allowing the measurement of very-low-fluorescence intensities from the analyzed sample. The excitation and detection optical axes were aligned using a beam splitter to make it possible to adjust the angle of the excitation beam with respect to the sample surface, allowing a high sensitivity of detection using the single-mode fibers. The streak images were acquired in photon-counting mode with 1300 expositions. The time-resolved emission dynamics were observed at the maximum of the emission peak and fitted to single exponential functions, enabling the assessment of the related decay times using Origin software. Such fits by single exponential functions indicate that the excited molecules do not give rise to any non-radiative decay [33].

3. Results and Discussions

The integuments of the brown parts of the *S. apicalis* dorsal fin exhibit dark spots when observed by optical microscopy (Figure 1b). These spots are due to melanophores that contain melanin vesicles, called melanosomes, that abundantly cover the surface of the scales (Figure 2a) [34–38]. In nature, there are two types of melanosomes: eumelanosomes and pheomelanosomes. The former are rod-shaped and contain eumelanin, giving rise to black, dark brown, gray, and blonde appearances. The latter are spherical and contain pheomelanin, leading to red and brown colorations. In the case of the *S. apicalis* dorsal fin, the observed organelles were spherical with a diameter of 450–500 nm, likely corresponding to pheomelanosomes (Figure 2a). The consensus in the scientific community is that fish melanosomes only contain eumelanin [39]. However, it has previously been suggested that phenomelanin occurs in the integuments of a strain of the common carp (*Cyprinus carpio*) [40]. It is likely that pheomelanin in fishes is more common than assumed. Future studies accounting for phylogeny and species richness should be conducted to investigate its prevalence in fishes.

In addition to light absorption, melanin, as a polymer, and regardless of the type, is also believed to strengthen biological materials, thanks to covalent cross-linking processes [41–48]. For instance, melanin in birds has been shown to contribute to the mechanical properties of feathers [42,45–47].

Melanins usually do not fluoresce in their natural state under excitation by visible or UV light [49,50]. However, under excitation by UV light with a wavelength within the range of 340–380 nm, the *S. apicalis* integuments surprisingly emitted light (Figure 3a,c). The main advantage of using the streak camera as a detection system in fluorescence experiments lies in the fact that it allows the simultaneous recording of the time-resolved fluorescence spectra responses (Figure 4). The emission peaks of the *S. apicalis* integuments were found to be located in the range of 474–478 nm with a FWHM ranging from 86 nm to 101 nm. This light emission corresponds to fluorescence, with a decay time of about 2.2–2.7 ns (Table 1). We believe that this is mostly due to the autofluorescence of molecules such as collagen, flavins, and reduced nicotinamide adenine dinucleotide (NADH) [51,52]. In particular, the NADH fluorescence spectrum matches our measurements [52].

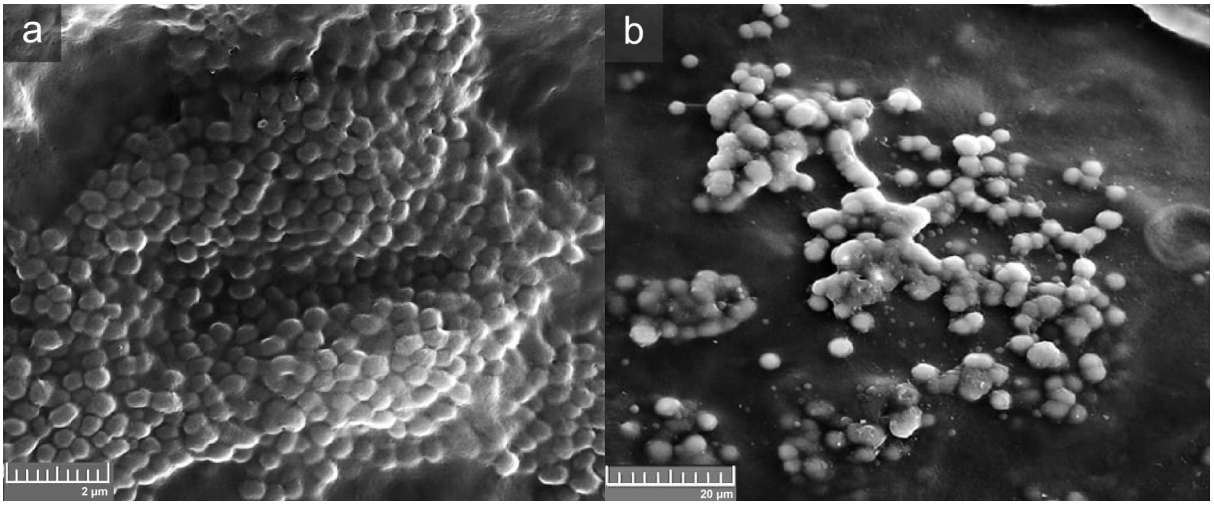


Figure 2. Representative micrographs of *Stegastes apicalis* dorsal fin skin sections. (**a**) Melanin granules, called melanosomes, are found in the integuments of the *S. apicalis* dorsal fin, as observed here by scanning electron microscopy, prior to oxidation by H_2O_2. (**b**) Upon oxidation by H_2O_2, these melanosomes agglomerate. Please note that (**a**,**b**) correspond to different magnifications.

Upon oxidation by H_2O_2, both the structure and the optical properties of the melanosomes were modified. Histologically, they agglomerated into more substantial and connected structures (Figure 2b). In addition, the fluorescence emission spectra of the fish integuments were modified in terms of shape, peak position, and FWHM (Figure 3b). When excited with UV light (from 340 to 380 nm), the emission peaks were longer shifted in the range of 523–531 nm, with a larger FWHM of 122–130 nm. The decay time (Figure 3d and Table 1) was also significantly shorter (from 1.66 to 2.02 ns), as also seen on the streak camera (Figure 4). The different values of peak location, FWHM, and decay time qualitatively indicate that, when treated with H_2O_2, very different states were excited, resulting in significantly different relaxation kinetics. Most likely, the difference in the fluorescent signals was caused by different chemical entities.

On one hand, the oxidation of melanin is known to give rise to fluorescence [50,53,54]. The spectra measured in this study are very close to the spectra reported for oxidized melanin [50,54]. Organic fluorophores and pigments like melanin are usually cyclic or polycyclic compounds with OH and COOH functional groups [33,54]. These groups are possible sites for reduction–oxidation reactions [25,54,55] caused by reactive peroxide and oxygen anions arising from H_2O_2 decomposition. Oxidation by H_2O_2 affects the electronic configuration of the molecules, leading to fluorescence emission. On the other hand, the oxidation process quenches the autofluorescence from some of the fluorescent materials of the fish integuments. ROS, therefore, have a direct influence on the integumental structure and the chromophores of *S. apicalis*. The fluorescence emission measured in this study are likely to be negligible for the signaling and behavior of *S. apicalis*. This is because the quantum yields of natural fluorophores are usually low [56–60], UV light propagates only over short distances in seawater [61], and the proportion of UV light in sunlight and moonlight is limited (i.e., there are ca. 6% of UV and 50% of visible light in the sunlight at sea level) [62]. However, oxidation affects the fluorescence emission of the fish integuments and most likely their color, which could affect the ecology and behavior of fishes, including in intra- and interspecific communication, temperature control, reproduction, and survival. Moreover, older fishes may be more impacted by such ROS oxidation, due to the longer exposure time. This might explain the degradation of their visual appearance and the loss of color during aging. Further physiological and behavioral investigations are needed to test these hypotheses with living animals in their natural marine environment. If the fluorescence emission may only be a likely by-product of another biological function, it could be exploited to detect, identify, and quantify the effects of ROS on fish integuments.

Table 1. Upon oxidation, the fluorescence response of the *Stegastes apicalis* dorsal fin integuments changed in terms of shape, peak wavelength λ_{max}, decay time τ, and FWHM.

	Wavelength (nm)			
	340	**360**	**370**	**380**
$\lambda_{max,\ no\ oxidation}$ (nm)	474	476	474	478
$\lambda_{max,\ oxidation}$ (nm)	523	524	528	531
$\tau_{no\ oxidation}$ (ns)	2.70	2.25	2.69	2.61
$\tau_{oxidation}$ (ns)	1.66	1.75	1.92	2.02
$FWHM_{no\ oxidation}$ (nm)	93	94	86	101
$FWHM_{oxidation}$ (nm)	122	130	126	126

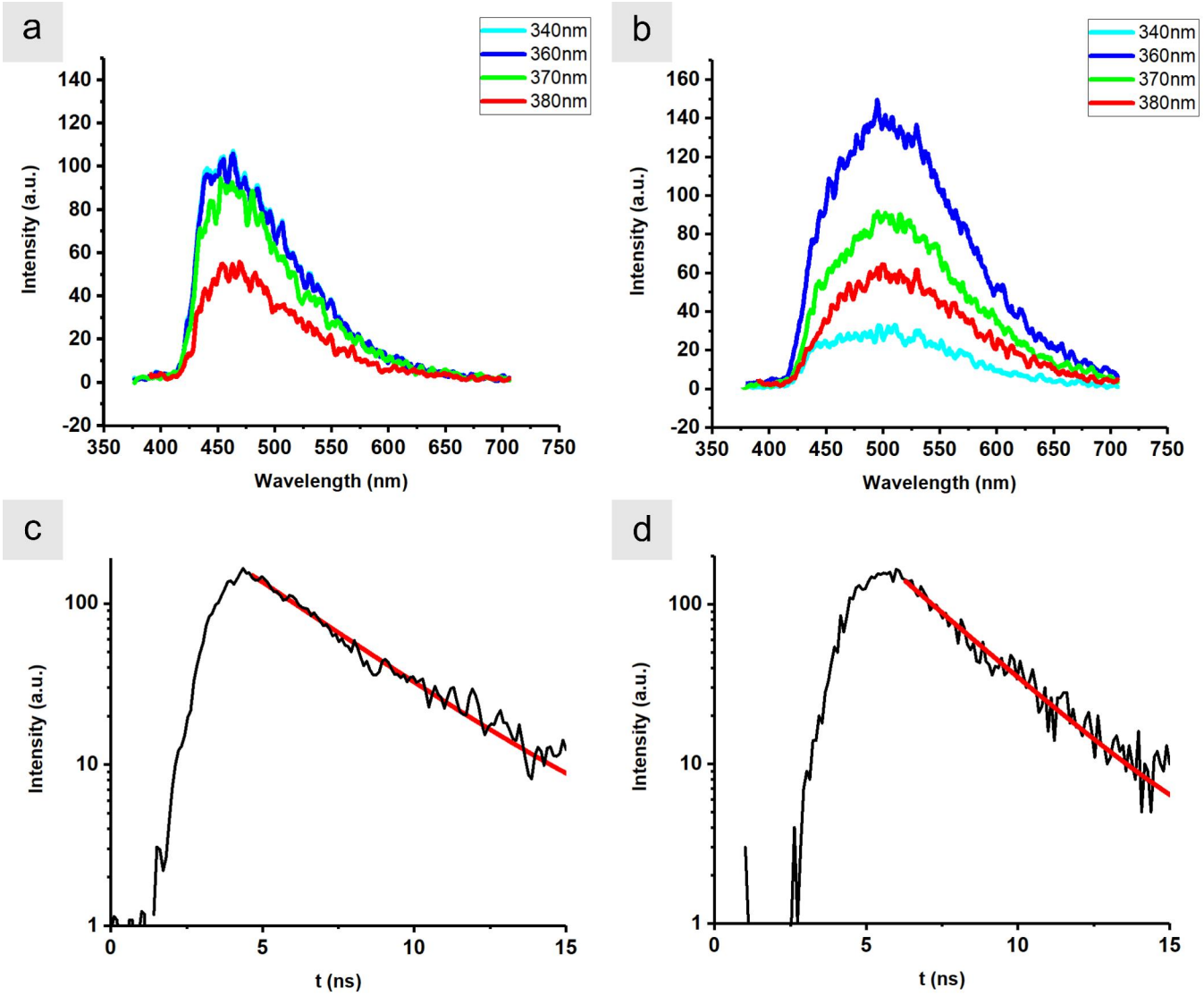


Figure 3. Upon excitation by UV light (the wavelength of which ranged from 340 nm to 380 nm), the integuments of the *Stegastes apicalis* dorsal fin emitted light by fluorescence. (**a**) The emission peak was located around 475 nm, with a FWHM of ca. 90-95 nm. (**b**) Upon oxidation by H_2O_2, the emission peak changed shape and shifted to ca. 530 nm, with a FWHM larger than 120 nm. The time-resolved measurements of the emitted intensities with an excitation wavelength of 360 nm were fitted with single exponential functions (the quality of the fits is given by coefficients of determination $R^2 = 0.980$ (**c**) and $R^2 = 0.983$ (**d**), respectively), allowing the assessment of the decay times of the integuments (**c**) before and (**d**) after oxidation.

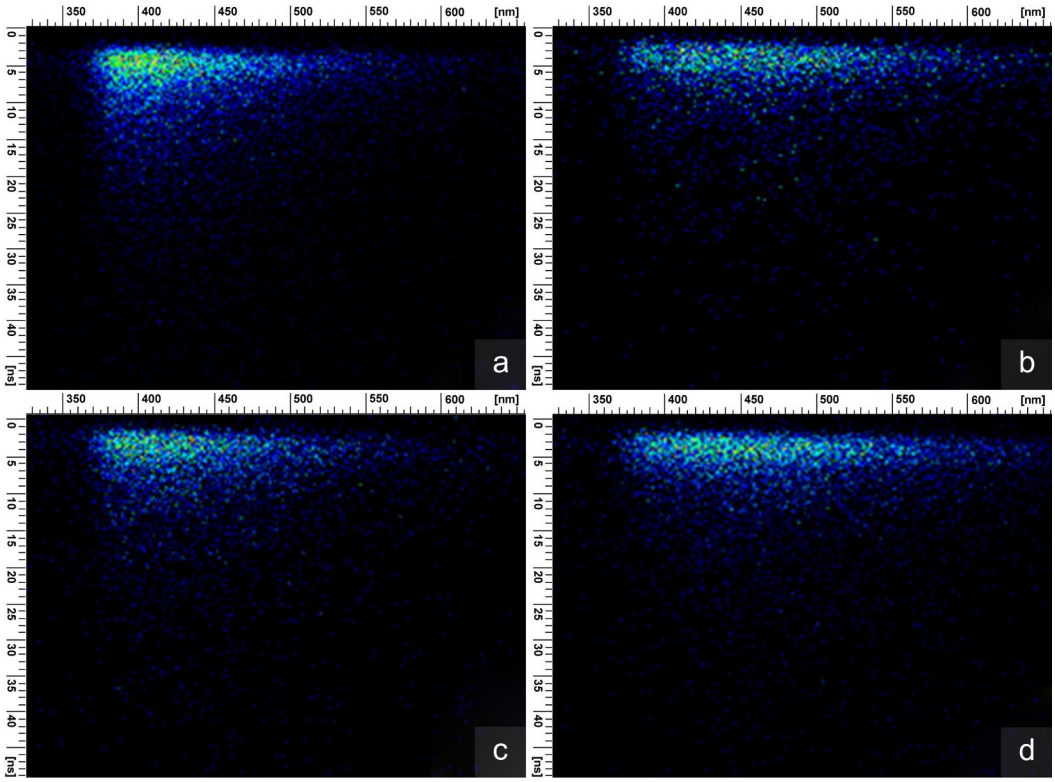


Figure 4. Upon oxidation with H_2O_2, the time-resolved fluorescence response of the *Stegastes apicalis* dorsal fin integuments considerably changes. Fluorescence emission was recorded with a streak camera with various excitation wavelengths, before (**a**,**c**) and after (**b**,**d**) oxidation. Horizontal profiles represent emission spectra and vertical profiles represent time-resolved measurements at selected excitation and emission wavelengths. (**a**) $\lambda_{ex} = 340$ nm before oxidation, (**b**) $\lambda_{ex} = 340$ nm after oxidation, (**c**) $\lambda_{ex} = 360$ nm before oxidation, (**d**) $\lambda_{ex} = 360$ nm after oxidation.

4. Conclusions

This study contributes to the growing body of scientific literature describing the effects of oxidation on biological organisms under different environmental stressors. We first observed the presence of spherical melanosomes in the integuments of *S. apicalis*, which most likely correspond to pheomelanosomes. As it appears that pheomelanin in fishes could be more common than assumed, we call for future investigations accounting for phylogeny and species richness to establish its prevalence in fishes. In addition, and most importantly, we provide some of the first data on how ROS might impact the visual appearance of biological organisms in the marine environment. Following the oxidation of the integuments, the observed pheomelanosomes agglomerated and the fluorescence response was considerably modified, most likely due to the quenching of the integuments' autofluorescence and the activation of fluorescence in the oxidized melanin. Hence, these changes can be tracked as markers for physiological stress caused by the surrounding environment, such as ROS. *S. apicalis* is here identified as a potential model for highlighting the consequences of such stress. The baseline data on how ROS affect the color of fishes that we have provided here create the possibility for more detailed investigations into the effects of ROS under natural conditions (e.g., clean versus polluted seawater). They also provide avenues to study, in detail, the ROS-induced agglomeration of melanosomes and the effects that changes in pH (e.g., due to ocean acidification) might have on these processes, as well as understanding the contributions from biotic and abiotic processes, including metabolic paths in marine environments.

Author Contributions: Conceptualization, S.R.M. and B.K.; methodology, S.R.M., V.L. and B.K.; validation, S.R.M., F.C., V.L., P.V., N.J.M. and B.K.; formal analysis, S.R.M., B.B., V.L. and B.K.; investigation, B.B. and V.L.; resources, S.R.M., F.C., N.J.M. and B.K.; data curation, B.B. and V.L.; writing—original draft preparation, S.R.M., V.L. and B.K.; writing—review and editing, F.C., P.V. and N.J.M.; visualization, B.B. and V.L.; supervision, B.K.; project administration, S.R.M. and B.K.; funding acquisition, S.R.M., F.C., N.J.M. and B.K. All authors have read and agreed to the published version of the manuscript.

Funding: S.R.M. was supported by the Belgian National Fund for Scientific Research (FRS-FNRS) (91400/1.B.309.18F) and a BEWARE Fellowship (Convention n°2110034) of the Walloon Region (COFUND Marie Skłodowska-Curie Actions of the European Union #847587) as a Postdoctoral Researcher. S.R.M. acknowledges a grant of the Agathon De Potter Fund of the Royal Academy of Science, Letters and Fine Arts of Belgium, a travel grant of FRS-FNRS, and a grant from the Namur Institute of Structured Matter (NISM). F.C. and N.J.M. were supported by the Australian Research Council (DE200100620 and FL140100197, respectively). BB and BK acknowledge the support of the of the EU: the EIC Pathfinder Challenges 2022 call through the Research Grant 101115149 (project ARTEMIS), the Office of Naval Research Global through the Research Grant N62902-22-1-2024 and the Ministry of Science, Technological Development and Innovation of the Republic of Serbia. B.K. also acknowledges financial support from FRS-FNRS; Inter-university Attraction Pole: Photonics@be (P7-35, Belgian Science Policy Office). The supporting bodies played no role in the design of the study, the collection of the samples, the analysis and interpretation of the data, and the writing of the manuscript.

Institutional Review Board Statement: The animal study protocol was approved by the Animal Ethics Committees of the Queensland Brain Institute of The University of Queensland (QBI/304/16-2018) and of the University of Belgrade (2019). The samples were collected in the framework of the Great Barrier Reef Marine Park Authority (GBRMPA) permit number G17/38160.1 and Fisheries Queensland permit number 180731. This research complies with European Community (EC) health rules as regards animal by-products and derived products not intended for human consumption (Regulation (EC) n°1069/2009—University of Namur, n°BE 705/0089).

Data Availability Statement: The data that support the findings of this study are available from the authors, upon reasonable request.

Acknowledgments: We acknowledge the Dingaal, Ngurrumungu, and Thanhil peoples as traditional owners of the lands and waters of the Lizard Island region from where the specimens were collected. We would like to thank the staff at Lizard Island Research Station (LIRS), Anne Hoggett, and Lyle Vail for support during field work. All authors acknowledge the help of colleagues from the Institute of Physics in Serbia and the KULeuven in Belgium in the preliminary phase of the presented study.

Conflicts of Interest: The authors declare no conflict of interest.

References

1. Kinoshita, S. *Structural Colors in the Realm of Nature*; World Scientific: Singapore, 2008.
2. Mouchet, S.R.; Vukusic, P. Structural colours in lepidopteran scales. In *Advances in Insect Physiology*; Elsevier: London, UK, 2018; Volume 54, pp. 1–53. [CrossRef]
3. Mouchet, S.R.; Deparis, O. *Natural Photonics and Bioinspiration*; Artech House: Norwood, MA, USA, 2021. Available online: https://us.artechhouse.com/Natural-Photonics-and-Bioinspiration-P2221.aspx (accessed on 28 June 2023).
4. Denton, E. Reflectors in Fishes. *Sci. Am.* **1971**, *224*, 64–72. [CrossRef]
5. Brown, F., Jr. Chromatophores and color change. In *Comparative Animal Physiology*; WB Saunders: Philadelphia, PA, USA, 1973; pp. 915–950.
6. Hawkes, J.W. The structure of fish skin. *Cell Tissue Res.* **1974**, *149*, 147–158. [CrossRef] [PubMed]
7. Kelsh, R.N.; Schmid, B.; Eisen, J.S. Genetic analysis of melanophore development in zebrafish embryos. *Dev. Biol.* **2000**, *225*, 277–293. [CrossRef]
8. Michiels, N.; Anthes, N.; Hart, N.; Herler, J.; Meixner, A.J.; Schleifenbaum, F.; Schulte, G.; Siebeck, U.E.; Sprenger, D.; Wucherer, M.F. Red fluorescence in reef fish: A novel signalling mechanism? *BMC Ecol.* **2008**, *8*, 16. [CrossRef] [PubMed]
9. Lagorio, M.G.; Cordon, G.B.; Iriel, A. Reviewing the relevance of fluorescence in biological systems. *Photochem. Photobiol. Sci.* **2015**, *14*, 1538–1559. [CrossRef]
10. Marshall, J.; Johnsen, S. Fluorescence as a means of colour signal enhancement. *Philos. Trans. R. Soc. B Biol. Sci.* **2017**, *372*, 20160335. [CrossRef]
11. Bond, C. *Biology of Fishes*; WB Sounders Company: Philadelphia, PA, USA, 1979.

12. Stepien, C.A. Color pattern and habitat differences between male, female and juvenile giant kelpfish (Blennioidei: Clinidae). *Bull. Mar. Sci.* **1987**, *41*, 45–58.
13. Hakkinen, J.; Korhonen, H.; Oikari, A.; Karjalainen, J. Melanin concentrations in vendace (*Coregonus albula*) Whitefish (*Coregonus lavaretus*) Larvae Five Boreal lakes with different optical properties. *Boreal Environ. Res.* **2003**, *8*, 193–202.
14. Stieb, S.M.; Cortesi, F.; Sueess, L.; Carleton, K.L.; Salzburger, W.; Marshall, N.J. Why UV vision and red vision are important for damselfish (Pomacentridae): Structural and expression variation in opsin genes. *Mol. Ecol.* **2017**, *26*, 1323–1342. [CrossRef]
15. Blough, N.V.; Zepp, R.G. Reactive oxygen species in natural waters. In *Active Oxygen in Chemistry*; Springer: Dordrecht, the Netherlands, 1995; pp. 280–333.
16. Manjun, Z. Determination of photochemically-generated reactive oxygen species in natural water. *J. Environ. Sci.* **2009**, *21*, 303–306.
17. Kieber, D.J.; Peake, B.; Scully, N.M. Reactive oxygen species in aquatic ecosystems. In *UV Effects in Aquatic Organisms and Ecosystems*; Helbling, E.W., Ed.; Royal Society of Chemistry: London, UK, 2003; pp. 251–276.
18. Morris, J.J.; Rose, A.L.; Lu, Z. Reactive oxygen species in the world ocean and their impacts on marine ecosystems. *Redox Biol.* **2022**, *52*, 102285. [CrossRef] [PubMed]
19. Fan, S.M. Photochemical and biochemical controls on reactive oxygen and iron speciation in the pelagic surface ocean. *Mar. Chem.* **2008**, *109*, 152–164. [CrossRef]
20. Müller, R.; Desel, C.; Steinhoff, F.S.; Wiencke, C.; Bischof, K. UV-radiation and elevated temperatures induce formation of reactive oxygen species in gametophytes of cold-temperate/Arctic kelps (Laminariales, Phaeophyceae). *Phycol. Res.* **2012**, *60*, 27–36. [CrossRef]
21. Celis-Plá, P.S.; Moenne, F.; Rodríguez-Rojas, F.; Pardo, D.; Lavergne, C.; Moenne, A.; Brown, M.T.; Huovinen, P.; Gómez, I.; Navarro, N.; et al. Antarctic intertidal macroalgae under predicted increased temperatures mediated by global climate change: Would they cope? *Sci. Total Environ.* **2020**, *740*, 140379. . [CrossRef]
22. Allen, G.R.; Emery, A.R. A review of the pomacentrid fishes of the genus *Stegastes* from the Indo-Pacific, with descriptions of two new species. In *Indo-Pacific Fishes*; Bishop Museum: Honolulu, HI, USA, 1985, Volume 3, pp. 1–31.
23. Sköld, H.N.; Aspengren, S.; Cheney, K.L.; Wallin, M. Fish Chromatophores—From Molecular Motors to Animal Behavior. *Int. Rev. Cell Mol. Biol.* **2016**, *321*, 171–219. [CrossRef]
24. Salis, P.; Lorin, T.; Laudet, V.; Frédérich, B. Magic Traits in Magic Fish: Understanding Color Pattern Evolution Using Reef Fish. *Trends Genet.* **2019**, *35*, 265–278. [CrossRef]
25. Smith, R.; Garrett, B.; Naqvi, K.; Fülöp, A.; Godfrey, S.; Marsh, J.; Chechik, V. Mechanistic insights into the bleaching of melanin by alkaline hydrogen peroxide. *Free Radic. Biol. Med.* **2017**, *108*, 110–117. [CrossRef]
26. Goda, M.; Fujii, R. Coloration and Chromatophores of the Domino Damsel, *Dascyllus trimaculatus*. *Zool. Sci.* **2001**, *18*, 165–174. [CrossRef]
27. Futter, C.E.; Ramalho, J.S.; Jaissle, G.B.; Seeliger, M.W.; Seabra, M.C. The Role of Rab27a in the Regulation of Melanosome Distribution within Retinal Pigment Epithelial Cells. *Mol. Biol. Cell* **2004**, *15*, 2264–2275. [CrossRef]
28. Franzen, A.J.; Cunha, M.M.; Miranda, K.; Hentschel, J.; Plattner, H.; da Silva, M.B.; Salgado, C.G.; de Souza, W.; Rozental, S. Ultrastructural characterization of melanosomes of the human pathogenic fungus *Fonsecaea pedrosoi*. *J. Struct. Biol.* **2008**, *162*, 75–84. [CrossRef]
29. Amiri, M.; Shaheen, H.M. Chromatophores and color revelation in the blue variant of the Siamese fighting fish (*Betta splendens*). *Micron* **2012**, *43*, 159–169. [CrossRef] [PubMed]
30. Ali, S.A.; Naaz, I. Comparative light and electron microscopic studies of dorsal skin melanophores of Indian toad, *Bufo melanostictus*. *J. Microsc. Ultrastruct.* **2014**, *2*, 230–235. [CrossRef]
31. Mouchet, S.R.; Van Hooijdonk, E.; Welch, V.L.; Louette, P.; Colomer, J.F.; Su, B.L.; Deparis, O. Liquid-induced colour change in a beetle: The concept of a photonic cell. *Sci. Rep.* **2016**, *6*, 19322. [CrossRef]
32. Dhungel, B.; Ohno, Y.; Matayoshi, R.; Iwasaki, M.; Taira, W.; Adhikari, K.; Gurung, R.; Otaki, J.M. Distal-less induces elemental color patterns in *Junonia* butterfly wings. *Zool. Lett.* **2016**, *2*, 4. [CrossRef]
33. Lakowicz, J.R. Introduction to fluorescence. In *Principles of Fluorescence Spectroscopy*; Springer: New York, NY, USA, 1999; pp. 1–23.
34. Lindgren, J.; Moyer, A.; Schweitzer, M.H.; Sjövall, P.; Uvdal, P.; Nilsson, D.E.; Heimdal, J.; Engdahl, A.; Gren, J.A.; Schultz, B.P.; et al. Interpreting melanin-based coloration through deep time: A critical review. *Proc. R. Soc. B Biol. Sci.* **2015**, *282*, 20150614. [CrossRef] [PubMed]
35. Donatti, L.; Fanta, E. Morphology of the retina in the freshwater fish *Metynnis Roosevelti* Eiggenmann (Characidae, Serrasalminae) and the effects of monochromatic red light. *Rev. Bras. Zool.* **1999**, *16*, 151–173. [CrossRef]
36. Kawauchi, H. Functions of Melanin-Concentrating Hormone in Fish. *J. Exp. Zool.* **2006**, *305A*, 751–760. [CrossRef]
37. Wolnicka-Glubis, A.; Pecio, A.; Podkowa, D.; Kolodziejczyk, L.M.; Plonka, P.M. Pheomelanin in the skin of *Hymenochirus Boettgeri* (Amphibia: Anura: Pipidae). *Exp. Dermatol.* **2012**, *21*, 535–561. [CrossRef]
38. Colleary, C.; Dolocan, A.; Gardner, J.; Singh, S.; Wuttke, M.; Rabenstein, R.; Habersetzer, J.; Schaal, S.; Feseha, M.; Clemens, M.; et al. Chemical, experimental, and morphological evidence for diagenetically altered melanin in exceptionally preserved fossils. *Proc. Natl. Acad. Sci. USA* **2015**, *112*, 12592–12597. [CrossRef]
39. Kottler, V.A.; Künstner, A.; Schartl, M. Pheomelanin in fish? *Pigment Cell Melanoma Res.* **2015**, *28*, 355–356. [CrossRef]

40. Xu, P.; Zhang, X.; Wang, X.; Li, J.; Liu, G.; Kuang, Y.; Xu, J.; Zheng, X.; Ren, L.; Wang, G.; et al. Genome sequence and genetic diversity of the common carp, *Cyprinus Carpio*. *Nat. Genet.* **2014**, *46*, 1212–1219. [CrossRef]
41. Riley, P. Materia Melanica: Further Dark Thoughts. *Pigment Cell Res.* **1992**, *5*, 101–106. . [CrossRef] [PubMed]
42. Bonser, R.H.C. Melanin and the Abrasion Resistance of Feathers. *Condor* **1995**, *97*, 590–591.
43. Liu, Y.; Hong, L.; Wakamatsu, K.; Ito, S.; Adhyaru, B.; Cheng, C.Y.; Bowers, C.R.; Simon, J.D. Comparison of Structural and Chemical Properties of Black and Red Human Hair Melanosomes. *Photochem. Photobiol.* **2005**, *81*, 135–144. . [CrossRef] [PubMed]
44. Moses, D.N.; Harreld, J.H.; Stucky, G.D.; Waite, J.H. Melanin and Glycera Jaws. *J. Biol. Chem.* **2006**, *281*, 34826–34832. [CrossRef] [PubMed]
45. Schreiber, R.W.; Schreiber, E.A.; Peele, A.M.; Burtt, Edward, H.J. Pattern of Damage to Albino Great Frigatebird Flight Feathers Supports Hypothesis of Abrasion by Airborne Particles. *Condor* **2006**, *108*, 736–741. [CrossRef]
46. Pannkuk, E.L.; Siefferman, L.M.; Butts, J.A. Colour phases of the eastern screech owl: A comparison of biomechanical variables of body contour feathers. *Funct. Ecol.* **2010**, *24*, 347–353. . [CrossRef]
47. Galván, I.; Solano, F. Bird Integumentary Melanins: Biosynthesis, Forms, Function and Evolution. *Int. J. Mol. Sci.* **2016**, *17*. [CrossRef]
48. Wang, Y.; Li, T.; Wang, X.; Ma, P.; Bai, H.; Dong, W.; Xie, Y.; Chen, M. Superior Performance of Polyurethane Based on Natural Melanin Nanoparticles. *Biomacromolecules* **2016**, *17*, 3782–378. [CrossRef]
49. Huang, Z.; Zeng, H.; Hamzavi, I.; Alajlan, A.; Tan, E.; McLean, D.I.; Lui, H. Cutaneous melanin exhibiting fluorescence emission under near-infrared light excitation. *J. Biomed. Opt.* **2006**, *11*, 034010. [CrossRef]
50. Fernandes, B.; Matamá, T.; Guimarães, D.; Gomes, A.; Cavaco-Paulo, A. Fluorescent quantification of melanin. *Pigment Cell Melanoma Res.* **2016**, *29*, 707–712. [CrossRef] [PubMed]
51. Zellweger, M.; Goujon, D.; Conde, R.; Forrer, M.; van den Bergh, H.; Wagnières, G. Absolute autofluorescence spectra of human healthy, metaplastic, and early cancerous bronchial tissue *in vivo*. *Appl. Opt.* **2001**, *40*, 3784–3791. [CrossRef] [PubMed]
52. Pu, Y.; Wang, W.; Yang, Y.; Alfano, R.R. Native fluorescence spectra of human cancerous and normal breast tissues analyzed with non-negative constraint methods. *Appl. Opt.* **2013**, *52*, 1293–1301. [CrossRef]
53. Sachs, H.W. Über die autogenen Pigmente, besonders das Lipofuscin und seine Abrenzung von Melanin. *Beitr. Pathol. Anat. Allg. Pathol.* **1943**, *108*, 268–314.
54. Kayatz, P.; Thumann, G.; Luther, T.T.; Jordan, J.F.; Bartz–Schmidt, K.U.; Esser, P.J.; Schraermeyer, U. Oxidation Causes Melanin Fluorescence. *Investig. Ophthalmol. Vis. Sci.* **2001**, *42*, 241–246.
55. Sarathy, S.R.; Mohseni, M. The impact of UV/H_2O_2 advanced oxidation on molecular size distribution of chromophoric natural organic matter. *Environ. Sci. Technol.* **2007**, *41*, 8315–8320. [CrossRef]
56. Iriel, A.; Lagorio, M.G. Is the flower fluorescence relevant in biocommunication? *Naturwissenschaften* **2010**, *97*, 915–924. [CrossRef]
57. Iriel, A.; Lagorio, M.G. Implications of reflectance and fluorescence of *Rhododendr. Indicum* Flowers Biosignaling. *Photochem. Photobiol. Sci.* **2010**, *9*, 342–348. [CrossRef]
58. Taboada, C.; Brunetti, A.E.; Pedron, F.N.; Carnevale Neto, F.; Estrin, D.A.; Bari, S.E.; Chemes, L.B.; Peporine Lopes, N.; Lagorio, M.G.; Faivovich, J. Naturally occurring fluorescence in frogs. *Proc. Natl. Acad. Sci. USA* **2017**, *114*, 3672–3677. [CrossRef]
59. Ladouce, M.; Barakat, T.; Su, B.L.; Deparis, O.; Mouchet, S.R. Scattering of ultraviolet light by avian eggshells. *Faraday Discuss.* **2020**, *223*, 63–80. [CrossRef]
60. Mouchet, S.R.; Verstraete, C.; Bokic, B.; Mara, D.; Dellieu, L.; Orr, A.G.; Deparis, O.; Van Deun, R.; Verbiest, T.; Vukusic, P.; et al. Revealing natural fluorescence in transparent insect wings by linear and nonlinear optical techniques. *J. Lumin.* **2023**, *254*, 119490. [CrossRef]
61. Hulburt, E.O. The Penetration of Ultraviolet Light into Pure Water and Sea Water. *J. Opt. Soc. Am.* **1928**, *17*, 15–22. [CrossRef]
62. Moan, J. Visible light and UV radiation. In *Radiation at Home, Outdoors and in the Workplace*; Brune, A., Hellborg, R., Persson, B., Pääkkönen, R., Eds.; Scandinavian Science Publisher: Oslo, Norway, 2001; pp. 69–85.

Disclaimer/Publisher's Note: The statements, opinions and data contained in all publications are solely those of the individual author(s) and contributor(s) and not of MDPI and/or the editor(s). MDPI and/or the editor(s) disclaim responsibility for any injury to people or property resulting from any ideas, methods, instructions or products referred to in the content.

jove | Engineering

DATE PUBLISHED November 5, 2026
DOI 10.3791/71107
URL jove.com/t/71107

Revealing Natural Photonic Architectures Through the Synergy of Holotomography and Nonlinear Optical Metrology

Yin Chang[1], **Zhao-Yuan Liu**[1], **Olga Vrbaški**[2], **Milica Živančević**[2], **Bojana Bokić**[2], **Graziano Preziosi**[3], **Maria Antonietta Ferrara**[3], **Branko Kolarić**[2,4]

[1]Department of Materials and Optoelectronic Science, National Sun Yat-sen University[2]Nanophotonics Laboratory, Photonics Center, Institute of Physics, University of Belgrade[3]Institute of Applied Sciences and Intelligent Systems, Unit of Naples, National Research Council[4]Micro- and Nano-Photonics Materials Group, University of Mons

Corresponding Authors : Yin Chang <yinchang@mail.nsysu.edu.tw>, Branko Kolarić <Branko.KOLARIC@umons.ac.be>

Citation

Chang, Y., Liu, Z.Y., Vrbaški, O., Živančević, M., Bokić, B., Preziosi, G., Ferrara, M.A., Kolarić, B. Revealing Natural Photonic Architectures Through the Synergy of Holotomography and Nonlinear Optical Metrology. *J. Vis. Exp.* (237), e71107, doi:10.3791/71107. (2026).

Abstract

Historically, photonics has prioritized long-range periodicity to control optical properties, exemplified by ideal photonic crystals. In contrast, biological systems operate under a fundamentally different design principle: short-range-order nanostructures, corrugations, and partially disordered architectures, rather than ideal long-range periodicity, govern optical functionality. Quantitatively linking such structural heterogeneity to optical response requires methods that can resolve both three-dimensional refractive-index distributions and local symmetry-dependent optical signals. This article presents a correlative holotomography (HT)–nonlinear optical (NLO) imaging protocol for thin, weakly scattering biological photonic specimens. The proposed metrology extends from qualitative phase imaging to quantitative HT and from static microscopy to dynamic NLO probing. Neither approach alone is sufficient to decode complex natural photonic architectures. HT provides label-free three-dimensional refractive-index maps, whereas NLO microscopy, particularly polarization-sensitive second-harmonic generation (SHG), reports local non-centrosymmetric organization and anisotropic optical response. Their integration enables a multiscale understanding that links three-dimensional refractive-index landscapes to molecular symmetry, growth dynamics, and energy-dissipation pathways. The protocol describes specimen selection, optical pre-screening, mounting, HT reconstruction, NLO acquisition, cross-modality registration, and quantitative correlative analysis. The workflow is designed to identify spatial associations between RI heterogeneity, RI gradients, and NLO responses. Such correlations provide a basis for hypothesis generation, including photon–phonon–mechanics mechanisms, and motivate future investigations of power-dependent, thermal, mechanical, and time-resolved controls. This method therefore provides a practical framework for studying structure–response relationships in biological photonic architectures while defining boundaries for future investigations of dynamic or adaptive photonic behavior.

Copyright © 2026, Journal of Visualized Experiments
Journal of Visualized Experiments

DOI 10.3791/71107

Introduction

Since Yablonovitch's proposal of photonic crystals in 1987, photonics research has largely pursued structures with perfect long-range periodicity to achieve photonic band gaps.

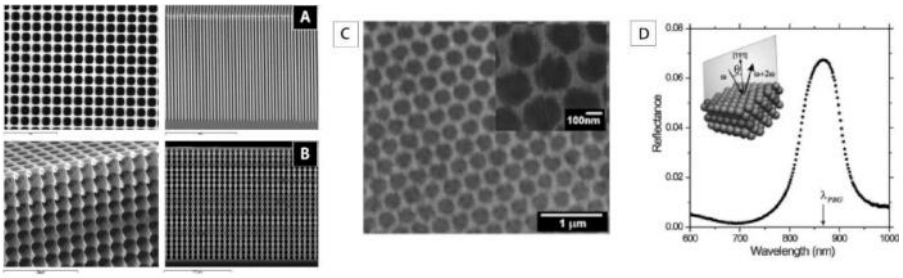


Figure 1: SEM images of macroporous silicon templates and a silicon inverse opal. (**A**) Two-dimensional (2D) macroporous silicon template. (**B**) Three-dimensional (3D) macroporous silicon template. (**C**) Field-emission scanning electron microscopy (FESEM) image of the silicon inverse opal. (**D**) Reflection spectrum of the opal. This figure has been reproduced from the work of González-Urbina L et al.[1]. Copyright obtained. Please click here to view a larger version of this figure.

This approach assumes that optical functionality arises primarily from long-range translational symmetry in periodic photonic structures (**Figure 1A–C**) and the presence of a photonic bandgap (**Figure 1D**)[1,2,3]. Biological systems, however, contradict this assumption.

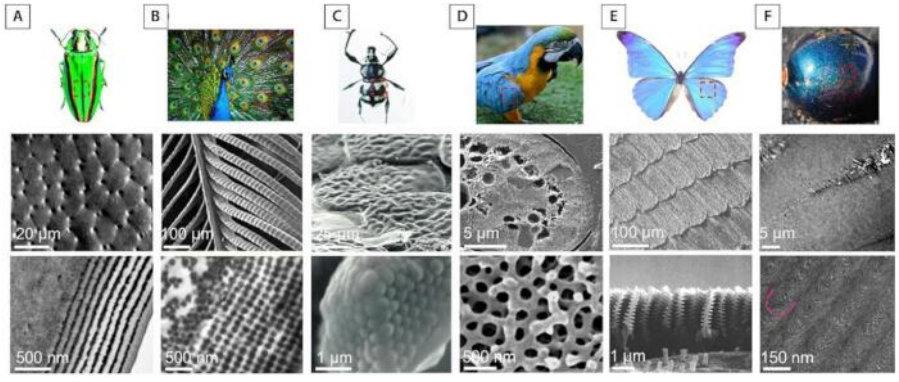


Figure 2: Static structural colors in nature. (**A**) The metallic green coloration of the jewel beetle is produced by a one-dimensional (1D) photonic crystal (PhC) comprising alternating assemblies of melanin and cellulose. (**B**) Three-dimensional (3D) PhC structures comprising ordered arrays of melanin particles in peacock feather tips. (**C**) Beetle scales exhibiting an opal-like photonic crystal structure that produces metallic coloration visible from multiple directions. (**D**) Scarlet macaw feather barbs exhibiting vivid non-iridescent blue coloration produced by their photonic structure. (**E**) Composite structures in Morpho butterfly wing scales, in which multilayer reflection produces structural coloration over a wide range of viewing angles. (**F**) Marble berry (Pollia condensata) fruit exhibiting spiral stacking of cellulose fibers that produces chirality-responsive structural coloration. PhC, photonic crystal. This figure has been adapted from Li et al.[4] under the Creative Commons Attribution 4.0 International license. Please click here to view a larger version of this figure.

Beetles, peacocks, scarlet macaws, butterflies, and marble berries exhibit diverse natural photonic architectures (**Figure 2A–F**) that produce structural coloration through different forms of nanoscale organization[4,5,6,7]. These systems rely on short-range orders embedded within disordered or amorphous networks, a design strategy historically dismissed as imperfection or noise. Only recently has it become clear that such architectures support optical phenomena beyond simple Bragg diffraction, including multiple scattering[8], Anderson localization[9], and broadband or isotropic bandgap formation in non-periodic and correlated disordered materials[9]. The central challenge is no longer recognizing these effects, but rather methodological: detecting them to reveal the structure-response relationship. How to quantitatively link biological structure to optical and thermomechanical function? How do disordered biological structures control light, dissipate energy, and respond mechanically under illumination? Addressing this question requires a metrological approach that exceeds the capabilities of

Copyright © 2026, Journal of Visualized Experiments

DOI 10.3791/71107

conventional imaging or spectroscopy alone, but links structure to symmetry, symmetry to dynamics, and dynamics to function.

HT as a quantitative lens on structural mapping: Traditional biological imaging techniques, such as phase-contrast microscopy, render transparent samples visible but do not provide intrinsic material parameters. HT combines holography with tomographic imaging to overcome these limitations, allowing for the quantitative mapping of the three-dimensional refractive index (RI) distribution of biological samples. The holographic method relies on recording an interference fringe pattern as a function of time, simultaneously capturing both the phase and amplitude information of light after its interaction with the sample[10,11,12,13]. Unlike electron microscopy, which achieves high spatial resolution but destroys the native biological context through dehydration, staining, or sectioning, HT enables label-free, quantitative imaging in a near-native state. By acquiring multiple holographic projections at different illumination angles and applying reconstruction algorithms, HT derives the volumetric RI distribution, providing direct insight into cellular morphology, internal organization, and material composition[14,15,16]. This approach allows precise, noninvasive measurements of biophysical parameters such as volume, dry mass density, subcellular structures, and intracellular dynamics.

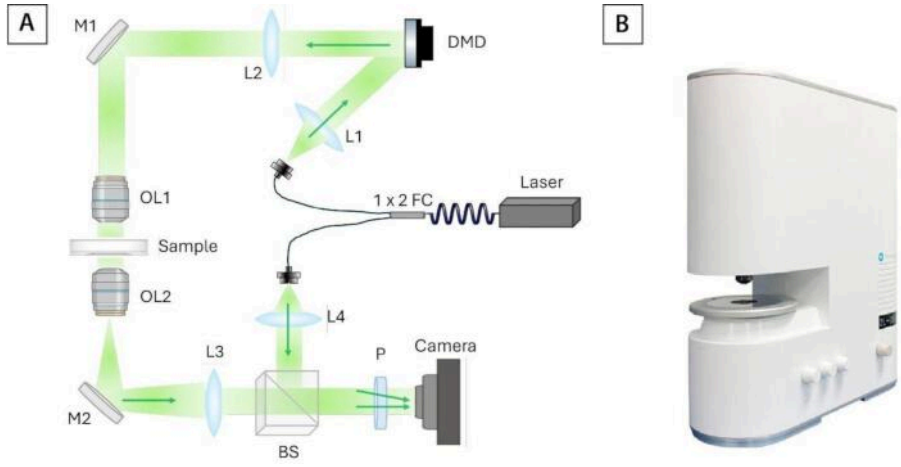


Figure 3: Optical configuration of the off-axis digital holographic tomography system. (**A**) Schematic of the optical layout. A fiber-coupled laser source (λ = 532 nm) is divided into sample and reference beams using a 1 × 2 single-mode fiber coupler. In the sample arm, the beam is collimated, spatially modulated by a digital micromirror device (DMD), and relayed through the imaging optics before passing through the specimen in a dual-objective configuration. The reference beam is independently collimated and recombined with the sample beam at the beam splitter. The resulting interferometric signal is filtered by a polarizer and recorded by a camera. (**B**) HT system used for image acquisition. Abbreviations: FC = fiber coupler; DMD = digital micromirror device; L = lens; M = mirror; OL = objective lens; BS = beam splitter; P = polarizer. Please click here to view a larger version of this figure.

Rather than simply producing contrast, HT yields a quantitatively meaningful map of RI, which in natural photonic materials function as an optical energy landscape. The recent progress on enhancing spatial resolution[17] exploiting a holographic microscope based on Mach-Zehnder interferometry, enables monitoring and determination of local differences in RI across the sample, and points out the subtle non-uniformities, such as Lévy-flight–like distributions, within heterogeneous natural photonic architecture. HT has demonstrated the ability to reconstruct biologically driven non-uniform architectures that lack periodicity yet support photonic band gaps. These reconstructions provide the structural boundary conditions required for thermodynamic and electrodynamic modeling of correlated disorders.

However, HT remains fundamentally a static imaging technique. While it can reveal the effect of stress on the structure and thus enable monitoring of the mechano-optical response[18], it cannot provide direct insight into the formation of these architectures, the emergence of symmetry, or their dynamic response to optical excitation. Nonlinear optics as a dynamic symmetry sensor tool: In addition to the optical properties of samples collected by linear techniques, substantially richer insight into material organization and dynamics can be obtained through high-intensity laser excitation, which activates NLO responses. Under strong electromagnetic fields, induced nonlinear susceptibilities give rise to techniques such as multiphoton excitation fluorescence, hyper-Rayleigh scattering, and harmonic generation, most prominently SHG and third-harmonic generation (THG)[19]. In two-photon excitation fluorescence (TPF), two photons are simultaneously absorbed to populate an excited electronic state, followed by the emission of a single photon, analogous to one-photon fluorescence but governed by different selection rules and spatial excitation probabilities[20] In contrast, SHG involves a coherent, instantaneous nonlinear polarization process in which two incident photons are converted into a single photon with

Copyright © 2026, Journal of Visualized Experiments

DOI 10.3791/71107

exactly twice the energy (half the wavelength) of the excitation. This process is allowed only in non-centrosymmetric media, making SHG intrinsically sensitive to symmetry breaking and molecular organization[21].

Multiphoton techniques offer several fundamental advantages over linear microscopy, particularly for thick, heterogeneous, or weakly fluorescing samples. Because multiphoton absorption is a higher-order process with a low probability; excitation is confined to a femtoliter-scale focal volume, enabling intrinsic optical sectioning without a confocal pinhole. This leads to increased imaging depth, improved signal collection efficiency, and reduced background scattering, while maintaining lateral resolutions approaching ~250 nm, comparable to the theoretical limit of confocal fluorescence microscopy [22]. The strong depth selectivity further minimizes out-of-focus photobleaching and photodamage, allowing non-destructive imaging of fragile or aged specimens. Importantly, these techniques require minimal or no sample preparation, in sharp contrast to electron microscopy, preserving native structure and composition. Beyond structural imaging, polarization-resolved SHG enables spatially resolved mapping of molecular orientation and degree of order within non-centrosymmetric components, providing access to local anisotropy and organizational heterogeneity that is invisible to linear contrast mechanisms[23].

Among nonlinear processes, SHG is particularly powerful as a reporter of molecular symmetry and collective organization, since its intensity scales with the square of the second-order susceptibility and vanishes in centrosymmetric environments. Historically, SHG microscopy in biology has been used primarily as a static imaging modality to visualize ordered structures such as collagen fibrils, myosin, and microtubules[24]. Here, however, the methodological emphasis shifts toward using nonlinear optical signals not merely as structural contrast, but as time-resolved probes of dynamic processes. When combined with controlled excitation and temporal resolution, NLO responses can report on transient symmetry breaking, collective molecular rearrangements, and evolving mesoscale organization.

This capability is particularly relevant for natural photonic structures, which form through non-equilibrium processes involving chemical oscillations, self-assembly, and symmetry breaking. Classical reaction–diffusion systems and oscillatory chemical reactions, such as the Briggs–Rauscher and Belousov–Zhabotinsky reactions, have long served as model systems for studying spatiotemporal pattern formation and chiral symmetry breaking[25,26]. In such systems, SHG has been shown to resolve transient chiral or non-centrosymmetric phases that remain invisible to linear optical techniques, highlighting its sensitivity to collective ordering during far-from-equilibrium dynamics. Extending these principles to biological and bio-derived photonic architectures opens a route to probing not only static structure–property relationships, but also the dynamic pathways through which complex, hierarchical materials self-assemble. Additionally, no sample preparation is required, which is a significant advantage over more complex microscopy methods such as SEM or TEM.

Methodological integration: aligning HT and NLO in space and time: The integration of HT and NLO is not sequential but convergent and should be interpreted first as a correlative structure–response workflow. HT measures where light localizes within a structure and identifies candidate regions where optical fields may be modified by local structure, while NLO, especially polarization-sensitive SHG, detects how molecular symmetry responds to that localization under excitation, thereby bridging molecular-scale symmetry dynamics with mesoscopic optical structure. The central output of the protocol is therefore not a standalone HT image or NLO image, but a registered dataset in which RI-derived structural metrics can be compared with NLO intensity and polarization response.

This correlative framework can motivate, but does not by itself prove mechanistic hypotheses involving photothermal, phononic, and mechanical coupling. Establishing such a photon–phonon–mechanics coupling requires additional measurements beyond the core protocol, including power-dependent NLO acquisition, temperature calibration, thermal diffusion estimates, strain-sensitive measurements, and comparison of the expected RI change with the instrumental RI sensitivity. In the present method article, photon–phonon–mechanics coupling is therefore treated as a testable future hypothesis rather than a demonstrated conclusion. A practical synchronization workflow is provided below:

Protocol

Details of the biological samples, reagents, consumables, instrumentation, and software used in this protocol are provided in the **Table of Materials**.

1. Specimen selection and optical pre-screening

1. Select thin, semi-transparent biological specimens (e.g., isolated wing scales or microtomed cuticles); avoid intact, heavily pigmented structures.
2. Verify under bright-field illumination that the region of interest (ROI) is visibly transmissive.
3. Position the specimen in the HT beam path and verify clear holographic fringe contrast without washout.
4. Acquire a test interferogram and inspect the phase map to ensure no severe phase wrapping, saturation, or boundary discontinuities.

Copyright © 2026, Journal of Visualized Experiments

DOI 10.3791/71107

5. Perform a rapid test RI reconstruction to verify spatially resolved interfaces free of streaking, ringing, or nonphysical gradients.
6. Re-run the reconstruction on the same ROI to confirm reproducible RI values within instrumental precision.
7. If steps 1.2–1.6 fail, translate the stage to a thinner area, isolate single layers, section the sample further, or apply a multiple-scattering reconstruction algorithm.

2. Sample preparation and optical access (reproducibility)

1. Select thin, optically accessible biological photonic samples that exhibit visible structural coloration under bright-field illumination and adequate transmission for HT acquisition. Avoid intact, thick elytra or heavily pigmented cuticles unless the specimens have been thinned or have passed optical pre-screening.

   NOTE: Suitable specimens include isolated butterfly wing scales, thin insect cuticle layers, peeled photonic layers, and cryo- or microtome-thinned sections.

2. Place the sample on an optically transparent glass-bottom dish or a No. 1.5 coverslip (~170 µm thick). Ensure that the sample lies flat without bending, folding, or stacking. Avoid compression, embedding, staining, or chemical fixation whenever possible.

   NOTE: Compression, embedding, staining, or fixation can alter RI distributions and mechanical compliance. If mechanical isolation, peeling, cryosectioning, or microtome sectioning is required, report the preparation procedure because the resulting RI and mechanical information may be preparation- and specimen-dependent.

3. If hydration is required, add 50–100 µL of distilled water or phosphate-buffered saline (PBS, pH 7.4) to fully immerse the sample throughout the experiment. Ensure optical access from both illumination and detection sides.
4. Carefully place a coverslip over the sample to minimize evaporation. Avoid trapping air bubbles.
5. Proceed to imaging within 2–3 min after mounting to prevent dehydration.

   NOTE: Sample integrity is critical. Sample dehydration or mechanical stress alters RI distribution and NLO response.

3. HT data acquisition

1. Position the biological sample in the recessed well of a specialized imaging dish, ensuring that it remains flat and stable.

   NOTE: The optical geometry enables multiple-angle illumination without repositioning the sample and facilitates spatial correspondence between modalities.

2. Place the mounted sample on a HT microscope equipped with a digital micromirror device (DMD) for multiple-angle illumination.
3. Fill the well with deionized water until the sample is completely submerged. Carefully place a coverslip over the well to prevent evaporation and maintain optical clarity.
4. Apply a small drop of deionized water directly onto the water-immersion objective (NA = 1.2).
5. Place an additional drop of water on the coverslip above the sample to complete the immersion path. Ensure that both water layers (on the objective and on the coverslip) are continuous with no air bubbles, providing optimal RI matching for high-quality imaging. Refer to **Figure 3A** for the optical configuration used for multiple-angle holographic acquisition and RI reconstruction, and **Figure 3B** for the HT system.
6. Acquire background holograms without the sample for phase correction.
7. Before acquiring the full angular dataset, acquire a short test hologram series from the selected region. Proceed only if fringe contrast is preserved, phase maps remain continuous after background correction, and no severe attenuation or saturation is observed. If the test acquisition shows poor fringe visibility, severe phase wrapping, or strong reconstruction artifacts, select a thinner or less pigmented region, reduce the imaging depth, or prepare a thinned/peeled specimen before continuing.
8. Acquire 48 holographic projections at multiple illumination angles spanning the numerical aperture of the system. The acquisition time is 2,5 fps for 3D RI reconstruction.
9. Reconstruct the three-dimensional RI distribution using the reconstruction software associated with the HT system. Set the lateral voxel size to 100–200 nm and the axial voxel size to 300–500 nm. Apply iterative reconstruction using 5–10 iterations and the Rytov approximation.
10. Use the system-specific algorithm provided by the HT platform to compute the volumetric RI distribution of the sample.

4. Identification of structurally relevant regions

1. Analyze the RI histogram and define RI ranges within the sample as follows: low RI, 1.33–1.38; medium RI, 1.38–1.50; and high RI, >1.50.

   NOTE: These ranges correspond approximately to aqueous regions, organic matrix, and dense structures, respectively.

Copyright © 2026, Journal of Visualized Experiments

DOI 10.3791/71107

2. Generate pseudocolored maps based on RI segmentation by assigning a distinct color to each RI range.
3. Use the segmented maps to identify structural or compositional variations and regions with distinct optical properties.
4. Adjust the RI thresholds as needed to highlight specific features or compare local variations across the sample.
5. Analyze the RI volume to identify regions with high RI contrast, strong spatial gradients, and interfaces between distinct structural domains.
6. Mark these regions as candidate sites for NLO probing.
7. Export the reconstructed RI volume for subsequent analysis and spatial registration.

NOTE: NLO signals are highly sensitive to local symmetry and field localization; selecting structurally informed regions reduces signal averaging and improves interpretability.

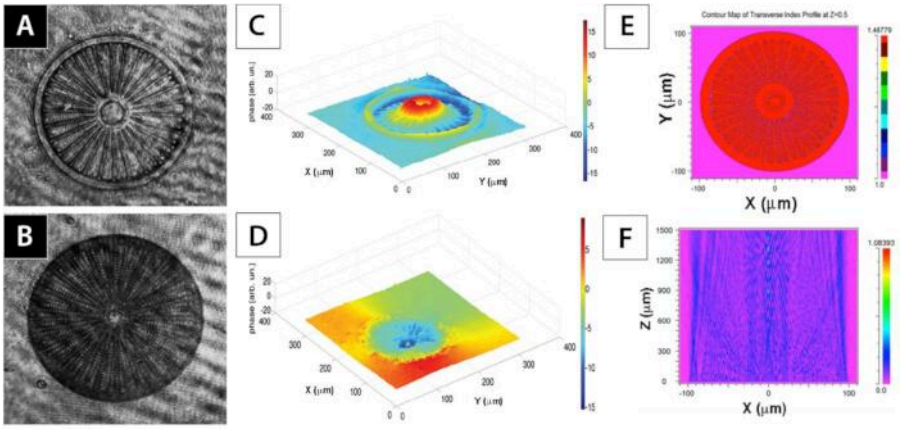


Figure 4: Digital holography and morphology-based optical modeling of a biological photonic diatom specimen. (**A**) Representative hologram acquired from the upper side of an Arachnoidiscus diatom valve. (**B**) Representative hologram acquired from the lower side of the valve. (**C**) Three-dimensional phase reconstruction of the upper-side holographic measurement. (**D**) Three-dimensional phase reconstruction of the lower-side holographic measurement. (**E**) Morphology-derived refractive-index model generated from the diatom valve ultrastructure and used for optical propagation simulation. (**F**) Representative structurally relevant region, such as the central flange, pores, or radiating costae, that may be selected as a candidate region for subsequent NLO interrogation in a future correlative HT–NLO workflow. This figure has been adapted from Ferrara et al.[32] under the Creative Commons Attribution 4.0 International license.Please click here to view a larger version of this figure.

5. NLO system setup

1. Turn on the femtosecond laser source with a repetition rate of approximately 80 MHz.
2. Align the pulsed laser source for multiphoton excitation.
3. Set the excitation wavelength to 780–820 nm. Configure the detection optics with a 390–410 nm bandpass filter for SHG imaging.
4. Implement polarization control for both excitation and detection, when available.
5. Calibrate the laser power to 1–10 mW at the sample plane while maintaining an adequate signal-to-noise ratio and avoiding thermal damage.
6. Set the image resolution to 512 x 512 pixels and the pixel dwell time to 1–5 µs. Average 2–4 scans per frame to improve the signal-to-noise ratio while minimizing thermal exposure.
7. Rotate the half-wave plate to control the polarization and acquire left- and right-polarized images separately.

NOTE: Monitor the sample for power-dependent artifacts during acquisition. Maintain the excitation power below 15 mW.

NOTE: Incorrect polarization alignment results in a weak or absent SHG signal.

6. Structurally guided NLO measurement

1. Identify structurally relevant regions in the reconstructed HT volume, including regions with high RI contrast, pronounced RI gradients, interfaces, or distinct structural domains.
2. Record the anatomical or morphological location and orientation of the selected region relative to recognizable sample features. Use these features to guide the selection of corresponding regions for subsequent NLO measurements.
3. Establish correspondence between structurally defined regions in the HT and NLO datasets rather than assuming pixel-by-pixel correspondence.

Copyright © 2026, Journal of Visualized Experiments

DOI 10.3791/71107

NOTE: HT and NLO probe different spatial scales and contrast mechanisms.

4. Acquire NLO signals from the selected regions under controlled excitation and polarization conditions. Compare the presence, magnitude, polarization dependence, or temporal evolution of the NLO response with the structural characteristics identified by HT. Representative NLO imaging and spectral readouts are shown in **Figure 5A–C**.

5. Repeat the measurements at five or more structurally distinct regions within the same sample.

   NOTE: The expected outcome is a localized SHG signal associated with structural heterogeneity.

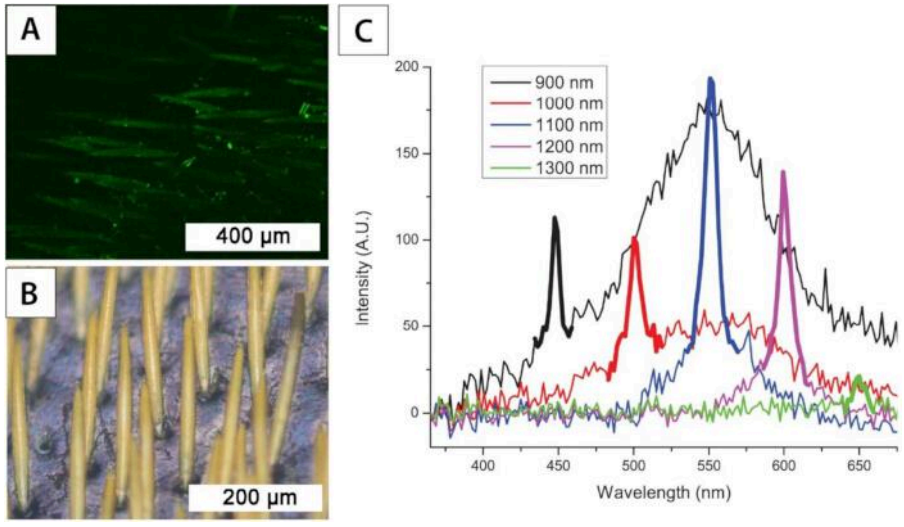


Figure 5: Literature-supported examples of NLO **readouts from biological and bio-derived materials**. (**A**) Representative NLO image acquired from a biological structure. (**B**) Corresponding structural image of the measured region. (**C**) Wavelength-dependent intensity spectra obtained at excitation wavelengths of 900, 1000, 1100, 1200, and 1300 nm. This figure has been reproduced from the work of Mouchet SR et al.[33]. Copyright obtained.
Please click here to view a larger version of this figure.

7. Time-resolved NLO acquisition (optional)

1. Maintain constant laser power and alignment.
2. For dynamic studies, perform repeated scans at intervals of 1–10 s for a total duration of <5 min.
3. Record signal evolution over time scales relevant to thermal relaxation, mechanical response, or molecular reorganization.
4. Maintain consistent excitation conditions across all time points. Use a motorized stage with drift correction, if available.

   NOTE: Time-dependent variation in SHG intensity may reflect structural dynamics.

8. Correlative analysis of structure and optical response

1. Identify the anatomical or morphological location of each NLO measurement relative to the structurally relevant region identified from the HT reconstruction. Correlate nonlinear signal intensity and polarization dependence with local RI features.
2. Compare the presence, magnitude, polarization dependence, and temporal evolution of the NLO response with the structural characteristics identified by HT at the corresponding region.

   NOTE: A published multimodal optical study illustrates feature-based correspondence using a chemical map (**Figure 6A**), a structural/optical map (**Figure 6B**), and corresponding spatial features (**Figure 6C**). Figure 6 illustrates the analytical principle rather than direct HT–NLO correlation.

Copyright © 2026, Journal of Visualized Experiments

DOI 10.3791/71107

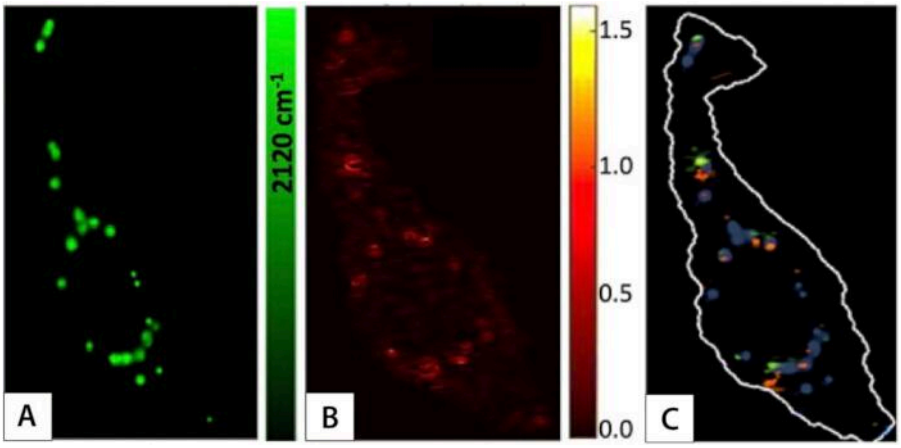


Figure 6: Example of feature-based multimodal correspondence. (**A**) Chemical map showing signals at 2120 cm^{-1}. (**B**) Structural/optical map. (**C**) Corresponding spatial features identified across the modalities. This figure has been adapted from Mangini M, et al.[34] under the Creative Commons Attribution 4.0 International license. Please click here to view a larger version of this figure.

9. Noise-aware interpretation

1. Acquire at least five repeated SHG measurements for each ROI under identical excitation power, polarization, detector gain, and environmental conditions.
2. Assess signal variability across the repeated measurements.
3. Calculate the mean, standard deviation, coefficient of variation, and temporal drift of the SHG intensity after background subtraction and laser-power correction.
4. Distinguish deterministic structural responses from stochastic fluctuations using appropriate statistical or stochastic modeling approaches and signals that remain consistent across repeated measurements.

   NOTE: Avoid interpreting single-point measurements as representative of global material behavior.

Results

HT reconstruction and structural assessment

Representative results obtained using this protocol are evaluated through a structured workflow that integrates HT reconstruction quality, NLO signal response, and dataset validation criteria, as summarized in **Table 1**. Following HT acquisition, a three-dimensional RI distribution is reconstructed. Representative holographic measurements acquired from opposite sides of the specimen are shown in **Figure 4A**,**B**, with the corresponding three-dimensional phase reconstructions shown in **Figure 4C**,**D**. Morphology-derived refractive-index modeling and structurally relevant regions that may guide subsequent NLO interrogation are illustrated in **Figure 4E**,**F**. These features correspond to the high-quality RI reconstruction condition defined in **Table 1** and serve as the primary criterion for accepting datasets for further analysis. The reconstructed RI volume (**Figure 4 C**,**D**) is then used to guide the selection of regions of interest (ROIs) for NLO probing. Regions exhibiting high RI contrast and sharp spatial gradients are selected, as these are associated with localized electromagnetic field enhancement. When NLO measurements are performed at these sites, strong and spatially localized signals such as SHG are observed. As indicated in **Table 1**, the presence of stable, spatially confined SHG signals that co-localize with high-RI regions is considered a valid condition for proceeding with quantitative analysis.

Dataset quality assessment and reproducibility

To ensure data reliability, all datasets are systematically evaluated using the criteria defined in **Table 1**. Sub-optimal results are identified based on characteristic features. For example, blurred RI reconstructions correspond to optical misalignment or the presence of air bubbles and are therefore rejected. Weak or spatially delocalized SHG signals are classified as conditional cases, requiring adjustment of polarization or excitation power before re-measurement. Similarly, temporal signal drift is typically associated with sample dehydration or thermal effects and leads to dataset exclusion. Under standard experimental conditions, approximately 10–20% of datasets may be excluded following this validation process. Only datasets that meet the acceptance criteria defined in **Table 1** are included in subsequent analysis. Quantitative outputs include spatially resolved RI distributions, localized nonlinear signal intensities, and polarization-dependent responses. Polarization-resolved SHG measurements further reveal structural anisotropy, enabling differentiation between ordered and disordered domains within heterogeneous photonic architectures. Consistent signal behavior across repeated measurements confirms experimental

Copyright © 2026, Journal of Visualized Experiments

DOI 10.3791/71107

reproducibility, corresponding to the "consistent signal across repeats" condition in **Table 1**.

Correlative HT–NLO analysis

Importantly, the combined HT–NLO approach enables direct correlation between structural features and optical responses beyond morphology alone. Localized photon confinement, identified through RI mapping, can enhance light–matter interactions. These effects are experimentally observed as variations in SHG intensity and polarization response, suggesting underlying photon–phonon–mechanical coupling within the heterogeneous structure.

Data validation and interpretation

The decision-making process for accepting, rejecting, or conditionally re-measuring datasets is formalized in **Table 1**. This decision matrix provides an operational framework for dataset validation and exclusion, ensuring reproducibility across different experimental conditions. By explicitly linking observed features to experimental decisions and corrective actions, the protocol minimizes user-dependent bias and improves the robustness of photonic characterization. For data interpretation, results obtained under accepted conditions should be used as the baseline. Observations such as unexpected RI gradients or anomalous nonlinear responses should be cross-referenced with the corresponding categories in **Table 1** to determine whether they arise from intrinsic structural features or experimental artifacts. Careful control of sample hydration, optical alignment, and excitation conditions is essential to maintain data fidelity and ensure accurate interpretation of structure–property relationships.

Observed Feature	Quantitative/ Qualitative Indicator	Likely Cause	Decision	Recommended Action	Impact on Data
High-quality RI reconstruction	RI variation ≥ 0.02; sharp interfaces; no spatial blur	Proper alignment; intact sample; stable environment	Accept	Proceed to NLO measurement	Valid dataset for analysis
Strong localized SHG signal	Spatially confined signal co-localized with high RI regions; stable intensity	Correct polarization; sufficient excitation power; structural anisotropy	Accept	Perform polarization-resolved measurements	Enables structure–property correlation
Consistent signal across repeats	<10% variation in intensity across repeated scans	Stable sample; minimal thermal drift	Accept	Include in quantitative analysis	High reproducibility
Blurred RI reconstruction	Loss of spatial resolution; smeared interfaces	Optical misalignment; air bubbles; vibration	Reject	Realign system; remove bubbles; stabilize setup	Invalid structural information
Weak or absent SHG signal	Signal near noise level; no spatial localization	Incorrect polarization; low laser power; centrosymmetric region	Conditional	Adjust polarization; increase power; verify ROI	Limited interpretability

Copyright © 2026, Journal of Visualized Experiments

DOI 10.3791/71107

Signal drift over time	Gradual intensity change during acquisition	Sample dehydration; thermal effects; laser instability	Reject	Rehydrate sample; reduce exposure; stabilize laser	Compromised temporal reliability
Artificial RI gradients	Unexpected RI increase at edges or surfaces	Dehydration; environmental exposure (>5 min in air)	Reject	Maintain hydration; minimize exposure time	Non-representative structure
Structural deformation	Distorted morphology; loss of optical contrast	Mechanical compression; improper mounting	Reject	Remount sample with minimal constraint	Alters intrinsic properties

Table 1: Decision matrix for data quality assessment and experimental validation. Summary of quantitative and qualitative criteria used to assess data quality, determine experimental validity, identify potential issues, and guide recommended actions for subsequent analysis.

Discussion

A critical determinant of success in this protocol lies in preserving the native structural and physicochemical state of the biological sample. The integration of HT and NLO metrology represents a critical paradigm shift from conventional imaging workflows that tolerate fixation or embedding and lack intrinsic molecular specificity. The core protocol outlined in this study hinges on a label-free, minimally invasive approach. By maintaining biological samples in a physiological buffer without mechanical compression or chemical fixation, the native RI distribution and mechanical compliance are perfectly preserved. Subsequent HT acquisition yields a quantitative 3D RI map, serving as a topological blueprint to guide precisely targeted NLO measurements, such as SHG. The scientific motivation for combining HT and NLO is that natural photonic structures are not defined solely by morphology. Their optical behavior can depend on refractive-index heterogeneity, local anisotropy, olecular organization, and the way these features respond to optical excitation. The value of the combined approach lies in determining whether these structural and NLO features are spatially linked. Despite its formidable capabilities, this dual-modality approach possesses inherent limitations. Several technical parameters require careful optimization and represent common sources of experimental variability. HT reconstruction fidelity is fundamentally constrained by the optical thickness, absorption, refractive-index contrast, and weak-scattering condition of the specimen. Conventional HT/ODT reconstructions often rely on linearized scattering models, such as Born- or Rytov-type approximations. For thicker, more complex, highly pigmented, or strongly absorbing biological photonic samples, these assumptions can break down because the measured field no longer represents a simple single-scattering response. In such cases, multiple scattering, reduced holographic fringe visibility, phase-unwrapping errors, and nonphysical RI artifacts can prevent reliable RI recovery[16,27,28,29].

Therefore, the present protocol should be applied primarily to thin, weakly scattering, optically accessible biological photonic specimens (such as isolated butterfly wing scales, peeled photonic layers, or microtome-thinned cuticles). Intact thick elytra and strongly pigmented cuticles are generally unsuitable for direct HT reconstruction. When mechanical isolation, peeling, or microtome thinning is required to meet optical pre-screening criteria, the specific preparation procedure must be explicitly reported, as such physical modifications may alter the native RI distribution and mechanical compliance of the specimen. When strong absorption or multiple scattering cannot be avoided, the resulting dataset should be excluded from quantitative HT–NLO correlation rather than interpreted as an absence of structure–function coupling. Alternatively, future implementations may employ longer-wavelength illumination, specimen-specific optical clearing, or multiple-scattering-aware reconstruction algorithms to extend this methodology to thicker or more strongly scattering biological photonic materials.

In HT acquisition, the quality of the reconstructed RI map depends strongly on angular sampling density, exposure time, and reconstruction algorithm parameters (e.g., iteration number and scattering approximation). Insufficient angular coverage or improper phase correction can result in reconstruction artifacts or loss of contrast. In NLO measurements, laser power, polarization alignment, and focal stability are critical. Excessive excitation power may induce local heating or photodamage, leading to time-dependent signal drift, whereas insufficient

Copyright © 2026, Journal of Visualized Experiments

DOI 10.3791/71107

power reduces signal-to-noise ratio. Concurrently, SHG is strictly limited to non-centrosymmetric structures. Incorrect polarization alignment can suppress SHG signals in anisotropic or non-entrosymmetric structures[3]. Troubleshooting should therefore include systematic checks of hydration state, optical alignment, polarization configuration, and repeated measurements ($n \geq 5$) to distinguish deterministic structural signals from stochastic fluctuations. The inclusion of sub-optimal datasets, such as low-signal or distorted reconstructions, are particularly valuable for identifying these failure modes and establishing practical operating boundaries.

Additionally, previous studies[12,13] have shown that holographic and interferometric approaches can reveal hidden dynamics in natural photonic structures and nonequilibrium chemical systems. In particular, holographic imaging has been used to monitor dynamic deformation in natural photonic structures and to detect stochastic phase-transition behavior in Briggs-Rauscher oscillatory reactions. These studies motivate future extensions of the present HT–NLO framework toward time-resolved and noise-aware analysis. In the present protocol, noise-aware analysis is limited to reproducibility and dataset-quality assessment, including repeatability testing, drift rejection, coefficient of variation, and autocorrelation-based screening. More advanced non-Markovian modeling is retained as a future extension for dedicated dynamic HT–NLO studies[30]. Such modeling would require a defined physical state variable, a specified governing equation, an observation model linking that state variable to measurable RI or SHG signals, and validation against simulated or control datasets. These approaches may enable the analysis of noise-history dependence and time-resolved nonlinear signals that cannot be fully captured by deterministic analyses. The present protocol can be adapted or modified depending on the sample type and experimental objective. For highly scattering or optically thick samples, reducing imaging depth or using lower numerical aperture objectives may improve reconstruction fidelity at the expense of spatial resolution. For dynamic studies, time-resolved acquisition can be implemented by repeated scanning under controlled excitation conditions; however, this requires active drift correction and stable environmental control. The NLO modality can also be extended beyond SHG to include two-photon excited fluorescence (TPEF) or third-harmonic generation (THG), depending on the molecular composition and symmetry of the sample[5,6]. Additionally, the RI segmentation thresholds used for structural identification may need to be adjusted for different material systems, particularly when transitioning from purely organic to partially mineralized biological structures. Looking forward, the methodological principles established here provide a foundation for deriving prerequisites for advancing both natural photonics and active metamaterial engineering.

In addition, by incorporating stochastic partial differential equations (SPDEs) to model noise-history dependence, this framework moves beyond deterministic assumptions, enabling the rigorous characterization of noise-driven biological dynamics. However, this protocol should not be interpreted as direct proof of a complete photon–phonon–mechanics cascade. In the absence of independent measurements of temperature rise, thermal diffusion, strain, or time-dependent RI modulation, etc. the present workflow supports correlative structure–response analysis rather than causal mechanistic assignment. Photon–phonon–mechanics coupling is therefore treated as a motivating hypothesis for future experiments rather than as a conclusion derived from the current protocol.

The same conceptual framework may inform future studies of adaptive and time-modulated photonic materials. Such extensions remain beyond the scope of the present method article. In particular, applications to self-modulating photonic devices, stochastic photonic dynamics, or photonic time crystals (PTCs)[31] would require dedicated sample platforms, externally controlled temporal modulation, quantitative time-resolved measurements, and theoretical modeling specific to those systems. These topics are therefore presented here only as future directions inspired by the HT–NLO correlative strategy, not as outcomes demonstrated by the current protocol.

Applications: The integrated HT–NLO–stochastic framework could be naturally extended to the photonic time crystal (PTC) domain. Whereas conventional photonic crystals produce frequency bandgaps because of spatial Bragg interference, PTCs produce momentum bandgaps, in which the RI varies periodically in time rather than in space. This phenomenon arises from time-refraction and time-reflection at temporal interfaces and can be rigorously analyzed using Floquet-Bloch theory in the time dimension. Experimental evidence has been reported in dynamically modulated microwave metamaterials, showing both momentum gaps and wave amplification consistent with PTC predictions[31]. From a metrological perspective, HT inherently quantifies spatial distributions of RI at high resolution, while NLO and time-resolved measurements characterize temporal modulation of optical properties. Integrating these modalities provides a framework for quantifying and interpreting space–time RI control in terms of both spatial structure and temporal dynamics, offering a pathway to characterizing and manipulating PTC behavior in laboratory systems. This perspective connects natural photonics, time-varying metamaterials, and the physics of temporal band structures into a unified conceptual lens. In PTCs, the temporal modulation creates momentum gaps rather than frequency gaps. Light within these gaps couples to complex frequencies, enabling exponential energy amplification. Group velocity becomes zero, localizing energy spatially while amplification proceeds. From a metrological standpoint, HT

Copyright © 2026, Journal of Visualized Experiments

DOI 10.3791/71107

characterizes spatial RI distributions, while NLO and time-resolved measurements probe temporal symmetry modulation, together providing a unified view of space–time photonic control. The possibility of studying PTC within HT directly links this methodology (developed for natural photonics study) to metamaterial science.

Conclusion:

The integration of HT and nonlinear optics establishes a unified methodological framework for decoding natural photonic architectures. Rather than treating disorder as a defect, this approach reveals it as a functional design principle: one that couples structure, symmetry, dynamics, and function across scales. Mastering photon–phonon– mechanics coupling enables a new class of self-modulating optical materials, enabling mutual excitation of external stimuli that light induces heat; heat induces mechanical deformation; deformation dynamically alters optical response. By embedding plasmonic nanoparticles into amorphous dielectric networks, such as the analogy to butterfly scales, engineers can create materials that change color, transparency, or bandgap in response to environmental stimuli. These bio-inspired designs abandon rigid periodicity in favor of adaptive correlated disorder, aligning engineering practice with biological strategy. The resulting metrology not only explains how nature builds resilient photonic materials but also provides actionable design rules for the next generation of adaptive optical devices.

Disclosures

All authors declare no conflict of interest regarding this manuscript.

Acknowledgments

Yin Chang acknowledges funding provided by the National Science and Technology Council, Taiwan (NSTC 115-2112-M-110-019-MY3; NSTC 115-2112-M-110-009-MY3), and the Bureau of Energy, Ministry of Economic Affairs, Taiwan, for research under Contract No. 115-D0101-1. Bojana Bokić and Branko Kolarić acknowledge funding provided by the Institute of Physics Belgrade through institutional funding from the Ministry of Education, Science, and Technological Development of the Republic of Serbia. Branko Kolarić additionally acknowledges support from F R S–FNRS. Olga Vrbaški, Milica Živančević, Bojana Bokić, Maria Antonietta Ferrara, and Branko Kolarić acknowledge support from the EU through the EIC Pathfinder Challenges 2022 call, Research Grant 101115149 (project ARTEMIS). The content reflects only the authors' views, and the European Commission is not responsible for any use that may be made of the information it contains.

References

1. González-Urbina L, et al. Linear and nonlinear optical properties of colloidal photonic crystals. Chem Rev. 2012;112:2268-2285. doi:10.1021/cr200063f.
2. Yablonovitch E, Gmitter TJ. Photonic band structure: The face-centered-cubic case. Phys Rev Lett. 1989;63(18):1950-1953. doi:10.1103/PhysRevLett.63.1950.
3. Verstraete C, Mouchet SR, Verbiest T, Kolaric B. Linear and nonlinear optical effects in biophotonic structures using classical and nonclassical light. J Biophotonics. 2019;12(1):e201800262. doi:10.1002/jbio.201800262.
4. Liu Y, Hou X, Song Y, Li M. Bioinspired reflective display based on photonic crystals. Interdiscip Mater. 2024;3(1):54-73. doi:10.1002/idm2.12138.
5. Mouchet SR, Deparis O. Natural Photonics and Bioinspiration. Artech House; Norwood, MA, USA; 2021.
6. Vasiljević D, et al. Thermal radiation management by natural photonic structures: Morimus asper funereus case. J Therm Biol. 2021;98:102932. doi:10.1016/j.jtherbio.2021.102932.
7. Mara D, et al. Revealing the wonder of natural photonics by nonlinear optics. Biomimetics. 2022;7(4):153. doi:10.3390/biomimetics7040153.
8. Rechtsman MC, et al. Amorphous photonic lattices: band gaps, effective mass, and suppressed transport. Phys Rev Lett. 2011;106(19):193904. doi:10.1103/PhysRevLett.106.193904.
9. Vasco JP, Hughes S. Anderson localization in disordered LN photonic crystal slab cavities. ACS Photonics. 2018;5(4):1262-1272. doi:10.1021/acsphotonics.7b00967.
10. Coppola G, Ferrara MA. Polarization-sensitive digital holographic imaging for characterization of microscopic samples: recent advances and perspectives. Appl Sci. 2020;10(13):4520. doi:10.3390/app10134520.
11. Cuche E, Marquet P, Depeursinge C. Simultaneous amplitude-contrast and quantitative phase-contrast microscopy by numerical reconstruction of Fresnel off-axis holograms. Appl Opt. 1999;38(34):6994-7001. doi:10.1364/AO.38.006994.
12. Pagnacco MC, et al. Stochastic phase transition dynamics in nonequilibrium system: holographic study. J Phys Chem C. 2023;127(22):10821-10825. doi:10.1021/acs.jpcc.3c01831.
13. Simovic-Pavlovic M, et al. Uncovering hidden dynamics of natural photonic structures using holographic imaging. J Vis Exp. 2022;(181):e63676. doi:10.3791/63676.
14. Ferrara MA, et al. Quantitative holographic analysis in stallion spermatozoa following cryopreservation. Sci Rep. 2025;15(1):43190. doi:10.1038/s41598-025-24885-w.
15. Khadem H, et al. Polarization-sensitive holotomography for multidimensional label-free imaging and characterization of lipid droplets in cancer cells. Adv Sci (Weinh). 2025;12(42):e09420. doi:10.1002/advs.202509420.
16. Kim G, et al. Holotomography. Nat Rev Methods Primers. 2024;4(1):51. doi:10.1038/s43586-024-00327-1.
17. Dardikman-Yoffe G, Mirsky SK, Barnea I, Shaked NT. High-resolution 4-D acquisition of freely swimming human sperm cells without staining. Sci Adv. 2020;6(15):eaay7619. doi:10.1126/sciadv.aay7619.

Copyright © 2026, Journal of Visualized Experiments

18. Simovic-Pavlovic M, et al. Thermophoretic effect in natural photonics: holographic study. Bioinspir Biomim. 2025;20(2):024001. doi:10.1088/1748-3190/adb6e8.
19. Boyd RW. Nonlinear Optics. 4th ed. Academic Press; London, UK; 2020.
20. Denk W, Strickler JH, Webb WW. Two-photon laser scanning fluorescence microscopy. Science. 1990;248(4951):73-76. doi:10.1126/science.2321027.
21. Shen YR. The Principles of Nonlinear Optics. Wiley; New York, NY, USA; 2002.
22. Zipfel WR, Williams RM, Webb WW. Nonlinear magic: multiphoton microscopy in the biosciences. Nat Biotechnol. 2003;21(11):1369-1377. doi:10.1038/nbt899.
23. Campagnola PJ, Loew LM. Second-harmonic imaging microscopy for visualizing biomolecular arrays in cells, tissues and organisms. Nat Biotechnol. 2003;21(11):1356-1360. doi:10.1038/nbt894.
24. Campagnola PJ, et al. Three-dimensional high-resolution second-harmonic generation imaging of endogenous structural proteins in biological tissues. Biophys J. 2002;82(1):493-508. doi:10.1016/S0006-3495(02)75414-3.
25. Prigogine I. Being and Becoming: Time and Complexity in the Physical Sciences. W. H. Freeman & Co.; San Francisco, CA, USA; 1981.
26. Epstein IR, Showalter K, Ross J. Nonlinear chemical dynamics: oscillations, patterns, and chaos. J Phys Chem. 1996;100(31):13132-13147. doi:10.1021/jp953547m.
27. Lim J, Ayoub AB, Antoine EE, Psaltis D. High-fidelity optical diffraction tomography of multiple scattering samples. Light Sci Appl. 2019;8:82. doi:10.1038/s41377-019-0195-1.
28. Soubies E, Pham TA, Unser M. Efficient inversion of multiple-scattering model for optical diffraction tomography. Opt Express. 2017;25(18):21786-21800.
29. Yasuhiko O, Takeuchi K, Yamada H, Ueda Y. Multiple-scattering suppressive refractive index tomography for the label-free quantitative assessment of multicellular spheroids. Biomed Opt Express. 2022;13(2):962-979.
30. Boguñá M, Lafuerza LF, Toral R, Serrano MA. Simulating non-Markovian stochastic processes. Phys Rev E. 2014;90(4):042108. doi:10.1103/PhysRevE.90.042108.
31. Xiong J, et al. Observation of wave amplification and temporal topological state in a non-synthetic photonic time crystal. Nat Commun. 2025;16(1):11182. doi:10.1038/s41467-025-66154-4.
32. Ferrara MA, et al. Optical properties of diatom nanostructured biosilica in Arachnoidiscus sp: micro-optics from mother nature. PLoS One. 2014;9(7):e103750.
33. Mouchet SR, et al. Unveiling the nonlinear optical response of Trictenotoma childreni longhorn beetle. J Biophotonics. 2019;12(9):e201800470.
34. Mangini M, et al. Cancer metabolic features allow discrimination of tumor from white blood cells by label-free multimodal optical imaging. Front Bioeng Biotechnol. 2023;11:1057216.

Copyright © 2026, Journal of Visualized Experiments

Institutional Repository - Research Portal
Dépôt Institutionnel - Portail de la Recherche
researchportal.unamur.be
University of Namur

RESEARCH OUTPUTS / RÉSULTATS DE RECHERCHE

Holographic and Nonlinear Optical Study of Natural Photonic Structures

Pavlović, Marina Simović; Bokić, Bojana; Verstraete, Charlotte; Vasiljević, Darko; Mouchet, Sébastien R.; Verbiest, Thierry; Kolarić, Branko

Published in:
2023 23rd International Conference on Transparent Optical Networks, ICTON 2023

DOI:
10.1109/icton59386.2023.10207525

Publication date:
2023

Document Version
Peer reviewed version

Link to publication

Citation for pulished version (HARVARD):
Pavlović, MS, Bokić, B, Verstraete, C, Vasiljević, D, Mouchet, SR, Verbiest, T & Kolarić, B 2023, Holographic and Nonlinear Optical Study of Natural Photonic Structures: Where Biology Meets Physics. in M Jaworski & M Marciniak (eds), *2023 23rd International Conference on Transparent Optical Networks, ICTON 2023.* International Conference on Transparent Optical Networks, vol. 2023-July, IEEE Computer Society, 23rd International Conference on Transparent Optical Networks, ICTON 2023, Bucharest, Romania, 2/07/23. https://doi.org/10.1109/icton59386.2023.10207525

General rights
Copyright and moral rights for the publications made accessible in the public portal are retained by the authors and/or other copyright owners and it is a condition of accessing publications that users recognise and abide by the legal requirements associated with these rights.

- Users may download and print one copy of any publication from the public portal for the purpose of private study or research.
- You may not further distribute the material or use it for any profit-making activity or commercial gain
- You may freely distribute the URL identifying the publication in the public portal ?

Take down policy
If you believe that this document breaches copyright please contact us providing details, and we will remove access to the work immediately and investigate your claim.

Download date: 23. Nov. 2026

Holographic and Nonlinear Optical Study of Natural Photonic Structures: Where Biology Meets Physics

Marina Simović Pavlović[1*], Bojana Bokić[2], Charlotte Verstraete[3], Darko Vasiljević[2], Sébastien R. Mouchet[4,5], Thierry Verbiest[3] and Branko Kolarić[2,6]

[1]Faculty of Mechanical Engineering, University of Belgrade, Kraljice Marije 16, 11120 Belgrade, Serbia; Tel: (00381) 604273777, e-mail: simovicmarina99@gmail.com*

[2]Photonics Center, Institute of Physics, University of Belgrade, Pregrevica 118, 11080 Belgrade, Serbia;

[3]Molecular Imaging and Photonics, Department of Chemistry, KU Leuven, 3001 Heverlee, Belgium;

[4]School of Physics, University of Exeter, Stocker Road, Exeter EX4 4QL, UK;

[5]Department of Physics & Namur Institute of Structured Matter (NISM), University of Namur, Rue de Bruxelles 61, 5000 Namur, Belgium;

[6]Micro- and Nanophotonic Materials Group, University of Mons, Place du Parc 20, 7000 Mons, Belgium;

ABSTRACT

Nano-optics exploits linear and nonlinear phenomena at the nanoscale to advance our understanding of materials and their interaction with light in both classical and quantum domains. This not only deepens our fundamental knowledge but also drives new photonics-based technologies, from sensing to communication. Nonlinear optics further offers a way to explore and leverage the complexity of natural structures for technological advancement. The presented research investigates natural photonic structures through holographic and nonlinear optical studies, revealing the correlations among their geometries, optical, and dynamic responses. These findings will inspire novel designs for optical devices and systems.

Keywords: nonlinear analysis, nonlinear optics, holography, natural photonics, biophotonics, optics.

1. INTRODUCTION

It has been known for a long time that colours in nature are not designed for beauty but often, of the utmost importance, for communication [1-3]. Colours in nature emerge due to the presence of chemical entities, physical



Figure 1. Many examples of structural colours are found in the integuments of natural organisms such as: (a) Morpho peleides, (b) dragonfly species, (c) the green rose chafer Cetonia aurata, (d) the Botany Bay diamond weevil Chrysolopus spectabilis, (e) some jumping spider species, (f) the mandrill Mandrillus sphinx, (g) the Indian peafowl Pavo cristatus, (h) the mallard Anas platyrhynchos, and (i) the neon tetra fish Paracheirodon innesi. Reproduced from https://pixabay.com/ accessed on 27 July 2022.

structures, or combination of both mechanisms. Structural colours, as a specific class of colouration, arise from the interaction of light with structured, periodically arranged materials, so called “photonic crystals”. Natural photonic structures occur most often in insects, birds, and reptiles. They stand out due to their complexity and distinct characteristics with respect to pigmentary colours (Fig. 1).

Besides the fundamental importance of revealing the link between natural photonic geometries and their optical response, the presented research is also vital for developing new applications in photonics and material science [2].

2. DISCUSSION

Using both holographic and nonlinear optical techniques, we unveiled correlations among the geometries, optical, and dynamic responses of natural photonic structures. Nonlinear optical methods provide a comprehensive understanding of the molecular properties of biomaterials due to their inherent sensitivity to symmetry [5]-[7]. Thanks to holography, we were able to observe detailed dynamic behaviour of nanostructures subjected to an external stimuli, such as heat generated by a laser light [4]. Alongside these techniques, we employed scanning electron microscopy (SEM) and transmission electron microscopy (TEM) to capture detailed images of *Trictenotoma childreni* (Fig. 2) as well as the nanostructures present in the wings of the *Nymphalidae* butterflies (Fig. 5A,5B).

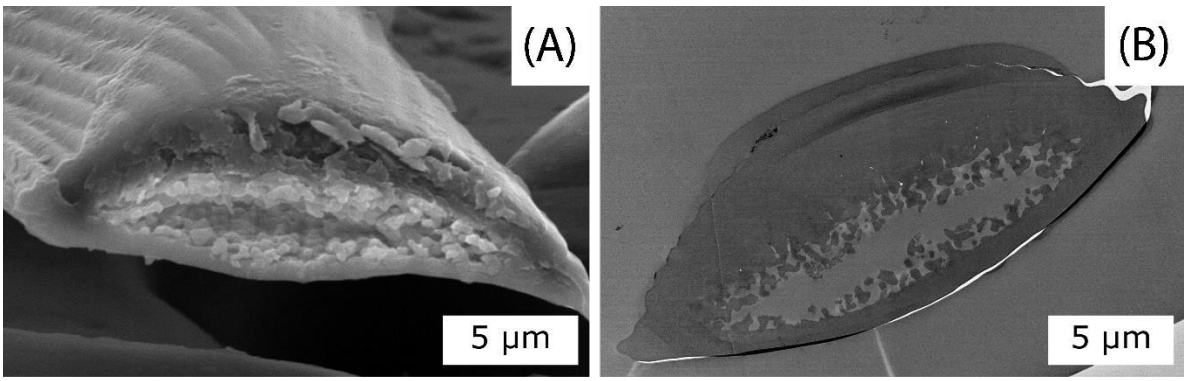


Figure 2. By using (a) SEM and (b) TEM images, we were able to observe a disordered structure present within the scales of T. childreni. Reproduced from Ref. [5] with permission from John Wiley and Sons.

Nonlinear optical analyses allowed us to elucidate the relationship between natural photonic structures and their optical response [3]-[8]. For instance, we were able to perform Second Harmonic Generation (SHG) images of the

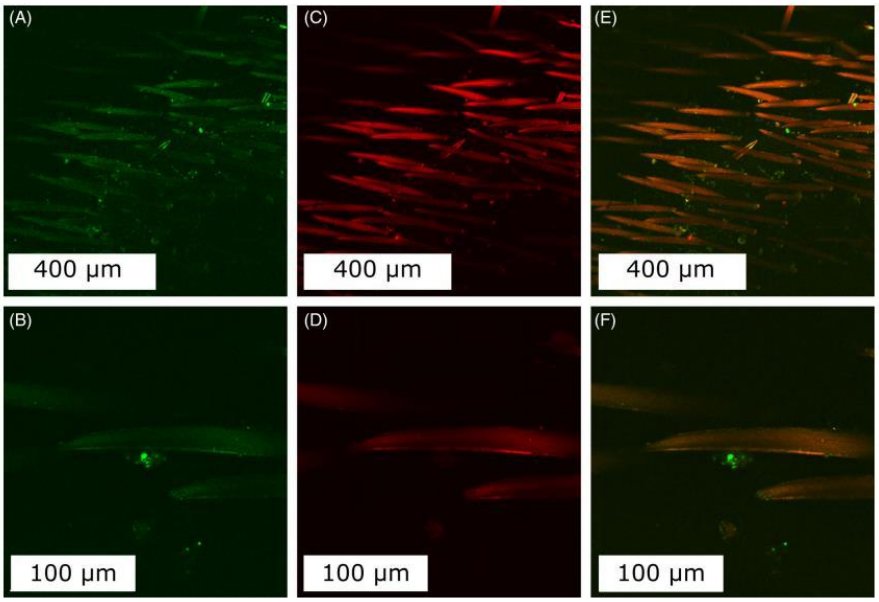


Figure 3. (a, b) SHG response, (c, d) 2PF response, and (e, f) superimposing of both signals (SHG + 2PF) from T. childreni's scales with a fundamental wavelength of 1000 nm. The six images clearly depict the scales. In (e) and (f), orange/yellow pixels represent the areas with both SHG and 2PF signals, while green and red pixels indicate the regions with only SHG and only 2PF signals, respectively. Reproduced from Ref. [5] with permission from John Wiley and Sons.

scales covering the elytra of *Trictenotoma childreni*, longhorn beetle, using a femtosecond laser with excitation wavelength of 1000 nm (Fig. 3).

The same excitation wavelength has also been used to measure the two-photon fluorescence (2PF) response (Fig. 4) [5]. All sharp spectral peaks in Fig. 4 correspond exactly to half of the excitation wavelengths, confirming that the signal originates from SHG. In cases where the excitation wavelengths were 900, 1000, and 1100 nm, a broader peak located around 550 nm is attributed to 2PF [5]. These results are consistent with the observations made in the multiphoton micrographs (Fig. 3), where a clear SHG signal was detected. Additionally, the 2PF spectra reveal that even at higher excitation wavelengths, such as 1200 nm and 1300 nm, a significant SHG signal persists.

However, our results show that the intensity of the SHG signal varies depending on the excitation wavelength (Fig. 3,4). Notably, the most intense SHG peak is observed at the wavelength that corresponds to the fluorescence emission maximum. This finding provides additional evidence to support the idea that the fluorophores are the origin of the SHG. The results suggest that the fluorophores are non-centrosymmetric or that their distribution within the scales is non-centrosymmetric and, therefore, non-random [5]. As it is widely recognised, second-order effects, such as SHG, are only possible in non-centrosymmetric media. This likely random distribution of the fluorophores might appear during the pupa stage of the beetle's scale development.

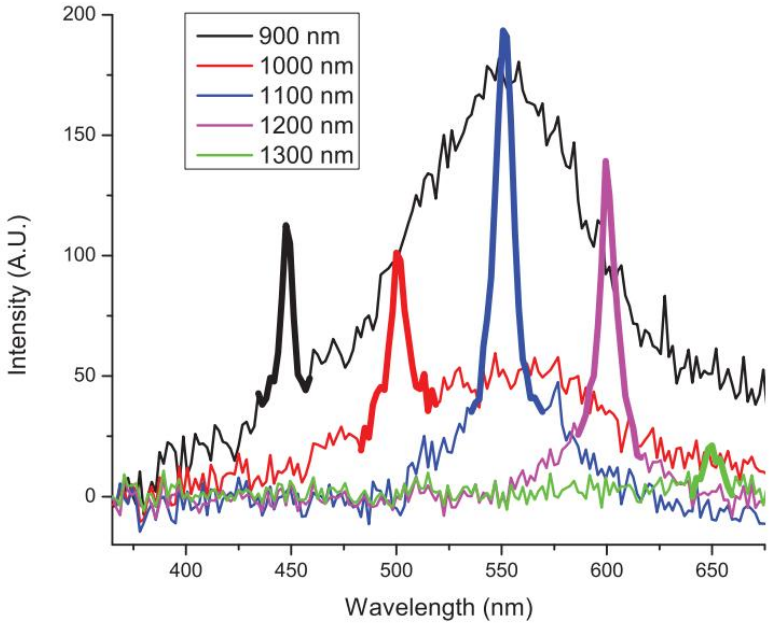


Figure 4. Multiphoton emission spectra of T. childreni's scales excited with wavelengths ranging from 900 to 1300 nm. A distinct SHG peak at half the respective wavelengths (indicated by thick lines) is observed with all excitation wavelengths. The broader peaks observed around 550 nm with all selected excitation wavelengths, except 1200 and 1300 nm, are attributed to 2PF. These results are consistent with the observations made using multiphoton microscopy (Fig. 3). Reproduced from Ref. [5] with permission from John Wiley and Sons.

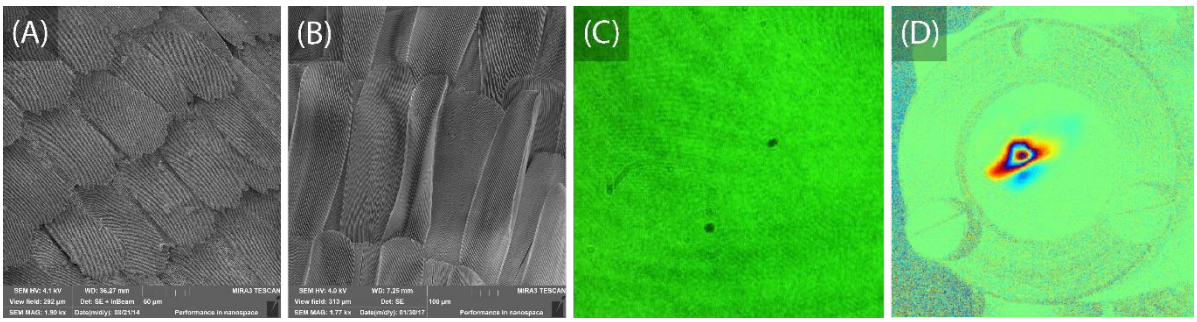


Figure 5. SEM images of (a) Apatura ilia, and (b) Morpho didius butterflies; Example of (c) holographic image, and (d) holographic reconstruction for Apatura ilia sample.

Our holographic investigation reveals thermal management and dynamics of natural photonic structures in *Apatura ilia* (Fig. 5C,5D) and *Morpho didius.* Our findings demonstrated a notable correlation between thermal management and the photonic band gap.

3. CONCLUSION

Our study relying on holography and nonlinear optics techniques sheds light on the relationship between the optical response of natural photonic structures, their geometry, and dynamics. These insights help to enhance our understanding of the role of fluorescence in insects. The findings of this study are crucial for the development of future applications of natural photonic structures in optics and material science.

ACKNOWLEDGEMENTS

MSP, BB, DV and BK acknowledge the support of the Office of Naval Research Global through the Research Grant N62902-22-1-2024. BB, DV and BK acknowledge funding provided by the Institute of Physics Belgrade, through the institutional funding by the Ministry of Science, Technological Development and Innovations of the Republic of Serbia. S.R.M. was supported by Wallonia-Brussels International (WBI) through a Postdoctoral Fellowship for Excellence program WBI.WORLD; by the Belgian National Fund for Scientific Research (FRS-FNRS) as a postdoctoral researcher (91400/1.B.309.18F); and by a BEWARE Fellowship (Convention n° 2110034) of the Walloon Region (Marie Skłodowska-Curie Actions of the European Union - COFUND - contract 847587), as a postdoctoral researcher. Additionally, B.K. acknowledges support from F.R.S.-FNRS.

REFERENCES

[1] P. Vukusic and J.R. Sambles: Photonic structures in biology, *Nature*, vol. 424. pp. 852-855, 2003.

[2] S.R. Mouchet and O. Deparis: Natural Photonics and Bioinspiration; Artech House: Boston, MA, USA, 2021.

[3] D. Mara *et al.:* Revealing the Wonder of Natural Photonics by Nonlinear Optics, *Biomimetics*, vol. 7(4). pp. 153, 2022.

[4] M. Simovic-Pavlovic *et al.*: Uncovering Hidden Dynamics of Natural Photonic Structures using Holographic Imaging, *J. Vis. Exp*., e63676, 2022.

[5] S.R. Mouchet *et al.*: Unveiling the nonlinear optical response of *Trictenotoma childreni* longhorn beetle, *J. Biophotonics*, e201800470, 2019.

[6] S.R. Mouchet *et al.*: Nonlinear optical spectroscopy and two-photon excited fluorescence spectroscopy reveal the excited states of fluorophores embedded in a beetle's elytra, *Interface Focus*, vol. 9. pp. 20180052, 2018.

[7] S.R. Mouchet *et al.*: Revealing natural fluorescence in transparent insect wings by linear and nonlinear optical techniques, *Journal of Luminescence*, vol. 254. pp. 119490, 2023.

[8] C. Verstraete *et al.*: Linear and nonlinear optical effects in biophotonic structures using classical and nonclassical light, *J. Biophotonics.* e201800262, 2018.

Breaking Barriers: Molding Thermodynamics by Geometry of Nanostructures

Marina Simović Pavlović[1,2*], Maja Pagnacco[3], Bojana Bokić[1], Darko Vasiljević[1], Marija Radmilović-Rađenović[1], Branislav Rađenović[1] and Branko Kolarić[1,4]

[1]Photonics Center, Institute of Physics, University of Belgrade, Pregrevica 118, 11080 Belgrade, Serbia

[2]Faculty of Mechanical Engineering, University of Belgrade, Kraljice Marije 16, 11120 Belgrade, Serbia

[3]Institute of Chemistry, Technology and Metallurgy, University of Belgrade, Njegoševa 12, Belgrade, Serbia

[4]Micro- and Nanophotonic Materials Group, University of Mons, Place du Parc 20, 7000 Mons, Belgium

[*]Tel: (00381) 604273777, e-mail: simovicmarina99@gmail.com

ABSTRACT

Convective, conductive, and radiative mechanisms of thermal and optical management are essential for life, and they are often interwoven with geometry in Nature. Nanostructured materials have properties that depend on size and shape, are entirely different from their bulk counterpart, and very often exhibit size-dependent physical responses. In this study, we reveal the effect of corrugation and geometry on thermodynamic properties, i.e., heat capacity. The presented results highlight that the multifaceted geometry of natural photonic structures strongly shapes the thermodynamic response of the composite system, and, in some extreme cases, exhibits negative heat capacity. Besides the fundamental importance of revealing the geometrical constraints responsible for unusual thermodynamic response, the presented study offers the concept of shaping heat capacity on command by controlling the geometry of the system without changing its chemistry.

Keywords: nanomaterials, heat capacity, natural photonics, thermodynamics, optics.

1. INTRODUCTION

Thermodynamics is the best example of phenomenological science, where development starts from observations and proceeds by induction and conjectures to general laws, often improperly called "principles" because these conjectures are not fundamental [1]. However, thermodynamics is ultimately connected with the development of atomic and quantum theory, even though thermodynamics keeps a distance from assumptions about the "ultimate" nature of things [2].

On the other hand, photonics, as part of optics, is not ultimately related to thermodynamics. However, in a broader sense, photonics is linked with the structuring of matter. Controlling the structuring affects optical properties, offering passive and active control of light and surface properties, i.e., wetting.

In a simple sense, the energy and entropy of a composite system, such as nanostructures, are additive over the constituent subsystems and do not depend on the system's size. The presence of an interface (a real, not ideal Gibbs interface) causes, in some cases, the appearance of discontinuity and size-dependent behavior.

In the study, we reveal the effect of corrugation on thermal management for the first time to our knowledge. The presented results highlight that the multifaceted geometry of natural photonic structures with rich and complex interfaces powerfully shapes the thermodynamic response of the composite system, and, in some extreme cases, the composite system exhibits a nonreciprocal response [3] or even a decrease in heat capacity that highlights the appearance of highly effective cooling properties.

2. EXPERIMENTAL METHODS

Specimens of *Morimus asper funereus* and *Euchroma giganteum* are air-dried and obtained as a gift from the collection of the Nanophotonics Lab, Institute of Physics, University of Belgrade. No further sample preparation was necessary for the described measurements apart from electron microscopy observation. All analyses are performed using the insects' wings. The schematic view of the setup used for measuring the temperature gradient is shown in Figure 1.

3. DISCUSSION

In this article, we reveal that natural photonic structures with complex geometries and multifaceted interfaces strongly affect thermodynamic properties of matter that, in extreme cases, lead to a system that exhibits significant decreases of heat capacity in some temperature ranges. The natural photonic structures [4, 5] have already been studied for active and passive control of light and various material applications. In this study, we recorded the thermodynamic response of natural photonic structures by measuring heat capacity as a function of temperature and using a thermal camera to monitor the distribution of thermal gradient after irradiating beetle elytra with a

Copyright notice: 979-8-3503-7732-3/24/$31.00 ©2024 IEEE

laser. The natural photonic structures of insects, mainly composed of polysaccharide chitin, are not broadly studied from a thermodynamic perspective, especially with the goal of exposing the effect of corrugations on thermodynamic response. First, we present DSC measurements of two beetle species (Fig. 2), namely *M. funereus* and *E. giganteum* that show the effect of the micro-architectures on the heat capacity as a function of temperature.

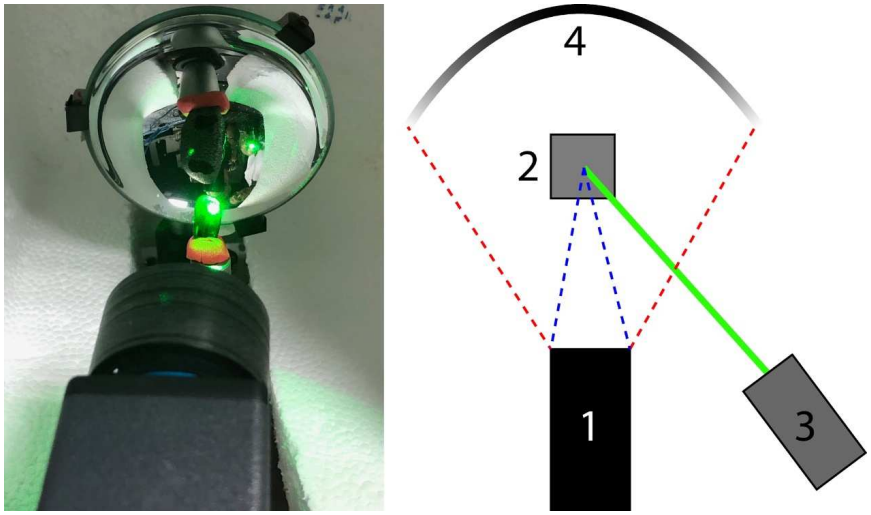


Figure 1. Setup for measuring the temperature gradient at elytra after irradiation with laser: (left) setup in the laboratory during the experiment, (right) scheme of the setup (1 - FLIR camera; 2 - aluminum mount with the sample; 3 - laser pointer at 532nm; 4 - spherical mirror).

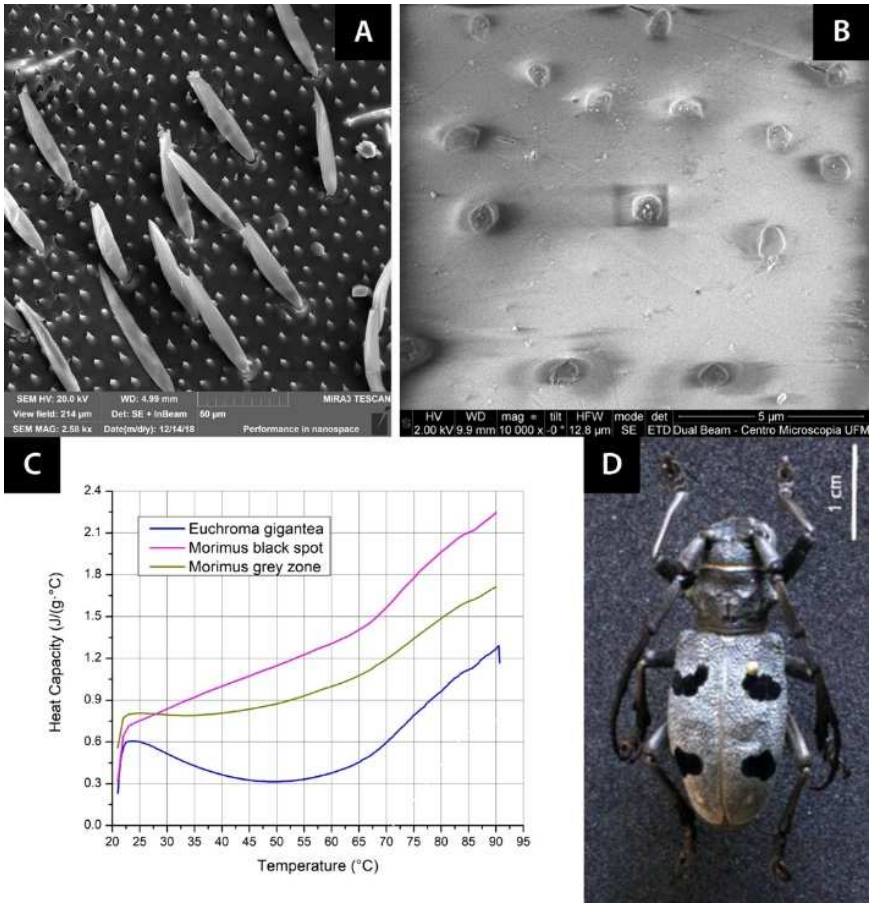


Figure 2. The microstructures occurring on (A) the elytra of Morimus asper funereus, and (B) Euchroma giganteum beetles observed by SEM. The heat capacity as a function of temperature is measured in the range of 20°C-90°C (C). An image of Morimus asper funereus (D). Figure (B) was reproduced from, Figure (D) was reproduced from [7].

Additionally, the *M. funereus* has a composite elytra consisting of a grey part with four black patches. In a previous study by co-authors of this article, it is shown that nanostructures occurring in the elytra of *M. funereus* manage heat transport [7] in an unusual way. In this account, the heat capacity of the black spots is independently investigated. In many systems, the increase in temperature causes the heat capacity to increase, and for many planar films, the observed dependence is linear or almost linear. The divergence of the heat capacity as a function of temperature from linearity indicates the effects of nano/micro-corrugation on heat management. Particularly in the case of *E. giganteum*, the functional dependence noticeably diverges from linearity: it exhibits a parabolic profile between 25 and 60°C (Fig. 3).

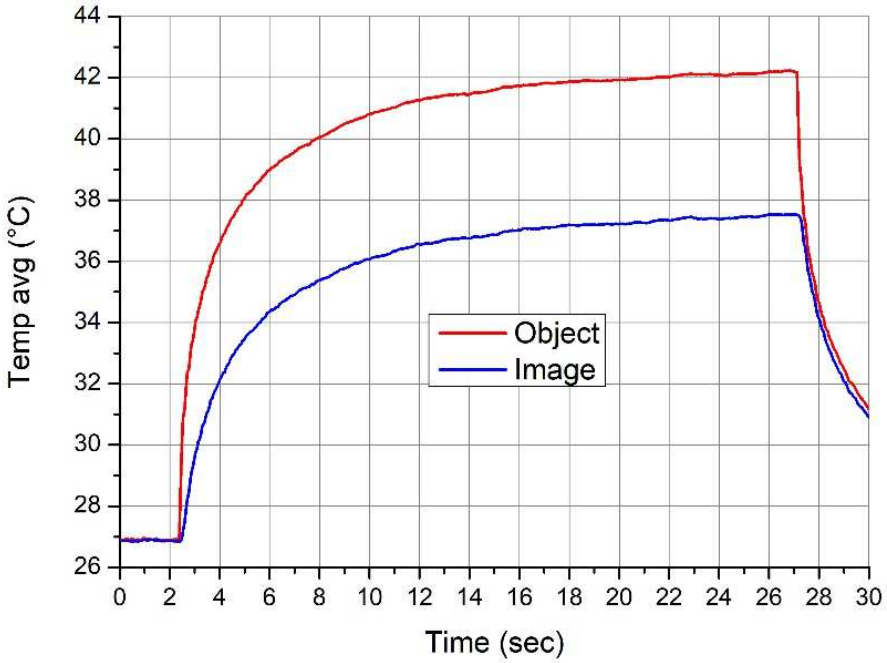


Figure 3. Average temperature differences of the outer (object) and inner (image) side of elytra illuminated by laser pointer at 650 nm.

The decrease of the heat capacity as a function of temperature perfectly matches the results obtained by irradiating elytra by laser. We did not expect to have any thermal gradient for such thin samples as elytra, but the results show highly effective cooling caused by the corrugation/nanostructures of elytra. Additionally, we perform image analysis using two-dimensional fast Fourier transformation (2D FFT), implemented in the Gwyddion software package for scanning probe microscopy data visualization and analysis.

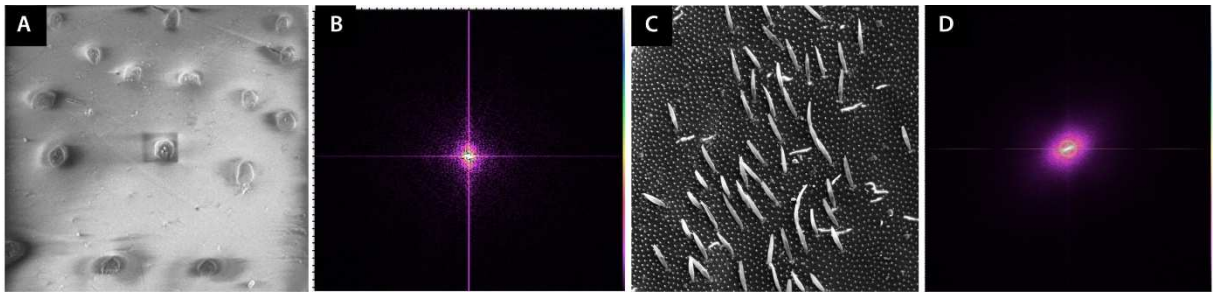


Figure 4. Euchroma giganteum – (A) SEM image of the elytra [6], (B) 2D FFT of Fig.4A image; Morimus asper funereus – (C) SEM image of the elytra, (D) 2D FFT of Fig.4C image.

The image analysis (Fig. 4) shows the effect of geometry on 2D FFT. When unusual heat management is observed (decrease of the heat capacity as a function of heating), the 2D FFT image shows that the periodicity is dominantly manifested in one direction (a linear form of the 2D FFT spectra). In contrast, in the case of well-expected thermal behavior, the 2D FFT images of the structure are almost circular, which means that two mutually normal directions are equally periodic.

4. CONCLUSIONS

However, our experimental results and theoretical analysis show that condensed systems with complex geometry and multiple interfaces shaped heat propagation in an unprecedented way and, in extreme cases, could cause a significant decrease in heat capacity values. The discovery of dependence between heat capacity and geometry in natural photonic structures offers the possibility to mimic these complex geometries for the development of highly energy-efficient materials. Additionally, the presented results show that Wolfgang Pauli was not entirely right in describing surface/interface as the devil's creation [8]. The presence of surface/interface indeed brings a lot of challenging tasks in the physical description of the system, but it also brings a plethora of new effects that could lead to new breakthroughs in material science and technology. Furthermore, the given article extends the power of photonics in the field of thermodynamics and offers the possibility of using the structuring of interfaces (not chemical modifications) to mold heat capacity and thermodynamic properties of materials.

ACKNOWLEDGEMENTS

All authors acknowledge the support of the EU: the EIC Pathfinder Challenges 2022 call through the Research Grant 101115149 (project ARTEMIS). The content reflects only the authors' view, and the European Commission is not responsible for any use that may be made of the information it contains. MSP, MP, BB, DV and BK acknowledge the support of the Office of Naval Research Global through the Research Grant N62902-22-1-2024. BB, DV, BK, MR-R and BR acknowledge funding provided by the Institute of Physics Belgrade, through the institutional funding by the Ministry of Science, Technological Development and Innovations of the Republic of Serbia. Additionally, B.K. acknowledges support from F.R.S.-FNRS.

REFERENCES

[1] M. Giovanelli: 'Like thermodynamics before Boltzmann.' On the emergence of Einstein's distinction between constructive and principle theories, *Studies in History and Philosophy of Modern Physics*, vol. 71. pp. 118-157, 2020.

[2] W. M. Haddad: Thermodynamics: The Unique Universal Science, *Entropy*, vol. 19(11), pp. 621, 2017.

[3] S. Yang, M. Liu, C. Zhao, S. Fan and C. Qiu: Nonreciprocal Thermal Photonics, Nature photonics, vol. 18. pp. 412-424, 2024.

[4] C. Verstraete et al.: Linear and nonlinear optical effects in biophotonic structures using classical and nonclassical light, J. Biophotonics. e201800262, 2018.

[5] S.R. Mouchet et al.: Revealing natural fluorescence in transparent insect wings by linear and nonlinear optical techniques, Journal of Luminescence, vol. 254. pp. 119490, 2023.

[6] R. L. Rincon-Celis, D. Bernal-Garcia, H. Vinck-Posada and G. Colorada.: FDFD Simulation to describe Iridescence Phenomena on *Euchroma gigantea*'s Elytra, *Revista de Fisica*, vol. 51., 2015.

[7] D. Vasiljevic, D. Pavlovic, V. Lazovic, B. Kolaric, B. Salatic, W. Zhang, D. Zhang and D. Pantelic: Thermal radiation management by natural photonic structures: *Morimus asper funereus* case, *Journal of Thermal Biology*, vol. 98. pp. 102932, 2021.

[8] https://www.espci.psl.eu/?page=article-print&id_article=8959

Revealing the beauty of natural photonics through the synergy of holotomography and nonlinear optical metrology

Yin Chang*[a], Bojana Bokić[b], Milica Živančević[b], Luka Krstić[b]. Olga Vrbaški[b], Branko Kolaric*[b,c]

[a]Department of Materials and Optoelectronic Science, National Sun Yat-sen University, Taiwan; [b]Nanophotonics Laboratory, Photonics Center, Institute of Physics, University of Belgrade, Pregrevica 118, 11080 Belgrade, Serbia; [c]Micro- and Nanophotonic Materials Group & Research Institute for Materials Science and Engineering, University of Mons, Belgium;
*Corresponding author: yc405@cantab.ac.uk; Branko.KOLARIC@umons.ac.be

ABSTRACT

In this article, we propose a concept that combines quantitative holotomography (HT) and nonlinear optics (NLO) to reveal structural heterogeneity in natural photonic materials quantitatively. This approach enables direct microscopic correlation between three-dimensional refractive index distributions and localized nonlinear optical responses beyond effective-medium descriptions.

Keywords: nonlinear optics, holotomography, natural photonics, photonic crystals

INTRODUCTION

Since Yablonovitch's proposal of photonic crystals in 1987, photonics research has largely pursued structures with perfect long-range periodicity to achieve photonic bandgaps [1]. Butterflies, beetles, and marine organisms routinely exhibit photonic structures that lack crystallinity over long length scales, yet still produce broadband reflection, angular robustness, and thermal resilience [2-4]. These systems rely on short-range order embedded within disordered or amorphous networks, a design strategy historically dismissed as imperfection or noise. Only recently has it become clear that such architectures support optical phenomena beyond simple Bragg diffraction, including multiple scattering [5], Anderson localization [6], and broadband or isotropic bandgap formation in non-periodic and correlated disordered materials [6]. In this article, we highlight the interest and impact of joint nonlinear optical and holotomography studies of photonic structures. We highlight the benefit of these techniques for revealing the details of structured matter at the nanoscale and its interaction with light. The proposed concept has the power to reveal the structural-optical response relationship from micro to macro levels, essential for various applications in materials science. The central challenge is rather methodological: detecting them to reveal the structure-response relationship. How to quantitatively link biological structure to optical and thermomechanical function? Is it possible to adjust color over a broad range by using almost the same components with light elements with low refractive index? So far, synthetic systems have not achieved this. How do these systems reach rainbow color while remaining highly constrained materials, and what are the fundamental challenges? Addressing these questions requires a metrological approach that exceeds the capabilities of conventional imaging or spectroscopy alone, linking structure to symmetry, symmetry to dynamics, and dynamics to function.

METHODOLOGY

Beyond the optical properties of samples measured with widely used linear techniques, high-intensity laser excitation can provide substantially richer insight into material organization and dynamics by activating nonlinear optical (NLO) responses. Under strong electromagnetic fields, induced nonlinear susceptibilities give rise to techniques such as multiphoton excitation fluorescence, hyper-Rayleigh scattering, and harmonic generation, most prominently second- and third-harmonic generation (SHG and THG) [7].

Light in Nature 2026, edited by Katherine Creath, Vasudevan Lakshminarayanan, Joseph A. Shaw,
Proc. of SPIE Vol. 14207, 1420704 · 2026 Published by SPIE
0277-786X · doi: 10.1117/12.3114433

Unlike electron microscopy, which achieves high spatial resolution but destroys the native biological context through dehydration, staining, or sectioning, HT enables label-free, quantitative imaging in a near-native state. By acquiring multiple holographic projections at different illumination angles and applying reconstruction algorithms, HT derives the volumetric RI distribution, providing direct insight into cellular morphology, internal organization, and material composition [8-10]. The power of HT is presented in Fig. 1 [11].

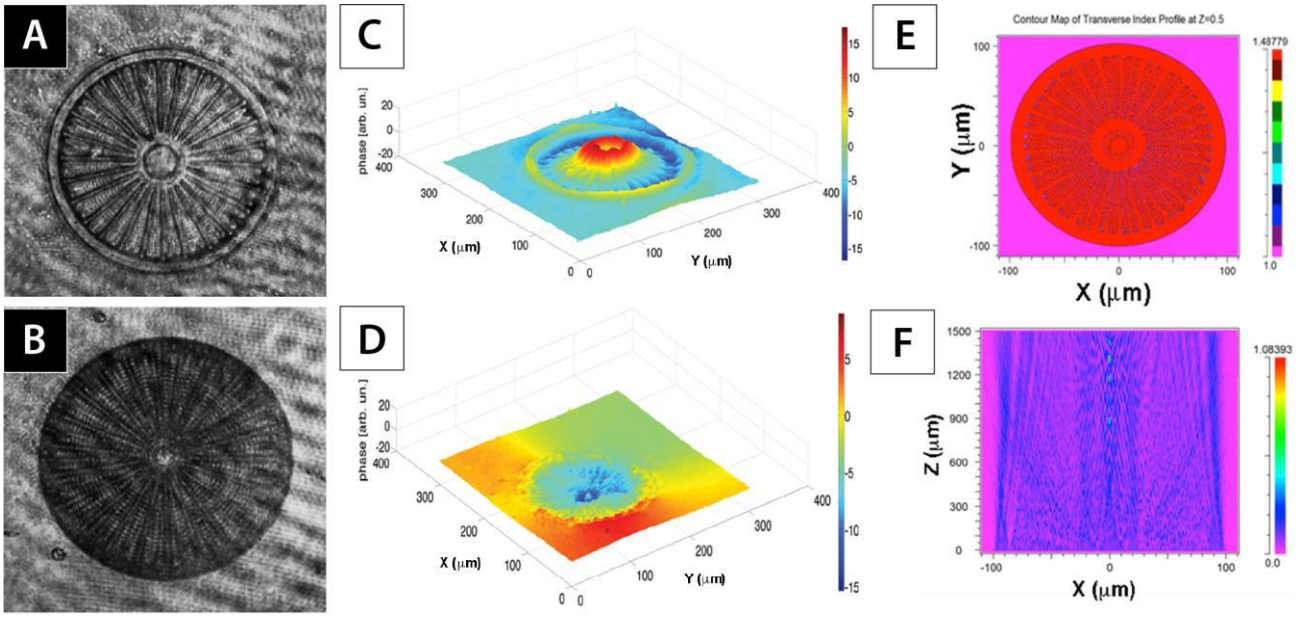


Figure 1. Digital holography and morphology-based optical modeling of a biological photonic diatom specimen. (A) Representative hologram acquired from the upper side of an Arachnoidiscus diatom valve. **(B)** Representative hologram acquired from the lower side of the valve. **(C)** Three-dimensional phase reconstruction of the upper-side holographic measurement. **(D)** Three-dimensional phase reconstruction of the lower-side holographic measurement. **(E)** Morphology-derived refractive-index model generated from the diatom valve ultrastructure and used for optical propagation simulation. **(F)** Representative structurally relevant region, such as the central flange, pores, or radiating costae, that may be selected as a candidate region for subsequent NLO interrogation in a future correlative HT–NLO workflow [11].

This approach allows precise, non-invasive measurements of biophysical parameters such as volume, dry mass density, subcellular structures, and intracellular dynamics. HT has shown it can reconstruct biologically driven, non-uniform architectures that lack periodicity yet support photonic bandgaps. These reconstructions provide the structural boundary conditions required for thermodynamic and electrodynamic modeling of correlated disorder. While it can reveal the effect of stress on the structure and thus enable monitoring of the mechano-optical response [12], it cannot directly reveal how these architectures form, how symmetry emerges, or how they respond dynamically to optical excitation.

CONCLUSION

In conclusion, we want to emphasize that the relationship between HT and NLO is not sequential but convergent and should be interpreted first as a correlative structure–response workflow. HT measures where light localizes within a structure and identifies candidate regions where optical fields may be modified by local structure, while NLO, especially polarization-sensitive SHG, detects how molecular symmetry responds to that localization under excitation; together, they bridge molecular-scale symmetry dynamics with mesoscopic optical structure. The protocol's central output is therefore not a standalone HT image or NLO image, but a registered dataset that enables comparison of RI-derived structural metrics with nonlinear optical intensity and polarization response. This correlative framework can motivate but does not by itself prove mechanistic hypotheses involving photothermal or phononic and mechanical coupling. The proposed synergy of HT and NLO optics opens a new way to unveil complex dynamics of natural photonics that could lead to various applications in materials science.

ACKNOWLEDGEMENTS

The authors acknowledge the financial support from the National Science an Technology Council, Taiwan (NSTC 115-2112-M-110 -019 -MY3; NSTC 115-2112-M-110-009-MY3), the Bureau of Energy, Ministry of Economic Affairs, Taiwan, for this research under Contract No. 115-D0101-1. B.B., M.Ž., L.K., O.V., and B.K. acknowledge the support of the EU: the EIC Pathfinder Challenges 2022 call through the Research Grant 101115149 (project ARTEMIS). The content reflects only the authors' views, and the European Commission is not responsible for any use that may be made of the information it contains.

REFERENCES

[1] González-Urbina, L., Baert, K., Kolaric, B., Pérez-Moreno, J. and Clays, K., "Linear and Nonlinear Optical Properties of Colloidal Photonic Crystals," Chem. Rev. 112(4), 2268–2285 (2012). https://doi.org/10.1021/cr200063f

[2] Mouchet, S. R. and Deparis, O., [Natural Photonics and Bioinspiration], Artech House, Norwood, MA, USA (2021).

[3] Vasiljević, D., et al., "Thermal radiation management by natural photonic structures: Morimus asper funereus case," J. Therm. Biol. 98, 102932 (2021). https://doi.org/10.1016/j.jtherbio.2021.102932

[4] Mara, D., et al., "Revealing the wonder of natural photonics by nonlinear optics," Biomimetics 7(4), 153 (2022). https://doi.org/10.3390/biomimetics7040153

[5] Rechtsman, M. C., et al., "Amorphous photonic lattices: band gaps, effective mass, and suppressed transport," Phys. Rev. Lett. 106(19), 193904 (2011). https://doi.org/10.1103/PhysRevLett.106.193904

[6] Vasco, J. P. and Hughes, S., "Anderson localization in disordered LN photonic crystal slab cavities," ACS Photonics 5(4), 1262–1272 (2018). https://doi.org/10.1021/acsphotonics.7b00967

[7] Boyd RW. Nonlinear Optics. 4th ed. Academic Press; London, UK; 2020.

[8] Ferrara, M. A., et al., "Quantitative holographic analysis in stallion spermatozoa following cryopreservation," Sci. Rep. 15(1), 43190 (2025). https://doi.org/10.1038/s41598-025-24885-w

[9] Khadem, H., et al., "Polarization-sensitive holotomography for multidimensional label-free imaging and characterization of lipid droplets in cancer cells," Adv. Sci. 12(42), e09420 (2025). https://doi.org/10.1002/advs.202509420

[10] Kim, G., et al., "Holotomography," Nat. Rev. Methods Primers 4(1), 51 (2024). https://doi.org/10.1038/s43586-024-00327-1

[11] Ferrara, M. A., et al., "Optical properties of diatom nanostructured biosilica in Arachnoidiscus sp: micro-optics from mother nature," PLoS One 9(7), e103750 (2014). https://doi.org/10.1371/journal.pone.0103750

[12] Simovic-Pavlovic, M., et al., "Thermophoretic effect in natural photonics: holographic study," Bioinspir. Biomim. 20(2), 024001 (2025). https://doi.org/10.1088/1748-3190/adb6e8

Revealing Self-organization of Granular Matter: From Fundamental Physics to Military Technology Applications

D. Janković[1], M. Simović Pavlović[2], M. Pagnacco[3], Z. Nikolić[4], B. Bokić[5], B. Kolarić[5,6], Lj. Tomić[7], D. Vasiljević[5]

[1] University of Defence, Military Academy, Veljka Lukića Kurjaka 33, Belgrade, Serbia;

[2] University of Belgrade, Faculty of Mechanical Engineering, Kraljice Marije 16, Belgrade, Serbia;

[3] University of Belgrade, Institute of Chemistry, Technology and Metallurgy, Njegoševa 12, Belgrade, Serbia;

[4] University of Belgrade, Faculty of Physics, Studentski trg 12, Belgrade, Serbia;

[5] Center for Photonics, Institute of Physics, University of Belgrade, Pregrevica 118, 11080 Belgrade, Serbia;

[6] Micro- and Nanophotonic Materials Group, University of Mons, Place du Parc 20, 7000 Mons, Belgium.

[7] Technical Test Center, Vojvode Stepe 445, 11000, Belgrade, Serbia

Abstract:

Besides fundamental importance, granular physics has made considerable progress in revealing the dynamics of large ensembles of interacting macroscopic particles and their pattern formation for various applications in material, food, and chemical technologies. In this study, optical images obtained by the fast camera have been used to reveal the organization of various granular substrates as a function of interaction with projectiles of different shapes and energies.
Specific patterns have been observed due to the energy dissipations after the impact. The obtained results indicate the possibility of manipulating granular matter to mold and direct/redirect the energy of the impact. This type of manipulation is of great importance for various applications, especially in the military domain.

References

[1] P. Zhang and Z.Y.A. Yin, "A novel deep learning-based modelling strategy from image of particles to mechanical properties for granular materials with CNN and BiLSTM. Computer Methods," Applied Mechanics and Engineering, vol. 382, pp. 113858, 2021.

[2] I.L. Guzman, M. Iskander, and S. Bless, "Visualization of impact cratering in granular media using quarter space penetration tests," Granular Matter, vol. 23(3), pp. 63, 2021.

Revealing the Impact of Different Shapes of Light on the Briggs-Rauscher Oscillatory Dynamics

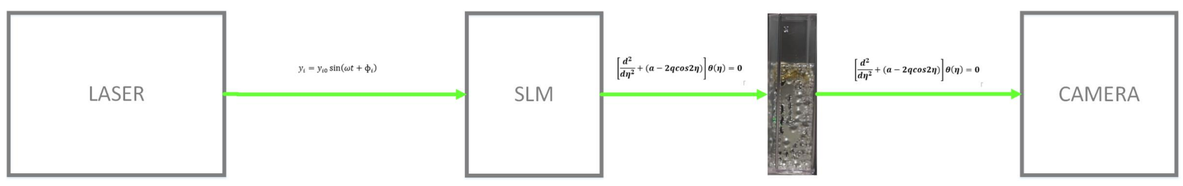
M. Simović Pavlović[1], M. Pagnacco[2], D. Vasiljević[3], B. Bokić[3], T. Verbiest[4], Y. Caudano[5], and B. Kolarić[3,6]

1 University of Belgrade, Faculty of Mechanical Engineering, Kraljice Marije 16, Belgrade, Serbia;
2 University of Belgrade, Institute of Chemistry, Technology and Metallurgy, Njegoševa 12, Belgrade, Serbia;
3 University of Belgrade, Center for Photonics, Institute of Physics, Pregrevica 118, Belgrade, Serbia;
4 University of Lueven, Chemistry Department, Laboratory of Molecular Imaging and Photonics, Leuven;
5 University of Namur, Department of Physics, Namur Institute for Complex Systems (naXys), Namur Institute of Structured Matter (NISM), Rue de Bruxelles 61, 5000 Namur, Belgium;
6 University of Mons, Micro- and Nanophotonic Materials Group, Place du Parc 20, 7000 Mons, Belgium.

Introduction:

The uniqueness of the Briggs-Rauscher oscillatory reaction is that it first follows a deterministic pattern (namely, an oscillatory behavior) and, later, exhibits a phase transition occurring randomly and without any known link with the previous deterministic state. We unveil in this study how the different topologies of electromagnetic waves affect the reaction kinetics and phase transition dynamics. The presented research uniquely unmasks the connection between the topology of light and matter dynamics. Simultaneously, it opens a new route for structured light applications in material science.

Experimental setup:



The schematic and simplified view of the experimental setup: laser, SLM, cuvette and camera. The BR reaction occurs in a cuvette of 2.5 ml.



RESULTS:

STATE I : Low iodide and iodine concentration. (Left)
STATE II : High iodide and iodine concentration, with solid iodine formation. (Right)

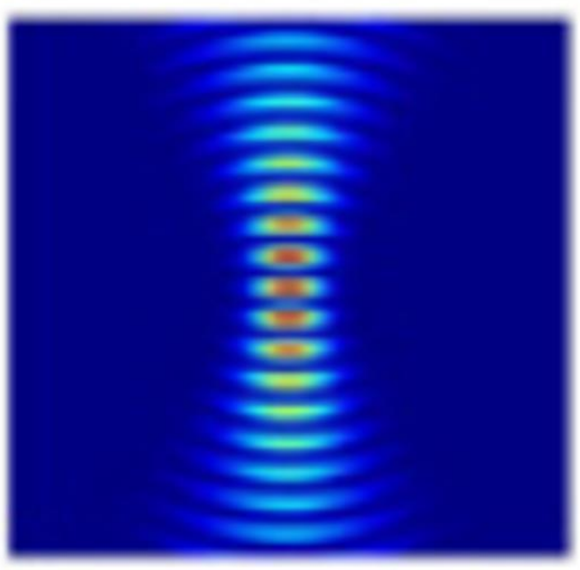


$$CH_2(COOH)_2 + IO_3^- + 2H_2O_2 + H^+ \xrightarrow{Mn^{2+}catalyst} CHI(COOH)_2 + 2O_2 + 3H_2O$$

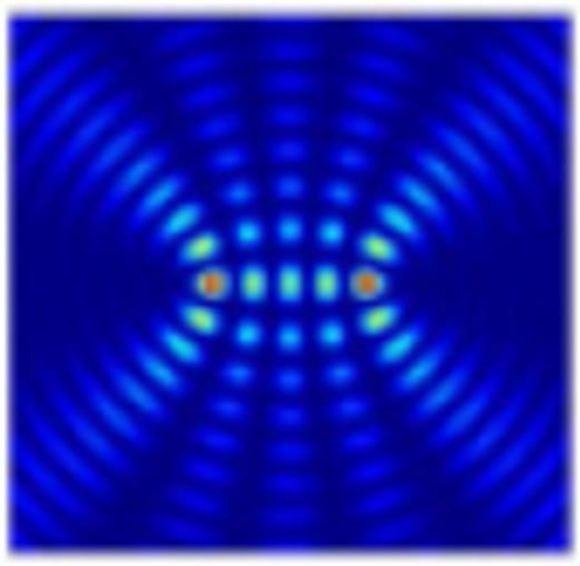
MATHIEU WAVES:
("m" is the order of the beam)

$$\left[\frac{d^2}{d\eta^2} + (a - 2q\cos 2\eta)\right]\theta(\eta) = 0$$

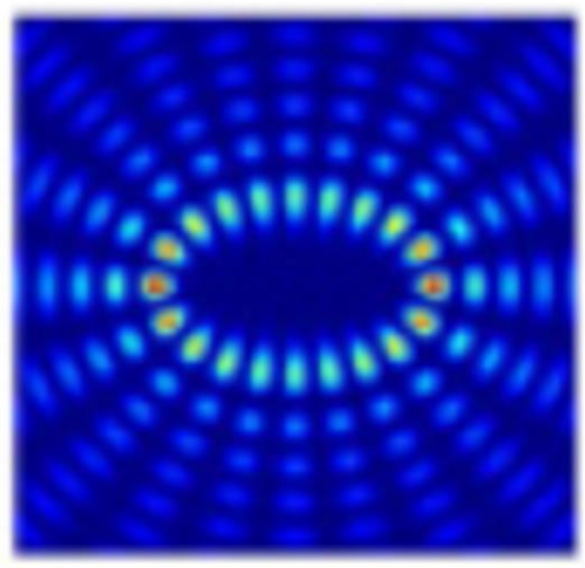
η – polar angle
q – dimensional parameter
θ - for the angular (normal) Mathieu equation



m=0
State I : 25 s
State II : 320 s



m=4
State I : 52 s
State II : 330 s



m=10
State I : 65 s
State II : 350 s

Conclusion:

Preliminary results offer the possibility of exploiting the topology of light for controlling stochastic processes. Furthermore, the presented study extends the application of light-matter interaction into non-equilibrium dynamics and thermodynamics fields.

References:

[1] M. Simovic-Pavlovic, M.C. Pagnacco, D. Grujic, B. Bokic, D. Vasiljevic, S. Mouchet, T. Verbiest, and B. Kolaric, „Uncovering Hidden Dynamics of Natural Photonic Structures using Holographic Imaging", Journal of Visualized Experiments (JOVE), pp. e63676, 2022.
[2] K. Y. Bliokh et al., „Roadmap on structured waves", submitted to Arxiv: 2301.05349v1, 2023.

Acknowledgement:
All authors acknowledge the support of the Office of Naval Research Global through the Research Grant N62902-22-1-2024.

REVEALING NON-EQUILIBRIUM DYNAMICS BY HOLOGRAPHY: THE CASE OF BRIGGS-RAUSCHER REACTION

Maja Pagnacco[1], Marina Simovic Pavlovic[2], Aleksandra Radulovic[3], Bojana Bokic[4], Darko Vasiljevic[4], Branko Kolaric[4,5]

[1] *University of Belgrade, Institute of Chemistry, Technology and Metallurgy, Njegoseva 12, Belgrade, Serbia*

[2] *University of Belgrade, Faculty of Mechanical Engineering, Kraljice Marije 16, Belgrade, Serbia*

[3] *University of Belgrade, Institute of General and Physical Chemistry, Studentski trg 12/V, Belgrade, Serbia*

[4] *University of Belgrade, Institute of Physics, Photonics Center, Pregrevica 118, Belgrade, Serbia*

[5] *Micro- and Nanophotonic Materials Group, University of Mons, Place du Parc 20, 7000 Mons, Belgium*

e-mail: simovicmarina99@gmail.com

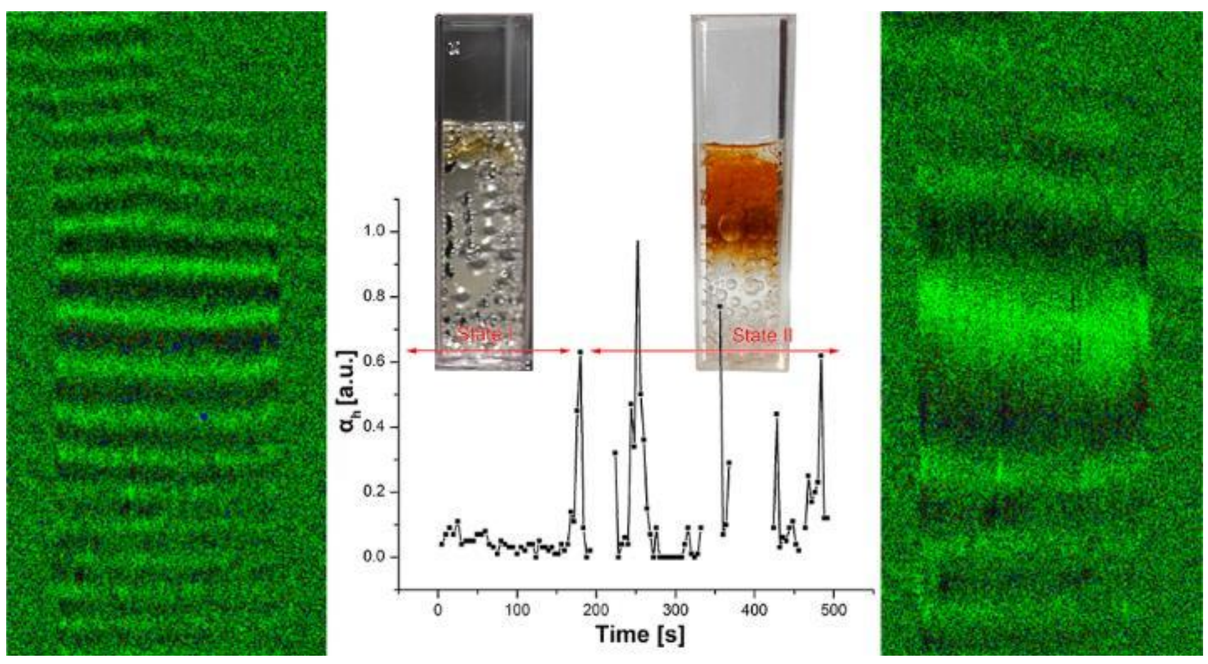
Introduction:

In this study, the interferometric (holographic) approach is used to unveil the dynamics of the phase transition, e.g., the formation of solid iodine in the Briggs-Rauscher (BR) non-equilibrium system. Subsequently, after deterministic oscillatory dynamics this system undergoes random transition from state I (low iodide and iodine concentration) to state II (high iodide and iodine concentration, with the formation of solid iodine).

$$CH_2(COOH)_2 + IO_3^- + 2H_2O_2 + H^+ \xrightarrow{Mn^{2+}catalyst} CHI(COOH)_2 + 2O_2 + 3H_2O$$

Experimental:

The observed interferometric pattern of dark and bright lines known as fringes is applied to monitor the changes in BR dynamics as a function of time. The pattern abruptly changes at the point of the phase transition.



Conclusion:

The power of holography is related to its ability to see the rise of the phase transition directly. At the same time, other methods, such as potentiometry (often used in non-equilibrium studies), are limited by secondary processes such as adsorption and electrode passivation. The holography opens the way to reveal nanoscale dynamics with minimal disturbances in various non-equilibrium systems.

References:

[1] Pagnacco, Maja C., et al. "Transition from Low to high iodide and iodine concentration states in the Briggs–Rauscher reaction: evidence on crazy clock behavior." J. Phys. Chem. A 2018, 122.2, 482-491.

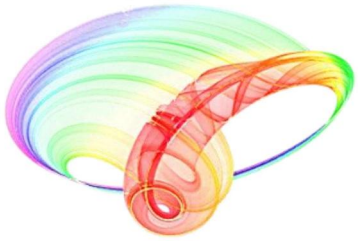
[2] Simovic-Pavlovic, M., Pagnacco, M.C., Grujic, D., Bokic, B., Vasiljevic, D., Mouchet, S., Verbiest, T., Kolaric, B. Uncovering Hidden Dynamics of Natural Photonic Structures using Holographic Imaging. *J. Vis. Exp.* **2022**, e63676.

(3) Pagnacco, Maja C., et al. “Stochastic Phase Transition Dynamics in Nonequilibrium System: Holographic Study" J. Phys. Chem. C 2023.

Acknowledgement:

All authors acknowledge the support of the Office of Naval Research Global through the Research Grant N62902-22-1-2024.

Book of abstracts



IX International School and Conference on Photonics

PHOTONICA2023

with joint events:

Understanding interaction light - biological surfaces: possibility for new electronic materials and devices

&

Biological and bioinspired structures for multispectral surveillance

&

Quantum sensing integration within microfluidic Lab-on-a Chips for biomedical applications

&

Advanced Biophysical Methods for Soil Targeted Fungi-Based Biocontrol Agents

August 28 - September 01, 2023, Belgrade, Serbia

Editors

Jelena Potočnik, Maja Popović, Dušan Božanić

Vinča Institute of Nuclear Sciences – National Institute of the Republic of Serbia, University of Belgrade

Belgrade, 2023

ABSTRACTS OF TUTORIAL, KEYNOTE, INVITED LECTURES, PROGRESS REPORTS AND CONTRIBUTED PAPERS

of

IX International School and Conference on Photonics

PHOTONICA2023

August 28 - September 01, 2023, Belgrade, Serbia

Editors
Jelena Potočnik, Maja Popović, Dušan Božanić

Publisher
Vinča Institute of Nuclear Sciences – National Institute of the Republic of Serbia, University of Belgrade
Mike Petrovića Alasa 12-14
11351 Vinča, Belgrade, Serbia

Printed by
Serbian Academy of Sciences and Arts

Number of copies
200

ISBN 978-86-7306-165-8
ISBN 978-86-7306-168-9 (Online)



This work is licensed under a Creative Commons Attribution-NonCommercial-NoDerivatives 4.0 International License, http://creativecommons.org/licenses/by-nc-nd/4.0/

PHOTONICA2023 – IX International School and Conference on Photonics (www.photonica.ac.rs) is organized by Vinča Institute of Nuclear Sciences - National Institute of the Republic of Serbia, University of Belgrade (www.vin.bg.ac.rs), Serbian Academy of Sciences and Arts (www.sanu.ac.rs), and Optical Society of Serbia (www.ods.org.rs).







Other institutions that helped the organization of this event are: Institute of Physics Belgrade, University of Belgrade (www.ipb.ac.rs), Faculty of Physics, University of Belgrade (www.ff.bg.ac.rs), School of Electrical Engineering, University of Belgrade (www.etf.bg.ac.rs), Institute of Chemistry, Technology and Metallurgy, University of Belgrade (www.ihtm.bg.ac.rs), Faculty of Technical Sciences, University of Novi Sad (www.ftn.uns.ac.rs), Faculty of Sciences and Mathematics, University of Niš (www.pmf.ni.ac.rs), Faculty of Biology, University of Belgrade (www.bio.bg.ac.rs) and Faculty of Sciences and Mathematics, University of Kragujevac (www.pmf.kg.ac.rs).

PHOTONICA2023 is organized under auspices and with support of the Ministry of Science, Technological Development and Innovation, Republic of Serbia (www.nitra.gov.rs). PHOTONICA2023 is supported and recognized by Optica (Formerly OSA) - The Optical Society (www.optica.org).





Revealing non-equilibrium dynamics by holography: The case of Briggs-Rauscher reaction

M. Pagnacco[1], M. Simovic Pavlovic[2], A. Radulovic[3], B. Bokic[4], D. Vasiljevic[4] and B. Kolaric[4,5]
[1]*University of Belgrade, Institute of Chemistry, Technology and Metallurgy, Njegoseva 12, Belgrade, Serbia*
[2]*University of Belgrade, Faculty of Mechanical Engineering, Kraljice Marije 16, Belgrade, Serbia*
[3]*University of Belgrade, Institute of General and Physical Chemistry, Studentski trg 12/V, Belgrade, Serbia*
[4]*University of Belgrade, Institute of Physics, Photonics Center, Pregrevica 118, Belgrade, Serbia*
[5]*Micro- and Nanophotonic Materials Group, University of Mons, Place du Parc 20, 7000 Mons, Belgium*
e-mail: simovicmarina99@gmail.com

In this study, the interferometric (holographic) approach is used to unveil the dynamics of the phase transition, e.g., the formation of solid iodine in the Briggs-Rauscher (BR) non-equilibrium system. Subsequently, after deterministic oscillatory dynamics this system undergoes random transition from state I (low iodide and iodine concentration) to state II (high iodide and iodine concentration, with the formation of solid iodine) [1].

The observed interferometric pattern of dark and bright lines known as fringes is applied to monitor the changes in BR dynamics as a function of time. The pattern abruptly changes at the point of the phase transition.

The power of holography is related to its ability to see the rise of the phase transition directly. At the same time, other methods, such as potentiometry (often used in non-equilibrium studies), are limited by secondary processes such as adsorption and electrode passivation. The holography opens the way to reveal nanoscale dynamics with minimal disturbances in various non-equilibrium systems [2].

REFERENCES

[1] M.C. Pagnacco *et al.*, J. Phys. Chem. A 122, 482 (2018).
[2] M. Simovic-Pavlovic *et al.*, J. Vis. Exp. 181, e63676 (2022).

Presenter: Bojana, Bokic
Twitter ID (if there is):

Sessions:

☐ Quantum, non-linear and laser optics
☒ Biosensing & Biophotonics: from micro- to nanoscale
☐ Optical design, manufacturing & imaging systems
☐ Nanophotonics, plasmonics & metamaterials

Geometry of Negative Heat Capacity Designed by Nature

Bojana Bokic[1], Sebastien Mouchet[2,] Sanja Ostojic[3], Maja Pagnacco[4], Marina Simovic[1], Darko Vasiljevic1, Marija Radmilovic-Radjenovic[1], Branislav Radjenovic[1], Thierry Verbiest[5], Branko Kolaric[1,6]

[1] Center for Photonics, Institute of Physics, University of Belgrade, 11080 Belgrade
[2] Department of Physics & Namur Institute of Structured Matter (NISM), University of Namur, 5000 Namur, Belgium; School of Physics, University of Exeter, Exeter EX4 4QL, U.K
[3] Institute of General and Physical Chemistry, Studentski trg 12/V, Belgrade, Serbia
[4] Center for Catalysis and Chemical Engineering, Institute of Chemistry, Technology and Metallurgy, University of Belgrade, 11000 Belgrade, Serbia
[5] Molecular Imaging and Photonics,Department of Chemistry, KU Leuven, 3001 Heverlee, Belgium
[6] Nanophotonic Materials Group, University of Mons, 7000 Mons, Belgium

Abstract: In nature, patterns of different sizes and forms are ubiquitous, ranging from the micro- and nano-worlds to the scale of galaxies and the universe itself. Life is intertwined with various geometric forms, such as the angles of atomic bonds within molecules, which determine configuration and, consequently, molecular reactivity. On a larger scale, this is evident in the spherical shape of cells, the helical spirals of DNA, and the lattice patterns of crystals and supramolecular assemblies. Nanostructured materials possess properties that depend on size and shape, distinctly differing from their bulk counterparts. In this account, we present experimental studies that reveal the effect of nanostructured geometry and its size on heat capacity. Beyond the fundamental importance of uncovering the geometrical constraints that could lead to the emergence of negative heat capacity in condensed systems, the study we present offers the possibility of tailoring heat capacity at will by manipulating the geometry without altering the chemistry of the system.

ON THE INTERPLAY BETWEEN GEOMETRY AND THERMODYNAMIC PROPERTIES IN NANOSTRUCTURED MATERIALS

Branko Kolarić, Darko Vasiljević, Bojana Bokić, Marija Radmilović-Radjenović, and Branislav Radjenović

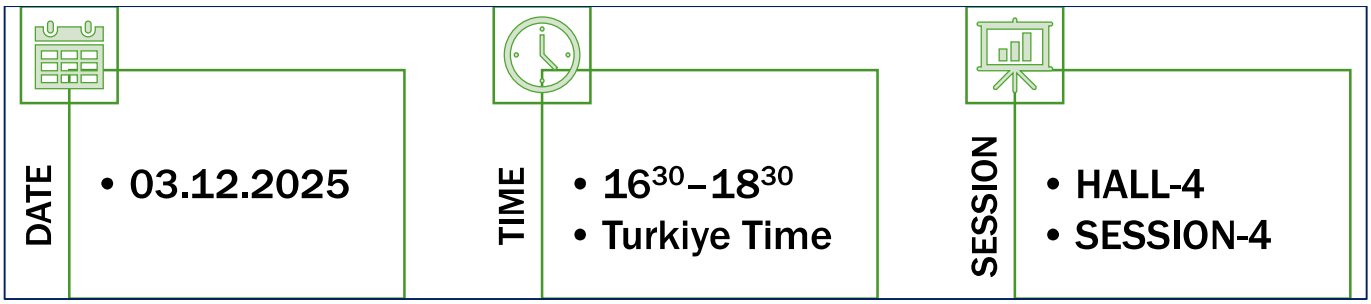
Photonics Center, Institute of Physics, University of Belgrade, Pregrevica 118, 11080 Belgrade, Serbia

ABSTRACT

This study investigates the interplay between geometry and thermodynamic properties in nanostructured materials, emphasizing the roles of convective, conductive, and radiative systems in thermal and optical control. We reveal that the corrugation and multifaceted geometry of natural photonic structures significantly shape their thermodynamic responses, with some configurations exhibiting negative heat capacity. These findings establish a connection between heat capacity and geometric form, suggesting that mimicking complex natural geometries could lead to the development of highly energy-efficient systems. Moreover, we propose a novel approach to shape heat capacity on demand by manipulating the geometry of materials without altering their chemical composition, highlighting the fundamental importance of geometrical constraints in achieving unusual thermodynamic behaviors.

Keywords: thermodynamic response, negative heat capacity, natural photonics, biophotonics, optics.

Authors acknowledge that this research was supported by the EUROPEAN INNOVATION COUNCIL AND SMES EXECUTIVE: EIC Pathfinder Challenges 2022 call through the Research Grant 101115149 (project ARTEMIS).



HEAD OF SESSION: Derra Mourad		
Shafayet HOSSAIN Afroja SULTANA Md A Razzaque SARKER	University of Rajshahi	SYNTHESIS OF $FETI_2O_4$ SPINEL VIA SOLID-STATE REACTION METHOD AND ITS THERMAL, OPTICAL, AND ELECTRICAL CHARACTERIZATION
Faisal Nazir	THE UNIVERSITY OF AGRICULTURE	PRODUCTION AND CHARACTERIZATION OF CARBON NANOTUBES FROM BIOCHAR UNDER MICROWAVE IRRADIATION
Belarbi Faten	Abdelhamid Ibn Badis University	EXPERIMENTAL STUDY OF ECO-FRIENDLY Cu_2SnS_3 THIN FILMS FOR SOLAR CELL APPLICATIONS
Branislav Radjenović Branko Kolarić Bojana Bokić Marija Radmilović-Radjenović Darko Vasiljević	University of Belgrade	GEOMETRIC EFFECTS ON THE THERMODYNAMIC PROPERTIES OF NANOSTRUCTURED MATERIALS
Zakariya Arbaoui Soufiane Elhadfi Mourad Boutahir Abdelhai Rahmani	Moulay Ismail University	BLACK PHOSPHORENE: A FIRST-PRINCIPLES STUDY FOR NEXT-GENERATION ENERGY HARVESTING
Prof. Dr. G. Nixon Samuel Vijayakumar Aishwarya. S Reshma. N Tharunikaa. P Tarnekaa. M Nivethitha. S.K Samiksha. R.K	R .M .K. Engineering College	REVIEW ON PLANCK'S QUANTUM THEORY
Derra Mourad	Ibn Zohr University	DAMAGE DETECTION METHODS FOR SQUARE-SECTION TUBES USING ULTRASONIC TECHNOLOGY
Afroja SULTANA Shafayet HOSSAIN Md A Razzaque SARKER	University of Rajshahi	THERMAL, OPTICAL, AND ELECTRICAL PROPERTY INVESTIGATION OF $FEAL_2O_4$ SPINEL OBTAINED BY SOLID-STATE REACTION METHOD
Abdelfateh BENMAKHLOUF Salah DAOUD Nadhira BIOUD Mohammed OULEDALI	University Mohamed El Bachir El Ibrahimi of Bordj Bou Arreridj University of Ahmed Draia National Polytechnic School Oran	MECHANICAL PROPERTIES OF CUBIC MgCa INTERMETALLIC COMPOUND UNDER HIGH COMPRESSION UP TO 7 GPa: DFT APPROACH

Meeting ID: 848 5448 4368 / Passcode: 090909

https://us02web.zoom.us/j/84854484368?pwd=wMotAXTV9hPAbbpcV3tbQ4fp3Z6K0m.1

THERMODYNAMIC EFFECTS OF STRUCTURAL COMPLEXITY IN NANOMATERIALS

Marija Radmilović-Radjenović, Branislav Radjenović, Darko Vasiljević, Bojana Bokić, and Branko Kolarić

Photonics Center, Institute of Physics, University of Belgrade, Pregrevica 118, 11080 Belgrade, Serbia;

ABSTRACT

This study examines how the geometry of nanostructured materials governs their thermodynamic behavior, with particular emphasis on the interplay among convective, conductive, and radiative heat transfer mechanisms in thermal and optical management. We demonstrate that intricate, corrugated architectures—inspired by natural photonic systems—can strongly influence thermodynamic responses, leading to rare phenomena such as negative heat capacity. Our findings reveal a direct and tunable relationship between geometric design and heat capacity, entirely independent of chemical composition. By showing that thermodynamic properties can be engineered solely through structural control, this work establishes geometry as a key design parameter for next-generation, energy-efficient materials and devices.

Keywords: thermodynamic response, negative heat capacity, natural photonics, biophotonics, optics.

Authors acknowledge that this research was supported by the EUROPEAN INNOVATION COUNCIL AND SMES EXECUTIVE: EIC Pathfinder Challenges 2022 call through the Research Grant 101115149 (project ARTEMIS).

Revealing Thermal Management in the Natural World by Holography

Katarina Nestorovic[1,2], Olga Vrbaški[3], Darko Vasiljević[3], Luka Krstic[4], Bojana Bokić[3], Branko Kolarić[3,5]

[1]*Military Technical Institute, Ratka Resanovica 1, 11030 Belgrade, Serbia, katarina.nestorovic993@gmail.com*
[2]*Military Academy, University of Defense, Veljka Lukica Kurjaka 33, 11042, Belgrade, Serbia*
[3]*Nanophotonics Laboratory, Photonics Center, Institute of Physics, University of Belgrade, Pregrevica 118, 11080 Belgrade, Serbia, olga.vrbaski@gmail.com, darko@ipb.ac.rs, bojana@ipb.ac.rs*
[4]*Faculty of Physics, University of Belgrade, Cara Dusana 13, 11000 Belgrade, Serbia, luka.krstic@ff.bg.ac.rs*
[5]*Micro and Nano Photonics Materials Group, University of Mons, Avenue Maistriau 19, B-7000 Mons, Belgium, Branko.KOLARIC@umons.ac.be*

The patterns of different scales influence and shape thermal management, making them essential for the survival of various biological species. Man-made photonic structures have prioritized long-range periodicity to control and shape their thermal and optical response. In contrast, biological systems operate under a fundamentally different design principle: short-range order nanostructures and corrugations that govern optical functionality rather than global crystallinity. The article presents a holographic study of various natural photonic systems (insects and butterflies), particularly the synergy of optical qualitative phase imaging with quantitative holotomography (HT) to reveal the thermal properties of these structures. The presented research opens up a new way to reveal the effect of complex geometry on thermal response in situ.